



FACULTÉ
DES SCIENCES



UNIVERSITÉ LIBRE DE BRUXELLES

Indirect Searches for Dark Matter in the Centre of the Milky Way with the IceCube Neutrino Telescope

Thesis submitted by Nadège Iovine

in fulfilment of the requirements of the PhD Degree in Physics (“Docteur en physique”)

Academic year 2021-2022

Supervisor: Professor Juan Antonio Aguilar Sánchez

Inter-University Institute for High Energies

Thesis jury:

Barbara Clerbaux (Université libre de Bruxelles, Chair)
Thomas Hambye (Université libre de Bruxelles, Secretary)
Juan Antonio Aguilar Sánchez (Université libre de Bruxelles)
Sergio Navas Concha (UGR Granada)
Kumiko Kotera (Institut d’Astrophysique de Paris)



Abstract

The existence of dark matter is now well accepted in view of the wide variety of observations that have led to its postulate. Presently, the main objective of dark matter experiments is to identify the nature of this non-visible matter. Assuming that dark matter is composed of massive particles that interact weakly with matter, it is predicted that dark matter will produce Standard Model particles when annihilating or decaying. These Standard Model particles could, in turn, produce stable charged particles found in cosmic radiation, as well as gamma-rays and neutrinos. The Milky Way is expected to be immersed in a dark matter halo with an enhanced density towards its centre. This over density would amplify the probability of dark matter particles to annihilate, making the Galactic Centre an ideal target for indirect dark matter searches. In this thesis, two indirect searches for dark matter annihilation in the Galactic Centre using data collected by two neutrino telescopes are presented.

The first analysis is a combined dark matter search using the ANTARES and the IceCube neutrino detectors. By combining a total of ~ 5.8 years and ~ 2.8 years of data collected respectively by ANTARES and IceCube, no neutrino excess was found in the direction of the Galactic Centre and limits on the dark matter annihilation cross-section, $\langle\sigma_{A\nu}\rangle$, were set. The limits thus obtained show a considerable improvement compared to the previous results derived separately by the two telescopes, for dark matter masses ranging from 50 GeV to 1 TeV. In order to carry out this first joint analysis, the analysis method as well as the parameters of the different models have been unified, providing a benchmark for future similar searches.

In the second analysis, a total of ~ 8.03 years of DeepCore data are used to search for neutrinos coming from dark matter annihilation in the centre of the galaxy at lower dark matter masses. This analysis aims to improve the detection potential for such a search. This low-energy dark matter search allows us to cover dark matter masses ranging from 5 GeV to 8 TeV. The sensitivities obtained for this analysis show considerable improvements over previous results from IceCube and other neutrino telescopes for the entire energy range considered.

Résumé

Recherche indirecte de matière noire au centre de la Voie Lactée à l'aide du télescope à neutrinos IceCube

L'existence de la matière noire est désormais bien acceptée au vu de la grande variété d'observations qui ont conduit à son postulat. À présent, le principal objectif des détecteurs de matière noire consiste à identifier la nature de cette manière non visible. À supposer que la matière noire soit composée de particules massives interagissant faiblement avec la matière, il est prédit que la matière noire produise des particules du modèle standard en s'annihilant ou se désintégrant. Ces particules du modèle standard pourraient à leur tour produire des particules chargées stables présentes dans les radiations cosmiques, ainsi que des rayons gamma et des neutrinos. Il est attendu que la Voie lactée soit immergée dans un halo de matière noire dont la densité augmente vers son centre. Cette concentration accrue favoriserait l'annihilation des particules de matière noire, faisant du centre galactique une cible idéale pour la recherche indirecte de matière noire. Dans cette thèse, deux recherches indirectes d'annihilation de matière noire dans le Centre Galactique à l'aide des données récoltées par deux télescopes à neutrinos sont présentées.

La première analyse consiste en une recherche combinée de matière noire à l'aide des détecteurs ANTARES et IceCube. En combinant un total ~ 5.8 et ~ 2.8 années de données récoltées respectivement par ANTARES et IceCube, aucun excès de neutrinos n'a été trouvé en direction du centre galactique et des limites sur la section efficace d'annihilation de la matière noire, $\langle\sigma_A v\rangle$, ont été déterminées. Les limites ainsi obtenues montrent une amélioration considérable par rapport aux résultats obtenus séparément par les deux télescopes pour des énergies allant de 50 GeV à 1 TeV. Afin de mener à bien cette première analyse conjointe, la méthode d'analyse ainsi que les paramètres des différents modèles ont été unifiés, fournissant un point de référence pour de futures recherches similaires.

Lors de la deuxième analyse, un total de ~ 8 ans de données de DeepCore est utilisé pour chercher des neutrinos provenant de l'annihilation de matière noire au centre de la galaxie pour des masses plus faibles. Cette analyse a pour but d'améliorer le potentiel de détection pour un tel type de recherche. Cette recherche de matière noire à basse énergie nous permet de couvrir des masses de matière noire allant de 5 GeV à 8 TeV. Les sensibilités obtenues pour cette analyse présentent des améliorations considérables par rapport aux résultats précédents d'IceCube et d'autres télescopes à neutrinos dans la gamme d'énergie considérée.

Acknowledgment

After five years spent searching for dark matter, the time has come to put on paper the research I have done during my PhD. All this work would not have been possible without the precious help of the wonderful people I had the chance to meet and to work with during this period.

First of all, I would like to express my deepest gratitude to Juan Antonio Aguilar Sánchez, who has been a very present and supportive supervisor during the five years I spent at the Inter-University Institute for High Energy (iihe). I started working under his supervision to complete my master's thesis and was fortunate enough to continue this research during my PhD. Thanks to your guidance, I was able to acquire the necessary knowledge and skills to conduct the work presented in this manuscript. Your insightful comments and expertise have been a great help throughout this PhD. I would also like to thank you for your kindness and understanding, which also helped me grow during the pursuit of this PhD.

I would also like to extend my warmest thanks to the members of the jury, who showed a great interest in my work. During the review process, Barbara Clerbaux, Thomas Hambye, Juan Antonio Aguilar Sánchez, Sergio Navas Concha, and Kumiko Kotera provided very useful comments after taking the time to carefully read the thesis. As part of my support committee, Thomas and Barbara were also involved in the early stages of my work, which they followed with attention throughout the last four years.

As a recipient of a FRIA grant, I gratefully acknowledge the financial support of the F.N.R.S. which allowed me to devote myself to the completion of this thesis.

My gratitude also goes to Christoph Tönnis and Sara Rebecca Gozzini for the work and effort they put in for the combined search carried out during the first part of my thesis. Rebecca was the contact person for the ANTARES collaboration and as such, she was of great help for this joint analysis. She also provided me with all the necessary ingredients required from the ANTARES side, which she kindly recomputed as many times as necessary for the smooth running of this analysis. As the primary analyser of the ANTARES analysis from which the data set used for the analysis were taken, Christoph was also very helpful and took the time to answer my numerous questions.

I will always keep a very good memory of the time spend at the iihe. I was lucky to find true friends among the many welcoming colleagues working at the institute. Although the pandemic deprived us of many moments that could be shared at the institute, it was a pleasure to work among you all. I have also been fortunate enough to share my workspace with the best office mate one could hope for, Daniela, who always had the right words to motivate me to move forward. I would also like to personally thank Sebastian who was of tremendous help during his too short time at

the institute.

Of course, I would also like to thank the entire IceCube collaboration for creating a friendly working environment and for all the help received by its members. I really enjoyed the bi-annual IceCube meetings and will keep very good memories of my times as a member of IceCube.

Last but not least, I would also like to take this opportunity to thank my family and friends for their precious support and understanding through my entire PhD. They made it possible for even the most stressful time in my life to be filled with moments of joy. I can say with certainty that I would not be where I am today without their love and cheers. For always being there for me, thank you.

Abbreviations

ADC	Analogue to Digital Converter
AGN	Active Galactic Nuclei
ARS	Analogue Ring Sampler
ATWD	Analogue Transient Waveform Digitiser
BAO	Baryon Acoustic Oscillation
BBN	Big Bang Nucleosynthesis
BDT	Boosted Decision Tree
B.R.	Branching Ratio
BSM	Beyond Standard Model
BSS	Bottom String Socket
CC	Charged Current
CDM	Cold Dark Matter
CI	Confidence Interval
CL	Confidence Level
CMB	Cosmic Microwave Background
CNB	Cosmic Neutrino Background
CNO	Carbon–Nitrogen–Oxygen
COG	Centre Of Gravity
CR	Cosmic Ray
DAQ	Data AcQuisition
DIS	Deep Inelastic Scattering
DM	Dark Matter
DOM	Digital Optical Module
DSNB	Diffuse Supernova Neutrino Background
dSphs	Dwarf Spheroidal galaxies
DWDM	Dense Wave length Division Multiplexing
EW	Electroweak

fADC	fast Analogue to Digital Converter
GBDT	Gradient Boosting Decision Trees
GC	Galactic Centre
GRB	Gamma Ray Burst
HE	High Energy
HFLBL	High Frequency Long Base Line
HLC	Hard Local Coincidence
HV	High Voltage
ICL	IceCube Laboratory
JB	Junction Box
KDE	Kernel Density Estimation
KK	Kaluza-Klein
Λ CDM	Lambda Cold Dark Matter
LC	Local Coincidence
LCM	Local Control Module
LE	Low Energy
LHC	Large Hadron Collider
LKP	Lightest of the Kaluza-Klein Particles
LLH	Log Likelihood
LPM	Landau-Pomeranchuk-Migdal
LSP	Lightest Supersymmetric Particle
MACHO	Massive Compact Halo Object
MC	Monte Carlo
MCPE	MC photo-electron
MEOC	Main Electro-Optical Cable
MLCM	Master Local Control Modules
MOND	Modified Newtonian Dynamics
MOU	Memorandum of Understanding
MSSM	Minimal Supersymmetric Standard Model
NC	Neutral Current
NFW	Navarro-Frenck-White
NRP	Nuclear Resonance Production
OM	Optical Module
OMF	Optical Module Frame
OW	OneWeight

PBH	Primordial Black Hole
PDF	Probability Density Function
PE	Photo-Electron
p.e.	pseudo-experiment
PID	Particle IDentifier
PMT	Photo-Multiplier Tube
QES	Quasi-Elastic Scattering
RA	Right Ascension
RAPCal	Reciprocal Active Pulsing Calibration
RES	Resonance
SCM	String Control Module
SD	Spin-Dependant
SI	Spin-Independant
SLOP	SLOW Particle
SM	Standard Model
SMT	Simple Multiple Triggers
SRT	Seeded Radius-Time
SUSY	SUPERSYMMETRY
TMVA	Toolkit for Multivariate Data Analysis
TS	Test Statistic
TVC	Time to Voltage Converter
UED	Universal Extra-Dimensions
UHECRs	Ultra-High Energetic Cosmic Ray
USStd	US Standard
UV	Ultra-Violet
VICH	Veto Identified Causal Hits
WIMP	Weakly Interacting Massive Particle

Contents

Abstract	i
Résumé	iii
Acknowledgment	v
Abbreviations	vii
Contents	xi
List of Figures	xv
List of Tables	xxi
Introduction	1
1 Neutrino astronomy	3
1.1 Neutrino interactions	3
1.2 Neutrino oscillation	6
1.3 Expected neutrino sources	8
1.3.1 Low energy neutrinos	8
1.3.2 High energy neutrinos	10
2 Cherenkov telescopes	13
2.1 Detection Method	13
2.1.1 Cherenkov effect	13
2.1.2 Photomultiplier tubes	15
2.2 Detector layouts	16
2.2.1 ANTARES	16
2.2.2 IceCube	17
2.3 Optical sensors	19
2.3.1 ANTARES	19
2.3.2 IceCube	19
2.4 Data acquisition	21
2.4.1 ANTARES	21
2.4.2 IceCube	22

2.5	Event topology in the detectors	24
2.5.1	Cascade events	25
2.5.2	Track events	26
2.5.3	Noise	27
2.6	Expected background	27
2.6.1	Cosmic Rays	28
2.6.2	Astrophysical neutrinos	32
2.6.3	Bio-luminescence	32
2.7	Optical properties of the detector mediums	32
2.7.1	Mediterranean Sea water	33
2.7.2	South Pole ice	34
2.8	Data processing	36
2.8.1	ANTARES	36
2.8.2	IceCube	37
2.9	Detector stability and calibration	38
2.9.1	ANTARES	38
2.9.2	IceCube	39
3	Dark Matter	41
3.1	Dark matter evidences	41
3.1.1	Mass discrepancy in galaxy clusters	41
3.1.2	Galactic rotation curves	42
3.1.3	Gravitational lensing	43
3.1.4	Cosmic microwave background	45
3.2	Dark matter candidates	47
3.2.1	Baryonic dark matter	48
3.2.2	Non-baryonic dark matter	48
3.2.3	Modified gravity	51
3.3	Dark matter detection	51
3.3.1	Direct dark matter searches	52
3.3.2	Indirect dark matter searches	55
3.3.3	Dark matter production at colliders	57
3.4	Expected neutrino signal from dark matter annihilation in the Galactic Centre	58
4	Combined dark matter search with ANTARES and IceCube	61
4.1	Monte Carlo simulation	62
4.1.1	ANTARES	62
4.1.2	IceCube	64
4.2	Visibility of the Galactic Centre	67
4.3	Event selection	67
4.3.1	ANTARES	68
4.3.2	IceCube	71
4.4	Signal expectation	78
4.4.1	Energy spectra	78
4.4.2	Dark matter halo profiles	80

4.5	Effective area and acceptance	81
4.6	Analysis method	82
4.6.1	Probability density functions	83
4.6.2	Likelihood formulation	84
4.6.3	Limit computation	86
4.7	Treatment of systematic uncertainties	87
4.7.1	Astrophysical uncertainty	87
4.7.2	Detector systematics	87
4.8	Results of the combined dark matter search	88
4.8.1	Unblinded results	88
4.8.2	Comparison to other experiments	93
5	Low energy dark matter search with eight years of IceCube data	97
5.1	Monte Carlo Simulation	97
5.1.1	Atmospheric muons	98
5.1.2	Neutrinos	98
5.1.3	Particle propagation and light production	99
5.1.4	Noise emulation and detector response	99
5.2	Event Selection	99
5.2.1	Level 3	100
5.2.2	Level 4	100
5.2.3	Level 5	101
5.2.4	Level 6	102
5.2.5	Level 7	103
5.3	Effective area	105
5.4	Signal Expectation	106
5.5	Analysis Method	108
5.5.1	Probability density functions	108
5.5.2	Limit computation	116
5.6	Sensitivities	118
5.6.1	Comparison to previous results	119
5.7	Treatment of systematic uncertainties	120
5.8	Unblinding procedure	124
5.8.1	Pre-unblinding check	124
5.8.2	Outlooks	126
	Conclusion	129
	Bibliography	131

List of Figures

1.1	Total CC cross-sections over energy (solid) for neutrinos (left) and anti-neutrinos (right) as a function of the neutrino energy. The individual contributions from QE (dashed), RES (dot-dashed) and DIS (dotted)	4
1.2	Feynman diagrams of the neutral current neutrino interactions (1) and the charged current interactions of ν_e (2), ν_μ (3), ν_τ (4)	5
1.3	Scattering cross-section of neutrinos as a function of energy taken	6
1.4	Measured and expected neutrino fluxes from possible neutrino sources as	9
2.1	Illustration of the Cherenkov effect. The left-hand figure shows the case in which the particle is moving with a speed $v < c/n$, while the right-side plot shows the situation in which the particle has a speed $v > c/n$	14
2.2	Schematic view of a photomultiplier tube	15
2.3	Schematic view of the ANTARES neutrino telescope located in the Mediterranean Sea	17
2.4	Schematic view of the IceCube neutrino telescope located at the South Pole. Credit: IceCube Collaboration	18
2.5	Schematic view of an optical module used in the ANTARES detector. Credit: ANTARES Collaboration	20
2.6	Schematic view of a digital optical module used in the IceCube detector. Credit: IceCube Collaboration	21
2.7	Illustration of the two events topologies for a track event (left) and a cascade event (right). Both events were observed by the IceCube neutrino telescope. The arrival time of the incident photons is indicated by the colour palette, where red marks the earliest hits and blue the late hits. The amount of deposited light recorded by a particular PMT is represented by the size of the DOM. Credit: IceCube Collaboration	24
2.8	Overall energy losses of electrons (left) and muons (right) in ice shown together with the individual contribution from the different undergoing processes	27
2.9	View of the detector triggered by pure noise hits in coincidence. Credit: IceCube Collaboration	28
2.10	The left panel shows the energy-weighted spectrum from air shower measurements performed by various experiments as a function of the energy. The right-hand panel shows the individual contributions of different particles to vertical	29

2.11	Angular distribution of the expected muon flux from atmospheric muons and muons induced by the interaction of atmospheric neutrinos with energies	31
2.12	Values of the absorption (blue dots) and scattering (red triangles) lengths measured at the location of the ANTARES neutrino telescope	33
2.13	Values of the absorption, $a(400)$, and the effective scattering, $b_e(400)$, coefficients as a function of depth for both the SPICE-Mie and SPICE-Lea	36
3.1	Measure of the rotation velocity of OB stars in M31 as a function of their	43
3.2	Merging sub-cluster 1E 0657-558, called the Bullet Cluster, as seen from	45
3.3	Temperature power spectrum of the CMB measured by Planck	46
3.4	Diagram of the possible interaction between SM and DM particles, where the three methods used to search for DM particles are represented.	52
3.5	90% C.L. upper limits on the spin-independent DM-nucleon	53
3.6	Single-hit oscillation residual rate measured by phase 1 and phase 2 of the DAMA/LIBRA experiment in the energy range from 2 to 6 keV as a function of	54
3.7	Comparison of the 90% C.L. limits set by neutrino and γ -ray experiments on the thermally-averaged self-annihilation cross-section $\langle\sigma_A v\rangle$ as a	57
3.8	Comparison of the 90% C.L. upper limits on the spin-independent (left) and spin-dependent (right) DM-nucleon cross-sections set by CMS (red lines) and	58
3.9	Left: Dark matter density, $\rho_{\text{DM}}(r)$, as a function of the radial distance to the Galactic Centre, r , for the NFW and Burkert profiles. Right: J-factor, $J(\Psi)$, as a function of the angular distance to the Galactic Centre, Ψ , for the NFW and Burkert profiles. Both the dark matter densities and J-factors are computed with halo parameters values taken from 3.11.	60
4.1	Schematic view of the cylindrical volume used for muon track generation in MUPAGE, referred to as the can.	63
4.2	Visibility of the ANTARES (left) and IceCube (right) neutrino telescopes in galactic coordinates, where the location of the Galactic Centre is marked by a red dot and the colour scale indicates the level of visibility.	68
4.3	Illustration of the veto used to reject atmospheric muons by selecting only events starting within the DeepCore volume shown as the blue delimitation in the upper part of the figure. The considered vetoed fiducial volume is highlighted in green in the lower part of the plot. Credit: IceCube collaboration.	73
4.4	Comparison of the PPC4 spectra (solid lines), which are used for the ANTARES-only analysis, and the spectra computed with Pythia 8.1 for the IceCube-only analysis (dashed lines). The muon neutrino spectra at Earth are shown for dark matter particles with masses of 100 GeV (left) and 1 TeV (right) annihilating through the four channels scanned for the combined analysis.	79

4.5	Comparison of neutrino effective area obtained for the IceCube (blue) and the ANTARES (green) detectors, which are computed with the simulation samples described respectively in the subsections 4.1.2 and 4.1.1 for events with declinations between $\delta_{GC} - 30^\circ$ and $\delta_{GC} + 30^\circ$.	81
4.6	Comparison of the acceptance computed for ANTARES (dashed lines) and IceCube (solid lines) for the four annihilation channels considered and the entire dark matter mass range.	82
4.7	ANTARES PDFs for the QFit (left) and λ Fit (right) reconstructions. Both histograms show the background PDF (teal) and the signal PDF for the $\tau^+\tau^-$ annihilation channel and NFW profile, assuming $m_{DM} = 100$ GeV (purple).	84
4.8	Top: IceCube background PDF obtained from data scrambled in RA, where the colour scale expresses the probability density. Bottom: IceCube signal PDF for $\tau^+\tau^-$ channel and $m_{DM} = 100$ GeV assuming the NFW profile.	85
4.9	Combined 90% C.L. upper limits on $\langle\sigma_{Av}\rangle$ for the NFW (left) and Burkert (right) dark matter halo profiles.	89
4.10	Comparison of the combined 90% C.L. upper limits (solid) and sensitivities (dashed) in terms of $\langle\sigma_{Av}\rangle$ shown alongside the expected 1σ (green) and 2σ (yellow) bands around the sensitivity.	91
4.11	Combined 90% C.L. upper limits on the $\langle\sigma_{Av}\rangle$ compared	92
4.12	Combined 90% C.L. upper limits on $\langle\sigma_{Av}\rangle$ as a function of the dark matter mass assuming the NFW halo profile and annihilation through $\tau^+\tau^-$. Limits	93
5.1	Comparison of the neutrino effective area obtained with the OscNext event selection (described in Section 5.2) and the IceCube sample used for the combined DM search presented in Section 4.3 for declinations ranging from $\delta_{GC} - 30^\circ$ to $\delta_{GC} + 30^\circ$.	106
5.2	Expected neutrino spectra at Earth for dark matter annihilation through the four channels considered and dark matter masses of 100 GeV (left) and 1 TeV (right).	107
5.3	Distribution of the background events as a function of the reconstructed energy, E_{reco} . The weighted contributions from the different MC samples are shown along the total background distribution. The weighted median is shown along the lower and upper bound containing 95% of the background.	108
5.4	Event distribution with respect to the particle ID. The weighted contributions from the different MC samples are shown along the total background distribution. The separations of the PID bins are indicated by the vertical grey lines.	110

5.5	Projections of the background PDF for third PID bin in Ψ_{reco} when no KDE is applied (shaded blue) compared to the PDF obtained with KDE built in $\log(\Psi_{reco}) - \log_{10}(E_{reco})$ with bandwidth computed with the Scott's rule of thumb (purple) and the cross-validation method (pink), along with the KDE built in $\Psi_{reco} - \log_{10}(E_{reco})$ with boundary reflection (green).	112
5.6	Three-dimensional background PDF split into the individual contributions of each of the three PID bins. The bottom right histogram shows the 2D projection of the events in Ψ_{reco} and $\log_{10}(E_{reco})$. The colour scale expresses the probability density.	113
5.7	Three-dimensional signal PDF split into the individual contributions of each of the three PID bins for DM particles with masses of 100 GeV annihilating through the $\tau^+\tau^-$ channel, assuming the NFW halo profile. The bottom right histogram shows the 2D projection of the events in Ψ_{reco} and $\log_{10}(E_{reco})$.	115
5.8	Comparison of the two-dimensional projections of the signal PDF in Ψ_{reco} (left) and $\log_{10}(E_{reco})$ and the raw histogram containing the signal events (right). This comparison is shown for DM particles with masses of 100 GeV annihilating through the $\nu_\mu\bar{\nu}_\mu$ channel, assuming the NFW halo profile. The colour scale expresses the probability density.	116
5.9	Test statistic distribution $f(q_\mu \mu)$ and $f(q_\mu 0)$ computed for dark matter particles with masses of 100 GeV (left) and 1000 GeV (right) annihilating through the $\tau^+\tau^-$ annihilation channel, assuming DM to be distributed according to the NFW halo profile. The median value of $f(q_\mu 0)$ and the percentage of $f(q_\mu \mu)$ falling on each part of this median value are also shown. The distribution $f(q_\mu \mu)$ is compared to a χ^2 fit (green line) in order to visualise the validity of the assumptions made in order to apply Wilks' theorem.	118
5.10	90% C.L. median upper limits on $\langle\sigma_A v\rangle$, which are quoted as sensitivities, shown for the NFW (left) and Burkert (right) dark matter halo profiles. The sensitivities are obtained with the oscNext samples, consisting of 8.03 years of DeepCore data.	119
5.11	90% C.L. sensitivity in terms of the thermally-averaged DM self-annihilation cross-section $\langle\sigma_A v\rangle$ for DM annihilation through $\tau^+\tau^-$, assuming the NFW halo profile. This sensitivity is presented alongside the latest published limits from IceCube and ANTARES, as well as the results from the combined DM search presented in Chapter 4.	120
5.12	Impact of the atmospheric flux (left) and detector (right) systematics on the 90% C.L. sensitivities for DM annihilation through the $\tau^+\tau^-$ channel, assuming DM distribution according to the NFW halo profile.	122
5.13	Impact of uncertainties on the free halo parameters used to compute the J-factor (shown in Table 3.1) for the NFW halo profile.	124

5.14	Comparisons of the MC background (histograms) and the data (dots) distributions in terms of the reconstructed energy. Each plot show the separate contribution from atmospheric neutrinos (purple) and muons (light blue) to the total background distribution (dark blue). The data/MC ratio is also shown in the lower panel of each figure.	125
5.15	Comparisons of the MC background (histograms) and the data (dots) distributions in terms of the opening angle to the Galactic Centre. Each plot show the separate contribution from atmospheric neutrinos (purple) and muons (light blue) to the total background distribution (dark blue). The data/MC ratio is also shown in the lower panel of each figure. . . .	126

List of Tables

1.1	Values of the mixing angles between the three neutrino flavours as well as the squared mass differences used for the two analyses discussed in this thesis. The	8
2.1	Effective scattering and absorption lengths of the Mediterranean seawater measured using a dedicated PMT and an isotropic light source with	34
3.1	Dark matter halo parameters of the NFW and the Burkert profiles	59
4.1	Summary of the initial cuts applied on ANTARES runs.	69
4.2	Overview of the data used for the ANTARES event selection.	71
4.3	Summary of the cuts and selection conditions applied at level 3.	74
4.4	Summary of the cuts and selection conditions applied at level 4.	75
4.5	Summary of the cuts and selection conditions applied at level 5.	76
4.6	Summary of the variables used for the BDT computed at level 6.	78
4.7	Final 90% C.L. combined sensitivities (left column) and 90% C.L. combined upper limits (right column) in terms of $\langle\sigma_A v\rangle$ for the NFW (upper table) and the Burkert (lower table) halo profiles.	94
5.1	Summary of the cuts and selection conditions applied at level 3.	100
5.2	Summary of the cuts and selection conditions applied at level 4.	101
5.3	Summary of the cuts and selection conditions applied at level 5.	102
5.4	Summary of the cuts and selection conditions applied at level 6 for the high statistic samples.	103
5.5	Summary of the cuts and selection conditions applied at level 7.	104
5.6	Summary of the dark matter mass and annihilation channel combinations scanned for the dark matter search in the GC with 8.03 years of DeepCore data.	109
5.7	Summary of the model parameters used for the four bulk ice systematic sets (upper half) and the four hole ice systematic sets (lower half).	123

Introduction

This thesis focuses on the search for neutrinos coming from dark matter annihilation in the centre of the Milky Way. It is split in two separate analyses, the first of which combines data of two experiments, while the other focuses on low energies.

This thesis is structured as follows. In chapter [1](#), the properties of neutrinos are introduced. These neutral particles have properties that make them ideal astrophysical messengers. As they only interact weakly with matter, neutrinos are not absorbed when going through dense regions of space. As a result, neutrinos can provide insights about regions opaque to photons. In addition, neutrinos can reach the Earth without being deflected by magnetic fields on their way since they are neutral particles and can thus be used to point back at the source. This chapter also explores possible neutrino sources.

As a result of the low interaction cross-section of neutrinos, a large volume of material is needed for their detection. In order to achieve such large detector volume at lesser costs, it is possible to deploy an array of photo-sensors in a naturally dark and dielectric medium, like seawater or the Antarctic ice. The deployed photo-detectors can then record the Cherenkov light created by secondary charged particles from neutrino interactions moving through the detector medium. For this thesis, two experiments are considered: the ANTARES neutrino telescope located in the Mediterranean Sea and the IceCube detector located at the South Pole. The lay-outs of both telescopes are described in detail in Chapter [2](#), along with the detection principle.

As early as in the 1930s, evidences in favour of "unseen matter" were given by astronomical observations. This so-called dark matter is responsible for about 27% of the total mass-energy of the Universe. Although the existence of dark matter is well-supported by a variety of observations, its properties remain unknown. One of the most accepted hypotheses to this day is that dark matter is made of Weakly Interacting Massive Particles (WIMPs), unobserved yet. These dark matter particles are expected to be non-relativistic, electromagnetically neutral, non-baryonic and interacting only through weak interactions. Several approaches are considered to search for these dark matter particles. The existing experimental techniques can be split in three main categories: the direct dark matter searches, the dark matter production at particle colliders and the indirect dark matter searches. This thesis is centred on the latter. Ground-based and space observatories could then detect these messengers. Indirect search experiments are looking for Standard Model (SM) particles produced by the annihilation or decay of dark matter. Among the SM particles produced by dark matter annihilation or decay, neutrinos can be produced in the final states. In Chapter [3](#), the evidence supporting the existence of dark matter are described in detail, along with

possible dark matter candidates. The detection methods and the expected signal from dark matter annihilation are also described in this chapter.

The first analysis, which consists of a dark matter search combining data from both the ANTARES and the IceCube detectors, is detailed in Chapter 4. Similar analyses were previously performed by each collaboration separately, providing corresponding limits on the thermally-averaged self-annihilation cross-section. For dark matter masses ranging from 50 GeV to 1 TeV, the limits obtained by each detector are of comparable order of magnitude. Therefore, this energy range is chosen to perform the combined search. In this work, the goal is to improve the detection potential by combining the data sets of both experiments in this particular mass range. This analysis is a continuation of my master thesis, whose objective was to evaluate the feasibility of such a combined search. In order to carry out this joint analysis, the differences between the approaches taken by the two detectors for this kind of dark matter searches had to be evaluated. Once identified, the parameters that differed were unified.

The second part of this thesis focuses on a dark matter search with IceCube at lower energies, for which an optimised data set with more years of data is used as described in Chapter 5. For the previous dark matter search conducted with IceCube, only three years of data were considered. Since then, more years of IceCube data were made available and this analysis uses slightly over eight years of data taken from 2012 to 2020. An event selection dedicated to perform atmospheric neutrino oscillation measurements is used. This event selection presents considerable improvement with respect to the samples previously used for similar searches, especially at the lowest energies. For this analysis, information about the energy and neutrino flavour of the events are introduced for the first time. The combination of these changes leads to non-negligible enhancements of the sensitivities obtained for this search with respect to previous IceCube analyses.

For both analyses, a binned likelihood method is used to search for an excess of signal neutrinos in the direction of the Galactic Centre. This likelihood method compares the data distribution to expectations deduced from the background and signal distributions. The null hypothesis assumes that data can be expressed from the background only, whereas the tested hypothesis expresses data as a combination of background and signal events. With this shape likelihood method, the most likely fraction of signal neutrinos in the experimental data is computed. The specifics of the analysis methods used for each analysis are described extensively in their respective dedicated chapters. Lastly, the outcomes of the two dark matter searches are outlined and discussed in Chapter 5.8.2, along with potential ways to improve such indirect dark matter searches.

Chapter 1

Neutrino astronomy

The existence of neutrinos was first postulated as a "desperate remedy" by W. Pauli in 1930 to solve the problem of the conservation of momentum, energy, and angular momentum in the beta decay process. Neutrinos are electrically neutral particles interacting weakly with matter. As these properties make them hard to detect, it was not until 1956 that neutrinos were observed for the first time [1]. There are three flavours of neutrinos, namely electron (ν_e), muon (ν_μ) and tau (ν_τ) neutrinos. Neutrinos are 1/2 spin fermions which are part of the lepton family, just as their charged counterpart particles: electrons (e^\pm), muons (μ^\pm) and taus (τ^\pm). Neutrinos are expected to have very small although non-null masses, as indicated from observations of neutrino oscillation. Thanks to their properties, neutrinos are ideal astrophysical messengers. As they only interact weakly with matter, neutrinos are not absorbed or scattered in dense regions of space, unlike photons or cosmic rays. Thus, they are able to travel freely from regions opaque to other messengers, paving the way to new discoveries. Furthermore, as neutrinos are neutral particles, they are not deflected by magnetic fields on their way to the Earth, carrying information about the source location. High energy neutrinos are expected to be produced by some of the most cataclysmic and interesting events occurring in the Universe, e.g. exploding stars, gamma ray bursts, supernova remnants, neutron stars, as well as annihilation of dark matter. In this chapter, the properties of neutrinos as well as their possible source are discussed in more detail.

1.1 Neutrino interactions

The existence of neutrinos is deduced from the charged particles produced during their interaction with matter via the weak nuclear force. Such interactions happen through the exchange of either neutral bosons (Z^0) for neutral current (NC) interactions or charged bosons (W^\pm) in the case of charged current (CC) interactions. In order to preserve the charge, the CC interactions of neutrinos lead to the creation of their associated charged leptons:

$$\nu_l + N \rightarrow l^- + X, \quad (1.1)$$

$$\bar{\nu}_l + N \rightarrow l^+ + X, \quad (1.2)$$

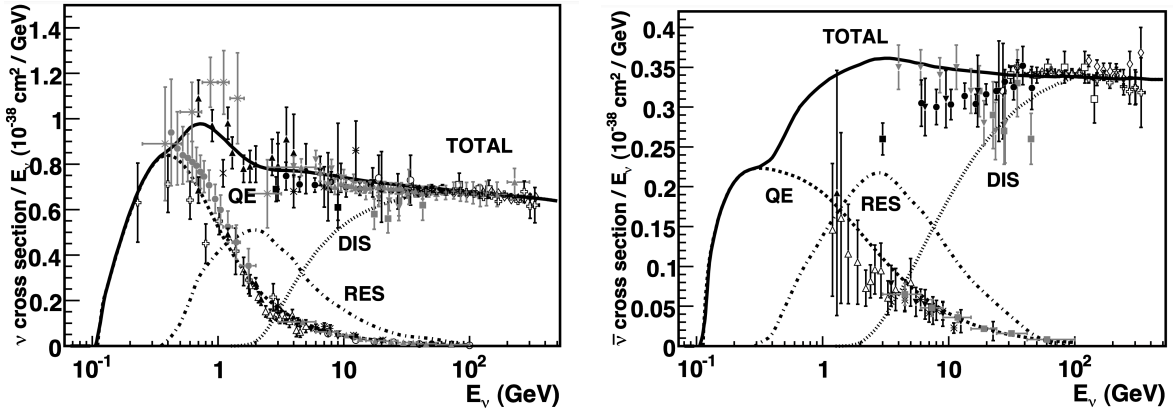


Figure 1.1—Total CC cross-sections over energy (solid) for neutrinos (left) and anti-neutrinos (right) as a function of the neutrino energy. The individual contributions from QE (dashed), RES (dot-dashed) and DIS (dotted) are also plotted [2].

where N indicates a nucleon and X is the hadronic shower resulting from the interaction. The index l denotes the one of the three neutrino flavours, i.e. e , μ or τ . For neutral current interactions, the incident neutrino scatter off the nucleon such that:

$$\nu_l + N \rightarrow \nu_l + X, \quad (1.3)$$

$$\bar{\nu}_l + N \rightarrow \bar{\nu}_l + X. \quad (1.4)$$

Based on the energy of the incident neutrino, three main categories of scattering processes can be defined: the elastic or quasi-elastic scattering, the resonance production (RES) and the deep inelastic scattering (DIS) [2]. Their individual contributions to the total (anti-)neutrino cross-section are visible in Figure 1.1 for CC interactions. For elastic and quasi-elastic scattering, the target nucleon remains almost unchanged as the quasi-totality of the incident momentum is transferred to the single (or few) nucleon(s) released from the target in the process. For CC interactions, this process is referred to as quasi-elastic scattering (QES) as there is a transfer of charge. As a result of the CC interaction of a neutrino, the scattered neutron will be converted into a proton, while the CC interaction of anti-neutrinos will cause the target proton to turn into a neutron. For NC interactions, the process is called elastic scattering as the scattered nucleon remain unchanged. Elastic and quasi-elastic scattering are the dominant scattering mechanisms for energies below 1 GeV. When considering energies ranging from 1 GeV to 10 GeV, the main scattering process is RES. In that specific case, the target nucleon can be excited by the neutrino and reach a resonance state, which can then decay into various mesons and nucleons. Finally, for energies above 10 GeV, neutrinos interact with matter through DIS. In this process, neutrinos are able to directly interact with the basic constituents of the targeted nucleon, i.e. quarks and gluons, and diffuse them individually. The incident neutrino "breaks" the original nucleon and creates an hadronic shower. Feynman diagrams illustrating these (anti-)neutrinos interactions are shown in Figure 1.2. Four specific cases can be distinguished depending on the neutrino flavour and the type of interaction (NC or CC). When interacting

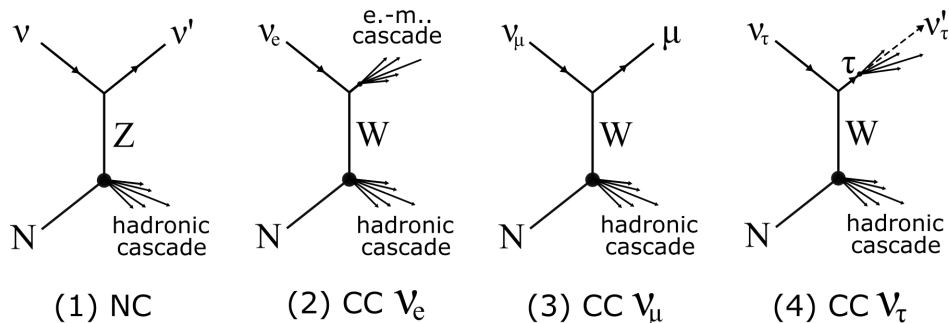


Figure 1.2—Feynman diagrams of the neutral current neutrino interactions (1) and the charged current interactions of ν_e (2), ν_μ (3), ν_τ (4).

with a nucleon of the medium through CC interactions, an electron (anti-)neutrino will create an electron (e^\pm). This resulting charged particles will quickly lose their energy, producing an electromagnetic shower. For CC interactions of muon (anti-)neutrinos, a muon (μ^\pm) is produced in a direction almost aligned with that of the incident neutrino. Lastly, for tau neutrino CC interactions, the tau lepton (τ^\pm) created has a short lifetime of about $\sim 2.8 \times 10^{-13}$ s, resulting in its rapid decay. The decay of this tau lepton can lead to the production of a muon with a $\sim 17\%$ branching ratio (B.R.), as well as to the creation of an electron or a hadron with a B.R. of $\sim 83\%$. The latter would result in the creation of electromagnetic or hadronic showers along with a tau neutrino.

Besides the interactions between neutrino and nucleon described above, electron anti-neutrinos can be involved in another type of interaction. Indeed, $\bar{\nu}_e$ can interact with the electrons of the surrounding medium and create a charged W-boson, such that:

$$\bar{\nu}_e + e^- \rightarrow W^- . \quad (1.5)$$

This resonant scattering interaction was predicted in 1960 and is known as the Glashow resonance [3]. As seen in Figure 1.3, a peak in the cross-section for such interaction is expected for electron neutrinos with energies of 6.3 PeV. The observation of a particle shower with a visible energy of 6.05 ± 0.72 PeV, consistent with a Glashow resonance event, was recently reported by the IceCube collaboration [4]. The observed event is categorised as an astrophysical neutrino with a 5σ confidence level (CL). The Glashow resonance origin of this event is favoured with a significance of 2.3σ over other NC and CC interaction scenarios.

Figures 1.3 also shows that the interaction cross-section of neutrinos increases linearly with energy when considering neutrinos with energies up to $\sim 10^6$ GeV. Above this energy, the interaction cross-section of neutrinos can be described by an energy power-law. Due to this increase of the neutrino interaction cross-section with energy, neutrinos with very high energies might get absorbed by matter. For neutrinos with energies of about 1 PeV, the mean free path in matter become similar to the Earth diameter. Therefore, neutrinos with energies higher than a few PeV will not be able to reach the detector from up-going directions as they will be absorbed by the Earth.

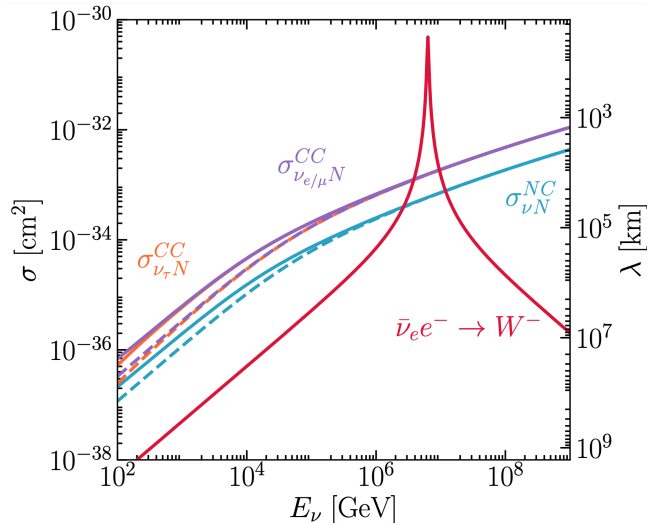


Figure 1.3—Scattering cross-section of neutrinos as a function of energy taken from [5]. The Glashow resonance case (red) is presented along with deep inelastic scattering processes associated to NC interactions of all neutrino flavours (blue), as well as to the CC interaction of both electron and muon neutrinos (purple) and tau neutrino (orange).

1.2 Neutrino oscillation

The principle of neutrino oscillation was introduced in the 1960s for two neutrino flavours [6], as well as for the mixing between neutrino and anti-neutrino states [7]. The effects of neutrino oscillation were first observed by the Super-Kamiokande observatory in 1998, using atmospheric neutrino measurements [8]. Neutrino oscillation can be explained by the mixing of different flavour eigenstates, ν_α , which are linear combinations defined from the mixing matrix, U and the mass eigenstates; ν_i :

$$\nu_\alpha = \sum_{i=1}^n U_{\alpha i} \nu_i, \quad (1.6)$$

where n is the number of neutrino flavours. When considering three neutrinos flavour eigenstates and under the assumption that neutrinos are Majorana particles, the mixing matrix can be expressed as

$$U = \begin{pmatrix} 1 & 0 & 0 \\ 0 & c_{23} & s_{23} \\ 0 & -s_{23} & c_{23} \end{pmatrix} \begin{pmatrix} c_{13} & 0 & s_{13}e^{-i\delta_{\text{CP}}} \\ 0 & 1 & 0 \\ -s_{13}e^{i\delta_{\text{CP}}} & 0 & c_{13} \end{pmatrix} \begin{pmatrix} c_{12} & s_{12} & 0 \\ -s_{12} & c_{12} & 0 \\ 0 & 0 & 1 \end{pmatrix} \begin{pmatrix} e^{i\eta_1} & 0 & 0 \\ 0 & e^{i\eta_2} & 0 \\ 0 & 0 & 1 \end{pmatrix}, \quad (1.7)$$

where $s_{ij} \equiv \sin(\theta_{ij})$, $c_{ij} \equiv \cos(\theta_{ij})$ and θ_{ij} is the mixing angle. This neutrino mixing matrix rely on three phase parameters in addition to the three mixing angles. Among these CP-violating phases, δ_{CP} is the Dirac phase, while the phases $\eta_i \in [0, 2\pi]$ are only relevant when assuming neutrinos to be Majorana particles. Therefore, when

considering neutrino to be Dirac particles, the last matrix of Equation [1.7](#) can be left out, resulting in the following oscillation matrix:

$$U = \begin{pmatrix} c_{12} c_{13} & s_{12} c_{13} & s_{13} e^{-i\delta_{\text{CP}}} \\ -s_{12} c_{23} - c_{12} s_{13} s_{23} e^{i\delta_{\text{CP}}} & c_{12} c_{23} - s_{12} s_{13} s_{23} e^{i\delta_{\text{CP}}} & c_{13} s_{23} \\ s_{12} s_{23} - c_{12} s_{13} c_{23} e^{i\delta_{\text{CP}}} & -c_{12} s_{23} - s_{12} s_{13} c_{23} e^{i\delta_{\text{CP}}} & c_{13} c_{23} \end{pmatrix}, \quad (1.8)$$

which is known as the Pontecorvo-Maki-Nakagawa-Sakata (PMNS) mixing matrix. There is currently no concrete evidence allowing to reach a consensus on whether neutrinos are Majorana or Dirac particles, which is why the two cases are discussed. The probability of a neutrino to oscillate from the α to the β flavour is given by:

$$P_{\nu_\alpha \rightarrow \nu_\beta} = |\langle \nu_\beta | \nu_\alpha(t) \rangle|^2 = \left| \sum_{i=1}^3 \sum_{j=1}^3 U_{\alpha i}^* U_{\beta j} \langle \nu_j | \nu_i(t) \rangle \right|^2, \quad (1.9)$$

where $|\nu_i(t)\rangle = e^{-iE_i t} |\nu_i(0)\rangle$ under the assumption that $|\nu\rangle$ is a plane wave. The energy of the neutrino mass eigenstate ν_i can be expressed as $E_i = \sqrt{p_i^2 + m_i^2}$, where m_i is the mass of the eigenstate ν_i and p_i is its momentum. As neutrinos are relativistic particles, one can assume $p_i \simeq p_j \equiv p \simeq E$, such that:

$$P_{\nu_\alpha \rightarrow \nu_\beta} = \delta_{\alpha\beta} - 4 \sum_{i<j}^3 \text{Re}[U_{\alpha i} U_{\beta i}^* U_{\alpha j}^* U_{\beta j}] \sin^2\left(\frac{\Delta m_{ij}^2 L}{4E}\right) + 2 \sum_{i<j}^3 \text{Im}[U_{\alpha i} U_{\beta i}^* U_{\alpha j}^* U_{\beta j}] \sin\left(\frac{\Delta m_{ij}^2 L}{2E}\right), \quad (1.10)$$

where $L \simeq ct$ is the distance travelled by the neutrino. When considering anti-neutrinos instead of neutrinos, the mixing matrix U in Equation [1.10](#) would be replaced by U^* , also affecting the sign of the last term of the equation which would then take the opposite value. Therefore, the term in the first line of Equation [1.10](#) is CP-conserving as it takes the same sign for neutrinos and anti-neutrinos, while the one on the second line is CP-violating. This equation also suggests that each neutrino flavour must have a different mass, i.e. $\Delta m_{ij} \equiv m_i^2 - m_j^2 \neq 0$, for neutrino oscillation to happen. This implies that, out of the three neutrino flavours, at least two of their mass eigenstates must be non-null. This can be expressed in terms of the two squared mass differences Δm_{21}^2 and Δm_{31}^2 . Consistent values of these parameters are found among the various oscillations experiments [\[9, 10\]](#). Similarly, they result in measurements of the mixing angles θ_{12} , θ_{13} and θ_{23} falling in good agreement, while δ_{CP} still need to be determined more precisely. The mass ordering of the three neutrino flavours is also still unknown. The values used in order to oscillate the neutrino flux from dark matter annihilation in the Galactic Centre (GC), described in Section [3.4](#), are shown in Table [1.1](#). The small mass differences between the three mass eigenvalues indicates that neutrino masses are all of similar values. Variations of these parameters values within the uncertainty levels of their measurements does not have a significant impact on this analysis.

Parameters	Units	Best fit value
θ_{12}	deg	33.46
θ_{23}	deg	47.9
θ_{13}	deg	8.41
Δm_{21}^2	10^{-5} eV^2	7.34
Δm_{32}^2	10^{-3} eV^2	2.419

Table 1.1: Values of the mixing angles between the three neutrino flavours as well as the squared mass differences used for the two analyses discussed in this thesis. The best fit values are taken from [9].

It has to be noted that the equations presented above apply for oscillation in vacuum. When considering neutrino oscillation in matter, one needs to account for the possible interactions between electron neutrinos and the electrons present in the medium. This results in a modification of the effective potential of electron neutrinos, thus having an impact on the neutrino squared mass differences and the neutrino mixing. This effect was named the MSW effect after Mikheyev, Smirnov and Wolfenstein [11, 12].

1.3 Expected neutrino sources

In this section, the dominant sources of neutrino fluxes at Earth are reviewed. The complete spectrum of possible neutrino sources is visible in Figure 1.4. The energy of the detected neutrinos provide information about their production mechanism and origin. In this regard, a classification of neutrinos in two main categories, i.e. low-energy (LE) and high-energy (HE) neutrinos, can be introduced. Neutrinos fall into the LE category if their energies are below a few tens of MeV, while the HE category consists of neutrinos with energies above 10 GeV. This classification, although arbitrary, reflects the mechanisms behind the production of these neutrinos. It should be noted that in this section and the following chapters, the term "neutrino" accounts for both neutrinos and anti-neutrinos since events generated by the ν and $\bar{\nu}$ are indistinguishably observed by the neutrino observatories considered for the two analyses presented in this thesis.

1.3.1 Low energy neutrinos

The neutrinos with the lowest energies are expected to be thermal relic neutrinos from the early Universe, constituting the Cosmic Neutrino Background (CNB or $C\nu B$) [14]. These neutrinos, predicted by the hot Big Bang model, should provide a glimpse of the Universe at the time of the neutrino decoupling, about one second after the Big Bang. The $C\nu B$ neutrinos are expected to have energies ranging from a few μeV to several meV. Although $C\nu B$ neutrinos have not yet been observed, their existence is corroborated by the excellent agreement between predictions and observations of its effects on the cosmic microwave background (CMB) and the big bang nucleosynthesis (BBN) [15].

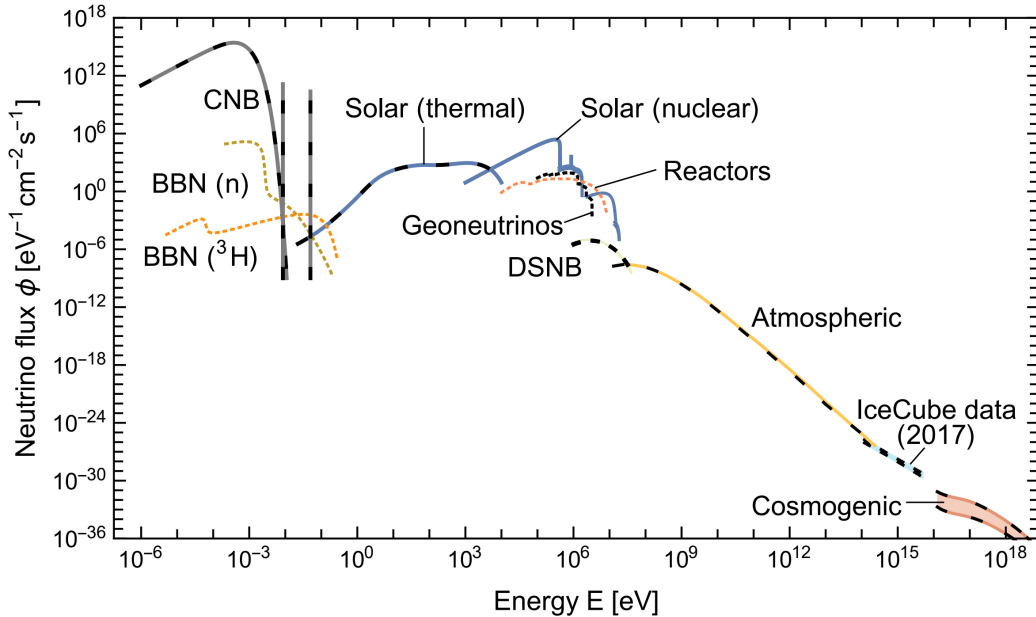


Figure 1.4—Measured and expected neutrino fluxes from possible neutrino sources as a function of the energy as taken from [13].

In the early Universe, a small flux of electron anti-neutrino was generated from the decay of neutrons and tritium nuclei. These neutrinos, referred to as BBN neutrinos, constitute the dominant contribution for energies between 10 and 100 MeV, as they fill the gap between $C\nu B$ neutrinos and solar neutrinos.

Meanwhile, neutrinos with energies in the sub-keV and keV range are produced by thermal processes in the Sun. The main thermal interactions involved in the production of solar neutrinos are Compton processes, plasmon decay, or even electron bremsstrahlung [16]. Low-energy neutrinos can also be produced in nuclear reactions, such as the ones occurring in the Sun. These neutrinos result from the fusion of hydrogen to helium through the proton-proton chain reaction or the carbon–nitrogen–oxygen (CNO) cycle. Unlike photons, the solar neutrino thus produced are able to escape the Sun without being scattered or deflected.

The decay of radioactive isotopes naturally present in the Earth can also result in the production of neutrinos. When decaying, these long-lived radioactive elements generate a flux of electron anti-neutrino in the MeV-range [17]. These neutrinos carry information about the abundance of natural radioactive isotopes in the Earth and could be used to probe the interior of our planet.

Neutrinos can also be generated by man-made sources, such as nuclear reactors. Reactor neutrinos arise from the beta-decay of the fission products and have typical energies of a few MeV. Nuclear reactors have played a historic part in the study of neutrino properties since they were involved in the first observation of neutrinos. These artificial sources still have an important role in the study of neutrino oscillation. They are used both by short-baseline experiments, such as RENO [18], Daya Bay [19] and Double Chooz [20], as well as by medium-baseline experiments, e.g. KamLAND [21] and JUNO [22].

Still in the MeV energy range, a neutrino flux from supernovae explosion has been

observed [23]. Core collapse of massive stars occur with a rate of about 10 events per second in the visible Universe. The transient neutrino signal from supernovae is considered to contribute to the diffuse supernova neutrino background (DSNB). Therefore, the DSNB is composed of the superposition of neutrino emissions from all the past star core collapses in the Universe [24]. Observation of this diffuse flux would provide information about, among other things, the redshift distribution of supernovae and the average energy released by these star core collapses. The neutrino flux from the DSNB is expected to be observable by the SuperK-Gd [25] and the Juno detectors, currently under construction.

1.3.2 High energy neutrinos

The two telescopes considered in this thesis are optimised for the observation of high energies neutrinos. The first observation of these astrophysical neutrinos were reported in 2013 by the IceCube collaboration. Similar astrophysical events, with energies in the TeV to PeV range, were since then observed by other experiments, such as the ANTARES neutrino telescope.

Covering a broad energy range extending from a few tenths of MeV to several PeV, the flux from atmospheric neutrinos originate from the interaction of Cosmic Rays (CR) in the Earth atmosphere. As their energy range is overlapping with the one of astrophysical neutrinos discussed above, atmospheric neutrinos constitute one of the main contributions to the background of both the ANTARES and the IceCube telescopes. They are therefore discussed as such in the section dedicated to the background expectation of the two neutrino experiments (Section 2.6).

High energy neutrinos are also believed to be produced by the interaction of cosmic rays in the source, its vicinity or even on their way to Earth. These neutrinos could be generated from proton-proton or proton-photon interactions, producing, among others, charged pions. The decay of these pions and the subsequent interactions will result in the production of neutrinos with a flavour ratio at the source of $\nu_e : \nu_\mu : \nu_\tau \simeq 1 : 2 : 0$. At Earth, the resulting flux is expected to demonstrate a ratio of about $1 : 1 : 1$ due to long-baseline neutrino oscillation. A possible CR source takes the form of Active Galactic Nuclei (AGN), which are expected to be powered by matter from the accretion disk falling into the black hole at the centre of the host galaxy. This would result in the creation of a jet structure, which could accelerate protons to high energies. When these jets are oriented towards the Earth, the AGN is referred to as a Blazar. In addition to being produced by the interaction of the CR accelerated in the AGN core region or inside the accretion disk, neutrinos could also be created directly in the relativistic jets. Another potential source of CR is given by Gamma Ray Bursts (GRBs), which are among the most energetic transient events observed in the Universe. GRBs consist of short pulses of gamma rays, lasting from a fraction of a second up to 100 seconds. These events are often split into short (< 2 s) and long (> 2 s) duration bursts. A possible explanation of the origin of short GRBs is that these events originate from the merger of neutron stars or massive stars collapsing into a black hole. These collisions will produce mesons rapidly decaying to muons and neutrinos. Long duration GRBs are commonly assumed to have for origin the death of massive stars. The production of neutrinos by GRBs results mainly from proton-photon interactions, generating kaons

and pions. These particles will, in turn, decay and give electron neutrinos as well as muon neutrinos [26].

Multi-messenger astronomy has proven to be a very promising tool to identify the source of the high energy diffuse neutrino flux. In September 2017, a first neutrino event was reported in concordance with a flare from the TXS 0506+056 gamma-ray blazar [27]. This observation is the first indication that blazars could constitute a high-energy neutrino source. As a result of this observation, a follow-up analysis was performed on a total of 9.5 years of data to search for a neutrino excess in the direction of TXS 0506+056 [28]. An excess was reported in this direction both in September 2014 and March 2015, providing a 3.5σ evidence in favour of the emission of neutrinos by TXS 0506+056.

Lastly, the expected neutrinos with the highest energies are known as cosmogenic neutrinos and have energies between tenth of PeV to tenth of Ee. These cosmogenic neutrinos are expected to arise from the interaction of ultra-high energetic cosmic rays (UHECRs) with the photons of the CMB. The origin of UHECRs is unknown, along with their production mechanisms. UHECRs are the highest energetic particle in the Universe, with energies ranging from 100 PeV to a hundred of Ee. The expected flux of cosmogenic neutrinos is very low, requiring an important detector volume and a long exposure in order to be detected.

Chapter 2

Cherenkov telescopes

In this chapter, the detection principle of neutrino telescopes is discussed. The geometry and performances of the two detectors considered for the analyses presented in this thesis, namely the ANTARES and the IceCube telescopes, are also explored in more details. Both ANTARES and IceCube are Cherenkov detectors optimised for the search of astrophysical neutrinos. Given the low interaction cross-section of neutrinos, a large volume of target material is required for their detection. Such important detector volume can be achieved by deploying a sparse array of photo-detectors in a deep, dark, and dielectric environment. This has been implemented by IceCube by setting up its photo-multipliers in the Antarctic ice at the South Pole, while ANTARES installed its detector lines at the bottom of the Mediterranean Sea.

2.1 Detection Method

As previously stated, neutrinos are only affected by the gravitational and the weak nuclear forces. As a result, the most efficient way to detect neutrinos is to deduce their properties from their weak interaction with a nucleus within or around a given detector volume. As indicated by equations [1.1](#) to [1.4](#), secondary relativistic charged particles are expected to be produced by such interactions. When travelling through a dielectric medium with a higher speed than the speed of light in the considered medium, these charged particles will emit Cherenkov light.

2.1.1 Cherenkov effect

The Cherenkov effect was first observed by P. Cherenkov in 1934 [\[29\]](#). This phenomenon is the result of the coherent superposition of electromagnetic waves caused by the polarisation of the medium by the electric field of the passing charged particle. As the electromagnetic waves are propagating through the medium with a phase equal to the speed of light over the refractive index, c/n , particles travelling with a speed such that $v < c/n$, are moving slower than the disturbance. This scenario is illustrated on the left panel of [Figure 2.1](#), where the electromagnetic waves propagate with phase difference, causing destructive interference. On the contrary, when a particle is moving through the medium with a speed $v > c/n$, the electromagnetic disturbances are in

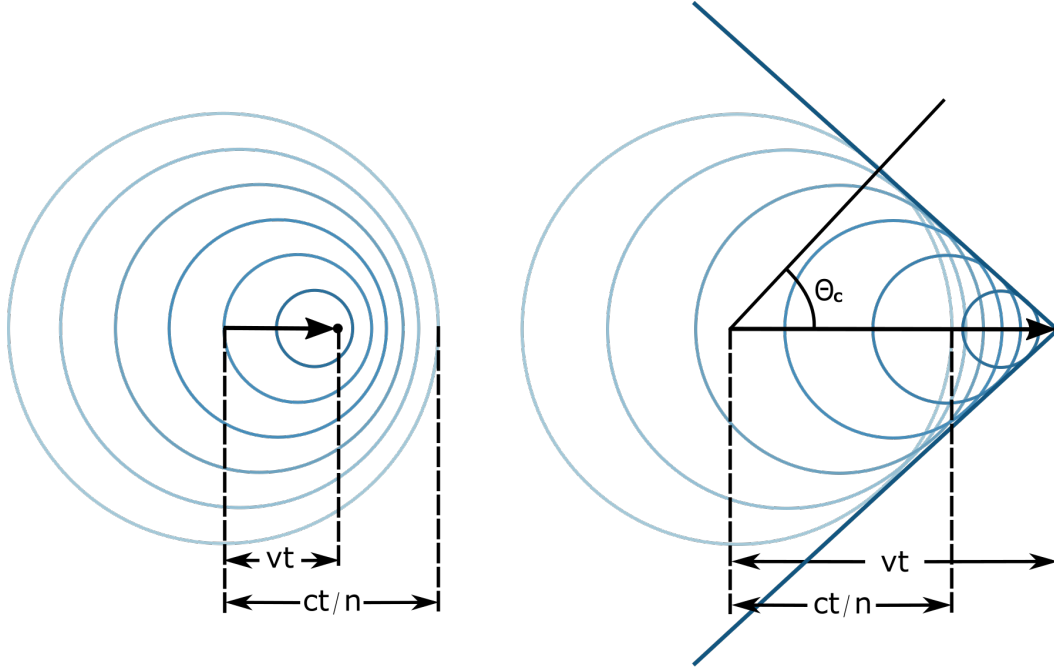


Figure 2.1—Illustration of the Cherenkov effect. The left-hand figure shows the case in which the particle is moving with a speed $v < c/n$, while the right-side plot shows the situation in which the particle has a speed $v > c/n$.

phase agreement. This specific case is shown on the right side of Figure 2.1, in which the individual wavefronts interfere constructively. The resulting plane wavefront moves in a specific direction forming an angle θ_c with the trajectory of the charged particle. This angle is referred to as the Cherenkov angle and can be characterised as

$$\cos \theta_c = \frac{ct/n}{vt} = \frac{1}{n\beta}, \quad (2.1)$$

where $\beta = v/c$. When considering the dielectric medium to be water ($n = 1.333$) or ice ($n = 1.309$), the characteristic opening angles are respectively taking the values of $\theta_c \sim 41^\circ$ and $\theta_c \sim 40^\circ$. The number of Cherenkov photons emitted by a charged particle for a travelled distance dx within the wavelength interval $d\lambda$ is given by the Frank-Tamm equation [30]:

$$\frac{d^2N}{dx d\lambda} = \frac{2\pi\alpha}{\lambda^2} \left(1 - \frac{1}{n^2\beta^2} \right), \quad (2.2)$$

where α is the fine structure constant equalling $1/137$. Equation 2.2 implies that smaller wavelengths have a higher contribution to the number of Cherenkov photons. Indeed, these photons are emitted with a wavelength dependence going as $1/\lambda^2$, for wavelengths ranging from 300 to 600 nm. For this reason, the spectrum of Cherenkov light peaks in the ultraviolet (UV) region, causing the produced light to appear blue to the naked eye.

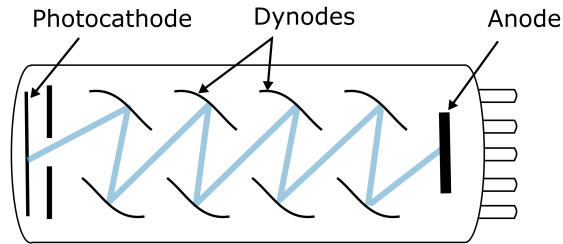


Figure 2.2–Schematic view of a photomultiplier tube.

When considering a relativistic charged particle moving in ice about 330 photons with wavelengths falling in the typical spectral response region of the IceCube optical sensors ($350 \text{ nm} \leq \lambda \leq 600 \text{ nm}$) are produced per travelled centimetre. From a similar calculation in seawater, about 200 photons with wavelengths between 300 nm and 600 nm, i.e. in the sensitive region of the ANTARES photo-sensors, are expected to be produced per centimetre.

2.1.2 Photomultiplier tubes

The optical sensors used by Cherenkov telescopes consists of photomultiplier tubes (PMTs), which are devices based on the photoelectric effect. A schematic view of a PMT is given in Figure [2.2](#). These devices are equipped with a photocathode, located at the end of the tube receiving the incident light. On the other end of the PMT an anode can be found, while a multitude of dynodes are arranged between these two extremities. When a photon arrives at the photo-cathode, it tears off an electron, referred to as photo-electron (PE), by photoelectric effect. The probability of this phenomenon to occur is known as the quantum efficiency and depends on the energy of the incident photon. Once released from the photocathode, the electron is accelerated due to the potential difference between the photocathode and the anode. On its way to the anode, the electron will hit the first dynode, releasing more electrons in the process. These electrons are in turn accelerated to the next dynode, extracting more electron on the way and thus creating a snowball effect. This way, the signal from the initial photo-electron is amplified before reaching the anode, providing a measurable electrical signal. This amplification is characterised by the gain of the PMT. In addition to the pulses created by photo-electrons, pre-pulses, after-pulses and late pulses can be recorded. Pre-pulses are recorded when the incident photon extracts a PE on the first dynode instead of doing so on the cathode, while late pulses are caused by electrons scattering back. After-pulses can happen a few hundreds of ns after the main pulse and are caused by residual gas inside the PMT. This gas, once ionised by the photo-electron or the electrons created in the amplification process, will contribute to the total photo-electron. More details on the PMTs used by ANTARES and IceCube will be given in the sections related to each detector.

2.2 Detector layouts

In this section, the layouts of the two neutrino telescopes considered in this thesis are detailed. Although they are both based on the same detection principle, the ANTARES and IceCube detectors have distinct specifications, such as their location, size or detection medium. ANTARES, which is the acronym for Astronomy with a Neutrino Telescope and Abyss Environmental RESearch, is an under-water Cherenkov detector. This neutrino telescope is located in the deep Mediterranean Sea at coordinates of $42^{\circ}48'N$, $6^{\circ}10'E$, about 40 km away from the coast of Toulon (France). The ANTARES detector was completed in May 2008, after a two-year deployment period. The data acquisition started before the finalisation of the full detector configuration, with only 5 deployed lines. IceCube is currently the largest neutrino telescope ever built with a total instrumented volume of one cubic kilometre. This detector is located at the South Pole and is buried one kilometre below the surface. The construction of the IceCube detector was carried out over a seven-year period from 2004 to 2010 and required the drilling of 86 boreholes in the Antarctic ice. The full configuration of the detector is often referred to as IceCube-86 or IC86. This distinction is made as data recording already started with partial detector configuration while IceCube was still in its construction phase. Similarly, data taken between May 2010 and May 2011 with the 79-strings configuration are referred to as IC79 data.

2.2.1 ANTARES

The ANTARES detector is composed of a total of 12 lines instrumented with light sensors designed to detect the Cherenkov photons produced by the passage of charged particles in the detector volume [31], as visible in Figure 2.3. The ANTARES lines are spread over an octagonal grid covering a surface of about 0.1 km^2 , with a horizontal distance between the lines of 60 m to 70 m. Each of these lines holds 25 storeys regrouping three Optical Modules (OMs) (see Section 2.3.1), with the exception of line 12. The topmost storeys of this particular line are equipped with hydrophones for the AMADEUS project, used for acoustic detection of neutrinos [32]. The ANTARES storeys consist of a supporting frame, known as the Optical Module Frame (OMF), supporting three OMs oriented downwards with angles of 45° . The required offshore electronics and processors are encased in a titanium container called Local Control Module (LCM). The storeys are attached to the string with a vertical spacing of 14.5 m over a height of 300 m starting 100 m above the seabed. This results in an instrumented volume of about 0.01 km^3 equipped with a total of 885 OMs. The lines are anchored to the seabed at a depth of about 2475 m with the help of 1.5 t iron ballasts, called Bottom String Sockets (BSS). As the ANTARES strings consist of 450 m long flexible cables, they are kept vertical by the mean of buoys. The movement of the individual lines is monitored using a combination of hydrophones and compasses installed within the detector volume. Devices used for geosciences and marine environment monitoring are also disseminated on the 12 detector lines, as well as on an additional and specially devoted line called the Instrumentation Line [33].

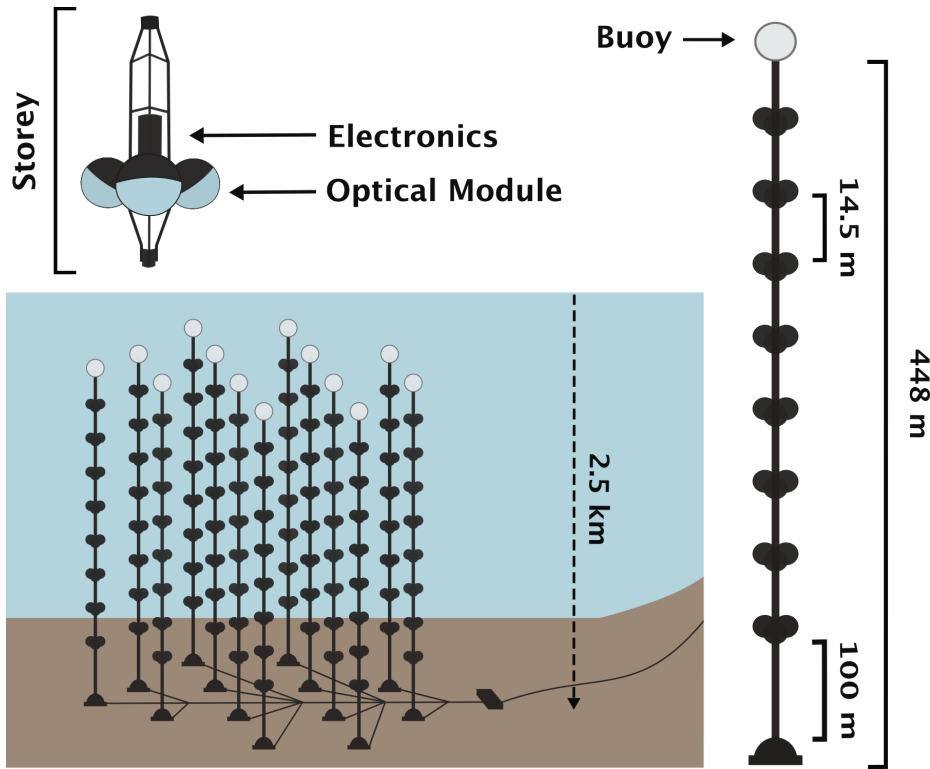


Figure 2.3—Schematic view of the ANTARES neutrino telescope located in the Mediterranean Sea.

2.2.2 IceCube

The IceCube detector consists of a total of 5,160 Digital Optical Modules (DOMs) (see Section 2.3.2) spread on 86 strings buried in the Antarctic ice [34]. Of these strings, 78 are deployed on an orthogonal grid with triangular sub-patterns. These strings are separated by an average distance of 125 metres and each cable holds 60 DOMs arranged evenly between depths of 1,450 to 2,450 meters with a vertical spacing of 17 metres. The eight remaining strings are laid out in a denser array located at the centre of the IceCube detector, constituting the DeepCore sub-detector [35], visible in green in Figure 2.4. The average spacing between these strings is reduced to 72 metres. Each DeepCore string still holds 60 DOMs separated in two blocks. The 10 first DOMs are located above the dust layer, at depths between 1.750 m and 1.850 m with a spacing of 10 m, while the other 50 DOMs are spaced by 7 m and located at depths from 2.100 m to 2.450 m. The aim of the DeepCore array is to enable the detection of neutrinos with energies down to 5 GeV. The innermost IceCube strings surrounding the DeepCore strings are also encompassed in the DeepCore sub-detector volume. The IceCube volume also contains the non-active decommissioned remains of its predecessor, the Antarctic Muon And Neutrino Detector Array (AMANDA), shown as a blue cylinder in Figure 2.4. As a complement to the in-ice instrumentation, a surface array of 81 IceTop stations is disposed over every IceCube strings, covering a total surface of 1 km². All IceTop stations consist of two ice tanks each holding two DOMs. This surface detector aims to detect showers of secondary particles created

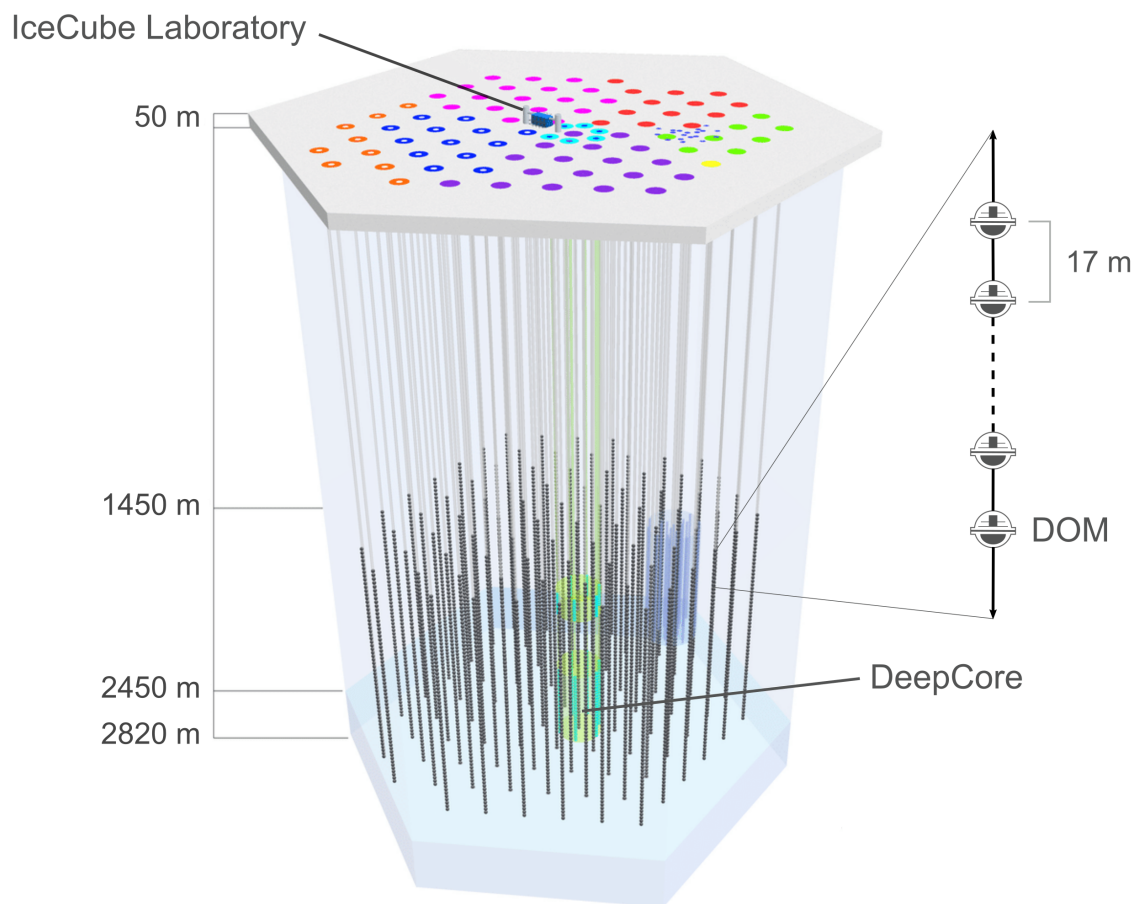


Figure 2.4—Schematic view of the IceCube neutrino telescope located at the South Pole. Credit: IceCube Collaboration.

by the interaction of Cosmic Rays in the upper atmosphere. IceTop is also used in concordance with IceCube in order to reduce the atmospheric muon background and to calibrate the detector.

2.3 Optical sensors

Both the ANTARES and IceCube neutrino telescopes use optical sensors to detect the Cherenkov light emitted by charged particles travelling within their instrumented volume. The optical sensors are the fundamental detection units of these telescopes. The different components included in these sensors are described in this section.

2.3.1 ANTARES

The basic photo-sensors used to detect Cherenkov photons in the ANTARES telescope are called Optical Modules (OM), which are first introduced in Section 2.2.1. These devices consist of a photomultiplier tube with a diameter of 254 mm, a variety of sensors, as well as the associated electronic components, all enclosed in a glass sphere with a diameter of 425 mm [36]. A schematic view of an OM and its different components can be seen in Figure 2.5. The OM glass is 15 mm thick, making it resistant to a pressure of up to 700 bar. The glass of the OM was chosen to have a refractive index similar to those of the PMT glass and the seawater, and displays a photon transparency of 95% above 350 nm. The sphere is made up of two half-spheres sealed together to make it watertight. The lower part of the OM houses the PMT and the optical glue which provides a smooth optical transition between the OM glass and the PMT. This glue also serves the purpose of holding the PMT and the magnetic shield in place. This magnetic shield consists of a wire envelope made of a nickel-iron alloy, called mu-metal. The presence of the magnetic shield is required by the fact that the trajectory of electrons inside the PMT can be modified by the magnetic field of the Earth. The use of the magnetic shield makes the response of the PMT more homogeneous on the whole surface of the photocathode. The necessary voltage is provided to the PMT by means of a high voltage (HV) converter, constituting the PMT base. The upper half of the OM, which is coated with black paint, holds the penetrator and a vacuum valve. The vacuum valve is used to control the internal pressure of the OM, while the penetrator serves as an electrical link between the inside and the outside of the glass sphere. In addition, each OM is supplied with a blue LED used for calibration, in particular the monitoring of the PMT transit time.

2.3.2 IceCube

The Digital Optical Modules (DOMs), which are first mentioned in Section 2.2.2, constitute the basic IceCube detection units used to measure the Cherenkov photons produced by charged particles moving through the detector. Each DOM contains a large downward facing photomultiplier with a diameter of 25 cm [37]. These DOMs also enclose all the electronics required for the acquisition and digitisation of the signal recorded by the PMTs, constituting the DOM mainboard. A schematic view of a DOM,

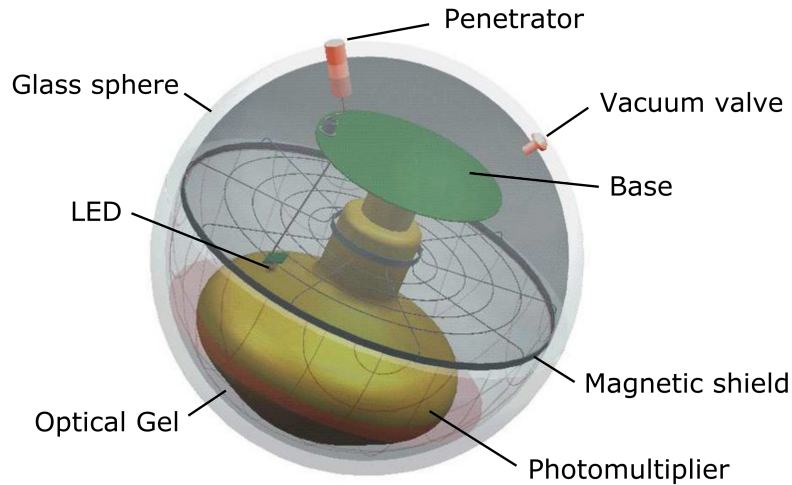


Figure 2.5—Schematic view of an optical module used in the ANTARES detector.
Credit: ANTARES Collaboration.

showing its components, is visible in Figure 2.6. The sphere of the DOM is made of 13 mm thick glass, resistant to pressure up to 690 bar. More specifically, borosilicate glass with a low potassium content is used in order to reduce noise from radioactive elements of the glass. The photon transmittance displayed by the glass sphere is of 93% at 400 nm. This optical transmission quickly decreases to 50% at 340 nm, introducing a cut-off in the wavelengths detectable by the PMT. The sphere is initially provided in two semi-spherical parts, which are later welded by an aluminium belt equipped with rubber seals on each side. The lower half of the DOM is equipped with the PMT, which is held in place by a silicone gel with an optical transmission of 97% at 400 nm. Just as for the ANTARES OM, this silicon gel acts as an optical glue between the glass sphere and the PMT, ensuring a refraction of less than 0.1% when light travels from one to the other. Similarly, the DOMs are also furnished with a mu-metal wire grid, reducing the Earth magnetic field inside the DOM by a factor 2.8. Without this magnetic shield, the characteristic of the PMT, such as its resolution and collection efficiency, are considerably lessened. The high voltage required by the PMT is handled through a HV divider connected to both the PMT and the HV control board. This control board, which is coupled to the DOM mainboard, is responsible for setting and reading the HV of the PMT. The mainboard consists of a single-board computer used for data acquisition, carrying the load of controlling all hardware housed in the DOM. The mainboard is also in charge of the digitisation of the PMT analogue outputs, for which the use of a delay board is also required (as described in Section 2.4.2). This delay board, located below the mainboard, is made of a 11.2 m-long cable laid out in a serpentine. In addition to this, each DOM contains a LED flasher board used for calibration and consisting of 12 LEDs with a wavelength of ~ 405 nm. In particular, the LED flasher boards are used to establish the time response and the position of the DOMs, as well as to determine the optical properties of the ice. The interior of the

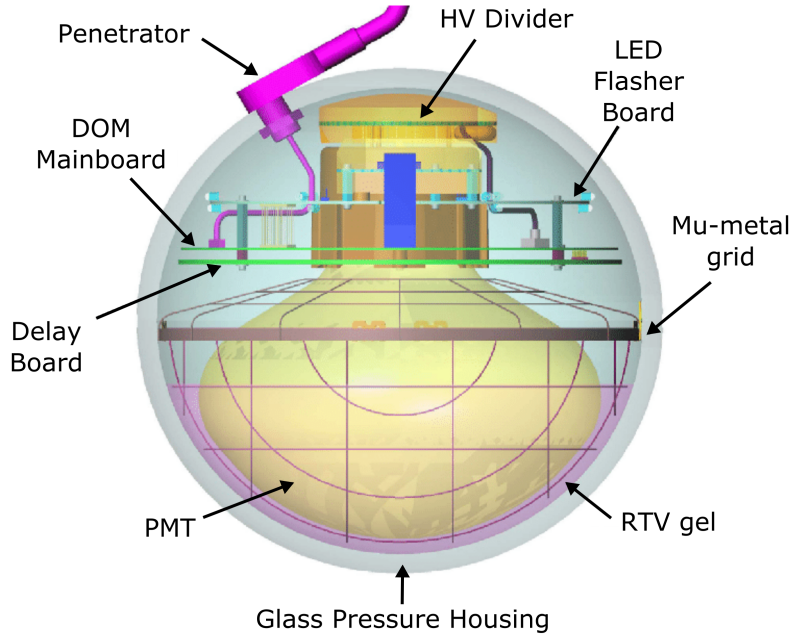


Figure 2.6—Schematic view of a digital optical module used in the IceCube detector. Credit: IceCube Collaboration.

DOM is connected to the outside by a penetrator carrying three pairs of wires through a ~ 16 mm hole in the glass sphere. Out of these wire pairs, one is used to bring electricity inside the OM and exchange digital information with the facility located on the surface of the ice. The four remaining cables have the purpose of exchanging information with neighbouring DOMs. Each DOM is attached to the string with the help of a harness made of steel cables bending the string around the glass sphere.

2.4 Data acquisition

In this section the data acquisition (DAQ) systems used by the ANTARES and the IceCube neutrino telescopes will be reviewed. A detailed description of the different components of each system will be given.

2.4.1 ANTARES

The DAQ system has several functions, including preparing the detector for data collection, transmitting the signals provided by the PMTs to the on-shore station, and converting them into a format that can be easily used to analyse the collected data. The hardware used for the DAQ system consists of a multitude of elements located both on-shore and offshore. The main goal of the electronic modules located underwater is to read out the information provided by the PMTs. These electronics parts are accommodated in the LCMs, which are titanium containers held by each storey. Among the components housed in a LCM, one mainboard equipped with two analogue ring samplers (ARS) [38] can be found per OM, as well as a local clock.

Digitisation of the signal

The ARS chips are responsible for the conversion of the analogue signal received from the PMT into a digital signal. More precisely, the ARSs are used to integrate the signal outputs of the PMTs falling above a certain threshold, typically set to 0.3 PE, and to assign a time to the related recorded hit. Each ARS consists of a semiconductor chip equipped with about 68 thousands transistors. In order to allow a synchronised timing among the entire detector, the ANTARES detector makes use of a 20 MHz clock signal dispatched to each ARS from the shore station. From this clock signal, a time stamp of 25 ns is associated to each recorded hit. A time to voltage converter (TVC) included in the ARS is then used to obtain a more precise timing measurement related to the PMT signal. Simultaneously, other parts of the ARS are used to integrate the PMT outputs. This integration is performed over a 35 ns time window with an adjustable sampling rate ranging from 150 MHz to 1 GHz. The charge of the hit is thus provided by the ARS as an analogue signal. An Analogue to Digital Converter (ADC) is then used to convert the hit charge information and the time stamp from the TVC into a digital signal.

Transfer of data to shore

The whole resulting digital data are sent to the shore station for further processing and storage. Only one LCM every fifth storey is responsible for the transfer of the data collected by all five storeys. These dedicated LCMs are referred to as Master Local Control Modules (MLCM). The MLCMs are all supplied with an Ethernet switch connected to a Dense Wave length Division Multiplexing (DWDM) encapsulated in the String Control Module (SCM) located on the BSS anchoring each line to the seabed. The outputs of each line are then collected via a junction box connected to every single DWDM. From this junction box, the offshore part of the DAQ is linked to the on-shore hardware via a sole electro-optical cable, referred to as the main electro-optical cable (MEOC). Similarly to the detector lines, the MEOC is composed of optic and copper cables. These cables are used to power the various parts of the detector, as well as to transfer data. The external part of the cables are made of three superposed layers of different protective materials. The on-shore part of the DAQ hardware consists of a set of computers whose purpose is to process the collected data. In this respect, a variety of filters are applied to make a first separation between the background and the significant physical signal as described in Section [2.8](#).

2.4.2 IceCube

The IceCube data acquisition system is split into several levels, each performing specific tasks. The main purpose of the DAQ is to detect, digitise and allocate a precise timing to the signal provided by the PMTs. The digitised information are then collected and sent to the IceCube Laboratory (ICL) building located on the surface, before being dispatched via satellite to data centres in the Northern Hemisphere.

Digitisation of the signal

The initial steps of the data acquisition are handled locally by the mainboard of each DOM. The output of the PMT is first sent to a discriminator, which evaluates if the signal falls above a predefined threshold, typically set to 0.25 PE. In the meantime, a duplicate of the signal is sent through the delay board in order to introduce a delay of 75 ns before entering the digitiser. This delay correspond to the time required by the discriminator to determine if the digitisation process of the PMT analogue waveform should be launched. When this condition is met, a digital output, referred to as a "hit", is created by the DOM mainboard from the pulse detected by the PMT [39]. Each hit consists of an estimate of the recorded charge, as well as information about the time at which the pulse occurred and its associated digitised waveform. In order to create this digitised waveform, the delayed output of the PMT is further separated to go through two kinds of digitising devices. The first of these devices is an Analogue Transient Waveform Digitiser (ATWD), which exhibits a sampling rate of 303 MHz. With this digitiser system, the waveform is sampled into 128 time bins with a width of 3.3 ns, resulting in a total coverage of 422 ns. On the other hand, the fast Analogue to Digital Converter (fADC) displays a sampling rates of 40 MHz and samples the waveform into larger time bins of 25 ns with a total time coverage of 6.4 μ s. This larger time interval of 6.4 μ s exceeds the time slot during which even the most energetic events are expected to generate Cherenkov photons detectable by the PMT. The digitised information is temporarily stored in the DOM as long as no transfer request is received from the ICL.

Local coincidence

In the spirit of limiting the data storage demand at the Pole and the quantity of data transferred from the South Pole to the Northern Hemisphere, online processing (discussed in Section 2.8) is applied directly in ice to distinguish relevant signal events from atmospheric muons and pure noise. The selection criteria are based on the local coincidence (LC) condition. Since DOMs are able to communicate with each other, a DOM can inform its neighbouring DOMs when it has registered a hit. This hit is labelled as Hard Local Coincidence (HLC) hit if at least one hit is recorded within a 1 μ s time window by one of the four nearest DOMs of the same string. Otherwise, the hit is tagged with the Soft Local Coincidence (SLC) marker. In this case, the only saved information consists of the time stamp, as well as three samples centred around the peak of the coarser output provided by the fADC. For HLC, the entire digitised waveform provided by ATWD and the fADC are kept.

Pulse extraction

As the digital waveform is not a convenient format on which to apply event reconstruction, the charge of the hit and its timing are computed. For this, a time correction is applied to the waveform in order to account for delays induced by the time required for the creation of the photo-electron in the PMT and the digitisation process. In order to infer the time and charge of the incident photon, the time-calibrated waveform is fitted with models representing the impact of both the PMT and the digitisation process. These extracted features are referred to as pulses. A collection of pulses

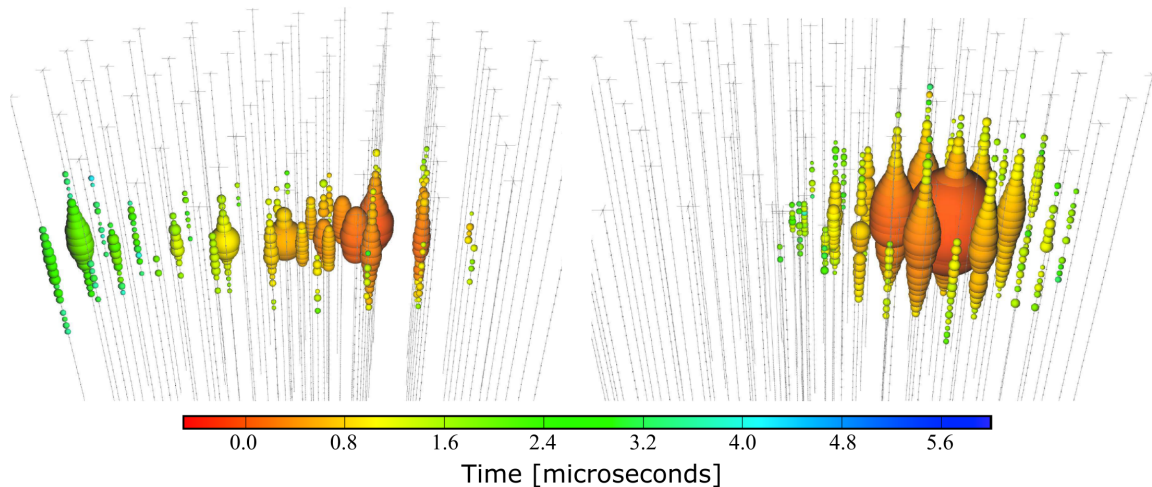


Figure 2.7—Illustration of the two events topologies for a track event (left) and a cascade event (right). Both events were observed by the IceCube neutrino telescope. The arrival time of the incident photons is indicated by the colour palette, where red marks the earliest hits and blue the late hits. The amount of deposited light recorded by a particular PMT is represented by the size of the DOM. Credit: IceCube Collaboration.

recorded by a DOM is called a pulse series and is used for subsequent reconstruction and event selection. The applied reconstruction could be altered by pure noise hits wrongly incorporated in the pulse series.

Hit cleaning

In order to reduce this noise contribution, a hit cleaning is applied to the pulse series. One distinction between hits induced by incident Cherenkov photons and pure noise hits is the fact that a temporal and spatial correlation is expected for the former. This principle is used by the seeded radius-time (SRT) cleaning algorithm. The SRT algorithm looks for spatio-temporal clustering of LC hits, which are used as seeds. This algorithm also includes non-LC hits for consecutive iterations if they are recorded under a distance of 150 m from a seed within a 1 μ s time interval. This process carries on until no more pulses fulfil the condition. The resulting pulses are known as SRT cleaned pulses. All this information is then sent to the ICL located on the surface. The ICL houses the string hub computers, each of which manages the information provided by an entire detector string. These string hubs are in charge of the in-ice triggers which will be discussed in the following.

2.5 Event topology in the detectors

In this section, the different event topologies that can be encountered in the ANTARES and the IceCube neutrino telescopes are discussed. In the previous chapter, an overview

of the particles produced during the interaction of neutrinos inside or in the vicinity of the detector was already given. Depending on the type of interaction (neutral or charged current) and the neutrino flavour, the events will take different forms in the detectors. The event topologies can be separated into two basic shapes, which will be discussed in more details below. The first type of event signature takes the form of a spherical pattern, while the second event signature consists of a cylindrical shape. The events with such topologies are commonly referred to as *cascade* events in the case of the former and as *track* events for the latter. Figure 2.7 shows such track (left) and cascade (right) events. Both panels display events recorded by the IceCube neutrino telescope. The colour palette indicates the arrival time of the incident photons, with red marking the earliest hits and blue the late hits, while the size of the represented DOM illustrates the amount of deposited light recorded by this particular PMT. The energy deposited in the detector for the track event shown in this figure amount to $71.4_{-9.0}^{+9.0}$ TeV, while the measured deposited energy for the cascade event displayed in the right-hand of the plot corresponds to $1040.7_{-144.4}^{+131.6}$ TeV.

Although the events are classified in two topologies, the first analysis presented in this thesis, which combines data from the ANTARES and IceCube neutrino observatories, only uses events selected as track-like. However, for the low energy dark matter search conducted during the second part of this thesis, both cascade-like and track-like events are part of the event selection, such that all neutrino flavours are considered.

2.5.1 Cascade events

Cascade events can originate from the charged interaction of an electron neutrino. Such interaction will create electrons or positrons, which will quickly lose energy over ionisation and bremsstrahlung. Ionisation is the process by which an electron is released from its atom through elastic scattering with a charged particle. Bremsstrahlung, translating to braking radiation, is a process resulting in the emission of photons from the deceleration of a charged particle in the medium. Above a certain energy defined as the critical energy E_c , bremsstrahlung becomes the main source of energy loss. For water and ice, this critical energy takes similar values of $E_c \sim 78$ MeV for electrons and $E_c \sim 76$ MeV for positrons [40]. The length of the electromagnetic cascade resulting from these processes, L , depends on the energy of the electron, E , such that, according to the Heitler model:

$$L = X_0 \frac{\log(E/E_c)}{\log(2)}, \quad (2.3)$$

where X_0 is the radiation length of electrons in the medium. The contribution from these dominant processes to the overall energy loss can be seen in the left panel of Figure 2.8. This figure also shows the Landau-Pomeranchuk-Migdal (LPM) effect, which is responsible for the suppression of bremsstrahlung and $e^+ - e^-$ pair production processes at high energies [41]. The energy loss of electrons occurs over a short distance, so that the resulting hits are approximately distributed according to a spherical symmetry. The NC interaction of neutrinos and the CC interaction of tau neutrinos can also give rise to cascade events. For NC interaction, the energy lost by the neutrino is

conveyed by the ensued hadronic cascade. In the case of CC interaction of a tau neutrino, a tau is created. As seen in Section 1.1, the decay of this short lifetime particle will essentially result in a hadronic cascade in about 83% of the cases. For all cascade events, the light deposited in the detector will take the form of a spherical event. These cascade events provide a good energy reconstruction, as they are typically well contained within the detector volume. However, such events have the disadvantage of having a poor angular resolution due to their very shape, which leads to the smearing of the angular information.

2.5.2 Track events

These events originate from the charged current interaction of muon neutrinos within the detector volume or in its vicinity. The CC interaction of tau neutrinos might also release a muon with a B.R. of $\sim 17\%$. The muon generated during such interactions propagates linearly through the detector, leaving hits in its path. As they travel in the detector, muons will lose energy through various processes. When considering muons, the energy loss mechanisms to take into consideration are bremsstrahlung, ionisation, $e^+ - e^-$ pair production, as well as inelastic photo-nuclear interactions. The individual contributions of the different mechanisms are visible in the right panel of Figure 2.8. The average energy loss of a muon over a distance dx can be estimated from:

$$-\left\langle \frac{dE_\mu}{dx} \right\rangle \simeq a + b E_\mu, \quad (2.4)$$

where a is the contribution from ionisation and b covers the contributions from the other processes. From detailed simulation of the muon energy loss, one obtains the following values of $a = 0.268 \text{ GeV mwe}^{-1}$ and $b = 0.470 \times 10^{-3} \text{ mwe}^{-1}$, where $\text{mwe} = 10^2 \text{ g/cm}^2$ [42]. From equation 2.4, an approximation of the mean range of a muon can be given as:

$$R_\mu \simeq \frac{1}{b} \log\left(1 + E_0 \frac{b}{a}\right), \quad (2.5)$$

where E_0 is the initial energy of the muon. Depending on their energy, muons can travel several kilometres in the ice. As a result, only part of their trajectory might be contained within the detector volume. This makes the estimation of their initial energy more difficult than for cascade events, leading to a poor energy reconstruction. The direction of the generated muon is almost perfectly aligned with the incident muon neutrino, especially when considering high energies. Therefore, track events present a good angular resolution as they allow for an easier reconstruction of the incident particle trajectory. A simple distinction between tracks and cascades is not always that perceptible as in some cases tracks might look cascade-like. For instance, low energy muons will leave shorter tracks in the detector, which might resemble cascades. Similarly, for tracks starting in a densely instrumented region of the detector, the associated hadronic cascade might be more discernible. If on top of that the muon did not pass near any optical sensors, the number of hits along its trajectory might be low, subsequently leading to the mis-reconstruction of the event as a cascade.

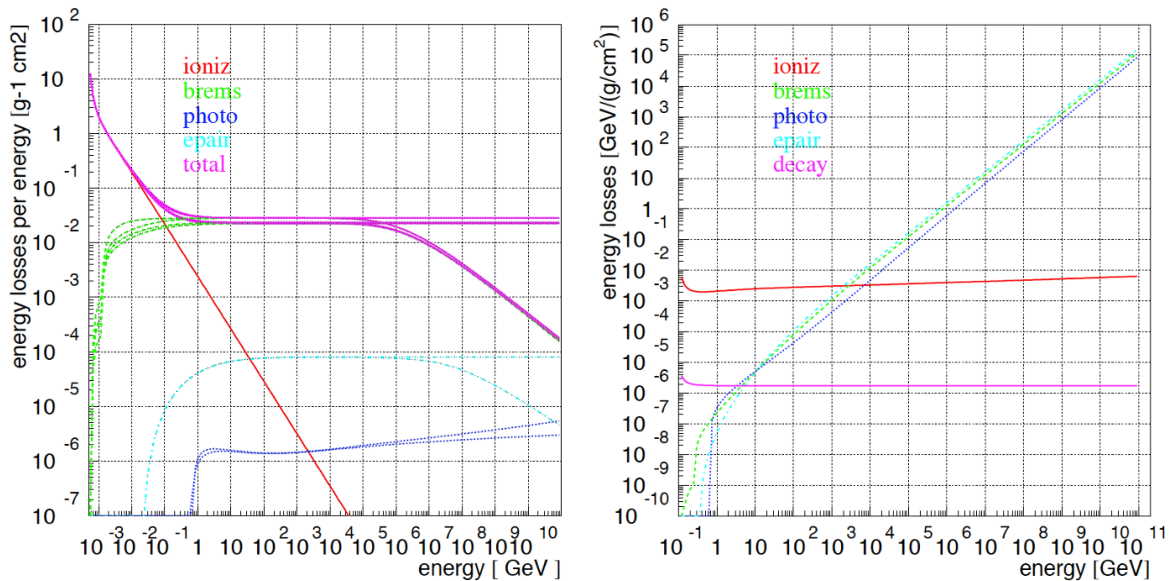


Figure 2.8—Overall energy losses of electrons (left) and muons (right) in ice shown together with the individual contribution from the different undergoing processes, where the electron energy loss plot also show LPM suppression of the cross-section [42].

2.5.3 Noise

Aside from cascade and track events, uncorrelated events are recorded by the optical sensors all around the detector, as represented in Figure 2.9. These events are referred to as noise and can have various sources. Such hits can be caused by the thermal noise from the photo-sensor electronics. In addition to these uncorrelated hits, the noise hits can occur in correlation with previous hits recorded by the same optical sensor. These correlated noise hits arise from dark noise, which regroup all processes emitting an electron from the PMT photocathode without an incident external photon. Dark noise hits can result from various phenomena, such as electronic noise or faint scintillation in the sensor sphere. These hits can also arise from the radioactive decay of the potassium-40 (^{40}K) contained in the glass of the pressurised spheres enclosing the PMTs used by ANTARES and IceCube. It is necessary to discard these noise hits before proceeding to the event reconstruction as their contribution might be misleading. The simulation of this noise, as well as the cuts applied to exclude the resulting hits are discussed in the sections relative to the event selections used for the two analyses presented in this thesis (see Chapter 4 and Chapter 5).

2.6 Expected background

The main background sources of the two neutrino telescopes considered in this thesis originate from the interaction of cosmic rays in the upper layers of the atmosphere. Although both ANTARES and IceCube are optimised for their detection, astrophysical neutrinos can constitute a source of background for dark matter searches with neutrino

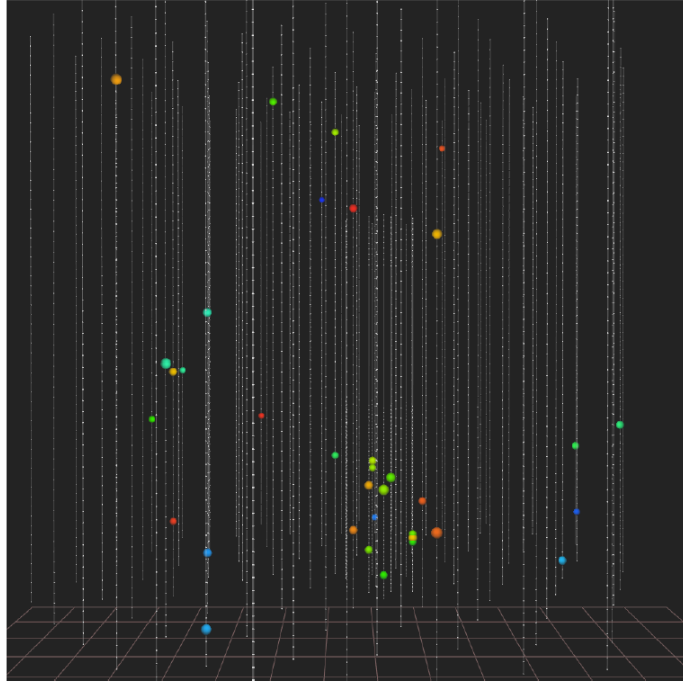


Figure 2.9—View of the detector triggered by pure noise hits in coincidence. Credit: IceCube Collaboration.

telescope. The noise hits discussed in Section 2.5.3 are also part of the background of the two detectors. However, the natural background from the radioactive decay of ^{40}K can also be used as signal to calibrate and monitor the gain of the PMTs deployed in the two neutrino detectors, as mentioned in Section 2.9. For ANTARES, an additional source of background has to be taken into account: bioluminescence. These different contributions are discussed in this section.

2.6.1 Cosmic Rays

Cosmic rays were discovered in 1912 based on observations made from a hot air balloon by V. Hess [43]. Following this discovery, various experiments have tried to determine the composition and spectrum of cosmic rays [44]. Primary cosmic rays consist of high-energy ionised atomic nuclei and charged elementary particles. Most of the primary cosmic ray flux is constituted of protons, p^+ , and helium nuclei, α^{2+} , with a smaller contribution from heavier and lighter particles, e.g. electrons, positrons and gamma rays. The measured flux of primary cosmic rays is often approximated by a broken power law such that:

$$\frac{dN}{dE} \propto E^{-\gamma}, \quad (2.6)$$

where the spectral index of the primary cosmic ray flux, γ , varies depending on the considered energy range, as visible on in the left panel of Figure 2.10. Below the first knee ($\sim 1\text{PeV}$), the spectral index takes values of $\gamma \simeq 2.7$, while for energies above the knee, a softening of the spectrum is visible such that it is best fitted by $\gamma \simeq 3.1$.

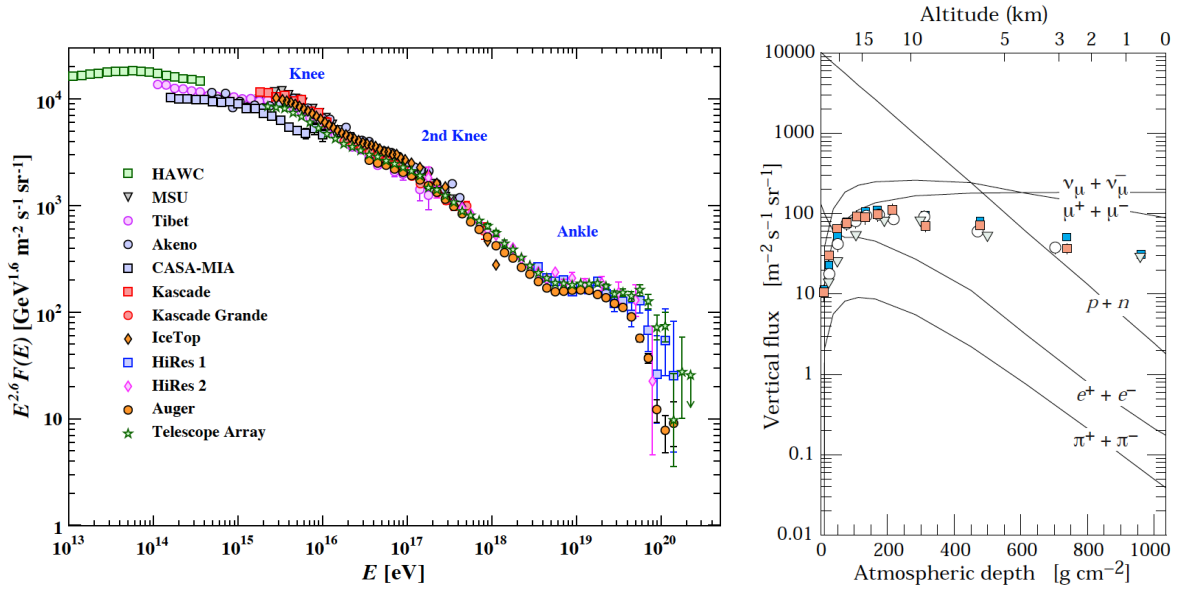


Figure 2.10—The left panel shows the energy-weighted spectrum from air shower measurements performed by various experiments as a function of the energy. The right-hand panel shows the individual contributions of different particles to vertical CR fluxes as a function of altitude. Both figures are taken from [10].

A slight hardening of the cosmic ray spectrum can later be observed around 10 EeV, resulting in the spectral feature known as the ankle.

When interacting with nuclei present in the upper layers of our atmosphere, primary cosmic ray particles generate showers of unstable secondary particles unfolding in the direction of the incident primary cosmic ray. In particular, such interactions will create charged mesons, like pions (π^\pm) or kaons (K^\pm), such that:

$$p^+(\alpha^{2+}, \dots) + N \rightarrow \pi^\pm(K^\pm) + X, \quad (2.7)$$

where N is the initial atmospheric nucleon and X is the hadronic shower resulting from the interaction. The charged mesons produced in the cosmic ray interaction will in turn decay or interact with nuclei of the atmosphere, creating lighter particles, such as muons and neutrinos. The following equations are representing possible decay scenarios of these secondary particles, with the corresponding branching ratio:

$$\pi^-(\pi^+) \rightarrow \mu^-(\mu^+) + \bar{\nu}_\mu(\nu_\mu), \quad (\sim 100\% \text{ B.R.}) \quad (2.8)$$

$$K^-(K^+) \rightarrow \mu^-(\mu^+) + \bar{\nu}_\mu(\nu_\mu), \quad (\sim 64\% \text{ B.R.}) \quad (2.9)$$

$$\rightarrow \pi^-(\pi^+) + \pi^0, \quad (\sim 21\% \text{ B.R.}) \quad (2.10)$$

$$\rightarrow \pi^0 + e^-(e^+) + \bar{\nu}_e(\nu_e), \quad (\sim 5\% \text{ B.R.}) \quad (2.11)$$

$$\rightarrow \pi^0 + \mu^-(\mu^+) + \bar{\nu}_\mu(\nu_\mu). \quad (\sim 3\% \text{ B.R.}) \quad (2.12)$$

Neutral and charged pions represent the dominant contribution to CR air showers. The charged pions will further decay into muons (anti-muons) and muon anti-neutrinos

(neutrinos) with a B.R. of almost a 100%, while the decay of neutral pions will result in electromagnetic showers due to the creation of photons and electrons:

$$\pi^0 \rightarrow \gamma + \gamma, \quad (\sim 99\% \text{ B.R.}) \quad (2.13)$$

$$\rightarrow \gamma + e^+ + e^-. \quad (\sim 1\% \text{ B.R.}) \quad (2.14)$$

In addition, the muons created in the atmospheric showers could decay before reaching the surface of the Earth, such that:

$$\mu^+(\mu^-) \rightarrow e^+(e^-) + \nu_e(\bar{\nu}_e) + \bar{\nu}_\mu(\nu_\mu), \quad (\sim 100\% \text{ B.R.}) \quad (2.15)$$

resulting in the dominant source of low-energy electrons at sea level. On the contrary of muons and neutrinos, the photons, electrons and positrons thus created have a short penetration range into matter. As a result, the dominant type of particles found in air showers at the surface of the Earth are atmospheric muons and neutrinos. This is visible in the right panel of Figure [2.10](#) showing the vertical fluxes of the various contributions to air showers as a function of altitude. At sea level, the vertical fluxes of atmospheric muons and neutrinos are of the order of $\sim 100 \text{ m}^{-2} \text{ s}^{-1} \text{ sr}^{-1}$, which is well above contributions from other particles.

In order to shield themselves from particles created in CR showers, experiments attempting to detect astrophysical neutrinos are typically built far below the surface of the Earth. This is the case of ANTARES and IceCube, which are respectively deployed 2 km underwater and 1.5 km deep in the ice. As a result, only atmospheric muons and neutrinos are able to reach the instrumented volumes and contribute to the background of these two detectors. Therefore, only these contributions will be discussed in the following.

Atmospheric muons

When considering the event rate in the detectors, the contribution from atmospheric muons becomes more important than the one of atmospheric neutrinos. This is due to the small interaction cross-section of neutrinos, causing only a fraction of them to be observed. On the contrary, atmospheric muons above a certain energy will almost all trigger the neutrino telescopes. With a rate six times as high as that of atmospheric neutrinos, atmospheric muons therefore represent the dominant contribution to the neutrino telescopes background. However, muons are only able to travel about a tenth of kilometres within the Earth. This implies that the flux of atmospheric muon reaching the detectors is strongly dependent on the direction considered. The atmospheric muons will be stopped by the Earth when considering negative zenith angles, as well as for positive zenith angles close to the horizon. As a result, only the down-going atmospheric muons are contributing to the background of the two telescopes, as shown in Figure [2.11](#). It is possible to reduce the contribution from atmospheric muons by only considering events starting within the detector volume. This condition makes it possible to distinguish between muons induced by muon neutrinos interacting in the detector volume and possible atmospheric muons. It has to be noted that neutrino-induced muons could also be entering the detector as the neutrino interaction could happen

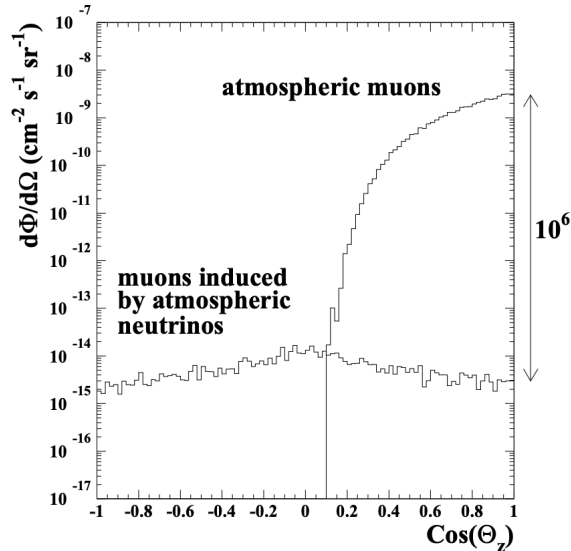


Figure 2.11—Angular distribution of the expected muon flux from atmospheric muons and muons induced by the interaction of atmospheric neutrinos with energies above 1 TeV at a depth of 2300 m in water [45].

outside the detection volume. However, rejecting all penetrating muons considerably reduces the atmospheric muon background. To ensure that the event is a starting track, the outer layers of the detector can be used as a veto region. The details about this veto and the various techniques used to reduce the atmospheric muon background are discussed in more detail when describing the event selections of the two analyses presented in this thesis.

Atmospheric neutrinos

Due to their small interaction cross-section, most neutrinos are able to cross the Earth without interacting. This information combined with the fact that the CR flux is approximately isotropic [46], indicates that atmospheric neutrinos will reach the detectors from all directions. This is visible in Figure 2.11, which shows the expected flux from muons induced by the interaction of atmospheric neutrinos. The visible peak at the horizon, i.e. $\cos\theta_z$ around zero, is due to the so-called secant theta effect. When pions and kaons propagate by grazing the surface of the Earth, they spend more time in a less dense region of the atmosphere in which they are more likely to decay, and thus create neutrinos, rather than to interact. Therefore, more neutrinos are produced due to this effect close to the horizon, resulting in an enhancement of the neutrino flux for these particular arrival directions.

Although the atmospheric neutrinos can be used as the main source of information to determine the oscillation parameters [47, 48], when searching for astrophysical neutrinos, they are only regarded as background. Unlike atmospheric muons, a simple distinction between atmospheric and signal neutrinos cannot be made by using a veto. Rather, one must rely on the reconstructed properties of the neutrinos, such as their energy, direction and arrival time, in order to separate both contributions. The

characteristics used to separate signal from background neutrinos in the two analyses presented in this thesis are discussed in their relative chapters.

2.6.2 Astrophysical neutrinos

Although their detection is the prime purpose of the ANTARES and IceCube neutrino telescopes, high-energy neutrinos from the diffuse flux can constitute a source of background for certain analyses. The contribution of the diffuse neutrino flux described in Section 1.3 is however negligible for the analyses presented in this thesis since they focus on low energies. The expected differential flux for diffuse galactic plane emission, taken from [49], is expressed as:

$$\frac{d\phi_{\nu_\mu+\bar{\nu}_\mu}}{dE} = \phi^{\nu_\mu+\bar{\nu}_\mu} \left(\frac{E}{100\text{TeV}} \right)^{-\gamma}, \quad (2.16)$$

for values of the spectral index and the normalisation factor given by $\gamma = 2.37 \pm 0.09$ and $\phi^{\nu_\mu+\bar{\nu}_\mu} = 1.44_{-0.26}^{+0.25} \times 10^{-18} \text{GeV}^{-1} \text{cm}^{-2} \text{s}^{-1} \text{sr}^{-1}$, respectively. Using this equation the event rate from the diffuse flux is evaluated to be two orders of magnitude below the expected event rate from dark matter annihilation through the muon-channel for a dark matter mass of 100 GeV.

2.6.3 Bio-luminescence

The term bioluminescence covers the production and emission of light by living organisms. This phenomenon, observed in particular in marine organisms, is due to biochemical reactions transforming chemical energy into light. As bioluminescence is influenced by environmental parameters such as the water temperature or the speed of the sea currents, this phenomenon is seasonal. In the Mediterranean Sea, the peak of bioluminescence activity is observed in spring. For ANTARES, bioluminescence results in recorded hits that are part of the detector background. As they might occur in concordance with hits from an actual event, bioluminescence hits might lead to misreconstruction of the coincident event. In order to avoid possible damages due to a large amount of recorded light during some maximum bioluminescence activity periods, the high voltage setting of the ANTARES detector can be briefly put in a reduced high voltage mode. This decrease in the high voltage applied to the OMs occurs when the trigger levels exceed a predefined level. The trigger conditions are then adapted to allow continuous data collection.

2.7 Optical properties of the detector mediums

To properly reconstruct the events based on the light recorded by the optical sensors, it is essential to have a good understanding of the characteristics of the detector medium. Since neutrino properties are reconstructed based on the arrival time of photons at the PMTs, the detector performance heavily depends on the proper knowledge of the processes affecting the propagation of Cherenkov photons between their emission point and the optical sensor recording the hit. While travelling through the detector medium,

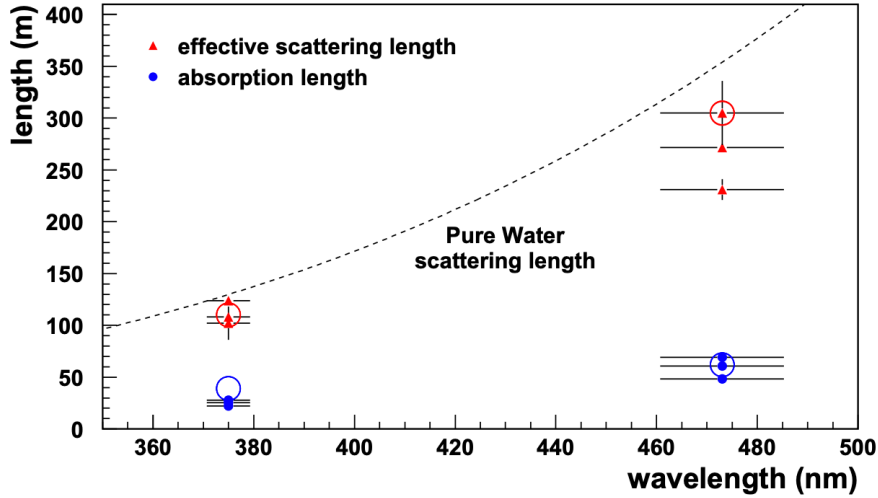


Figure 2.12—Values of the absorption (blue dots) and scattering (red triangles) lengths measured at the location of the ANTARES neutrino telescope with both UV (375 nm) and blue (473 nm) light sources [50]. The dashed line show the scattering length in pure water as a function of the wavelength.

photons are subject to absorption and scattering. Therefore, the required parameters to describe the propagation of photons through a dielectric medium are:

- the average distance travelled by a photon before absorption,
- the average distance travelled between successive photon scatterings,
- the angular distribution of the new photon orientation at each given scattering location.

A good knowledge of these coefficients is also necessary to perform the inverse operation which consists in simulating events and propagating the produced Cherenkov light in the detector. In this section, the velocity of light, as well as the scattering and absorption lengths of the ANTARES and the IceCube telescope media, respectively seawater and ice, are studied.

2.7.1 Mediterranean Sea water

The effects of the scattering and absorption of Cherenkov light in the ANTARES detector medium are characterised using two respective parameters. As a strong correlation is observed between the scattering length, λ_{scatt} , and the scattering angular distribution a parameter regrouping both contributions is defined as follows:

$$\lambda_{\text{scatt}}^{\text{eff}} = \frac{\lambda_{\text{scatt}}}{1 - \langle \cos \theta \rangle}, \quad (2.17)$$

with $\langle \cos(\theta) \rangle$ being the average cosine of the scattering angular distribution. The effective scattering length, $\lambda_{\text{scatt}}^{\text{eff}}$, is then used along the absorption length, λ_{abs} , in order to describe the properties of the seawater. It has to be noted that these parameters differ

Wavelength	$\lambda_{\text{scatt}}^{\text{eff}}$	λ_{abs}
375 nm	122 m	26 m
473 nm	265 m	60 m

Table 2.1: Effective scattering and absorption lengths of the Mediterranean seawater measured using a dedicated PMT and an isotropic light source with wavelengths of 375 nm and 473 nm [50].

depending on the wavelength of the Cherenkov photons. In addition, seasonal changes of the type and the amount of sediment present in the water of the Mediterranean Sea could lead to a variation of these parameters. The first measurements of $\lambda_{\text{scatt}}^{\text{eff}}$ and λ_{abs} were conducted prior to the deployment of the 12 ANTARES instrumented lines, with the help of a PMT installed on a dedicated line [50]. This PMT was used to detect the light from an isotropic source in various configurations, such as for variations of the distance between the source and the PMT. Two different types of LEDs were used in order to measure the seawater properties for two different wavelengths: UV (375 nm) and blue (473 nm) LEDs. These measurements performed with both UV and blue light are visible for the absorption (blue dots) and scattering (red triangles) lengths in Figure 2.12, along with the relative uncertainties. The resulting values of $\lambda_{\text{scatt}}^{\text{eff}}$ and λ_{abs} presented in Table 2.1. The uncertainty on the absorption length can result in an error of 5% on the effective area of the telescope for energies of the PeV scale and up to 15% for energies ~ 100 GeV. The uncertainties of the effective scattering will have an impact on the angular resolution of the reconstructed events with errors between 0.05° and 0.1° . Further measurements of the scattering and absorption lengths were later performed once the detector completion was reached, employing the same optical beacons used for calibration purposes [51].

In order to properly reconstruct the events from the light recorded by the OMs, the group velocity, v_g of light in the seawater needs to be determined. This group velocity is defined as:

$$v_g = \frac{c}{n_g} - \frac{c \cdot k}{n_g^2} \frac{dn_g}{d\omega}, \quad (2.18)$$

where n_g is the group refraction index, ω is the wave packet frequency and k is the wave number. From Equation 2.1, one can see that the group velocity influences the opening angle of the Cherenkov cone and therefore the reconstruction of the events recorded by the detector. In addition, it plays an important role in the time calibration as the expected delay of the arrival time of the calibration signal are based on this velocity. Measurements of the group refraction index were performed with the help of the optical beacons [52]. For this, the LED intensities were varied, along with the distance between the LED beacon and the PMT used for the measurement.

2.7.2 South Pole ice

Since the South Pole ice was formed from snow accumulation over at least 165 thousand years [53], it presents a layered structure. As the pressure increases with depth, the

air bubbles shaped during the ice formation are slowly assimilated to the ice molecules themselves, creating gas clathrate hydrates. At the South Pole, this phenomenon occurs at depths below 1200 m [54], meaning that underneath this depth, the photon scattering due to air bubbles becomes negligible. This constitutes the main reason why the IceCube DOMs were deployed at depths between 1450 m and 2450 m. However, it has to be noted that the ice contained in the boreholes went through a much quicker refreezing process. As a result, the borehole ice, often referred to as hole ice, exhibits remaining air bubbles which will affect the propagation of the photons. Impurities of the ice, known as dust, also contribute to degrading the optical properties of the ice. For depths between 1970 m and 2100 m, the concentration of impurities reach a higher level, further degrading the ice properties. The ice in this region of the detector, known as the dust layer, formed $\sim 65,000$ years ago and contains a high concentration of volcanic ashes.

With the aim of describing the effects of the absorption and the scattering of photons in the Antarctic ice, two coefficients are introduced. The first of these parameters is the effective scattering coefficient, b_e , defined as:

$$b_e = b (1 - \langle \cos \theta \rangle), \quad (2.19)$$

where θ is the deflection angle at each scatter point and $b = 1/\lambda_{\text{scatt}}$ is the geometrical scattering coefficient, with λ_{scatt} being the average distance between successive scatters. The second parameter is the absorption coefficient, a , defined as the inverse of the absorption length, λ_{abs} . These coefficients themselves are a function of other parameters such as the wavelength of the photons and the depth in ice:

$$a(\lambda) = a_{\text{dust}}(400) \left(\frac{\lambda}{400} \right)^{-\kappa} + Ae^{-B/\lambda} (1 + 0.01 \delta\tau), \quad (2.20)$$

$$b_e(\lambda) = b_e(400) \left(\frac{\lambda}{400} \right)^{-\alpha}, \quad (2.21)$$

where the absorption coefficient, $a(\lambda)$, is given by the sum of two separate contributions. The first contribution, a_{dust} , is the component related to the presence of dust in the ice, while the second contribution takes into consideration the depth-dependant temperature of the pure ice, $\delta\tau$. The parameters α , κ , A and B are defined in [55]. These global parameters are part of the six parameters used by the SPICE-Mie ice-model, along a_{dust} and b_e for a 400 nm photon wavelength [56]. With this algorithm, the scattering angle distribution takes the form of a Mie scattering with impurities modelled as spheres. A second more recent algorithm, called SPICE-Lea, is also used to model the Antarctic ice. Three additional parameters are introduced in this algorithm to consider the azimuth dependence of the photon scattering processes as observed in the optical anisotropy of the South Pole ice reported in [57].

In both cases, dedicated measurements using the LEDs equipped on each DOM were conducted in order to determine these parameters [56]. For this, the light emitted by the LEDs of a specific DOM is observed by nearby DOMs. By this means, the arrival time of the photons as well as the total deposited charge are recorded for various detector depths. The recorded data are then fitted in order to find the scattering and

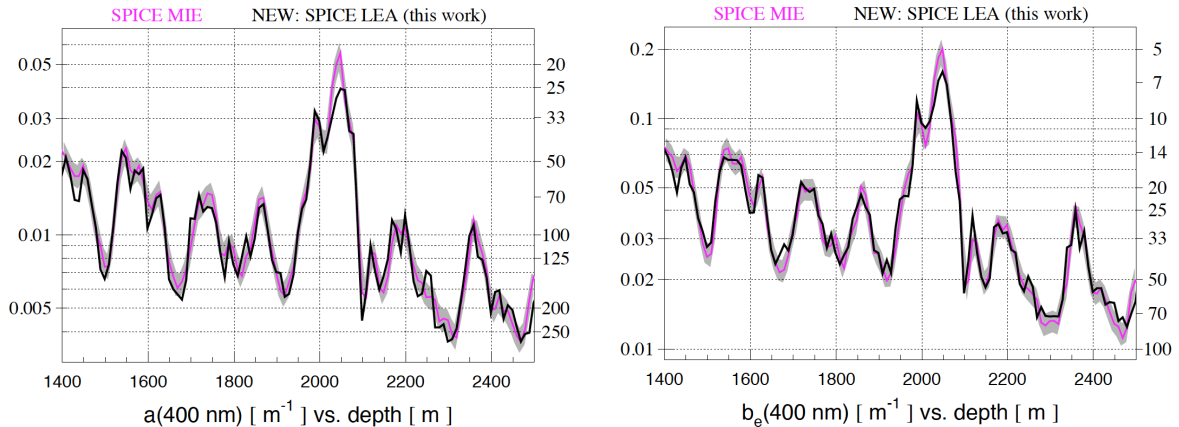


Figure 2.13—Values of the absorption, $a(400)$, and the effective scattering, $b_e(400)$, coefficients as a function of depth for both the SPICE-Mie and SPICE-Lea ice-models (taken from [57]).

absorption parameters that best describe the observations. The resulting absorption (left) and effective scattering (right) coefficients are shown in Figure 2.13 as a function of the depth for a considered wavelength of 400 nm for both the SPICE-Mie and the SPICE-Lea ice-models.

2.8 Data processing

In this section the first levels of data processing applied to ANTARES and IceCube data are described. This is motivated by the will to reduce the amount of data collected by both detectors in order to facilitate the data transfer and further event selections.

2.8.1 ANTARES

The daily amount of data recorded by the 885 OMs of the ANTARES detector sums up to 4 TB of data. A non-negligible portion of the hits recorded by the PMTs are caused by bioluminescence and potassium decays, resulting in an average rate from pure noise of 50 kHz. With the purpose of reducing the volume of recorded data, a set of triggers are employed to discard events representing no interest for the physics studied by the ANTARES detector, e.g. pure noise events and bioluminescence hits. If the conditions of at least one trigger are met, the hit is kept. The triggers are based on temporal and spatial correlation between the recorded hits. This reduces the contribution of uncorrelated pure noise hits to less than 10% of the total background rate. The various triggers used by ANTARES are organised in trigger levels, the first of which is used to exclude hits with less than 0.3 PE. This trigger level, known as L0, is applied locally by electronic devices contained in the LCM. The subsequent trigger levels are handled after the transfer of data to the shore. The first of this on-shore triggers only selects events for which at least two L0 hits are recorded by the same storey or for which the recorded L0 hit has more than 3 PE. The latter condition is known as the high threshold filter and can be adapted to require at least 10 PE. The set of hits satisfying these triggering

conditions are referred to as L1 hits. The following trigger level is known as the T-level and looks for coincident L1 hits recorded by neighbouring storeys of the same line. Further trigger levels applied to reject background hits typically request multiple T-hits to be recorded. These triggers often look for causal correlations between these hits. The resulting data sets are divided into runs of typical durations of eight hours. This organisation of the data in runs allows for modifications of the detector setup from one run to the other. These data files are stored as ROOT files and are then sent to a data centre located in Lyon. From there on, various reconstructions are applied on the events using a framework called SeaTray. The resulting reconstructed events are saved under a file format specific to ANTARES, known as AntDST.

2.8.2 IceCube

The successive selections applied to IceCube data are split in various levels. The first of these selection levels, referred to as Level 1 (L1), is applied using an online processing system that relies on information provided by LC hits. From LC information, a variety of triggers is defined. Among those filters, the one considered for the event selections presented in this thesis is the Simple Multiple Trigger (SMT). This basic trigger is activated whenever a certain number of HLC hits is recorded within a predefined time interval of a few microseconds. In particular, the SMT3 trigger requires three DOMs of the DeepCore fiducial volume to record HLC hits within a time interval of $2.5\ \mu\text{s}$. If this condition is met, an extended readout window centred on the HLC is created. The data recorded during this predefined time interval, generally set to $20\ \mu\text{s}$, are referred to as IceCube events. These so-called events consist of the digital waveforms provided by each of the DOMs that recorded a hit during this period. The event rate obtained from SMT3 is considerably lower than the trigger rate of the entire IceCube detector (global trigger rate), with about 250 Hz compared to 2.9 kHz. The global trigger rate regroups all individual triggers, with an extended readout window of $\pm 10\ \mu\text{s}$ around the original trigger time interval. The resulting data flow at trigger level still amounts to about 1 TB/day, which is well above the data volume allowed to be transferred by satellite. For this reason, the amount of data is further reduced to about 100 GB/day by applying filters directly at the South Pole. This filtering level is known as Level 2 (L2) and constitutes the common basis for consecutive event selections carried out for individual analyses. Events are tagged depending on whether they fulfil or not certain conditions, such as restrictions on the energy, the direction or the topology of the event. Level 2 regroups all the events that satisfied the conditions of at least one filter. A variety of filters are applied at this level, each having the purpose of selecting specific types of events. Once the filters are applied, the resulting Level 2 data selection is sent via satellite to the data centre located at the University of Madison (Wisconsin), where it is accessible to the entire collaboration. The events are stored in files with a format specific to IceCube known as i3-files. The data are divided into in so-called runs, with a typical run duration of eight hours. For each run, a frame containing the related detector geometry, calibration and detector status (called GCD frame) is saved along the physics frame containing the triggered events.

2.9 Detector stability and calibration

In order to ensure the proper operation of the detectors, calibration processes were designed. In this section, the various steps of this in-situ calibration and the stability of both detectors are specified.

2.9.1 ANTARES

The ANTARES neutrino telescope achieves an angular resolution of less than 0.3° for track events with energies above a few TeV. To maintain such high quality angular resolution, the detector relies heavily on continuous in-situ calibration processes. As the ANTARES lines are flexible, their movements due to sea currents are constantly monitored in order to guarantee a good event reconstruction. For this, the relative positions of the optical modules are measured, along their respective orientations. A high precision on the photon arrival time is also required to ensure a good event reconstruction.

Position calibration

The relative positions of the OMs are monitored using a High Frequency Long Base Line (HFLBL) acoustic system with a precision below 10 cm. This system determines the 3D location of hydrophones disposed along the detector lines using a triangulation method. For this, emitters are anchored to the seabed at the base of each line and are complemented by a set of autonomous transponders located in between lines on the seabed. In addition to this, the orientation of each storey is monitored using tiltmeter-compass sensors hosted by each storey. This set of sensors provides the tilting angle of each storey with respect to the detector line, as well as the storey orientation relative to magnetic North. The current location of the entire detector with respect to the celestial sky is also tracked at all times using a GPS system. This monitoring is necessary in order to locate the origin of the incoming neutrinos. Due to the rotation of the Earth, the local coordinate system of the ANTARES telescope finds itself shifted with respect to the celestial sky. This rotation is of the order of 1° every two minutes.

Time calibration

In order to guarantee a precision on the photon arrival time of the order of ns, a weekly time calibration of the detector is performed. The clock system of ANTARES is used to allocate both a relative and an absolute timing. The absolute time serves as input time to the GPS system used to compute the celestial coordinates of an event. It is also pertinent to determine if a specific transient source is at the origin of the neutrino event. While the absolute time is related to recorded neutrino events and is set by a GPS clock system, the relative time is linked to the timing of the individual hits recorded by the PMTs. For the reconstruction, and thus the angular resolution, only the relative timing is of interest. In order to correct for the time delay due to the electronics connecting the LCMs to the shore, an internal clock calibration is used. With this method, the time delays between the shore station clock and the clocks installed in each LCM are determined. Further calibration is still required to evaluate

the delay between the arrival of the recorded photon and its processing by the LCM. Various methods were developed for the calibration of this delay, involving external light sources. One of these sources takes the form of LED beacons, which are disposed in four different locations within the detector volume. A laser beacon system is also used to measure the time delay within every single line. For this three lasers anchored to the seabed at the bottom of three different lines are used to send light in the direction of neighbouring lines. Another possible external source of light for time and efficiency calibration is provided by the decay of radioactive ^{40}K present in seawater. When occurring within few meters of a storey, the light produced by the β -decay of ^{40}K can be measured as a coincident signal by two OMs, and the time difference between the two hits can be measured. Lastly, the variations of the transit time of each PMT, i.e. the time between a photon hitting the photocathode and the PMT output signal, are monitored using the LED housed in each OM.

2.9.2 IceCube

Since its completion, the IceCube neutrino telescope has proven to be quite stable with an operating time fraction (uptime) reaching an average of $\sim 99\%$. As a result, the collection of data is only stopped (downtime) for the purpose of detector calibration, or in the rare occurrences of a software bug. Unlike ANTARES, the relative position of the DOMs in IceCube does not need to be monitored as the ice of the detector is not subject to shear. Nonetheless, some DOMs were removed from the IceCube configuration due to loss of communication or electronic failures. To date, about 80 out of the 5160 DOMs initially deployed are considered to be dead DOMs. Most of these DOMs were already non-operational at the time of their deployment. Some of these DOMs might also have died as a result of prolonged power failures, during which the temperature of the DOMs can drop and cause electronic failures. These dead DOMs also have an impact on the running conditions of their neighbouring DOMs as LC conditions cannot be properly checked and are instead set to always trigger.

DOM calibration

The calibration process applied to the DOMs are regrouped under a single software known as DOMCal. As the operation status of the IceCube detector is quite stable, the calibration of the DOM is only performed annually. Through this, each DOM is subject to a calibration of the time required between the production of the photo-electron and the completion of the digitisation process. This measurement is done with the help of the dedicated low-luminosity LED installed on the mainboard of each DOM. Unlike the LEDs of the flasher board, this LED is used to light up the PMT of the very DOM it is contained in. The measured transiting time is processed by the DOMCal software and is then used as a time correction during the pulse extraction process. An individual calibration of the electronics hosted by the mainboard is also performed during the early maintenance process. The properties of the ATWD, such as its sampling speed and its voltage levels, are individually calibrated. This basic calibration process is later refined using a waveform calibration. A regular adjustment of the voltage of the individual DOMs is also applied in order to maintain a constant PMT gain of about

10^7 . This calibration is performed using dark noise hits for which the charge recorded before amplification is known. For each applied voltage level, a histogram displaying the recorded charges is computed. By fitting each histogram with a Gaussian, the gain at each voltage level is determined. Using this information, the voltage related to the desirable gain is identified.

Time calibration

A continuous calibration of the individual DOM clocks is performed through a procedure known as Reciprocal Active Pulsing Calibration (RAPCal). The RAPCal procedure allows the clock of each DOM to be synchronised with the GPS clock located in the ICL. This way, the entire detector runs under a standard time known with a precision of 2 ns. A pulse from the ICL to each DOM is sent during pauses of the data transmission. When receiving this signal, the DOM generates a pulse with similar shape which is sent back to the ICL. These two pulses are time-stamped both when they are sent and when they arrive. The offset between the local and the global clocks is computed from these two sets of timestamps, as well as from the respective waveforms.

Chapter 3

Dark Matter

In the 1930s, astronomers started to report mismatches between the observed average velocity dispersion and the expected velocity dispersion of galaxies for several galaxy clusters. A first attempt to explain these observations assumed the existence of non-luminous astrophysical objects, the so-called dark matter. The term dark matter was first introduced in this context by the Swiss astronomer F. Zwicky. At the time, dark matter was only assumed to be made of the same matter as ordinary astrophysical objects, such as cold stars or inter-stellar gas. It was not before the 1970s that these assumptions were considered to be in tension with the current understanding of our Universe. More recent hypotheses suggest that dark matter is more likely to be composed of non-baryonic matter. However, the very nature of dark matter remains uncertain. In the first section of this chapter, some observational evidences suggesting the existence of dark matter are discussed. From this, the required characteristics of dark matter are inferred and a compilation of possible candidates is cited in Section 3.2. The three main categories of dark matter searches are listed in Section 3.3, along with the current limits from the related experiments. Lastly, the relevant aspects of dark matter phenomenology for indirect dark matter searches are described in Section 3.4.

3.1 Dark matter evidences

3.1.1 Mass discrepancy in galaxy clusters

The first hint of the existence of dark matter arose from the noticeable dispersion in the velocity of several galaxies of the Coma cluster pointed out by Zwicky in 1933 [58]. By applying the virial theorem, Zwicky estimated the total mass of the Coma cluster as the product of the 800 observed galaxies in the cluster, for an averaged galaxy mass of 10^9 solar mass (M_{\odot}). Under the assumption that the cluster is in dynamic equilibrium, the virial theorem is expressed as:

$$\langle T \rangle = -\frac{1}{2} \langle U \rangle, \quad (3.1)$$

where T and U are the kinetic and potential energies, respectively. For an object of mass m (here a galaxy) moving with a speed $v(r)$ at a radial distance r from the centre

of the considered system, i.e. the galaxy cluster, one then gets:

$$\frac{mv^2(r)}{2} = \frac{mM(r)G}{2r}, \quad (3.2)$$

where G is the gravitational constant and $M(r)$ is the mass contained inside a sphere of radius r . The potential energy of the system was then computed under the assumption that the Coma cluster could be approximated by a sphere with a radius of $\sim 10^6$ light-years (ly). The resulting expected velocity dispersion equalled 80 km s^{-1} , whereas the average velocity dispersion observed along the line-of-sight was of $\sim 1000 \text{ km s}^{-1}$. Zwicky concluded that, if accurate, these calculations implied that the amount of invisible matter in the cluster was far greater than the amount of luminous matter. In 1937, Zwicky fine-tuned his computation with the purpose of estimating the average mass of galaxies in the Coma cluster [59]. This time, he assumed that the Coma cluster consisted of 1000 galaxies contained within a radius of 2×10^6 ly. Using the virial theorem with an observed velocity dispersion of 700 km s^{-1} led to a limit on the average galaxy mass of $4.5 \times 10^{13} M_{\odot}$. Under the assumption that the galaxies in the cluster have an average absolute luminosity of $8.5 \times 10^7 L_{\odot}$, the average mass-to-light ratio of these galaxies was then estimated to be around 500. Even though these estimations were based on an outdated value of the Hubble constant of $H_0 = 558 \text{ km s}^{-1} \text{ Mpc}^{-1}$ taken from [60], using the most recent value of $H_0 = 67.66 \text{ km s}^{-1} \text{ Mpc}^{-1}$ [61] to rescale the results still gives a mass-to-light ratio of $\sim 500 \times 67.66/558 = 60.6$. This large mass-to-light ratio indicates the presence of dark matter in the Coma cluster. In the meantime, similar observations were made by S. Smith when studying the Virgo cluster in 1936 [62]. At the time, no consensus was reached on the existence of dark matter.

3.1.2 Galactic rotation curves

The study of the rotation curves of spiral galaxies provides strong indications in favour of dark matter and played a crucial role in its discovery. These rotation curves represent the orbital velocity distributions of massive objects within a given galaxy, expressed as a function of their radial distance to its centre. Rotation curves were measured as early as the first half of the 20th century for close-by galaxies, such as the Andromeda Galaxy (M31). Boosted by the discovery of the 21-cm radio line in 1951 [63-65] and the fast progress in the field of radio astronomy, a succession of rotation curve measurements were made in the following years. A common feature of all these rotation curves is that they are "flat", meaning that the orbital velocity does not decrease with the radial distance, while Newtonian dynamics predicts

$$v(r) = \sqrt{\frac{GM(r)}{r}}, \quad (3.3)$$

when taking only visible matter into account. The fact that observations show a rather constant velocity at large radial distances suggests the presence of a large amount of dark matter in the outer parts of the galaxies, with $M(r) \propto r$ and thus the dark matter density going as $\rho(r) \propto 1/r^2$. However, it was not until the 1970s that these observations were considered to be in disagreement with the current understanding of

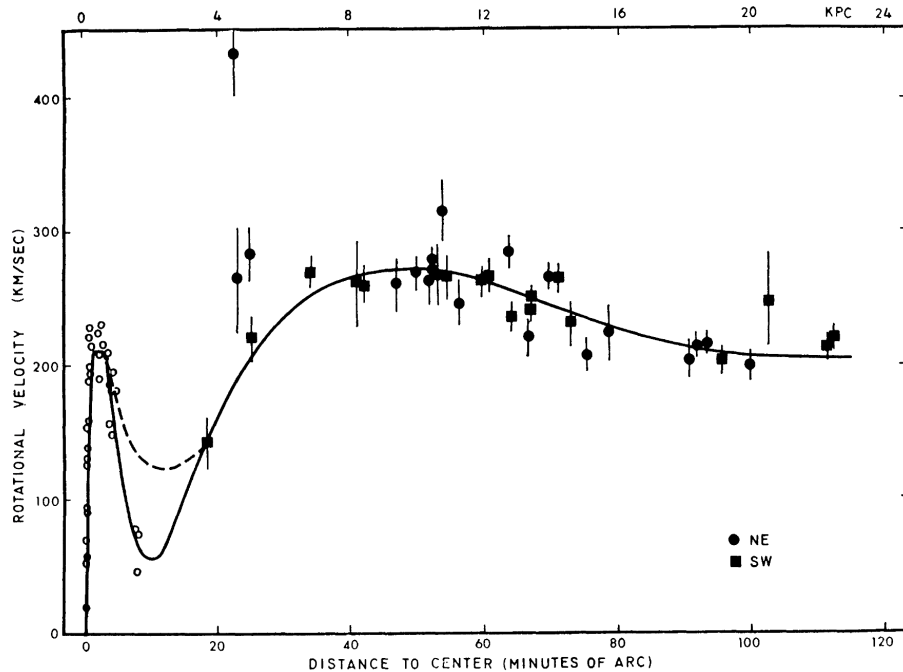


Figure 3.1—Measure of the rotation velocity of OB stars in M31 as a function of their distance to the centre of the galaxy taken from [66].

the dynamics of galaxies. At the time, this unseen matter was assumed to take the form of faint objects or cold interstellar gas. The most famous rotation curve measurements were presented in 1970 by V. Rubin and W. K. Ford. Their refined measurements of the M31 rotation curve were taken using an image tube spectrograph [66]. Their results extended to large radii, and they too showed that the velocity was fairly constant with increasing radius values, as can be seen in Figure 3.1. The same year, Freeman noticed that the observed maxima of the rotation curves of galaxies M33 and NGC 300 both peaked at greater radii than expected [67]. From this, Freeman concluded that additional undetected matter must be present in these galaxies.

3.1.3 Gravitational lensing

As massive objects curve space-time, the trajectory of light can be bent when going near such objects. As a result, the image of distant sources can be distorted by massive galaxies and galaxy clusters, which can act as gravitational lenses when standing between these sources and the observer. The distinction between three types of gravitational lensing can be made: strong lensing, weak lensing and micro-lensing. In the case of strong gravitational lensing, the massive object standing between the source and the observer is large enough to distort the image of the source. These distortions can take the form of arcs which can appear multiple times, forming a ring around the lens known as an Einstein ring. For weak gravitational lensing, the lens is not massive enough to cause strong distortions of the observed object. Therefore, a statistical analysis needs to be performed on the distortion of many background sources to obtain the properties of the lens. For micro-lensing, there is no visible distortion and the lensing

is rather observed from the variations in time of the intensity of the light measured from the studied object. The amount of matter required to explain the observations can be deduced from the strength of the distortions using

$$\alpha = \frac{4GM}{c^2 b}, \quad (3.4)$$

where α is the photon deflection angle, b is the distance of the closest approach and M is the mass of the lensing object to be constrained. Observations show large discrepancies between the mass inferred from gravitational lensing and the mass of the lensing object expected from visible matter [68].

The Bullet cluster

The Bullet cluster (1E 0657-56) is perhaps the most famous system studied through gravitational lensing, as it led to one of the most conclusive evidence of dark matter. This cluster is part of a merging system first observed in the late 1990s [69], which results from the collision of this bullet-shaped sub-cluster with the main cluster of the system (1E0657558). The collision of the two cluster happened approximately in the plane of the sky at a redshift of $z=0.296$. The cores of the respective clusters crossed each other about 100 million years ago. The first hint of the dark matter presence in the Bullet Cluster is its high mass-to-luminosity ratio, indicating an important amount of unseen matter in the galaxy cluster. From observations of the weak gravitational lensing effects on background galaxies, the gravitational potential of the resulting cluster was mapped [70]. The contours of the mass estimate from weak gravitational lensing reconstructions for the merging clusters are shown in Figure 3.2. In parallel, X-ray observations tell us more about the distribution of plasma in this galaxy cluster. During the merger of the two galaxy clusters, the galaxies of the respective clusters are expected to behave like collision-less particles and be largely unaffected as they pass through each other. Meanwhile, the gas cloud of the two galaxy clusters would be slowed down by electromagnetic interactions. This can be seen in the right panel of Figure 3.2, where the bulk of the X-ray emission from the ionised gas is visible in yellow. Assuming that no dark matter is present in the Bullet cluster, the plasma component should dominate the total mass of the cluster, with a contribution about ten times larger than the mass of the galaxies in the cluster. Thus, the reconstructed gravitational potential should be located around the X-ray emitting plasma. However, the contours of the mass estimate resulting from the weak lensing analysis are centred around the galaxies of the two merging clusters, well away from the plasma. This implies the existence of two dark matter halos that crossed without interacting, which must be more massive than the plasma and well-separated from it. The importance of this observation stands in the fact that a clear separation is seen between the postulated dark matter and the baryonic matter as a result of the two cluster merger, making this observation difficult to explain with other theories attempting to explain the mass deficit, such as modified laws of gravity (see Section 3.2.3).

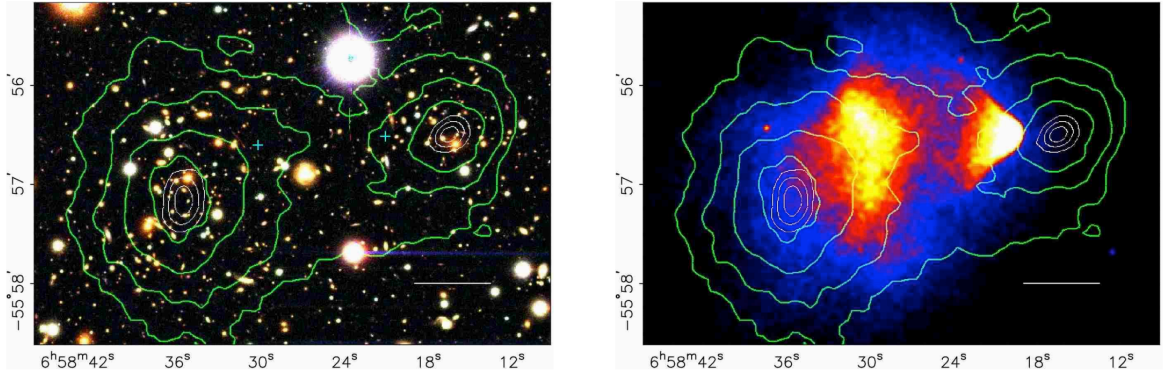


Figure 3.2—Merging sub-cluster 1E 0657-558, called the Bullet Cluster, as seen from optical (right) and X-Ray (left) observations. The main cluster (1E 0657-56) of the merging system is also visible on the left-side of both pictures. The white bar indicates a distance 200 kpc at the location of the cluster. The green contours in both panels represent the weak gravitational lensing reconstruction. The inner white contours show the errors on the position of the gravitational peaks at 68.3 %, 95.5 % and 99.7 % CL. The cyan crosses (left figure) mark the location of the centres used to measure masses of the X-ray emitting plasma clouds.

3.1.4 Cosmic microwave background

The accidental discovery of the Cosmic Microwave Background (CMB) by A. Penzias and R. W. Wilson in the mid-1960s [71] marked a turning point in our understanding of the universe. The CMB provides a glimpse of the early stage of the Universe, and renders perhaps the strongest evidence that dark matter must be non-baryonic. In its earliest stage, the Universe was much denser and hotter, such that photons were not yet decoupled from the baryonic matter. As the Universe expanded, matter grew colder until it was eventually possible for electrons and protons to be bound into neutral hydrogen atoms. This point in time is referred to as the recombination epoch and marks the moment from which photons were able to travel freely through space due to the expansion of the Universe. The CMB consists of relic photons from the moment of the recombination. As suggested by its name, the CMB cannot be observed with traditional optical telescopes but instead with sufficiently sensitive radio telescopes, and more precisely in the microwave region of the radio spectrum.

Baryon acoustic oscillations

Observations of the CMB show a rather homogeneous distribution of photons over the entire sky, with small-scale anisotropies due to variations of the mass distribution at the epoch of the photon emission. Before the recombination, variations in the baryonic matter density were amplified as denser regions were attracting more baryonic matter, forming gravitational potential wells. This effect was counterbalanced by the radiation pressure of the photons coupled to this baryonic matter, which had a repelling effect once a certain density was reached. As a result, the baryon-photon fluid oscillated between hills and wells present in the total potential. This phenomenon, which suddenly stopped at the recombination epoch, is known as the Baryon Acoustic Os-

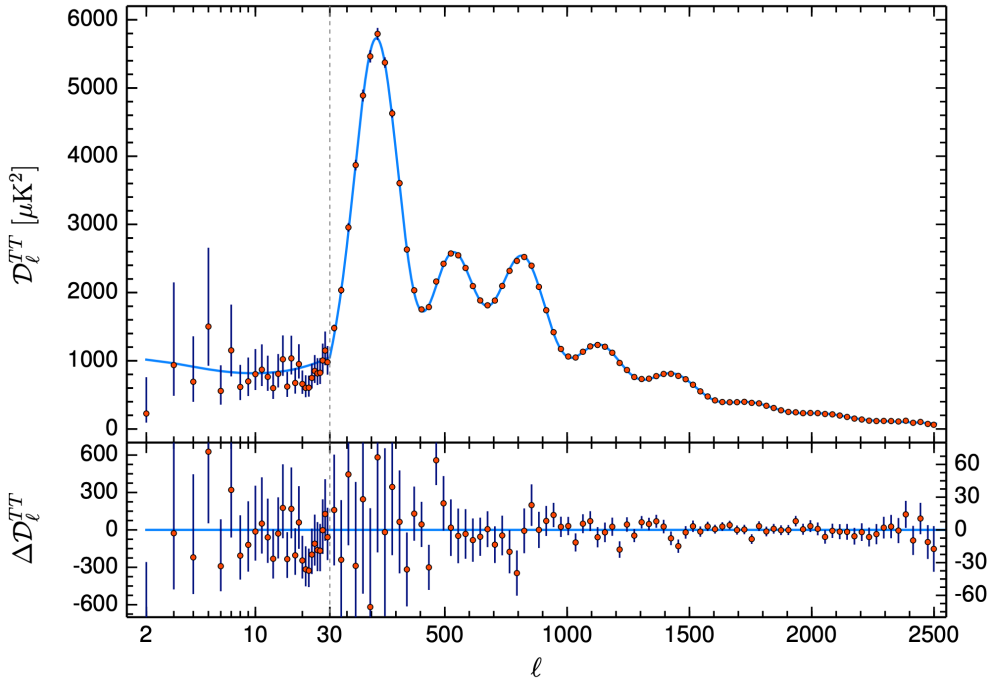


Figure 3.3—Temperature power spectrum of the CMB measured by Planck taken from [61]. Upper panel: Measurement showing seven acoustic peaks. The solid blue line shows the theoretical spectrum given by the Λ CDM-model. Lower panel: Residuals with respect to the Λ CDM model. The $\pm 1\sigma$ uncertainties are represented by the error bars.

cillations (BAOs). The resulting inhomogeneities in the density distribution translate into temperature variations imprinted in the CMB.

A characterisation of these fluctuations can be derived from the temperature power spectrum of the CMB from Planck measurements shown in Figure 3.3 [61]. This mapping of the CMB temperature in terms of spherical harmonic functions relies on the energy density of the Universe, as well as on its separation into the different energy and matter constituents. For instance, the ratio between the heights of the first and second peaks provide indications about the quantity of baryonic matter in the Universe, while the subsequent peaks attest of the amount of dark matter. This is due to the fact that the abundance of baryons in the early Universe had an influence on both the gravitational potential and radiation pressure, scaling the first peak up or down depending on whether more or less baryons were present. A modification of the amount of non-baryonic matter in the early Universe would only affect the gravitational potential while leaving the radiation pressure unchanged. This way, a smaller or larger amount of dark matter would either attenuate or amplify the impact of the radiation pressure, causing the amplitude of the BAOs to respectively drop or raise. As a result, information about the amount of baryonic and dark matter contained in the Universe at the present time can be derived by fitting a cosmological model to this measured power spectra.

Lambda cold dark matter model

As of today, the best representation of the observed data is given by the Lambda Cold Dark Matter (Λ CDM) model. This model, also known as the standard model of cosmology, offers a description of our Universe in terms of three components: the dark energy, Λ , the baryonic matter and cold dark matter (CDM). Under the assumption of a flat spatial geometry of the Universe, the mass-energy density of these individual components can be expressed with respect to the critical density, ρ_c , such that:

$$\Omega_X = \rho_X / \rho_c, \quad (3.5)$$

with X indicating the different components and $\rho_c = 3H_0^2/8\pi G$, with G and $H_0 = 67.66 \pm 0.42 \text{ km s}^{-1} \text{ Mpc}^{-1}$ being the gravitational and the Hubble constants, respectively. As a result, the total mass-energy density fraction of the Universe can be formulated as the sum of these individual components, such that $\Omega_{\text{tot}} = \sum_X \Omega_X = 1$. In particular, Ω_{tot} can be split between its dark energy, Ω_Λ , and its matter, Ω_m , contributions. By fitting the Λ CDM model on the spectrum shown in Figure [3.3](#), the following values are obtained:

$$\Omega_\Lambda h^2 = 0.31537 \pm 0.00256, \quad (3.6)$$

$$\Omega_m h^2 = 0.14240 \pm 0.00087, \quad (3.7)$$

where the matter contribution (Ω_m) can be further divided in terms of cold dark matter (Ω_c) and baryonic matter (Ω_b):

$$\Omega_c h^2 = 0.11933 \pm 0.00091, \quad (3.8)$$

$$\Omega_b h^2 = 0.02242 \pm 0.00014, \quad (3.9)$$

with $h = H_0/(100 \text{ km s}^{-1} \text{ Mpc}^{-1})$ being the dimensionless Hubble parameter.

3.2 Dark matter candidates

Since astrophysical evidences are based solely on the gravitational effects of dark matter, very few properties can be deduced from these observations. As a result, a multitude of candidates have been put forward in order to explain the observed mass deficit in the Universe. The proposed theories can be divided in three major categories, the first of which postulate dark matter to be made of baryonic non-luminous matter, such as brown dwarfs or planets. The second category of theories aims at explaining the observed gravitational effects of dark matter by modifying the gravitational laws instead of postulating the existence of unseen matter. The third category assumes that DM consists of non-baryonic matter, often inferring the existence of new massive particles. The properties of such particles are constrained by astrophysical observations, such that the postulated DM particles should be massive, non-relativistic and non-baryonic. In this section, more details about the properties of the candidates mentioned above are discussed.

3.2.1 Baryonic dark matter

As mentioned in Section 3.1, CMB measurements tell us that the vast majority of dark matter must be non-baryonic. However, a small fraction of the unseen matter in our Universe could still be made of baryonic matter. This contribution could take the form of Massive Compact Halo Objects (MACHOs), such as brown dwarfs and planets. Searches for the gravitational effects of MACHOs were carried out using micro-lensing. Observations of stars in the Magellanic Clouds made it possible to probe the fraction of MACHOs in the Milky Way, within a certain mass range [72, 73]. These studies also exclude MACHOs to constitute the main contribution to the mass of spherical dark matter halos, for masses ranging from $0.6 \times 10^{-7} M_{\odot}$ to $15 M_{\odot}$.

However, one type of object belonging to the MACHO class has recently received renewed interest as a plausible DM candidate. The idea that (parts of) dark matter could be made of primordial black holes (PBH) still holds for a certain range of masses [74]. PBH were first theorised in the 1960s by Y. Zel'dovich and I. Novikov [75], before the mechanism behind their formation was studied thoroughly by S. Hawking [76]. PBH are expected to have formed in the early Universe, during the radiation dominated era. As these black holes are not created by the core collapse of stars, PBH were expected to exhibit a broad range of masses. Nonetheless, some constraints on the possible PBH mass range have been set [77]. For instance, Hawking evaporation limits, obtained among others from extragalactic γ -ray background and CMB anisotropies, exclude PBH with masses below 10^{17} g. Higher PBH (above 10^{23} g) are ruled out by astrophysical observations, such as micro-lensing. Under the assumption that PBHs make up a large fraction of DM, their detection with future gravitational wave experiments would be possible [78].

3.2.2 Non-baryonic dark matter

There are strong indications in favour of non-baryonic dark matter, mostly derived from CMB observations. These observational evidences also constrain the properties of dark matter particles. Their very non-baryonic nature tells us that these particles must be colour neutral, which means that they must not interact via the strong force. As indicated by its name, dark matter is also expected to remain unaffected by electromagnetic interactions and should therefore exhibit a neutral electrical charge. However, dark matter particles could still interact via the weak force. In addition, CMB observations and N-body simulations of the Universe evolution tend to prefer non-relativistic (cold) dark matter candidates over a warm or hot dark matter scenario. As the gravitational effects of dark matter are still witnessed to this day, the lightest dark matter particle must have a lifetime equal to or greater than the age of the Universe ($\sim 1 \times 10^{17}$ s). Constraints on the decay lifetime of dark matter particles have been set by γ -ray experiments, setting a lower limit of $\sim 1 \times 10^{26}$ s [79]. In order to fit the current DM density, dark matter annihilation must also be sparse, yet not banned under the assumption that dark matter reached thermodynamic equilibrium in the early Universe.

Most non-baryonic dark matter candidates are particles postulated outside the standard model, although some SM particles have been considered as possible DM candi-

dates. Cold dark matter candidates, which mainly fall under the description of weakly interacting massive particles (WIMPs), are described in greater depth in the following paragraphs. Noteworthy WIMP candidates are Kaluza-Klein particles and supersymmetric particles, such as the neutralino and the gravitino. Although hot and warm dark matter scenarios are disfavoured, some of their plausible candidates are also studied in more details, namely neutrinos, sterile neutrinos and axions.

Hot and warm dark matter candidates

Among particles of the SM, neutrinos have long been considered as good candidates for hot dark matter since they satisfy various constraints that dark matter particles must meet. Although neutrinos could explain part of the dark matter, their abundance in the Universe is not sufficient to represent its key contribution. One can estimate the total relic density of neutrinos, Ω_ν , from

$$\Omega_\nu h^2 = \sum_{i=1}^3 \frac{m_{\nu_i}}{93 \text{ eV}}, \quad (3.10)$$

where i represents the neutrino flavour and m_{ν_i} is the associated neutrino mass. The latest constraint on neutrino masses set from tritium decay by the KATRIN experiment gives a 90% C.L. upper limit of 1.1 eV for the electronic neutrino mass [80]. From this result, an upper bound on the total relic neutrino density can be deduced, giving

$$\Omega_\nu h^2 \lesssim 0.035, \quad (3.11)$$

which is valid for the different neutrino flavours since they have similar masses, as mentioned in Section 1.2.

Sterile neutrinos, which are theoretical particles similar to SM neutrinos, are also often put forward as dark matter particles. This neutrino state is recurrently introduced in order to explain observed anomalies in the oscillation of the three active neutrino flavours. Unlike SM neutrinos, sterile neutrinos would not be subject to the weak interaction but could still mix with regular neutrinos via oscillation. Based on the sterile neutrino mass, this neutrino state could also qualify as a cold dark matter candidate [81].

First introduced in order to resolve the CP violation problem [82], axions are also popular dark matter candidates. Constraints on the mass of axions set by laboratory experiments as well as astrophysical observations tell us that axions must be extremely light particles with masses below 0.01 eV. However, axions are still reasonable DM candidates as it is feasible to make them meet all the current constraints on dark matter [83].

Cold dark matter candidates

The most commonly accepted cold dark matter candidates are WIMPs, which consist of massive particles interacting weakly with ordinary matter. The prominence of WIMPs stems from the fact that they are postulated independently in several extensions of the

SM that were created in attempts to solve issues with no link to dark matter, such as the unification of all the fundamental interactions.

One of these extensions of the SM is the supersymmetry (SUSY) theory. Supersymmetric models postulate the existence of symmetry between fermions and bosons, i.e. between the components of matter and the mediators of fundamental interactions. This way, each SM fermion is assumed to have a supersymmetric bosonic counterpart, known as sfermion, just as every SM boson is assumed to have a fermionic super-partner, referred to as bosino. Among the existing supersymmetric models, the minimal supersymmetric standard model (MSSM) reduce the number of required fields to the minimum, introducing only one Higgs field in addition to the supersymmetric partners of the SM bosons and fermions. Another property of the MSSM is the conservation of the R-parity. For SM particles, the R-parity equals 1 while it takes values of -1 for their relative super-partners. Therefore, the decay of super-particles must yield an odd number of lighter super-particles, implying that the lightest supersymmetric particle (LSP) must be stable and constitute a good DM candidate. Under the assumption that super-partners are Majorana particles, pair-annihilation into SM particles would also be possible. One of the potential LSP often considered as a plausible WIMP candidate is the neutralino. Neutralinos results from the mixing of the super-partners of the gauge bosons B and W_3 , as well as the two neutral Higgs bosons H_1^0 and H_2^0 , with four mass eigenstates denoted as $\tilde{\chi}_1^0$, $\tilde{\chi}_2^0$, $\tilde{\chi}_3^0$ and $\tilde{\chi}_4^0$. In the following, the lightest neutralino, $\tilde{\chi}_1^0$, is simply referred to as the neutralino, χ . This neutralino can be written as a linear combination of \tilde{B} , \tilde{W}_3 , \tilde{H}_1^0 and \tilde{H}_2^0 , according to:

$$\chi = N_{11}\tilde{B} + N_{12}\tilde{W}_3 + N_{13}\tilde{H}_1^0 + N_{14}\tilde{H}_2^0, \quad (3.12)$$

where N_{11} and N_{12} provide the gaugino fraction $f_G = N_{11}^2 + N_{12}^2$, while the higgsino fraction is given by $f_H = N_{13}^2 + N_{14}^2$. At the present time, neutralinos are predicted to be highly non-relativistic and to self-annihilate into, among other things, fermions and anti-fermions pairs, in particular heavy fermions such as muon and tau leptons, as well as top, bottom and charm quarks. The pair-annihilation of neutralinos could also result into pairs of gauge bosons, i.e. W^+W^- and Z^0Z^0 .

Another extension of the SM arise from the attempt of unifying all fundamental interactions through the postulate of extra-dimension theories. The idea of introducing a fourth spatial dimension to unite gravity and electromagnetism was first suggested by Kaluza in 1921 [84]. These extra-dimensions scenarios also provide a possible cold dark matter candidate under the form of the lightest of the Kaluza-Klein particles (LKP) [85]. The Kaluza-Klein (KK) particles are associated to the first excitation of the SM particles when considering extra-dimensions theories in which the SM particles and fields can propagate through all dimensions of the space-time, known as universal extra-dimensions (UED). In UED theories, LKPs are often affiliated with the first Kaluza-Klein excitation of photons, i.e. the first excitation of the hyper-charge gauge boson, denoted as $B^{(1)}$ or $\gamma^{(1)}$ [86]. KK photons are not the only possible Kaluza-Klein particles to be potential dark matter candidates, also KK neutrinos and KK gravitons are considered as possible LKP. Most of the Kaluza-Klein particles are expected to have masses falling in the GeV range.

WIMPs are expected to have been produced in the early Universe along SM parti-

cles. At this epoch, the creation and annihilation rates of dark matter cancelled out, so that thermodynamic equilibrium was reached. As the Universe started its expansion, the rate of DM annihilation decreased and became smaller than the expansion rate of the Universe, causing DM particles to decouple. The moment from which the thermal equilibrium between DM particles could no longer be preserved is known as the DM freeze-out. The abundance of relic dark matter from the freeze-out epoch can be estimated as the following expression [87]

$$\Omega_{DM} h^2 \sim \frac{3 \times 10^{-27} \text{cm}^3, \text{s}^{-1}}{\langle \sigma_{Av} \rangle} \quad (3.13)$$

which relies on the average of the DM self-annihilation cross-section multiplied by the relative velocity, $\langle \sigma_{Av} \rangle$. When replacing the right term of Equation 3.13 by the DM density given in Equation 3.8 from CMB estimates, one gets a thermally-averaged DM self-annihilation cross-section of the order of $\langle \sigma_{Av} \rangle \simeq 10^{-26} \text{cm}^3 \text{s}^{-1}$, which corresponds to the weak scale also known as the "natural scale". The fact that it is possible to obtain the right DM abundance from a particle on the weak mass scale interacting via the electroweak force and predicted independently by SUSY theories is known in the literature as the "WIMP miracle".

3.2.3 Modified gravity

As mentioned previously, alternative theories were proposed in order to explain the flat behaviour of galaxy rotation curves. Rather than postulating the existence of more matter, these models attempt to solve the apparent discrepancies by modifying the laws of gravity. Among those theories, the Modified Newtonian Dynamic (MOND) suggests modifications of the Newtonian's laws of dynamics in the low acceleration regime [88]. Although the orbital velocity of matter in galaxies is successfully determined by the MOND approach from the baryonic mass distribution, some observations, such as the Bullet Cluster, are more difficult to explain using this theory. Furthermore, the inclusion of general relativity in the MOND theory turned out to be a complicated task. Therefore, the existence of dark matter (preferably cold) is favoured over such modified gravity theories [89].

3.3 Dark matter detection

In order to learn about the nature of dark matter, it is necessary to observe more than just its gravitational effects on visible matter. Assuming that dark matter is weakly coupled to the SM, three main detection principles can be used to search for dark matter particles. In Figure 3.4, these methods are represented with different orientations of the same basic diagram describing the interaction of two dark matter particles with two SM particles. Looking at the diagram from right to left shows how particle accelerators attempt to find evidences of dark matter via the production of dark matter particles during the collision of SM particles. When read from top to bottom, the diagram represents how to directly search for dark matter. Direct detection experiments look for the scattering of dark matter particles on SM particles. Lastly,

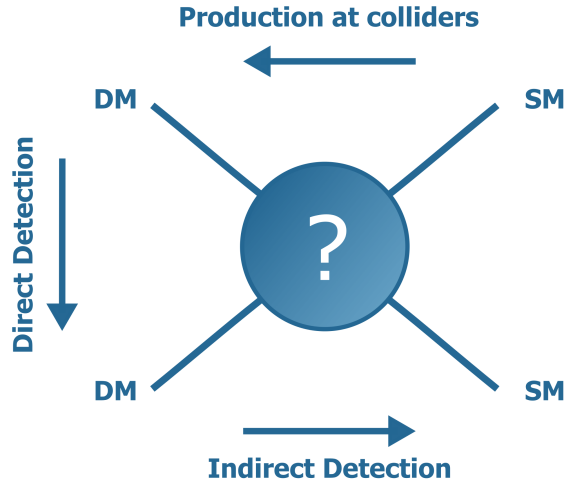


Figure 3.4—Diagram of the possible interaction between SM and DM particles, where the three methods used to search for DM particles are represented.

going through the diagram from left to right represents the indirect search for dark matter. Indirect detection experiments try to detect the final state particles created by the pair-annihilation of dark matter particles, e.g. neutrinos, photons. In this section, the aforementioned detection methods are described in more detail, with an emphasis on indirect detection since it is the method of interest in this thesis.

3.3.1 Direct dark matter searches

During its movement around the Sun and the Milky Way, the Earth crosses the dark matter halo that surrounds our galaxy, making it possible for dark matter particles to collide with ordinary matter. The goal of direct detection experiments is to measure the recoils caused by the scattering of dark matter particles with nuclei of the detector target material. As the rate of dark matter collisions with ordinary matter is expected to be well below the cosmic ray rate, direct search experiments are typically located in deep underground facilities in order to be shielded from atmospheric background. To observe the dark matter scattering, the recoil energy is measured either via its heat deposition in the medium (using phonons), the ionisation of the medium (using electrons), or the production of scintillation radiation from excited target atoms (using photons). In order to discriminate between nucleus recoil originating from dark matter scattering and background events, most indirect search experiments aim at detecting two of these signal signatures. Based on the chosen recoil signature(s), different materials are used as target. While liquid noble gas is often used to measure scintillation light, germanium is preferred for ionisation, and super-cooled crystals are commonly employed to estimate the heat deposition. In addition to its dependence on the detector response, the expected DM-SM collision rate is influenced by the DM-nucleon scattering cross-section and the mass of the dark matter particles, together with astrophysical parameters such as the local dark matter density and the local dark matter

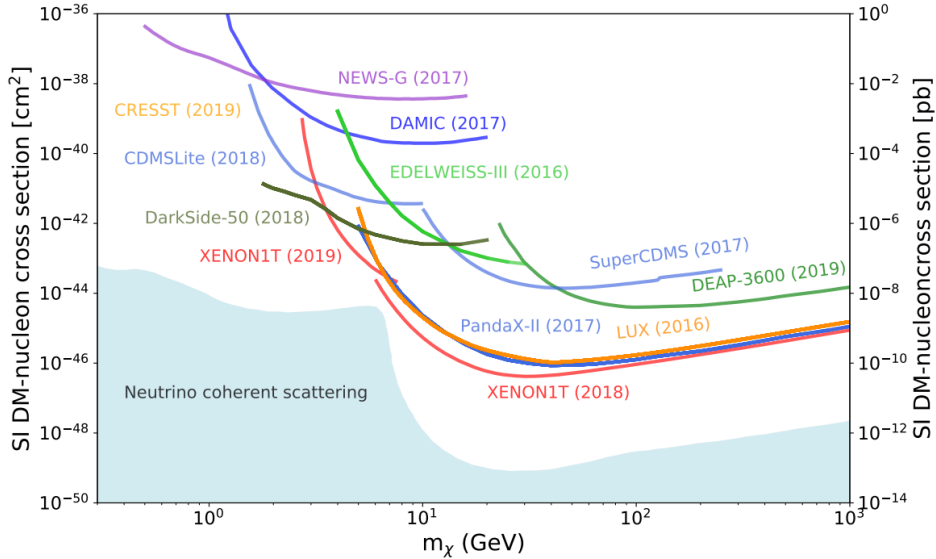


Figure 3.5—90% C.L. upper limits on the spin-independent DM-nucleon scattering cross-section with respect to the mass of DM particle taken from [10].

velocity distribution. Under the assumption that the dark matter particles have a spin, the DM-nucleon scattering cross-section can be separated into a spin-dependent (SD), σ_{SD} , and a spin-independent (SI), σ_{SI} , contribution. As the SI cross-section is proportional to the square of the atomic number, A_N^2 , direct search experiments often consider target materials with a high atomic number. On the other hand, the SD cross-section is constant with increasing atomic number and is thus expected to scale as $\sigma_{SI} \propto A_N^2 \sigma_{SD}$. As a result, stronger limits are set on the SI cross-section.

To date, the strongest constraints on the SI DM-nucleon interaction cross-section are set by liquid noble gas detectors, as visible in Figure 3.5. Liquid xenon experiments looking for both scintillation and ionisation signals, such as XENON1T [90], PandaX-II [91], LUX [92], probe DM masses down to 6 GeV and can constrain the SI DM-nucleon cross-section down to $4.1 \times 10^{-47} \text{ cm}^2$ for dark matter particles with a mass of 30 GeV. In liquid argon experiments, e.g. DEAP-3600 [93], DarkSide-50 [94], pulse shape discrimination is used to distinguish nuclear recoils from electronic recoils. As the expected DM signal takes the form of nuclear recoil, it can thus be separated from the electromagnetic background. Concurrently, solid state cryogenic detectors, like SuperCDMS [95], EDELWEISS [96] and CRESST [97], are using semiconducting or scintillating crystals to measure phonons from the heat deposition, along with either ionisation or scintillation readouts.

The most stringent limits on the SD DM-nucleon cross-section are currently set by a joint effort of the IceCube neutrino experiment and the PICO-60 C3F8 dark matter detector [98]. The PICO experiment operates with a bubble chamber filled with superheated C_3F_8 . The technique used by this detector consists of measuring nuclear recoil by observing the bubble formation caused by the energy deposition from DM scattering in the chamber [99]. For this, a set of high-resolution cameras are used along acoustic transducers.

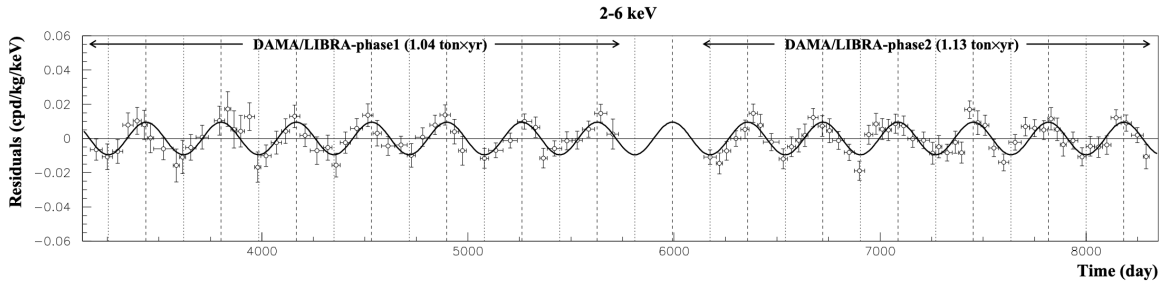


Figure 3.6—Single-hit oscillation residual rate measured by phase 1 and phase 2 of the DAMA/LIBRA experiment in the energy range from 2 to 6 keV as a function of time taken from [101]. The solid line shows the function fitted to data in order to obtain the best estimate of the amplitude, A , which is defined as $A \cos(\omega(t - t_0))$. The phase t_0 is set to the fixed value of 152.5 days (June, 2nd), while the considered period $T = 2\pi/\omega$ is of 1 year.

Annual modulations

Another approach used in direct detection experiments consists of looking for annual modulations of the DM-nucleon recoil rate in a crystal. Such variations could arise from the rotation of the Earth around the Sun, causing variations of the relative velocity between the dark matter halo around the Milky Way and the Earth. The maximum event rate of corresponding to this annual modulation is expected to occur on the June 2nd of each year. The DAMA/LIBRA experiments uses high purity NaI(Tl) scintillators to measure this annual modulation [100]. The DAMA/LIBRA detector and its predecessor, DAMA/NaI, observed an annual modulation of their event rate in concordance with the predicted date with a 12.9σ significance over 20 annual cycles [101]. The amplitude of the observed modulation is of (0.0103 ± 0.0008) events/(kg day keV) for energies ranging from 2 to 6 keV. This residual rate is visible in Figure 3.6 for measurements taken by both DAMA/NAI and DAMA/LIBRA.

The results from the DAMA collaboration remain highly controversial as other experiments like Xenon1T, PandaX or LUX have explored the same parameter space without being able to confirm this claim. In order to be able to confirm or rule out those results, it is necessary to conduct measurements with similar NaI targets. Several projects are part of this investigation effort, among them the COSINE-100 [102] and the ANAIS-112 [103] detectors. The COSINE-100 experiment consists of a collaborative effort of the DM-Ice experiment [104] and the KIMS collaboration [105]. The first results from COSINE-100 gave the best fit modulation amplitude of (0.0083 ± 0.0068) events/(kg day keV) with 1.7 years of data and for energies ranging from 2 to 6 keV. COSINE-100 is expecting to achieve a 3σ coverage of the parameter space probed by DAMA after collecting five years of data. The annual modulation with NaI scintillators (ANAIS) is operating since 2017 in an underground laboratory in Spain. The best fit modulation amplitude obtained for the energy range between 2 and 6 keV with 3 years of ANAIS data is (0.0003 ± 0.0037) events/(kg day keV). This value is incompatible with DAMA/LIBRA measurements at 3.3σ .

3.3.2 Indirect dark matter searches

Indirect search experiments look for an excess in the flux of SM particles from massive astrophysical objects in which a large concentration of dark matter is expected. The expected rate of SM particles from dark matter decay or pair-annihilation is proportional to the DM density in the case of the former and to the squared DM density for the latter. Therefore, regions with a high DM concentration constitute promising targets. As galaxies are assumed to be embedded in dark matter halos with an increased density towards the centre, galaxy clusters and the centre of the Milky Way are typical regions of interest. Additionally, dark matter particles can accumulate gravitationally at the centre of massive objects after losing energy via scattering. For this reason, indirect search experiments are also looking for dark matter signal from local sources, such as the Sun or the Earth. Rather than observing dark matter itself, indirect search experiments aim to detect the stable particles directly produced by the annihilation or decay of dark matter particles, or resulting from the subsequent decay of these secondary particles. Numerous type of experiments search for indirect indications of the presence of dark matter through messengers such as the stable charged particles found in cosmic radiations, as well as photons and neutrinos. Similarly to direct detection, indirect search experiments are subject to large systematic uncertainties arising from the astrophysical assumptions made for the dark matter search. In particular, they strongly rely on the choice of the dark matter halo model, as well as on other parameters such as the local dark matter density (see the discussion in Section 3.4).

γ -ray experiments

Astroparticle experiments, such as H.E.S.S. [106], VERITAS [107], MAGIC [108], and the Fermi Large Area Telescope (Fermi-LAT) [109] can search for high energy γ -rays resulting from dark matter annihilation or decay [110–112]. These γ -ray telescopes have the leading limits on the thermally-averaged self-annihilation cross-section, $\langle\sigma_{A\nu}\rangle$, as can be seen in Figure 3.7. In addition to being easy to detect, the strength of photons as messengers is that they travel through space without being affected by magnetic fields, allowing us to point straight back at their origin. However, photons can be absorbed or deflected by gas or dust in their path to Earth, making dense regions opaque to γ -ray telescopes. In addition, the foreground of light emission, as well as its background, are difficult to model and are subject to large sources of uncertainty. This is especially true when looking at the Galactic Centre or the Galactic plane, as these regions are densely populated by numerous luminous objects, some of which are below the point source sensitivity level of current instruments. Taking these elements into consideration, dwarf spheroidal galaxies (dSphs) are well-designated targets for dark matter searches with γ -ray telescopes as they exhibit a high mass-to-light ratio, while having a lower foreground photon emission than the Galactic Centre.

Cosmic ray experiments

While charged particles cannot be used to point back to their source, cosmic ray experiments can nevertheless look for an excess of anti-matter particles in the cosmic

ray spectrum as an indication of the presence of dark matter since there are few astrophysical sources of anti-matter. Such analyses were performed by PAMELA [113], Fermi-LAT and AMS-2 [114]. Interestingly, an increased positron flux at high energies was observed by all three experiments [115–117], whilst the contribution from positron is expected to decrease at these energies according to standard models of cosmic ray propagation. While this excess could be explained as a signal from dark matter decay or annihilation, this observation is also consistent with standard astrophysical phenomenon, such as a contribution from supernovae remnants or pulsars.

Neutrino experiments

Neutrinos can also be used in indirect dark matter searches since they could be created as primary or secondary produced in the annihilation or decay of DM particles. In addition to being electrically neutrals and thus travelling through space affected only by gravitational fields, the low interaction cross-section of neutrinos allow them to escape dense regions that cannot be probed with photons.

As a result, neutrino telescopes can study targets, like the Galactic Centre, by looking for an excess of high-energy neutrinos coming from this direction. Such indirect dark matter search were performed by the ANTARES and the IceCube detectors for the centre of the Milky Way [118, 119]. Local targets, such as the Earth [120, 121] or the Sun [122, 123], are also considered for dark matter searches with neutrinos.

Looking at Figure 3.7, one might however wonder what could be gained by searching for dark matter with neutrino telescopes. This figure shows the limits set by ANTARES and IceCube for dark matter annihilation into the $\tau^+\tau^-$ when looking at the Galactic Centre, compared to the limits obtained by various γ -ray experiments from dwarf spheroidal galaxies. For this particular channel, neutrino experiments are only competitive for energies above 10 TeV, with limits from γ -ray experiments being several orders of magnitude better at the lowest energies. This is however not true for all possible dark matter annihilation channels. For instance, dark matter could annihilate directly into one of the three neutrino flavours, which would result in an expected neutrino signal consisting of monochromatic lines, more distinguishable against background. Thanks to these sharp spectral features, neutrino telescopes are able to set the strongest constraint when considering dark matter annihilation through into $\nu_e\bar{\nu}_e$, $\nu_\mu\bar{\nu}_\mu$ and $\nu_\tau\bar{\nu}_\tau$.

As a result, theoretical models allowing dark matter annihilation into the neutrino channels have attracted interest. A list of the models which could lead to an observable monochromatic neutrino flux is provided in [124]. These models take into account various constraints such as the neutrino mass or the limits set by direct detection experiments. As the neutrino flux predicted by these investigated models would not be observable by current neutrino experiments as it is, processes which could boost the annihilation cross-section into neutrinos are also studied. A possible enhancement of this cross-section could arise from the Sommerfeld effect. For Sommerfeld enhancement to occur, dark matter must couple to a lighter mediator, which can be transferred between the dark matter particles before their annihilation. The impact of this enhancement depends on the mass and the velocity of the considered dark matter particles. Therefore, peaks can be seen in the expected annihilation cross-section for certain dark matter

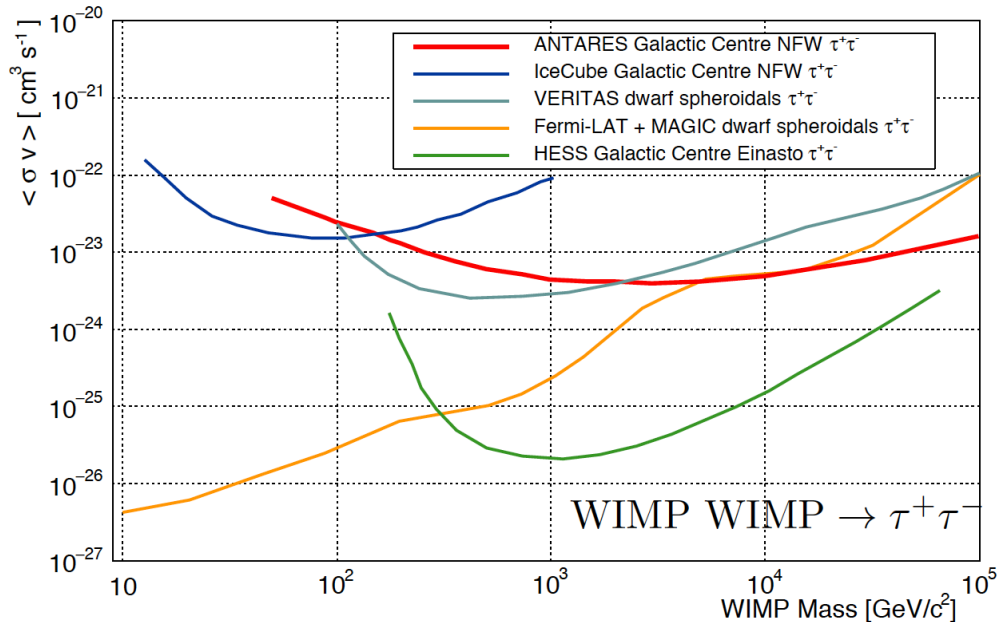


Figure 3.7—Comparison of the 90% C.L. limits set by neutrino and γ -ray experiments on the thermally-averaged self-annihilation cross-section $\langle \sigma v \rangle$ as a function of the dark matter mass taken from [125] for dark matter annihilation into the $\tau^+\tau^-$ channel and the NFW halo profile.

masses. Depending on the models, the Sommerfeld peaks could bring the expected neutrino flux from dark matter annihilation into the neutrino channels to a level detectable by the ANTARES and the IceCube detectors.

The two analyses conducted during the course of this thesis consist of indirect dark matter searches with neutrino telescopes and will be discussed in more details in the following two chapters. In particular, these searches are looking for neutrinos from dark matter self-annihilation in the Galactic Centre. For the second analysis presented in this dissertation, dark matter annihilation into the "golden" neutrino channels is evaluated.

3.3.3 Dark matter production at colliders

As mentioned previously, dark matter could be weakly coupled to the SM or could interact with SM particles via beyond Standard Model (BSM) interactions. Such coupling to the SM would make it possible to create dark matter particles in pair-collisions of SM particles happening at particle accelerators, like the Large Hadron Collider (LHC) [126]. Such searches typically assume that dark matter escapes the detector without interacting, which implies that the signal signature corresponds to missing momentum and energy observed in the detector. Unlike direct and indirect dark matter experiments, DM searches at colliders have the advantage of not relying on astrophysical parameters subject to large source of uncertainties. These searches are however not entirely model independent as they still rely on assumption on the interaction channel. Different strategies can then be adopted to look for DM signal. The first approach consists of looking for events with missing transverse energy \cancel{E}_T .

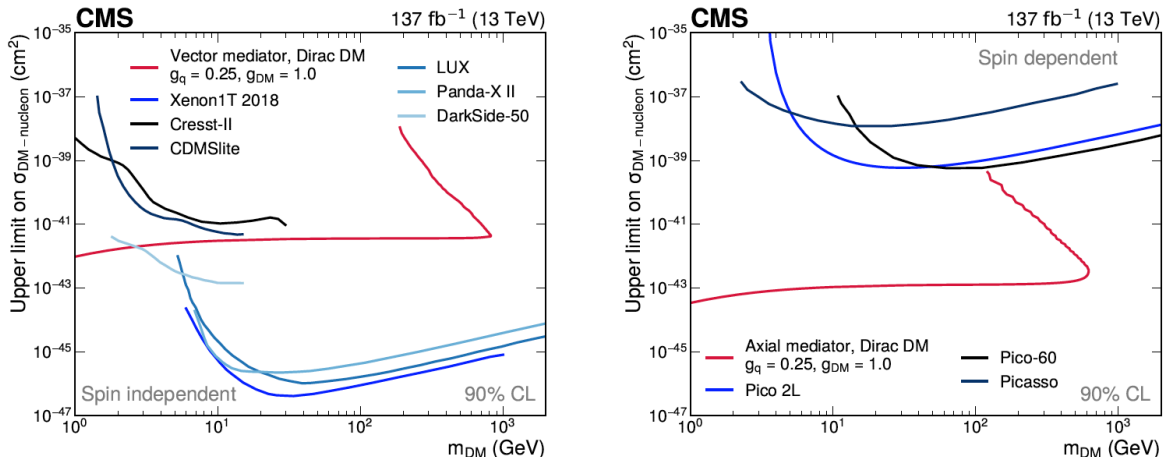


Figure 3.8—Comparison of the 90% C.L. upper limits on the spin-independent (left) and spin-dependent (right) DM-nucleon cross-sections set by CMS (red lines) and direct detection experiments (blue lines) shown as a function of the DM mass, as taken from [127]. The CMS upper limits are obtained with the choice of the mediator couplings $g_q = 0.25$ and $g_{DM} = 1.0$.

Another method is to search for an excess or deficit in the observed distributions of certain variables when compared to the theoretical predictions. Such deviation in the distribution would indicate the existence of new physical processes, with a possible link to DM. So far, no DM signal was observed by particle colliders, rather limits on the DM mass, interaction cross-sections and coupling to SM were set. Figure 3.8 shows limits on the spin-independent (left) and spin-dependent (right) DM-nucleon interaction cross-sections set by CMS [127], compared to constraints established by various direct detection experiments. The model used to set the CMS constraints assumes dark matter particles to be Dirac fermions, with a mediator coupling to quark of $g_q = 0.25$ and a mediator coupling to dark matter of $g_{DM} = 1.0$.

3.4 Expected neutrino signal from dark matter annihilation in the Galactic Centre

Our work focuses on the search for neutrinos from dark matter annihilation in the Galactic Centre. Such indirect dark matter search strongly relies on the assumptions made about the distribution of dark matter in the galaxy. Various dark matter halo profiles can be used in order to model the dark matter halos surrounding galaxies and galaxy clusters. For a large portion of these profiles, the dark matter density distribution can be expressed as a function of the distance to the centre of the galaxy, r , by a generalisation of the Zhao profile [128]:

$$\rho_{DM}(r) = \frac{\rho_0}{\left(\delta + \frac{r}{r_s}\right)^\gamma \cdot \left[1 + \left(\frac{r}{r_s}\right)^\alpha\right]^{(\beta-\gamma)/\alpha}}, \quad (3.14)$$

where ρ_0 is the normalisation density and r_s is the scale radius. Both of these free pa-

Parameters	Units	NFW	Burkert
$(\alpha, \beta, \gamma, \delta)$	–	(1,3,1,0)	(2,3,1,1)
r_s	kpc	$16.1^{+17}_{-7.8}$	$9.3^{+5.6}_{-4.2}$
ρ_0	$10^7 M_\odot/\text{kpc}^3$	$1.4^{+2.9}_{-0.93}$	$4.1^{+6.2}_{-1.6}$
ρ_\odot	GeV/cm^3	$0.471^{+0.048}_{-0.061}$	$0.487^{+0.075}_{-0.088}$

Table 3.1: Dark matter halo parameters of the NFW and the Burkert profiles taken from [129], where r_s is the scale radius, ρ_0 is the normalisation density and ρ_\odot is the local DM density observed at the location of the Sun, r_\odot .

Parameters have to be estimated for each galaxy. For the two analyses presented in this thesis, the values of these parameters are taken from [129], in which these parameters are fitted in order to best represent the DM distribution of our galaxy based on various observations. In order to recover the local DM density, ρ_\odot , observed at the location of the Sun, r_\odot , the profile distributions are normalised. The dimensionless parameters $(\alpha, \beta, \gamma, \delta)$ are used to characterise the shape of the profile. In this thesis, two benchmark halo profiles are used: the Navarro-Frenk-White (NFW) [130] and Burkert [131] profiles. The free parameters $(\alpha, \beta, \gamma, \delta)$ depend on the halo model considered, taking the values (1,3,1,0) for the NFW profile and (2,3,1,1) for the Burkert profiles.

For the NFW profile, the DM distribution diverges as r tends to zero. Such halo profile is referred to as a "cusped" profile and results in a highly concentrated signal towards the central region. The Burkert profile, on the other hand, displays a more constant behaviour of the DM density distribution close to the core. Profiles with similar behaviour are known as "cored" profiles. The resulting signal appears more spread out, making it more difficult to detect. These two profiles are considered in order to account for uncertainties on the DM distribution in galaxies. While observations of the star kinematics in dwarf and gas-rich galaxies favour a DM distribution according to cored density profiles, N-body simulations prefer cuspy profiles. This inconsistency is known as the core-cusp problem [132].

The dark matter density for both halo models is computed using the CLUMPY package [133]. The free parameters used as inputs in the software are presented in Table 3.1. Spherical symmetry is assumed for both halo profiles and eventual deviations from this particular assumption, such as elliptically shaped halos, are not taken into consideration. The resulting dark matter densities are shown in Figure 3.9 for both the NFW and Burkert halo profiles. Whereas these two halo profiles diverge by orders of magnitude towards the central region, they are in rather good agreement for radial distances outside the solar circle ($R_\odot = 8.5 \text{ kpc}$). Since astrophysical observations do not allow to set strong constraints on the local dark matter density, this quantity is subject to considerable uncertainties, as visible in Table 3.1. For the parameters considered in this analysis, this uncertainty can be larger than a factor 2.

As the dark matter particles present in the halo could annihilate, a quantity called the J-factor, which encloses information about the intensity of this process, is defined. The J-factor is expressed as the integral over the solid angle, $\Delta\Omega$, of the squared dark

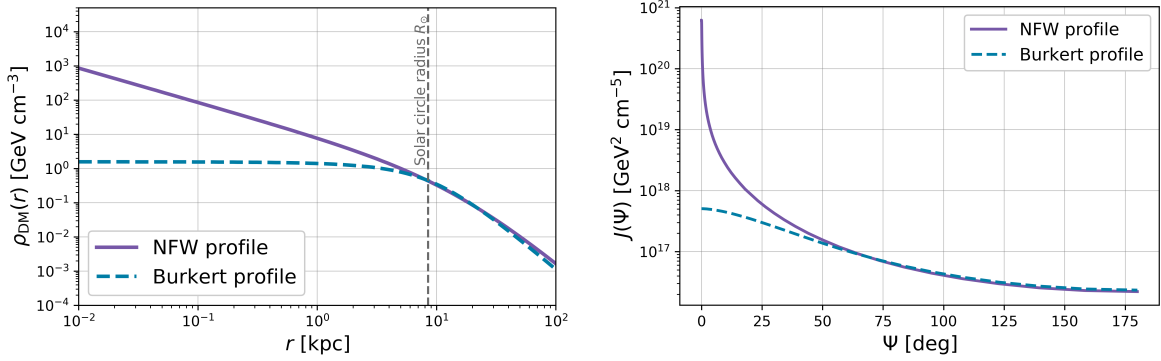


Figure 3.9—Left: Dark matter density, $\rho_{\text{DM}}(r)$, as a function of the radial distance to the Galactic Centre, r , for the NFW and Burkert profiles. Right: J-factor, $J(\Psi)$, as a function of the angular distance to the Galactic Centre, Ψ , for the NFW and Burkert profiles. Both the dark matter densities and J-factors are computed with halo parameters values taken from [3.1](#).

matter density, the whole estimated along the line of sight (l.o.s):

$$J = \int_{\Delta\Omega} d\Omega(\Psi) \int_{\text{l.o.s}} \rho_{\text{DM}}^2(r(l, \Psi)) dl. \quad (3.15)$$

Similarly to what is done for the dark matter density, CLUMPY is used to compute the J-Factors for both the NFW and Burkert profiles. The resulting J-factors are shown as a function of the opening angle with respect to the Galactic Centre, Ψ , in [Figure 3.9](#).

Along with information about the source morphology, provided by the J-factor, another important theoretical input is the spectra of secondary particles produced by the annihilation of dark matter particles. In our work, this information is expressed under the form of the differential number of neutrino per dark matter annihilation, dN_ν/dE_ν . The energy distribution of neutrinos depends on the mass of the dark matter, m_{DM} , as well as on the dark matter annihilation channel. For a given dark matter model, dN_ν/dE_ν is defined as the sum over all possible annihilation channels, scaled by the associated branching ratios. As this work is not focusing on a particular dark matter candidate, a 100% B.R. into one of the considered annihilation channels is considered. The neutrino spectra considered for the two analyses are detailed in the respective dedicated chapters (see [Sections 4.4](#) and [5.4](#)).

From these ingredients, the expected differential flux of neutrino from dark matter self-annihilation can be expressed as follows:

$$\frac{d\phi_\nu}{dE_\nu} = \frac{1}{4\pi} \frac{\langle\sigma_A v\rangle}{2m_{\text{DM}}^2} \frac{dN_\nu}{dE_\nu} J, \quad (3.16)$$

where $\langle\sigma_A v\rangle$ is the thermally-averaged self-annihilation cross-section. The factor 4π results from the spherical uniformity assumed for the dark matter annihilation, while the factor $1/2$ and the squared mass account for the fact that two dark matter particles are needed per annihilation, as well as the squared dark matter density present in the J-factor as seen in [Equation 3.15](#).

Chapter 4

Combined dark matter search with ANTARES and IceCube

This chapter describes the first search for neutrinos from dark matter self-annihilation in the Galactic Centre performed with both the ANTARES and the IceCube neutrino telescopes. Since this search uses data from two detectors, a Memorandum of Understanding (MoU) was required between the two collaborations. After discussions, it was decided to share data samples from already published dark matter searches. As a result, the data set developed to search for dark matter in the centre of the Milky Way with 9 years of ANTARES data [118] is considered along the data sample from the 3 years search for dark matter in the centre of our galaxy with IceCube [119]. Rather than providing the raw event information, the two collaborations agreed to exchange the already weighted angular distributions of the events. As the lead analyst of this joint analysis, I was also the primary IceCube liaison, communicating predominantly with Sara Rebecca Gozzini, who took the role of contact person for ANTARES.

The Monte Carlo (MC) events used for the combined dark matter search, which were simulated for the separate ANTARES and IceCube analyses discussed above, are presented in Section 4.1. In addition to being used in order to verify the assumptions made about the detectors during the event selection process performed independently for the two previous ANTARES and IceCube dark matter searches, these simulation sets are also required to mimic the signal expectation of our analysis. As the two telescopes are located in different hemispheres, they will have a dissimilar view of the Galactic Centre, as seen in Section 4.2. While ANTARES has a privileged view of the centre of our galaxy, a veto region needs to be considered for IceCube. The respective event selections used for the two telescopes are described in Section 4.3. The selection steps outlined in that section are not specific to this combined analysis as both event selections are used in the exact state they were created for the respective ANTARES and IceCube searches. In Section 4.4, the signal expectations from dark matter annihilation in the Galactic Centre are exposed. The first step of this joint analysis consists of unifying the various ingredients going into the computation of the signal expectations. Section 4.5 shows comparisons of the effective area and acceptance of both detectors. The analysis method considered for this search is presented in Section 4.6, while the treatment of systematic uncertainties is overviewed in Section 4.7. Finally, the results are shown and discussed in Section 4.8.

4.1 Monte Carlo simulation

The various steps applied to simulate the Monte Carlo simulations used for this analysis are described in this section. These simulation samples are taken respectively from [118] for ANTARES and from [119] for IceCube. In addition to being used to get a better understanding of the detector properties during the event selection process performed separately for the two analyses cited earlier, these simulation samples are also needed to estimate the neutrino signal from dark matter annihilation in the Galactic Centre (see Section 4.6.1). Even though the tools used to generate the MC simulations are different for ANTARES and IceCube, the main steps of the simulation chain can be summarised similarly. First, the primary particles are simulated following a particular distribution. Since only muons and neutrinos are able to reach the two telescopes considered, only those particles are taken into consideration. Following the interaction of these muons or neutrinos, secondary particles are generated and propagated through the detector medium. The light generated by these secondary particles is in turn simulated along the propagation of these photons through water or ice. The noise from ambient light is also mimicked with MC simulations. Finally, the detector response is simulated.

4.1.1 ANTARES

For ANTARES, the production of atmospheric muons and their propagation to the surface is handled using a combination of MUPAGE [134, 135] and CORSIKA. The simulated neutrinos, on the other hand, are generated and propagated with the GENHEN package [136]. As background estimation will be built from the data distribution, the sole purpose of the atmospheric muon simulations is to be compared with the data in order to cross-check the event selection and validate the simulation. For each data run, atmospheric muons and neutrinos simulation runs are produced.

Atmospheric muons

First, the MUPAGE (MUon GEnerator from PArametric formulas) MC generator is used to simulate atmospheric muon bundles. In order to spare computational time, MUPAGE uses parametric formulas to estimate the atmospheric muon flux and the angular distribution of the muon bundle [137]. These parametric expressions are valid when considering depths between 1.5 and 5 km and zenith angles ranging from 0° to 85° . The parameterisation used to generate the muon bundles is computed beforehand using the COsmic Ray SIMulations for KASCADE (CORSIKA) [138]. The muon tracks are generated starting on the surface of an imaginary cylindrical volume surrounding the instrumented detector [139], as illustrated in Figure 4.1. This volume, called the can, has for purpose to optimise the computation time required for simulation while making sure all relevant events are kept. This is done by defining the can in such a way that muon tracks not crossing this cylinder will also be unlikely to deposit Cherenkov light in the instrumented detector volume.

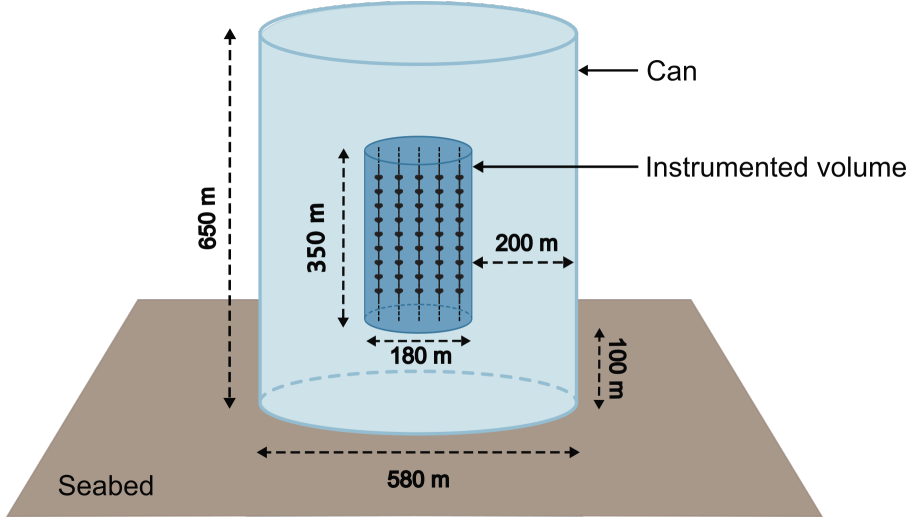


Figure 4.1—Schematic view of the cylindrical volume used for muon track generation in MUPAGE, referred to as the can.

Neutrinos

The GENHEN framework is used in order to simulate neutrinos. The package also generates the secondary particles produced by the interaction of these neutrinos with nuclei in the detector or its surroundings. All neutrino flavours are considered in the GENHEN package, with interaction through either the neutral or charged current. The spectrum used to generate the neutrino simulations is a power-law $E^{-\gamma}$, with a spectra index γ chosen to equal 1.7. These GENHEN sets are later re-weighted to compute the expected signal from dark matter self-annihilation in the Galactic Centre. The generation volume considered for GENHEN cannot be restricted to the can, as it is the case for CORSIKA. For high energy neutrinos, the muons produced in the interaction of muon neutrinos can reach several hundreds of metres. Therefore, a cylinder with a volume considerably larger than the can has to be used, with a radius of 25 km and a 25 km height. Each simulated event is allocated a statistical weight, w_2 , which is proportional to the probability of the neutrino to be detected after its interaction within the ANTARES detector volume or its surroundings. This weight can be expressed as:

$$w_2 = I \cdot I_{\text{Energy}} (1 - P_{\text{Earth}}) \sigma_{\text{CC}} V_{\text{sens}} \rho_{\text{N}} E^{\gamma} T, \quad (4.1)$$

where the factors I and I_{Energy} respectively compensate for the usage of only part of the sky and the limited energy range used for the simulations. The probability of the neutrino to be absorbed by the Earth is represented by P_{Earth} , while σ_{CC} is the charged-current interaction cross-section for neutrino-nucleon leading to the production of muons. The sensitive volume, V_{sens} , the nucleon density of water, ρ_{N} , and the livetime, T , are also considered in the computation of w_2 . Lastly, E^{γ} corrects for the energy spectrum used during the production of the simulation samples. This weight can be used in order to re-weight the simulation sets to match any flux assumption,

using the following expression:

$$w_3 = \phi_{\nu+\bar{\nu}} w_2, \quad (4.2)$$

with $\phi_{\nu+\bar{\nu}}$ being the corresponding neutrino flux at the detector.

Particle propagation and light production

The propagation of muons is handled using the MUon SIMulation Code (MUSIC) [140] for both the CORSIKA and the GENHEN samples. The Cherenkov light produced by the passage of these muons is then simulated using KM3 [141], which is based on the GEANT4 toolkit [142]. This code also contains a modified version of MUSIC which, in addition to propagating muons, estimates the point from which the Cherenkov photons are emitted. With this, the photons are produced individually from metre-long muon track parts. The Cherenkov photons thus created are in turn propagated from the track to the optical modules, taking into account absorption and scattering in the seawater. KM3 works with tables containing the distributions of all OM hits, as well as the arrival times of muons with various arrival directions and energies.

Noise emulation and detector response

Once the Cherenkov photons are produced and propagated to the OMs, the noise level needs to be estimated. This evaluation of the optical background is done with the SeaTray package [143]. The decay of ^{40}K is taken into account under the form of 60 kHz PMT hits. The noise from bio-luminescence, on the other hand, is estimated from actual data due to its increased modelling complexity. This is possible thanks to the Run-by-Run simulation procedure implemented in ANTARES [144]. This simulation method account for the variations of the data acquisition conditions in the unstable environment of the Mediterranean Sea based on variables extracted directly from the corresponding recorded runs. Finally, the detector response is computed with a software specific to the ANTARES collaboration, called TriggerEfficiency [144].

4.1.2 IceCube

Two different sets of simulation tools are used for this analysis, depending on the particle type. For muons, CORSIKA is used, while neutrinos are simulated with the GENIE neutrino MC generator [145]. Similarly to what is done in ANTARES, the background will be taken from scrambled data. Therefore, CORSIKA simulations are only used to ensure the quality of the event selection.

Atmospheric muons

Simulations of the atmospheric muon background are obtained using CORSIKA. This software is used to generate extensive air showers assuming various primary particles, e.g. protons and iron nuclei. After the first interaction, an extensive air shower is initiated and secondary particles are tracked including their interaction with the atmosphere and decay until they reached the ground or the shower stops. For the

simulations used in our analysis, the hadronic interactions at high energies are modelled with SIBYLL [146]. The SIBYLL event generator, which is based on the mini-jet model [147, 148], includes hadron-hadron interactions as well as hadron-nucleus interactions. The choice of cosmic rays considered is narrowed to H, He, N, Al and Fe, with an energy distribution based on the GaisserH3a model [149]. The propagation of the simulated neutrinos is not done with CORSIKA itself but rather using the GENIE data sets described in the next subsection. Since all other particles, except muons, are absorbed by the ice before being able to reach the instrumented IceCube volume, only air shower muons are propagated to the detector. However, the complete CORSIKA simulation is applied up to that point to get the proper energy distribution of the simulated muons.

Neutrinos

The neutrinos and the secondary particles produced as a result of their interaction with the detector medium are modelled using GENIE. For this analysis, neutrinos with energies ranging from 1 GeV to 1 TeV are simulated. Since these simulation sets were produced to study atmospheric neutrino oscillation, the spectrum assumed for their production is similar to what is expected for atmospheric neutrinos. Nonetheless, the simulation samples can be re-weight in order to match any assumption on the neutrino flux. This is possible thanks to a quantity estimated for each simulated event, called OneWeight (OW). This weight also corrects the fact that all simulated neutrinos are forced to interact within the detector in order to save computation time. Besides including the shape of the energy spectrum used to generate the events, OneWeight contains the interaction probability of each event, as well as information on the generation volume and solid angle. This quantity is expressed in units [GeV sr cm²] and is used as follows in order to obtain the number of neutrino events, $N_{\nu+\bar{\nu}}$:

$$N_{\nu+\bar{\nu}} = \frac{\phi_{\nu+\bar{\nu}} \cdot OW}{N_{\text{Events}} \cdot c_{\text{type}}}, \quad (4.3)$$

where $\phi_{\nu+\bar{\nu}}$ is the neutrino flux assumed for the analysis, N_{Events} is the number of generated events in the sample considered. Since neutrinos and anti-neutrinos are generated unevenly in GENIE simulations, a correction factor, c_{type} , is also evaluated, which equals 0.7 for neutrinos and 0.3 for anti-neutrinos. GENIE includes the treatment of the main scattering mechanisms discussed in Section 1.1, namely deep-inelastic scattering, elastic and quasi-elastic scattering, as well as resonant interactions. Quasi-elastic scattering processes are computed with the Llewellyn-Smith model [150], while elastic scattering is simulated according to the model suggested by Ahrens et al. in [151]. The resonance production is included through the Rein-Sehgal model [152] and deep inelastic scattering is included following the model introduced by Bodek and Yang [153].

Particle propagation and light production

PROPOSAL is used for propagation of particles produced with CORSIKA [154]. This complete tool includes the propagation of any secondary leptons that could be produced by the muon and simulates the Cherenkov photon emitted as the particles go

through the ice. When propagating the particles, energy losses due to ionisation of the detector medium are considered along stochastic losses. Meanwhile, the propagation of electrons and photons with energies below 100 MeV, as well as tau leptons, is handled with GEANT4. The same goes for hadrons with energies below 30 GeV and the muons produced from hadron decays. For hadrons exceeding this energy, the production of Cherenkov photons is estimated from a parametrisation of the hadronic cascade rather than from the individual propagation of particles in the cascade. The photons produced are then propagated with the CLsim project if their energy exceeds 100 MeV. The CLsim project is specific to IceCube and relies on the IceTray framework based on GEANT4. This software propagates the photons individually, taking into consideration both the absorption and scattering in the ice. If reaching a PMT, a probability of detection is assigned to the photon depending on the arrival direction and wavelength. Since the ice in the borehole has different properties than the bulk ice, further computation of the photon probability to reach the DOM is computed with respect to the incident angle of the photon. Moreover, only a restricted wavelength range can be detected by the DOMs, making it necessary to determine a probability linked to the acceptance to the wavelength of each photon. Lastly, the quantum efficiency of the DOM is considered through an additional probability weight associated to the arriving photon.

Noise emulation and detector response

The detector noise is simulated using the Vuvuzela project [155]. Using this software, thermal electronic noise is considered, along non-thermal noise. Thermal noise arise from the emission of electrons from the photocathode in the absence of an incident photon, while non-thermal noise results from the radioactive decay of the ^{40}K contained in the glass of the DOMs. This is taken into account by adding extra photo-electrons within a $10 \mu\text{s}$ time window around the photo-electrons created by the previously simulated Cherenkov photons. The uncorrelated noise hits originating from the thermal electronic noise are simulated following a Poisson distribution with a rate of $\sim 20 \text{ Hz}$ and a uniform time distribution. The radioactive decay give rise to correlated noise hits, of which the initial hits are also sampled from a Poisson distribution, but this time with a rate of 200 Hz , assuming uniform time distribution. The correlated hits are then drawn from a Poisson distribution for which the mean is set to 8 hits. The relative time difference between these additional events and the correlated initial hit are set following a log-normal distribution. The DOM response is then computed using the PMTResponseSimulator software [156]. The first step is to simulate the behaviour of the photo-multiplier tubes, for which the amplified charge at the anode is computed from a charge distribution based on measurements made with PMTs deployed in IceCube. Even if these distributions can vary from one PMT to the other, the same charge distribution is assumed for all DOMs when simulating the detector response. The contributions from pre-pulses and late pulses are taken into account with a respective occurrence probability of 0.7% and 3.5% . When simulating the photo-electrons, a 5.9% probability of producing an after-pulse is also assumed. Due to some non-uniformities in the PMTs, a random contribution in the time distribution is also included. Finally, the PMT saturation is accounted for by lowering the amplitude

of the produced pulses. With the PMT outputs now simulated, the DOMLauncher software can be used to generate the response of the electronics, following the same digitisation process as the actual IceCube modules.

4.2 Visibility of the Galactic Centre

Given the geographic location and size difference of the two telescopes, distinct techniques were used to reduce the atmospheric background. Since the ANTARES and IceCube detectors are located in two different hemispheres, they will have dissimilar views of the same object. In our case, the source considered is the Galactic Centre, which is located in the Southern Hemisphere at declination $\delta_{GC} \sim -29.01^\circ$. As previously mentioned, atmospheric muons and neutrinos created by the interaction of cosmic rays in the upper atmosphere represent the main background of neutrino detectors, with a dominant contribution from atmospheric muons. Nevertheless, for up-going directions, the contribution from atmospheric muons is suppressed as they get absorbed by matter on their way across the Earth. As a result, the atmospheric neutrinos are the only remaining background from CR interactions when considering directions below the horizon of the detector.

As ANTARES does not have a fixed view of the Galactic Centre, only events coming from declinations below -47° are always up-going in the detector. Events with declinations between -47° and 47° are seen as up-going events for only part of the sidereal day, while declinations above 47° are always above the horizon of ANTARES. This implies that the Galactic Centre is seen below the horizon of the detector about 75% of the time. The respective Galactic Centre views of the two telescopes are schematised in Figure 4.2, where the Galactic Centre location is indicated in red and the colour scale represents the percentage of time spent below the horizon of the detector. Due to the particular geographical location of IceCube, the Galactic Centre is always seen at the same zenith coordinate, $\theta_{GC} = \delta_{GC} + 90^\circ$, as for IceCube one can obtain the zenith angle by adding 90° to the declination value. This means that the IceCube detector is at disadvantage for this analysis, since events with declinations between 0° and -90° are seen as down-going events in the detector. Therefore, events coming from the Galactic Centre fall above the horizon of IceCube, where atmospheric muons represent the main contribution to the background. This implies that the outer parts of the IceCube detector need to be used as a veto region in order to reduce the background from atmospheric muons. As a result, the fiducial volume considered for IceCube is considerably reduced while the entire detector volume can be used for ANTARES.

4.3 Event selection

As stated earlier, the data samples used for this joint dark matter search are taken from already published analyses carried separately by the ANTARES and the IceCube collaborations. This analysis combines nine years of ANTARES data from the dark matter search described in [118] with three years of IceCube data taken from [119]. No modifications are applied to these samples, which are therefore exactly the same as those used for the separate previous analyses. A description of the various cuts

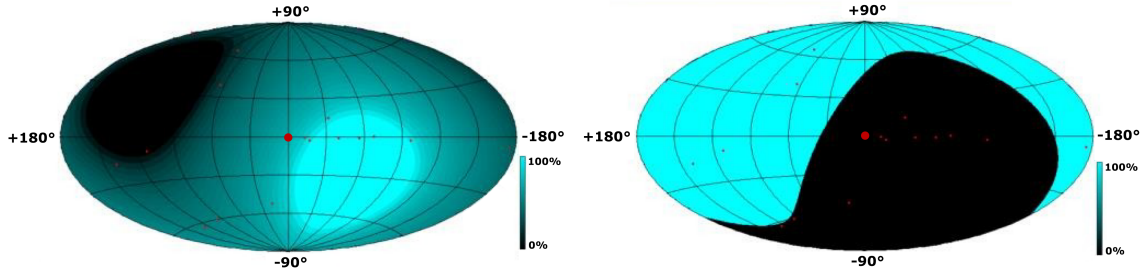


Figure 4.2—Visibility of the ANTARES (left) and IceCube (right) neutrino telescopes in galactic coordinates, where the location of the Galactic Centre is marked by a red dot and the colour scale indicates the level of visibility.

and algorithms applied in order to obtain the ANTARES and the IceCube samples from the searches cited above are described in subsections [4.3.1](#) and [4.3.2](#), respectively. The resulting event selections consist of track events and are optimised to search for neutrinos from dark matter annihilation in the Galactic Centre. While the ANTARES sample only selects up-going tracks, the IceCube event selection contains tracks from all directions of the sky.

4.3.1 ANTARES

Nine years of ANTARES data are considered for this analysis, with data taken between 2007 and 2015. As previously mentioned, the recorded data are split into runs of several hours. Various cuts are applied on these runs in order to obtain the final event selection used for this analysis. The aim of these cuts is to select up-going track-like events. As these cuts strongly favoured muon neutrinos, only this flavour is considered in the final sample.

Pre-reconstruction cuts

The first step of the event selection is to exclude problematic runs. Some runs recorded by ANTARES show poor data quality, which can be caused by multiple factors, such as issues with the electronics or the event triggers. In case of high bioluminescence, the quality of the run can also be strongly affected. In order to be able to sort out runs, they are each allocated a quality parameter called the basic run quality. To be selected, runs have to fulfil the conditions mentioned in Table [4.1](#). The first of the criteria is that the duration of the run must exceed 1 s. It is also required that there is at least an average of one active Analogue Ring Sampler during the entire duration of the run and that the synchronisation did not fail. Additionally, the time difference, ΔT , between the total run duration, T_{Tot} , and the effective time, T_{eff} , must be under 450 s. Finally, the rate given by the 3N trigger, which is designed to check for cluster of hits, must be between 10 mHz and 100 Hz.

When meeting these criteria, runs are assigned a basic run quality equal to 1 or a greater value. For low quality runs, this parameter is set to zero and the run is rejected.

Cut	Selection criteria
I	Run duration > 1 s
II	Active ARS during run > 1
III	No synchronisation fail
IV	$\Delta T = T_{\text{Tot}} - T_{\text{eff}} < 450$ s
V	$\text{Rate}_{\text{Trigger3N}} \in [10^{-2}, 10^2]$ Hz

Table 4.1: Summary of the initial cuts applied on ANTARES runs.

Table 4.2 provides an overview of the runs kept after this first selection, separated in different measurement periods. The beginning of the different detector configuration periods is marked by the change of detector configuration, i.e. the variation of the number of strings used, or the start of a new year. Several interruptions of data acquisition took place during these periods, explaining the discrepancies between the total livetime and the duration of each period. These disruptions have various reasons such as communication failures with part of the detectors or power outage in the La-Seyne-Sur-Mer shore station. The variations over time of the number of considered lines result, among other things, from the deployment periods of the detector lines.

Event reconstruction

Before reconstruction, ANTARES data consists of the collection of single hits recorded by the OMs. For each hit, the arrival time of the photon and the integrated charge are stored. From these values, the properties of the particle responsible for these hits can be deduced using reconstruction algorithms. A first fit, mostly relying on hit coincidences, is applied to the hit distribution. The purpose of this initial fit is to allow the exclusion of uncorrelated noise. Once this first hit selection is performed, more complex reconstructions are applied to the events. Among the ANTARES collaboration, two reconstruction algorithms are used depending on the energy deposited in the detector.

The QFit [157] algorithm is able to reconstruct single-line events, i.e. events for which only one line of the detector is hit by photons. For this reason, the QFit reconstruction is favoured when considering low energy neutrinos, typically below 250 GeV. For single-line events, only the zenith information of the event is reconstructed. These particular events are thus treated separately from events recorded by OMs on more than one line, for which a multi-line fit procedure is applied. Since QFit does not consider the relative movement of the strings due to water streams, further uncertainties are linked to this reconstruction. However, it makes this algorithm more computationally efficient, allowing QFit to also be run online as a first event reconstruction.

The quality function, Q , is constructed as a χ^2 fit, from which the final value is used as a quality parameter:

$$Q = \sum_{i=1}^{N_{\text{hit}}} \left(\frac{(t_\gamma - t_i)^2}{\sigma_i^2} + \frac{A(a_i) D(d_\gamma)}{\langle a \rangle d_0} \right), \quad (4.4)$$

where N_{hit} is the total number of hits selected for the fit and $\langle a \rangle$ is the averaged hit

charge. The normalisation, d_0 , is chosen to be equal to 50 m, as the typical signal in a PMT pointing towards the Cherenkov cone is of the order of 1 PE for this distance. The arrival time of the photon as estimated at the current iteration of the fit is represented by t_γ , while t_i is the incident time of the i th hit and σ_i is the timing uncertainty. The function $A(a_i)$ is defined as:

$$A(a_i) = \frac{a_0 a'_i}{\sqrt{a_0^2 + a_i'^2}}, \quad (4.5)$$

where a'_i is the corrected hit charge, which takes into consideration the angular acceptance of the storey. The aim of the $A(a_i)$ function is to ensure that the hit charge, a_i , does not exceed the artificial saturation value a_0 . Similarly, the role of the $D(d_\gamma)$ function is to make sure a minimum distance, d_1 , is considered for the fit:

$$D(d_\gamma) = \sqrt{d_1^2 + (d_\gamma)^2}, \quad (4.6)$$

where d_γ is the fitted distance at the current iteration. The saturation parameters a_0 and d_0 are artificially set to reduce background hits. While, the product of the corrected charge and the distance, $a'_i d_\gamma$, will be left unchanged by equations [4.5](#) and [4.6](#) in the case of Cherenkov light, this is not the case for background events. This results from the fact that, when neglecting effects from the propagation medium, Cherenkov light linearly decreases with the distance to the OM. Therefore, the product of corrected charge and the distance are assumed to be constant, i.e. $a'_i d_\gamma = a_0 d_1$. In the case of ANTARES, this constant $a_0 d_1$ is expected to be of 50 m×PE, which is equivalent to observing a photo-electron at a distance of 50 m from the OM.

The λ Fit [\[158\]](#) algorithm consists of multiple consecutive reconstructions. During the initial step, a linear χ^2 fit is used in order to obtain the track parameters necessary for the likelihood fit. Indeed, the maximisation procedure requires track parameters close to the optimal values since the likelihood function has several local maxima. This procedure is then repeated a number of times, assuming different starting points and directions for the tracks. The quality of the final likelihood fit is given by the parameter

$$\lambda = \frac{\log(\mathcal{L})}{N_{\text{hit}} - 5} + 0.1 (N_{\text{comp}} - 1), \quad (4.7)$$

which takes the number of degrees of freedom into consideration. In the case of this fit, this number is equivalent to the number of hits, N_{hit} , from which the number of fitted parameters is subtracted. The maximum value of the likelihood function is given by \mathcal{L} and N_{comp} represents the number of times the same results were obtained when repeating the first steps of the algorithm with different initial values. In addition to the quality parameter λ , which can be used to reject poorly reconstructed events, the angular uncertainty on the muon track direction, β , is estimated as

$$\beta = \sqrt{\sin^2(\theta_{\text{rec}}) \sigma_\phi^2 + \sigma_\theta^2}. \quad (4.8)$$

where σ_ϕ and σ_θ are the errors on the azimuth angle and the zenith angle yield from the covariance matrix, respectively.

Year	Number of lines	Run ID	Number of runs	Livetime [days]
2007	5	25800-31048	1466	192.3
2008	10	31051-32491	301	36.2
	9	32525-34389	346	45.3
	10	34392-34427	21	1.9
	12	34432-38230	1318	96.6
2009	12	38241-38357	36	2.4
	11	38363-39589	504	45.5
	10	39590-41677	392	48.05
	9	41679-44109	516	87.3
	8	44112-44326	49	8.5
	10	44472-45538	166	18.3
2010	10	45540-51886	1399	147
	9	51897-52853	399	41.9
	12	52894-54252	614	51.1
2011	12	54253-61904	3118	275.4
2012	12	61908-68170	2418	223.7
2013	12	68692-73064	844	164.7
2014	10	73065-79221	975	262
2015	10	79226-83070	1010	353.9

Table 4.2: Overview of the data used for the ANTARES event selection.

Post-reconstruction cuts

Cuts on the respective quality parameters of the λ Fit and Q Fit reconstructions are optimised independently for the various dark matter assumptions, i.e. the dark matter halo model, annihilation channels and dark matter masses. For λ Fit, the cut on the angular uncertainty β is also optimised. All values of β above 1° are rejected at an early stage of the analysis as the average angular resolution for event reconstructed with λ Fit are below this cut when considering DM masses above 100 GeV. The optimum cuts turned out to be quite similar for most combination of annihilation channel and dark matter mass. Therefore, it was decided to use the same cut for all given combination of dark matter mass, annihilation channel and halo profile. The cut considered for the Q Fit algorithm is $Q < 0.7$, while $\lambda > -5.4$ is used for λ Fit.

4.3.2 IceCube

The IceCube event selection consists of three years of data recorded with the 86-string configuration from May 2012 to May 2014. The sample only take into account data

taken with the final detector configuration, which was completed in December 2010. Since there are inconsistencies in the DeepCore filter rate for data recorded in 2011, the first year of IC86 data is not considered in this event selection. The goal of this event selection is to pick track-like events starting within the DeepCore sub-detector volume. Starting events are generally originating from the CC interactions of muon neutrinos within the fiducial volume. Similarly to ANTARES, IceCube data are also divided into runs, with a standard duration of 8 hours per run. In order to obtain the final data set, various cuts and event selections are applied on these runs. In IceCube, the steps leading to the final event selection are split into so-called levels. The level which constitutes the common basis for consecutive event selections carried out for individual analyses is called level 2. This level regroups all the events that passed at least one event filter.

Level 3

The idea behind the cuts applied at this level, which are listed in Table 4.3, is to reduce the contributions from pure noise hits and atmospheric muons. While the ANTARES neutrino telescope has a privileged position to observe the Galactic Centre, the outer parts of the IceCube detector need to be used as a veto in order to reduce background from atmospheric muons. As a result, the effective volume of the detector is reduced to the 8 DeepCore strings and the 7 IceCube strings surrounding the sub-detector. Furthermore, only DOMs located at depths between 2140 m and 2420 m are considered. With a resulting fiducial volume of 0.015 km^3 , the instrumented volume considered for IceCube is comparable to the ANTARES detector volume, which is around 0.01 km^3 . A schematic view of the fiducial volume considered for this combined analysis is represented in Figure 4.3, where the blue line shows the delimitation of the DeepCore sub-detector. This selection is done by the DeepCore filter, which has for purpose to only select events starting within the DeepCore fiducial volume. First, hits happening in the fiducial volume are selected and the corrected centre of gravity (COG) is computed. The hits occurring in the veto region are assumed to be the result of Cherenkov photons created by passing charged particles. For each of these individual hits, the speed of a particle that would travel from the considered hit in the veto region to the COG is then computed. If the speed of this hypothetical particle is close to the speed of light, i.e. between 0.25 m ns^{-1} and 0.4 m ns^{-1} , the hit is labelled as a VetoWindowHit. Events with more than one VetoWindowHit are rejected while events with no hit in the veto region are automatically selected.

In order to further reduce the contribution from atmospheric muons, two additional cuts are considered along the DeepCore filter. Namely, events with SRT hits recorded by DOMs above $z = -9 \text{ m}$ are rejected. The rejected region corresponds to the upper-half of the IceCube detector volume. The second complementary criterion requires the first three SRT hits to be recorded in the DeepCore fiducial volume. Another goal of the cuts applied at level 3 is to ensure a certain event quality in order to run the first event reconstructions. For this reason, events with hits registered on less than three strings are excluded from the sample. This cut is motivated by the fact that it is only possible to deduce the interaction vertex of the event when considering at least three strings. For single-string events one can only reconstruct the zenith, and it is possible

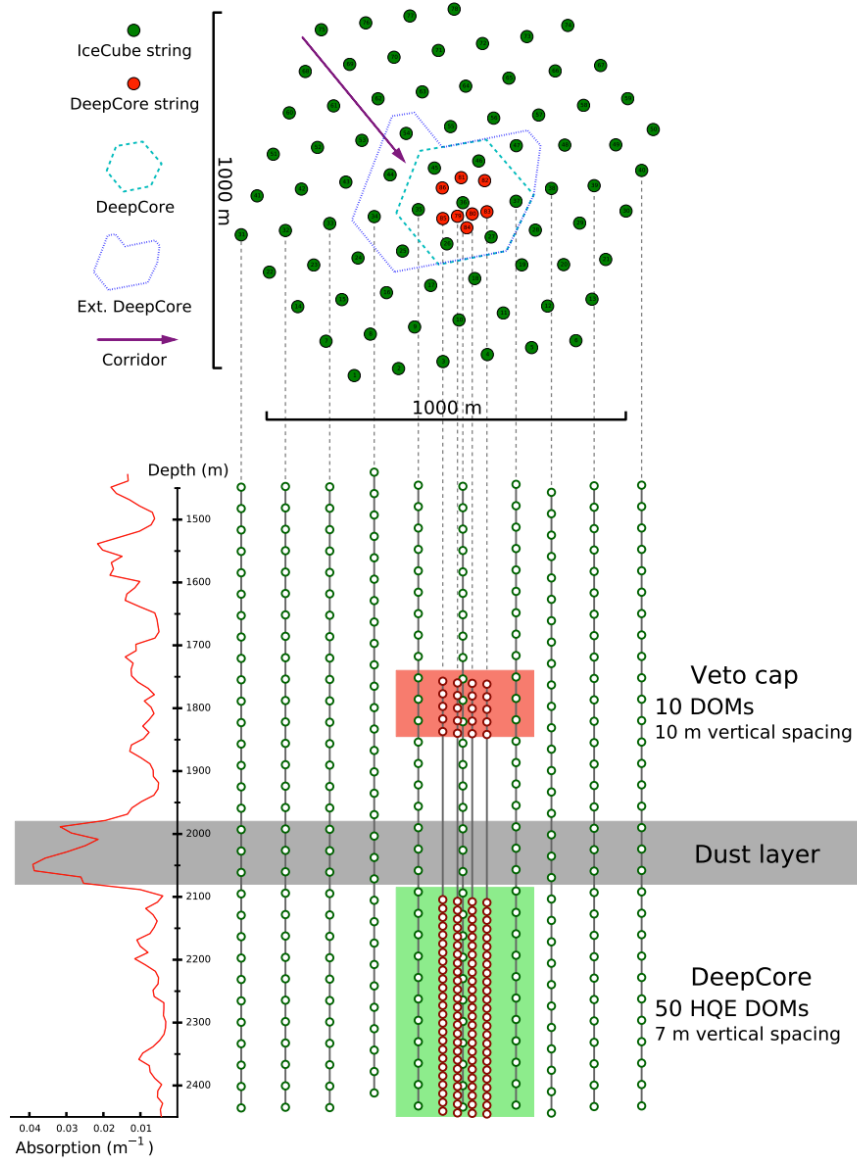


Figure 4.3—Illustration of the veto used to reject atmospheric muons by selecting only events starting within the DeepCore volume shown as the blue delimitation in the upper part of the figure. The considered vetoed fiducial volume is highlighted in green in the lower part of the plot. Credit: IceCube collaboration.

Cut	Selection criteria
I	DeepCore filter conditions are met
II	No pulses recorded by DOMs above $z = -9$ m
III	First 3 pulses are in DeepCore volume
IV	$N_{\text{str}} > 3$
V	$N_{\text{ch}} > 10$

Table 4.3: Summary of the cuts and selection conditions applied at level 3.

to get an indication on the azimuth when taking two-string events into account. In the same vein, a cut is applied on the number of hit DOMs. When a DOM registers at least one hit, it is referred to as a channel. Applying a cut on the number of channel, N_{ch} , also reduces the noise contribution, which becomes almost non-existent for $N_{\text{ch}} > 10$. These consecutive cuts reduce considerably the background from atmospheric muons and pure noise events, resulting in a diminution of the experimental data rate by almost four orders of magnitude.

Level 4

Before defining the cuts described in Table 4.4, reconstruction algorithms are applied to the samples. The first and most basic of these reconstructions is the improved LineFit algorithm [159]. This algorithm attempts to fit an infinite line through the triggered DOMs without considering the geometry of the Cherenkov emission. Rather, the light emission is assumed to follow a plane wave, which makes this algorithm fast. The improved LineFit outputs are considered as seeds for more complex subsequent reconstructions. In particular, information such as the direction and the arrival time of the event are used to run the Single-Photo-Electron-Fit (SPEFit) algorithm [160]. SPEFit focuses solely on the first hits recorded by each DOM, with the assumption that the first hit is subject to less scattering. This likelihood based reconstruction algorithm is used to estimate the best suited parameters of an infinite line fitted to our data.

Based on the SPEFit reconstruction, a first cut is applied to only keep events with reconstructed zeniths falling within a 40° band centred around the Galactic Centre. In addition to the zenith cut, events with low SPEFit likelihood values, i.e. with high values of $\text{LLH} = -\log(\mathcal{L})$, are also excluded. Since events with more hits are expected to have higher LLH values due to the increased number of terms in the LLH calculation, a reduced LLH value, $\text{rLLH} = \text{LLH}/(n_{\text{ch}} - 5)$, is defined by normalising the LLH with the number of channels, n_{ch} . The next step of the L4 event selection is to characterise the quality of the reconstructed event direction. For this, the paraboloid algorithm is used to obtain an uncertainty on the reconstructed direction by fitting a two-dimensional parabola around the minimum of the zenith-azimuth likelihood plane. The angular uncertainty is then defined as

$$\sigma_{\text{paraboloid}} = \frac{\sqrt{\sigma_1^2 + \sigma_2^2}}{2}, \quad (4.9)$$

Cut	Selection criteria
I	$\theta_{SPEFit4} \in [\theta_{GC} - 20^\circ, \theta_{GC} + 20^\circ]$
II	$(rLLH = LLH_{SPEFit4}/(n_{ch} - 5)) < 11$
III	$\sigma_{paraboloid} < 0.05$
IV	$L_{FR} < 600m$
V	$r_{FR} < 250m$
VI	$\sigma_z < 80m$
VI	RTVeto < 3 hits

Table 4.4: Summary of the cuts and selection conditions applied at level 4.

where σ_1 and σ_2 are the two axes of the $1\text{-}\sigma$ confidence ellipse.

While SPEFit only considers DOMs with a recorded hit, the likelihood-based reconstruction named FiniteReco takes all DOMs into account. The inclusion of DOMs with no recorded hits is possible thanks to the use of photon tables. These tables encode the probability for a photon to be detected by a DOM for a given hypothetical track in the detector and are generated using SPICE-Mie. This probability depends on various factors such as the relative orientation and distance of the DOM with respect to the track, as well as the length and direction of the considered track. The probabilities of detecting the Cherenkov photons produced by a muon moving through IceCube is computed by simulating a muon with a starting depth between -800 and 800 meters, which propagates through the detector with a specific zenith angle in $[0^\circ, 180^\circ]$. The detection probability of the resulting Cherenkov photons are then encoded up to a given distance, depending on the energy of the event, and the corresponding distributions are expressed in terms of time and position. A multidimensional spline is then applied in order to allow a smooth interpolation across all considered generation depths and zenith angles. FiniteReco takes as input the position and the direction of the track given by SPEFit. The algorithm then only varies the interaction point and stopping point of the track to compute its most probable length [161]. From this, a first cut is applied that require the track length to be shorter than 600 m. A second cut ensures that the interaction vertex reconstructed with FiniteReco is contained within a cylinder with a radius of 250 m located around the central string of DeepCore. Together, these two cuts reduce the background from atmospheric muons.

In addition to these criteria, the hit projection on the vertical axis of the detector, z , is used to discriminate atmospheric muons from signal neutrinos. For this, a cut is applied on the weighted charge spread, σ_z . Atmospheric muons sneaking through the detector are more likely to cause hits higher up in the IceCube detector than a starting neutrino event. As σ_z tend to be larger for atmospheric muons than for starting neutrino events, background from atmospheric muon can be reduced by only selecting events with σ_z below 80 m.

Once the cuts previously defined are applied, an additional filter called RTVeto is considered [162]. The pulses occurring outside the fiducial volume are identified as RTVetoPulses if they are recorded before the end of the first SRT cleaned pulses and are not tagged as SRT cleaned pulses. Each RTVetoPulse is then used to seed an

Cut	Selection criteria
I	$\theta_{SPEFitA} \in [\theta_{GC} - 10^\circ, \theta_{GC} + 20^\circ]$
II	ConeHits < 2 hits
III	$\log(\mathcal{L})/(n_{ch} - 5) < 18$
IV	RZCut conditions satisfied

Table 4.5: Summary of the cuts and selection conditions applied at level 5.

algorithm based on the radial distance (R) and the time (T) in order to find clusters of hits, which returns the size of the largest hit clusters. As incoming muons will most likely leave hits in the veto region before entering the DeepCore fiducial volume, they are expected to create the largest hit clusters. Therefore, the size of the clusters can be used to distinguish atmospheric muons from starting neutrinos. If an event presents a cluster of more than three hits fulfilling conditions of the RTVeto, it is rejected.

Level 5

The cuts applied at level 5 have for sole focus to reduce the contribution from atmospheric muons and are listed in Table 4.5. To this end, the zenith range considered is further narrowed by only considering event with reconstructed zenith angles ranging from $\theta_{GC} - 10^\circ$ to $\theta_{GC} + 20^\circ$. This cut reduces the background contribution by 25%, while keeping 85% of the expected signal. Additional parameters are computed to help identify sneaky atmospheric muons by considering hits recorded in the veto volume. For instance, ConeHits are calculated by taking all pulses into account, while only SRT pulses were considered for previous cuts. These ConeHits are defined as the number of pulses within a cone with an opening angle of 20° pointing towards the reconstructed interaction vertex and occurring within a time frame of $1 \mu\text{s}$ beginning $0.5 \mu\text{s}$ after the reconstructed time of the interaction. This value is expected to equal zero for events starting in the fiducial volume, whereas it should be non-null for atmospheric muons. Since some noise hits could be recorded within the previously defined cone and be identified as ConeHits, the applied cut rejects events with more than 2 ConeHits rather than all events with a number of ConeHits above zero. Similarly, CylinderHits are defined as the hits recorded in a cylindrical volume of fixed radius extended backwards from the reconstructed interaction vertex and which are not identified as SRT cleaned pulses. The likelihood value of the track reconstructed from CylinderHits is calculated by applying the likelihood fit used for SPEFit. For starting events, the likelihood values should be small, while for atmospheric muons the hits might be in good agreements with the reconstructed track, leading to higher likelihood values. Therefore, the relative cut rejects events with $\log(\mathcal{L})/(n_{ch} - 5) < 18$, for a cylinder radius of 250 m. Lastly, a two-dimensional space cut, called RZCut, is applied. The two variables considered for this cut are the radius, r , and the z -position of the first hit of the SRT cleaned pulses,

$z_{FirstHit}$.

Level 6

The cuts applied at this level, which are visible in Table 4.6, are no longer based on single variables and are rather defined from the combination of several of them, using Boosted Decision Trees (BDTs) [163]. BDTs are machine learning algorithms which are here used to distinguish between signal and background. They rely on a decision tool using a tree-like construction, boosted by putting the emphasising on previously mis-classified events during following iterations. The process is supervised by first teaching the algorithm which events constitute signal or background events, using training samples of randomly selected events from the experimental data and expected signal samples. The events are classified as background or signal based on a cut on the variable with the most separation power. The event tagged as background after a cut, also called leaf, are not rejected but are rather further classified at the next leaf where a cut is applied on a different variable. Once the decision tree is built, the actually samples are passed into the BDT. At the end of the process, a BDT score is allocated to the event, corresponding to the signal fraction at the final leaf. BDT scores typically range from -1 (background) to 1 (signal), i.e. the closer the BDT score is to 1, the more likely the event is of signal origin. Several variables were first considered in the BDT computation, among which only seven were used in the final BDT. These variables are all listed in Table 4.6 by order of importance. Two of these variables are given by the Veto Identified Causal Hits (VICH) algorithm [164, 165]. This algorithm is designed to identify hits, caused by remaining muons, which are causally connected to a DeepCore event. Even though correlated, both the number of channels and the total charge given by the VICH algorithm are used in the BDT, as both of them independently allow to distinguish between signal and data. At this stage of the event selection, an additional reconstruction, called HybridReco, is applied. For this reconstruction, photon tables fitting all parameters of interest are used. This is possible since the event rate is further reduce by the cuts applied at level 5, making it less computationally intensive to run more precise reconstructions. A total of eight parameters are used when computing these photon tables. The angular information (azimuth and zenith angle) is used along information about the position of the interaction vertex (x,y,z,t), the track length (L) and the energy of the hadronic cascade ($E_{cascade}$). HybridReco fits simultaneously a likelihood based on all eight parameters. The multi-modal sampling algorithm, called MultiNest [166], is then used to produce a posterior sample from the multi-modal distributions given by HybridReco. MultiNest is a Bayesian inference tool used as a minimiser for the 8-dimensional likelihood obtained with HybridReco. The use of HybridReco and MultiNest results in a considerable gain in the precision of the track length and the position of the interaction vertex, as well as in a small enhancement of the angular resolution of the event. Among the variables obtained with HybridReco/MultiNest, the radius $r^{HR/MN}$ describing the distance in the $x^{HR/MN} - y^{HR/MN}$ plane is used along the $y^{HR/MN}$ coordinate and the reconstructed zenith angle, $\theta^{HR/MN}$. From the track information obtained from HybridReco/MultiNest, ConeHits are reevaluated. Using these more precise reconstructions, cones with opening angles ranging from 5° to 50° are computed. Different opening angles are evaluated as their purpose is to account for a possible imprecision in the direction of the event, which should be correlated with the resolution of the event. Since the resolution depends on

Importance	BDT Variables
I	VICH, Number of channels
II	$r^{HR/MN}$
III	ConeHits (10°)
IV	VICH, Total charge
V	$y^{HR/MN}$
VI	$LLH_{Contained}^{FR} - LLH_{Infinite}^{FR}$
VII	$\Theta_{zen}^{HR/MN}$

Table 4.6: Summary of the variables used for the BDT computed at level 6.

the energy, the open angle of the considered cone should vary for different energies and thus different dark matter masses. However, a fixed opening angle of 10° is chosen in order to use the same BDT for all dark matter masses. The last considered variable going into the BDT is the likelihood ratio of contained tracks over infinite tracks, given by FiniteReco. This value, which gives an indication of the most probable of two scenarios, can also be retrieved by subtracting the logarithm of these likelihood values. For this analysis, the BDT is implemented using the Toolkit for Multivariate data Analysis (TMVA) package [167]. The BDT is trained for a signal from dark matter particles with a mass of 100 GeV annihilating through the W^+W^- channel, assuming the NFW halo profile. After studying the effect of various cuts on the IceCube-only sensitivities, the optimised BDT cut is chosen to only select events with a BDT score above 0.25.

4.4 Signal expectation

As described in Section 3.4, several ingredients are needed in order to mimic the expected neutrino flux from dark matter annihilation in the galactic centre. For the sake of consistency, it was important to make sure that the ingredients going into the computation of the signal expectations were the same for both ANTARES and IceCube. Therefore, the first important task that I performed for this analysis was to study the potential differences between the weighting components used for both the dark matter search in the Milky Way with nine years of ANTARES data [118] and the search for dark matter annihilation with three years of IceCube data [119]. In the following subsections, the neutrino spectra from dark matter annihilation, as well as the dark matter halo profiles considered by the two collaborations for their respective searches are exposed. The final unified ingredients chosen for the combined dark matter search, as well as the motivation behind these choices are discussed also discussed below.

4.4.1 Energy spectra

The neutrino spectra from dark matter annihilation, dN/dE_ν , depends on the mass of the dark matter particle and the annihilation channel considered. For this combined

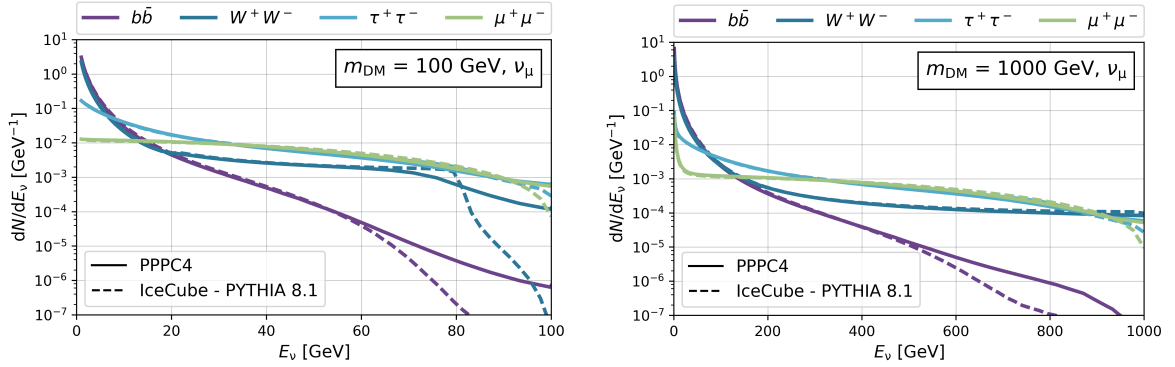


Figure 4.4—Comparison of the PPC4 spectra (solid lines), which are used for the ANTARES-only analysis, and the spectra computed with Pythia 8.1 for the IceCube-only analysis (dashed lines). The muon neutrino spectra at Earth are shown for dark matter particles with masses of 100 GeV (left) and 1 TeV (right) annihilating through the four channels scanned for the combined analysis.

analysis, the dark matter masses ranging from 50 GeV to 1 TeV are scanned and dark matter annihilation through the four following channels is explored: W^+W^- , $\mu^+\mu^-$, $\tau^+\tau^-$ and $b\bar{b}$. A 100% B.R. into one of these channels is assumed, and each specific case is evaluated for all dark matter masses in the investigated range. The choice of this particular range is motivated by the fact that for these energies, the sensitivities on $\langle\sigma_A v\rangle$ set by ANTARES and IceCube are similar, making it ideal for a combined search. In the attempt to unify the different components of the ANTARES and the IceCube individual analyses, some discrepancies between the spectra used by the two collaborations were brought to light.

While the ANTARES-only search used neutrino spectra known as the PPC4 spectra [168], the IceCube spectra were computed directly with the PYTHIA 8.1 event generator [169]. Similarly to what was done in IceCube, PYTHIA 8.1 is also used in order to obtain the energy spectra of the messenger as encoded in the PPC4 tables. In both cases, the dark matter self-annihilation is simulated by the decay of a generic resonance, \mathcal{D} , with a mass equal to twice the dark matter mass ($m_{\mathcal{D}} = 2 m_{\text{DM}}$) with PYTHIA 8.1. This generic resonance is constrained to decay into one of the considered dark matter annihilation channels, with a branching ratio of 100%. The neutrinos produced during this simulated dark matter annihilation process are then saved into histograms as a function of their energies. The resulting distributions provide the neutrino energy spectrum for the particular dark matter mass, m_{DM} , and annihilation channel assumed for the simulation. For the PPC4 tables, the energy spectra are provided for $(\bar{\nu})_{e,\mu,\tau}$, e^\pm , γ , \bar{p} , \bar{d} from dark matter annihilation into a variety of primary channels and various dark matter masses. These tables are expressed as a function of the energy fraction $x = K/m_{\text{DM}}$, with K being the kinematic energy of the final messenger in the rest frame of \mathcal{D} . The resulting PPC4 spectra are given in terms of $dN/d\log(x)$. In the case of the IceCube-only spectra, the histograms show dN/dE as a function of the energy of the neutrinos.

Although the same event generator is used to compute the spectra considered for

the respective ANTARES and IceCube analyses, some differences are visible between them. A comparison of the PPPC4 and IceCube-only neutrino spectra is shown in Figure 4.4 for all the dark matter annihilation channels considered in this joint analysis. These plots show the expected muon neutrino spectra at Earth when considering dark matter particles with masses of 100 GeV (left) and 1 TeV (right). The first noticeable difference between these spectra is the fact that the PPPC4 tables take electroweak (EW) corrections into consideration, while this contribution is ignored during the computation of the IceCube-only spectra. More precisely, the EW radiation processes are added to PYTHIA following directives from [170] during the simulation of the PPPC4 spectra. These EW corrections are expected to be non-negligible for dark matter masses above the weak scale, i.e. above the mass of the W and the Z bosons. The emission of W and Z bosons is responsible for the presence of more hadrons in the final state, which considerably modifies the messenger fluxes at low energies when considering dark matter masses well above the mass of the W and the Z bosons. The second modification applied to PYTHIA when computing the PPPC4 tables was to change the hadron decay tables to ensure that hadrons, which are otherwise treated as stable particles, would decay according to the branching ratio stated in [171].

As more factors were taken into account during their computation, the PPPC4 spectra are preferred in this analysis. Since the available tables contain the spectra at production, oscillation still needs to be accounted for in order to get the expected neutrino spectra at Earth. For this, the oscillation parameters listed in Table 1.1 are used. When comparing the sensitivities computed with the PPPC4 spectra to the official sensitivities obtained with the previously used spectra, the IceCube-only sensitivities are affected by up to 25 %.

The investigation of the possible differences between the spectra used by both experiments carried out for this combined analysis also brought to light an interpolation issue of the PPPC4 tables in the ANTARES-only search. This inaccuracy resulted from an approximation of the spectra with an overly rough binning during the computation of the signal expectation by ANTARES, leading to an over estimation of the relative acceptances for neutrino from dark matter annihilation. The correction of this error led to the erratum of the 9 years ANTARES Galactic Centre dark matter search [118].

4.4.2 Dark matter halo profiles

In order to compute the J-factor needed to estimate the signal expectation, information about the dark matter distribution in the Galactic Centre is required. As stated previously, the determination of the dark matter halo shape is subject to many uncertainties. For this reason, two different models are considered in this analysis: the NFW and the Burkert halo profiles [130, 131]. For consistency, the halo parameters used in the calculation of the halo profile functions should be the same for both experiments. After investigation, it turned out that the model parameters originally considered by the two experiments were both taken from [129]. Although the same parameters were used, the ANTARES-only dark matter search used the CLUMPY software [133] to compute the J-factor, while an internal project called DMHaloModels was considered for the IceCube-only analysis. Both pieces of software are computing the dark matter density function and the J-factor from parameters such as the local dark matter

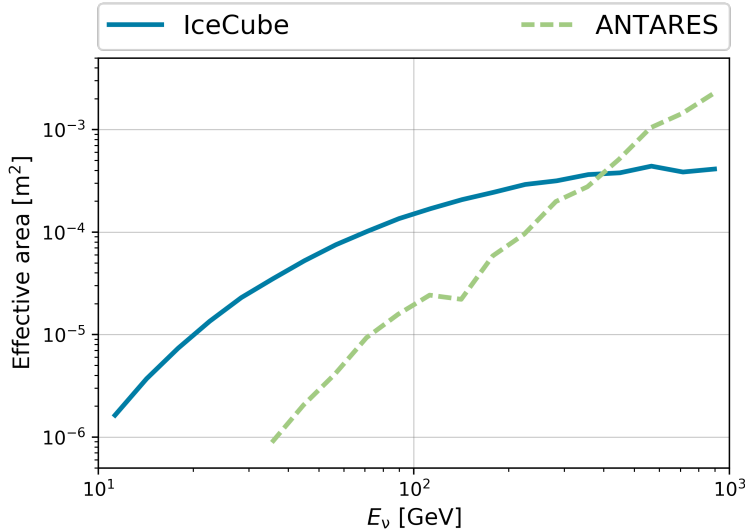


Figure 4.5—Comparison of neutrino effective area obtained for the IceCube (blue) and the ANTARES (green) detectors, which are computed with the simulation samples described respectively in the subsections [4.1.2](#) and [4.1.1](#) for events with declinations between $\delta_{GC} - 30^\circ$ and $\delta_{GC} + 30^\circ$.

density, ρ_\odot , and the scale radius, r_s . When comparing the ANTARES and IceCube J-factors, slight differences between the two curves were noticeable. After an in-depth study, an error in the computation of the J-factor with the DMHaloModels software was found for the IceCube analysis. The value encoded as the local density for the evaluation of the halo function was in fact the scaled density, ρ_0 . This resulted in an over-evaluation of the J-factor, which is corrected by using the exact same J-factor for both experiments. For this, the J-factors are computed with CLUMPY using the halo parameters shown in Table [3.1](#). The resulting dark matter halo densities and J-factors for both the NFW and the Burkert profiles are shown in Figure [3.9](#) of Section [3.4](#), respectively.

4.5 Effective area and acceptance

The effective area, A_{eff} , represents the surface area covered by a theoretical detector with a 100% detection efficiency measuring the same neutrino rate as the actual detector. This value is computed from the MC simulations. For IceCube, the effective area is obtained by filling OneWeight into a histogram logarithmically binned in neutrino energy, E_ν . The values of each bin are then corrected for their width in energy and solid angle. Similarly, the ANTARES effective area is obtained from the previously defined weight w_2 plotted in a histogram with the exact same binning. A comparison of these two neutrino effective areas can be seen in Figure [4.5](#). In order to provide a fair comparison between the two telescopes in the context of this analysis, only declinations between $\delta_{GC} - 30^\circ$ and $\delta_{GC} + 30^\circ$ are considered. For ANTARES, two different event reconstructions, described thoroughly in subsection [4.3.1](#), are used depending on

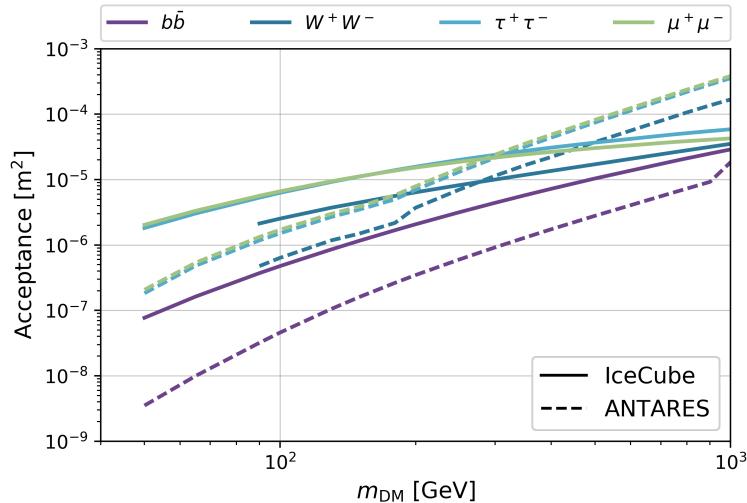


Figure 4.6—Comparison of the acceptance computed for ANTARES (dashed lines) and IceCube (solid lines) for the four annihilation channels considered and the entire dark matter mass range.

the energy. Therefore, the effective area is computed for the two different simulation samples obtained from these reconstructions. It is the switching point between the effective area computed with these two reconstructed simulation samples that causes the visible bump in the ANTARES curve at around 150 GeV.

The effective area can be used in order to determine the acceptance, which quantifies the detector response to a specific spectrum. For this analysis, the acceptance, A , is computed from the convolution of the effective area with the expected neutrino spectra from dark matter self-annihilation, dN_ν/dE_ν :

$$A = \int_{E_{\text{th}}}^{m_{\text{DM}}} A_{\text{eff}}(E_\nu) \frac{dN_\nu}{dE_\nu} dE_\nu, \quad (4.10)$$

where E_{th} is the energy threshold of the detector and m_{DM} is the mass of the dark matter particle considered. The acceptance has to be evaluated for each dark matter mass and annihilation channel. The acceptances of the ANTARES and the IceCube detectors are compared in Figure 4.6, for all four dark matter annihilation considered in this analysis. The point where the ANTARES and the IceCube acceptances cross each other strongly depends on the annihilation channel considered. For a soft neutrino spectra, such as DM annihilation through the $b\bar{b}$ channel, IceCube dominates the entire mass range considered. For harder channels such as W^+W^- , the crossing point between the two experiment curves moves to lower masses.

4.6 Analysis method

In order to search for an excess of signal neutrinos in the direction of the Galactic Centre, a binned likelihood method is applied to our samples. With this method, the shape of the data distribution is compared to expectations from the background and

signal distributions. As stated earlier, signal expectations are evaluated for various dark matter masses ranging from 50 GeV to 1 TeV, while assuming dark matter self-annihilation through either muons ($\mu^+\mu^-$), taus ($\tau^+\tau^-$), W-bosons (W^+W^-) or b-quarks ($b\bar{b}$). The two dark matter halo profiles considered are the NFW and Burkert profiles. The likelihood is computed for each possible combination of dark matter halo profile, annihilation channel and mass. It has to be noted that the analysis method described below is the same as the one used for the dark matter search with three years of IceCube data [119]. However, the definition of the combined likelihood and the relative experiment weights (described in subsection 4.6.3) are specific to this analysis.

4.6.1 Probability density functions

In this subsection, the probability density functions (PDFs) used for the combined analysis are described. As it was decided not to share data files directly between the two collaborations, the required information are exchanged under the form of PDFs. Therefore, these PDFs are built separately by each collaboration, following a similar construction to that used for their respective previous analysis. This way, two different types of distributions are created for each experiment, namely the background and signal PDFs. For both experiments, the signal PDFs are built from generic neutrino simulations weighted in order to mimic the expected neutrino signal, while the background distributions are created from experimental data. At a later stage of the analysis, the distributions of the data recorded by each experiment are also exchanged, which take the same form as the signal and background PDFs.

For ANTARES, two types of distributions are used, depending on the reconstruction considered. In both cases, the ANTARES PDFs consist of 1-dimensional distributions of the angular distance between the events and the Galactic Centre. As only the zenith can be reconstructed for *QFit*, the PDFs represent distributions of $\Delta \cos(\theta) = \cos(\theta_{\text{GC}}) - \cos(\theta_{\text{event}})$, where θ_{GC} is the zenith angle of the Galactic Centre and θ_{event} is the zenith of the reconstructed event. The *QFit* PDFs are build using 28 bins in $\Delta \cos(\theta)$ between -1 and 0.14, as seen in the left panel of Figure 4.7. Using *λ Fit*, both the azimuth and zenith angles can be reconstructed. Therefore, the *λ Fit* PDFs consist of 1-dimensional histograms of the opening angle to the Galactic Centre, Ψ . For these PDFs, 15 bins are considered in Ψ , ranging from 0° to 30° (see right panel of Figure 4.7). These PDFs differ from the one used for the ANTARES autonomous limit only in that the natural scale is used in Ψ instead of the logarithmic scale. In the case of IceCube, the PDFs were chosen to be two-dimensional distributions of the events in right ascension (RA) and declination (δ), as visible in Figure 4.8. These 2D histograms are divided in 10 bins in RA ranging from $-\pi$ to π rad and 6 bins in δ covering the range between -1 to 1 rad.

The signal PDFs are build by weighting the simulated neutrino events with a given neutrino spectrum and source morphology, following equation 3.16. These weighted events are then used to build the histograms, following the binning defined earlier. This results in a different signal PDF for each combination of dark matter mass, annihilation channel and halo profile. As specified in Section 4.4, the ingredients going into the computation of the signal PDFs are the same for both experiments.

Assuming the uniformity of the atmospheric background in RA, the background

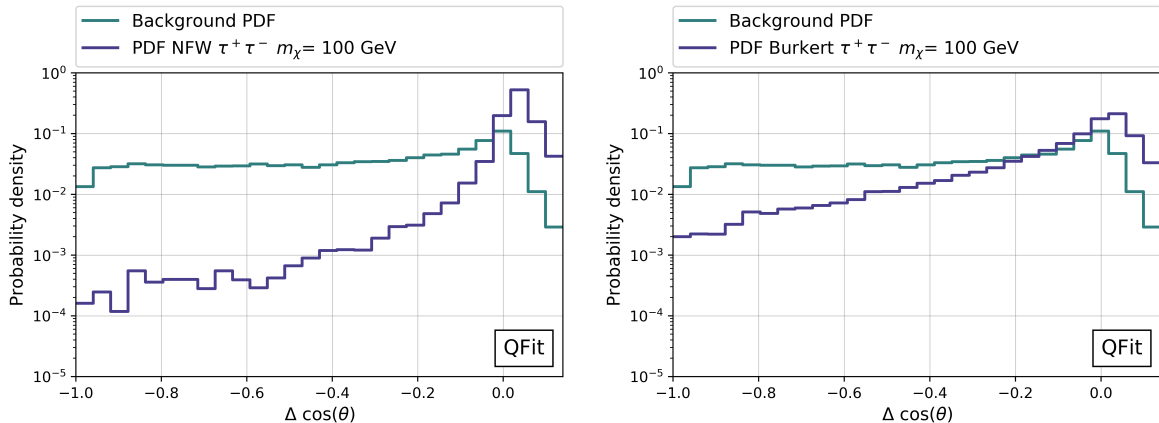


Figure 4.7—ANTARES PDFs for the Q Fit (left) and λ Fit (right) reconstructions. Both histograms show the background PDF (teal) and the signal PDF for the $\tau^+\tau^-$ annihilation channel and NFW profile, assuming $m_{\text{DM}} = 100$ GeV (purple).

PDFs are computed from scrambled data. For ANTARES, the λ Fit background PDF is obtained by assigning random RA values to the events, while Q Fit background PDF is created by giving random arrival times to the events. Similarly, the IceCube background PDF is built from data scrambled in RA, from which the scrambled signal expectations were subtracted according to:

$$f_{\text{bg}} = \frac{1}{(1 - \mu)} (f_{\text{scr.data}} - \mu f_{\text{scr.sig}}), \quad (4.11)$$

where $f_{\text{scr.data}}$ is the PDF obtained from data scrambled in RA, $f_{\text{scr.sig}}$ is the scrambled signal PDF computed by scrambling the signal PDF in RA and $\mu \in [0, 1]$ is the signal fraction in the total sample. The data distributions, built from unscrambled experimental data, are only created and exchanged after the unblinding approval.

4.6.2 Likelihood formulation

From the background and signal PDFs, the expected fraction of events in a particular bin i is defined as:

$$f^i(\mu) = \mu f_{\text{sig}}^i + (1 - \mu) f_{\text{bg}}^i, \quad (4.12)$$

where $\mu \in [0, 1]$ is the fraction of signal events, while f_{bg}^i and f_{sig}^i are respectively the content of the background and signal PDFs of the bin i . The likelihood is expressed as the product over all bins of the Poisson probabilities to observe n_{obs}^i events in the bin i , assuming a particular signal fraction μ :

$$\mathcal{L}(\mu) = \prod_{i=0}^{n_{\text{bins}}} \frac{(n_{\text{obs}}^{\text{tot}} f^i(\mu))^{n_{\text{obs}}^i}}{n_{\text{obs}}^i!} e^{-n_{\text{obs}}^{\text{tot}} f^i(\mu)}. \quad (4.13)$$

For each bin i , the number of observed events, n_{obs}^i , is compared to the number of expected events, which is given by the total number of events in the data sample, $n_{\text{obs}}^{\text{tot}}$,

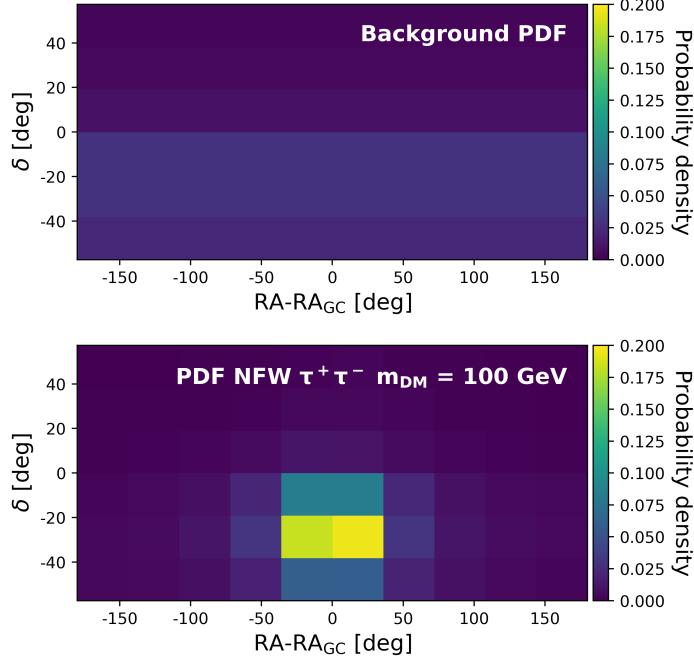


Figure 4.8–Top: IceCube background PDF obtained from data scrambled in RA, where the colour scale expresses the probability density. **Bottom:** IceCube signal PDF for $\tau^+\tau^-$ channel and $m_{\text{DM}} = 100$ GeV assuming the NFW profile.

and the fraction of events in that particular bin for a given signal fraction, $f^i(\mu)$. An important step of this joint analysis consists of combining the individual data sets of the two experiments at the likelihood level. Therefore, once computed separately for ANTARES and IceCube, the individual likelihoods are merged into a single combined likelihood, such that:

$$\mathcal{L}_c(\mu) = \prod_{k=A,I} \mathcal{L}_k(\mu_k), \quad (4.14)$$

where each of the individual likelihoods relies on a different signal fraction, μ_k , relative to the experiment k , with A and I standing for ANTARES and IceCube, respectively. In order to obtain only one signal fraction, μ , according to which the combined likelihood, $\mathcal{L}_c(\mu)$, can be maximised, the individual signal fractions can be rewritten according to the following expression:

$$\mu_k = \frac{\eta_{\text{sig}}^k}{N_{\text{tot}}^k} = \frac{\eta_{\text{sig}}^k / (\eta_{\text{sig}}^A + \eta_{\text{sig}}^I)}{N_{\text{tot}}^k / (N_{\text{tot}}^A + N_{\text{tot}}^I)} \frac{\eta_{\text{sig}}^A + \eta_{\text{sig}}^I}{N_{\text{tot}}^A + N_{\text{tot}}^I} = w_k \frac{\eta_{\text{sig}}}{N_{\text{tot}}} = w_k \mu, \quad (4.15)$$

where N_{tot} represents the total number of background events and is obtained by summing the total number of ANTARES, N_{tot}^A , and IceCube, N_{tot}^I , background events. Similarly, the total signal acceptance, η_{sig} , is given by the sum of the individual acceptances, η_{sig}^k , defined as:

$$\eta_{\text{sig}}^k = \frac{1}{8\pi} \frac{J}{T_{\text{live}}^k} m_{\text{DM}}^2 \int A_{\text{eff}}^k(E) \frac{dN_\nu}{dE_\nu} dE, \quad (4.16)$$

with A_{eff}^k being the detector effective area and T_{live} being the livetime of the experiment. Following Equation [4.15](#), the individual signal fraction, μ_k , can be expressed in terms of the overall signal fraction, μ , with w_k being the relative weight of the individual experiment k . These weights have to be computed for each combination of dark matter mass, annihilation channel and halo profile.

4.6.3 Limit computation

The binned likelihood method used for this analysis provides the best fitted value of the parameter of interest, i.e. the fraction of signal event in the considered data sample, μ_{best} . First, the likelihood method evaluates the degree of concordance between the observed data and the tested hypothesis. For this, a quantity called test statistic (TS) is computed, which quantifies the deviation from the considered hypothesis. The TS used for this analysis is defined as the likelihood ratio introduced by Feldman and Cousins [\[172\]](#), which takes the form of

$$TS \equiv R(\mu) = \frac{\mathcal{L}_c(\mu)}{\mathcal{L}_c(\mu_{\text{best}})}, \quad (4.17)$$

where μ indicates the fraction of signal events in the data sample and μ_{best} is the signal fraction maximising the likelihood function. In order to only fit physical values of the signal fraction, the considered interval is reduced to $\mu \in [0, 1]$. By construction $R(\mu)$ is expected to be inferior or equal to 1 since the fact that μ_{best} maximises the likelihood implies that $\mathcal{L}_c(\mu) \leq \mathcal{L}_c(\mu_{\text{best}})$ for all possible values of the signal fraction μ .

The acceptance interval is constructed from the values of the resulting likelihood ratio, denoted as ranks, following the unifying ordering principle. This way, the interval construction starts with the highest ranking values and builds up by including smaller ranks until the desired coverage α , known as the confidence level, is met. With this approach, under-coverage caused by "flip-flopping" is avoided. The resulting acceptance interval takes the form of $[R_{\text{critical}}^\alpha(\mu), 1]$, where $R_{\text{critical}}^\alpha(\mu)$ is the critical rank corresponding to the lowest value of the ranked distribution. The upper limit on the signal fraction is computed by identifying the value of μ for which $R(\mu) \leq R_{\text{critical}}^\alpha(\mu)$ is satisfied for all $\mu > \mu_{\text{best}}$. Similarly, the lower limit is obtained by finding the μ for which the condition $R(\mu) \geq R_{\text{critical}}^\alpha(\mu)$ is met for $0 < \mu < \mu_{\text{best}}$. In order to find $R_{\text{critical}}^\alpha(\mu)$, numerous pseudo-experiments (p.e.) need to be generated for various values of μ . For the result presented in this thesis, a confidence interval of $\alpha = 90\%$ is considered.

The sensitivities of this analysis are computed by sampling 100,000 p.e. from the background-only distribution. For every single of these pseudo-experiments, the 90% C.L. upper limit on the signal fraction, μ_{90} , is computed from 10,000 pseudo-experiments for each considered signal fraction μ ranging from 0 to 0.01 with 100 steps. The sensitivity, $\hat{\mu}_{90}$, is defined as the median value of the individual upper limits. The distribution of these upper limits is also used to build the 1σ and 2σ uncertainty intervals of the sensitivities. Following the same method, the best estimate of the signal fraction is built for unblinded data. If this value is in concordance with the background-only hypothesis, the relative upper limit, μ_{90} , is determined.

4.7 Treatment of systematic uncertainties

Two types of uncertainties are considered in this analysis. The first category consists of uncertainties resulting from theoretical predictions of dark matter properties, while the second type is linked to detector systematics. As the background expectations are drawn from data, these systematic uncertainties will only affect the signal simulations. While detector systematics will have an impact on the detection efficiency, the astrophysical systematics will affect the expected number of signal events from dark matter annihilation in the Galactic Centre. The treatment of these systematic effects were studied thoroughly for the individual dark matter searches with nine years of ANTARES data [118] and three years of IceCube data [119]. Therefore, the same implementation of these systematic effects is applied for this combined analysis, where the values of the impact of the detector systematics are taken from the respective papers.

4.7.1 Astrophysical uncertainty

Among these two types of systematics, uncertainty on the characterisation of dark matter halo represent the main source of uncertainties for this analysis. As previously mentioned, two different halo profiles are considered in order to account for conjectures about the shape of the dark matter halo. In this analysis, the results obtained for both the NFW and Burkert halo profiles are presented. The impact of considering a cuspy or core halo profile is visible in Figure 4.9, where the limits obtained for the NFW and Burkert profiles are presented side by side. In addition to this, the choice of model parameters used to compute the J-factors for each halo model has a considerable impact. For instance, computing the J-factor with alternative model parameters taken from [173] in place of the parameters used in this analysis (see Table 3.1) leads to up to a factor 1.5 change of the combined limits.

4.7.2 Detector systematics

The dominant source of detector systematics for the ANTARES neutrino telescope results from uncertainties on the direction of the reconstructed track. This systematic is accounted for by using the customary approach applied to point source searches with ANTARES data. As seen in Section 2.9, the event reconstruction strongly relies on the time resolution of the detector, which is affected by the transit time of the PMT, as well as by the accuracy of the calibration of the clock system used by the detector. The level of precision with which the monitoring of the relative positions of the OMs is performed also has an important impact on the reconstruction of the event. The contributions from these uncertainties result in an effect of about 15% on the angular resolution of the event [174]. In practice, uncertainties on the angular resolution of the tracks are thus implemented by smearing the corresponding signal distribution by 15% when computing the signal PDFs.

Likewise, the various systematics of the IceCube telescope translate into uncertainties on the angular resolution of the events. Indeed, the event reconstruction is influenced by several factors such as the efficiency of the PMTs and the model chosen to mimic the ice properties. These uncertainties are investigated by the mean of

dedicated MC simulations. These MC samples are generated in a similar way as the nominal sets used to build the PDFs, with the difference that the values of the baseline models are varied by $\pm 1\sigma$. To account for uncertainties of the ice properties, two different sets of MCs are generated, one for the bulk ice and one for the hole ice. This separation arises from the fact that the ice formation process, and therefore the ice properties, are different for the two cases (see Section 2.7). While the South Pole ice (bulk ice) formed over thousands of years, the ice in the boreholes (hole ice) is the result of a much quicker refreezing process. In both cases, the values of the scattering and absorption lengths are modified. For the bulk ice, this affects the sensitivities by 5 to 15% with respect to the nominal sensitivities. Increasing the scattering length in the hole ice causes the worsening of about 25 to 30% of the sensitivities. Conversely, shortening the scattering length induces improvements from 5 to 10% of the sensitivities. Modifications of the detection efficiency of photons by the IceCube DOMs result in an improvement or a worsening of the sensitivities by 5 to 40%. Under the assumption that they are independent, the different systematic contributions are summed in quadrature in order to obtain the overall uncertainty. This is taken into account in the final combined results by conservatively scaling the signal acceptance relative to IceCube, η_{sig}^I , by 38%.

4.8 Results of the combined dark matter search

In this section, the results of the first combined search for dark matter in the Galactic Centre conducted with the ANTARES and the IceCube neutrino telescopes are presented and discussed extensively. Following the likelihood method described in Section 4.6, the sensitivities of this joint analysis are first computed. These sensitivities are shown and detailed in the following. Once the analysis finalised, the same method is applied to the experimental data. However, before proceeding to this final step, the analysis had to be reviewed by both the ANTARES and IceCube collaborations. Following these reviews, the unblinding of the information on the arrival direction of the events was approved, and the data histograms were exchanged. No neutrino excess corresponding to a signal from dark matter annihilation in the centre of the galaxy could be found by combining the data sets from ANTARES and IceCube at the likelihood level. Therefore, limits on the thermally-averaged self-annihilation cross-section are set, which are shown in subsection 4.8.1.

4.8.1 Unblinded results

The resulting unblinded ANTARES data set consists of a total of 1,077 events reconstructed with $Q\text{Fit}$ and 15,651 events reconstructed with λFit , for a total livetime of 2,101.6 days. The unblinded IceCube data set is composed of a total of 22,622 events recorded over a livetime of 1,007 days. Following the method described in Section 4.6, the best estimate of the signal fraction, μ_{best} , is computed for unblinded data. These results depend on the halo model considered and are evaluated for a given dark matter mass and annihilation channel. Scanning through the considered signal expectations, all computed signal fractions are consistent with the background-only hypothesis. Since

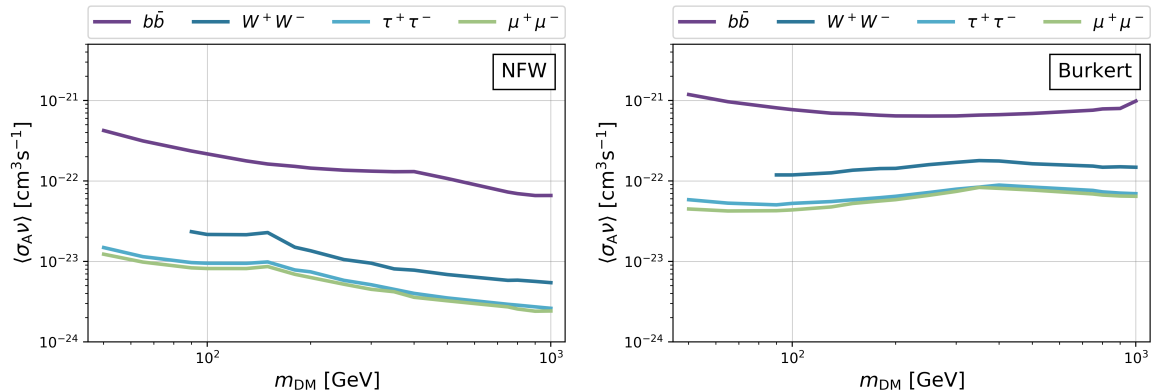


Figure 4.9—Combined 90% C.L. upper limits on $\langle\sigma_A v\rangle$ for the NFW (left) and Burkert (right) dark matter halo profiles.

no significant excess of neutrinos from dark matter annihilation in the Galactic Centre is seen, the corresponding 90% C.L. upper limits on the signal fraction, μ_{90} , are computed. These upper limits expressed in terms of signal fraction can be converted to limits on the thermally-averaged self-annihilation cross-section, $\langle\sigma_A v\rangle$, following the equation

$$\langle\sigma_A v\rangle = \frac{\mu_{90} N_{\text{tot}}}{\eta_{\text{sig}}}, \quad (4.18)$$

for each combination of dark matter halo profile, annihilation channel and mass.

The 90% C.L. upper limits obtained for all dark matter masses and annihilation channels are presented in Table 4.7 for both halo profiles. The 90% C.L. median upper limits, quoted as sensitivities, are also shown in this table for all the signal combinations scanned for this joint analysis. These limits and all the results shown in this section include treatment of the systematics, following the directive described in Section 4.7. The combined upper limits on $\langle\sigma_A v\rangle$ are also shown in Figure 4.9 as a function of the dark matter mass for all annihilation channel considered, assuming the NFW (left) and Burkert (right) profiles.

As shown in Table 4.7 and Figure 4.9, a large difference is visible between the limits obtained for the NFW and the Burkert profiles. Such difference results mainly from the fact that cuspy halo profiles, such as the NFW profile, lead to more peaked signal signatures which are more easily distinguishable against background. This effect leads to stronger limits for cuspy halo profile when compared to core profile distributions such as the Burkert profile. In addition, the two event reconstructions used for ANTARES play a role in explaining the different trends in the limits obtained for the NFW and Burkert profiles. The mass at which the transition between the two reconstructions takes place is chosen according to a balance between the quality of the reconstruction and the number of reconstructed events. For cuspy profiles, the improved angular resolution provided by the λ Fit reconstruction is highly beneficial, pushing the transition point to lower dark matter masses and setting strong constraints at higher masses. For core profiles, which are flatter with respect to the opening angle to the Galactic Centre, Ψ , the goodness of the angular resolution has less impact. As a result, the limits

obtained with the QFit reconstruction dominate most of the dark matter range for the Burkert profile. The limits also strongly depends on the dark matter annihilation considered, with annihilation through $\tau^+\tau^-$ and $\mu^+\mu^-$ resulting in stronger limits than for the $b\bar{b}$ and W^+W^- annihilation channels. This difference result from the shape of the neutrino spectra predicted for each channel. As visible in Figure 4.4, dark matter annihilation into the $\tau^+\tau^-$ and $\mu^+\mu^-$ provide fairly similar spectral shapes, while the other two channels present softer spectra. This is especially true for $b\bar{b}$, for which the main spectral contribution is seen towards the lowest neutrino energies.

The same combined upper limits are shown in Figure 4.10 alongside the relative median sensitivities for all dark matter annihilation channels and halo profiles. The expected 1σ and 2σ bands around the 90% C.L. sensitivities are also shown in green and yellow, respectively. The combined limits present deviation from the expected median sensitivities for several dark matter masses across all annihilation channels and halos considered. These deviations, which result from statistical fluctuations, are however well-contained within the 1σ band and are therefore not significant. It should be noted that ANTARES and IceCube handle these type of under-fluctuations differently. While the IceCube collaboration presents the limits as they are even when their values are lower than the sensitivities, the ANTARES collaboration usually labels the said sensitivities as limits in such cases. For the combined analysis, both collaborations agreed to keep the limits unchanged. The effect of this difference in the treatment of statistical fluctuations adds to the gain obtained from the combination of ANTARES and IceCube data sets.

When comparing these ANTARES and IceCube stand-alone limits to the combined limits, an enhancement of up to a factor 2 can be seen in the mass range considered. This improvement is visible in Figure 4.11, where the combined limits are compared to the individual ANTARES and IceCube limits taken from [118] and [119], respectively. The upper for plots show these limits for the NFW halo profile, while the bottom four display the limits for the Burkert halo profile. For dark matter annihilation through the $b\bar{b}$, W^+W^- and $\mu^+\mu^-$ channels distributed according to the Burkert halo profile, the ANTARES stand-alone limits are not shown as they were never made public. Therefore, for these particular combinations of channel and halo profile, the combined limit is only compared to the individual IceCube limit. A consistent improvement is visible for limits obtained for the all signal expectation combinations, aside from the limit obtained for the $b\bar{b}$ channel when considering the Burkert profile. For this particular signal combination, the dominant contribution to the combined limit is given by IceCube. This is due to the very soft neutrino spectrum given by dark matter annihilation into $b\bar{b}$, which causes the total signal acceptance to be dominated by IceCube for the entire dark matter range.

The different treatment of statistical under-fluctuations by the ANTARES and IceCube collaboration mentioned above also plays a role in the improvement of the combined limits for higher dark matter masses. While the ANTARES limits are set to the related sensitivities, the combined limits are kept identical despite the under-fluctuations. The conjunction of the benefits from the combination of the two data sets and the divergent approach of under-fluctuations with respect to the ANTARES analysis is responsible for the gap between the ANTARES-only limits and the combined limits visible around 1 TeV in Figure 4.12. For this energy range, one would

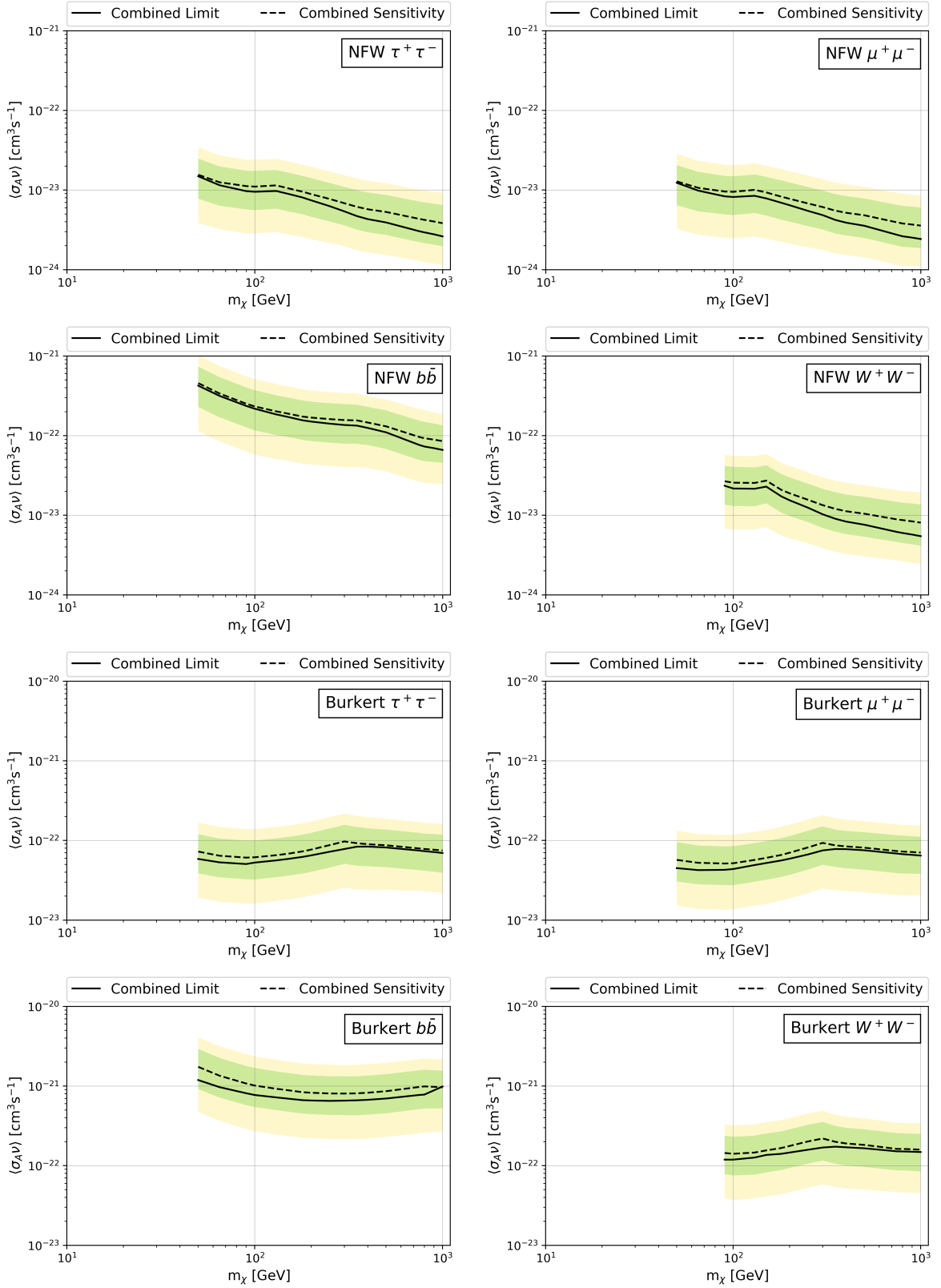


Figure 4.10—Comparison of the combined 90% C.L. upper limits (solid) and sensitivities (dashed) in terms of $\langle\sigma_{AV}\rangle$ shown alongside the expected 1σ (green) and 2σ (yellow) bands around the sensitivity.

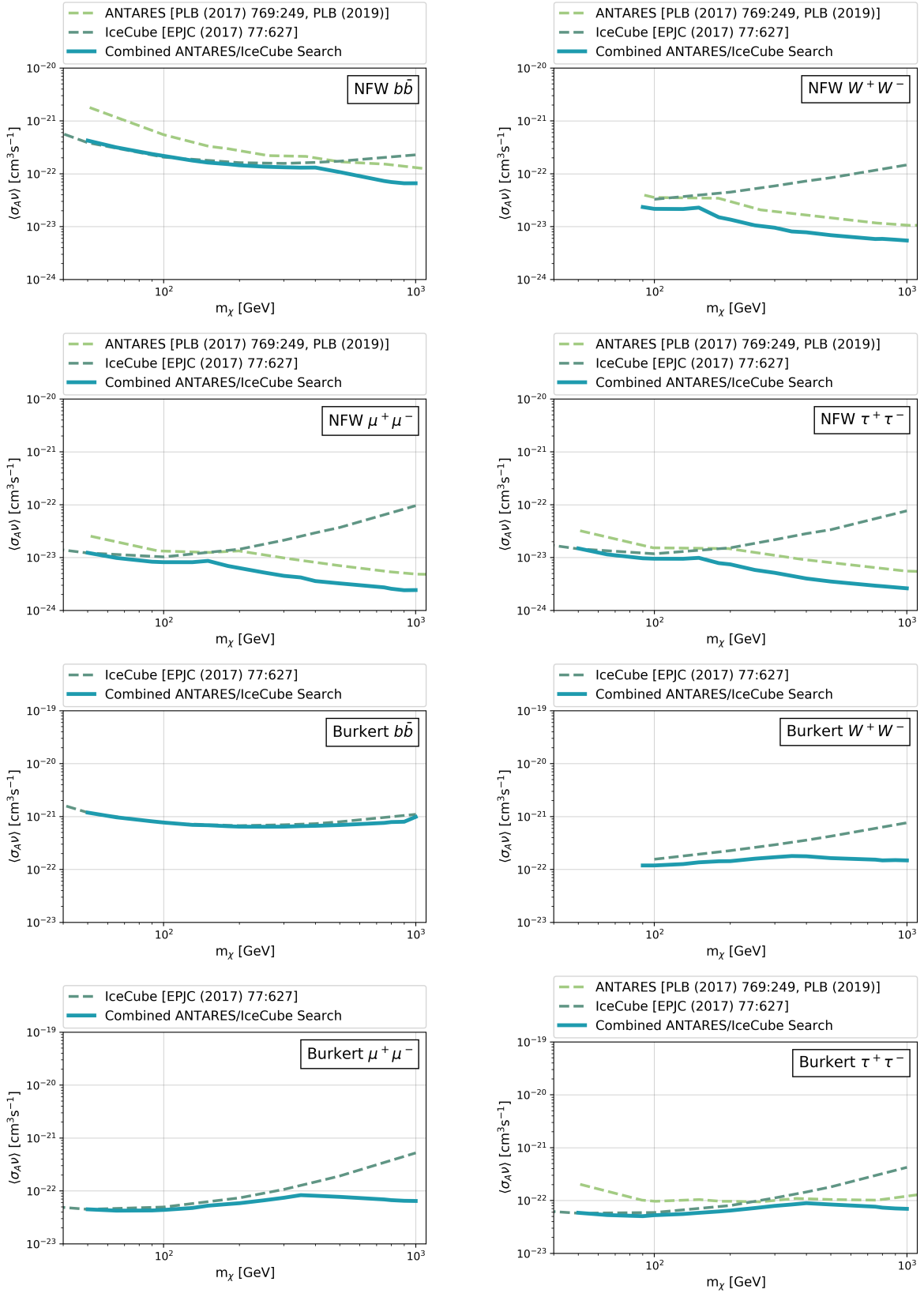


Figure 4.11—Combined 90% C.L. upper limits on the $\langle\sigma_A v\rangle$ compared to the individual limits from ANTARES [118] and IceCube [119] searches.

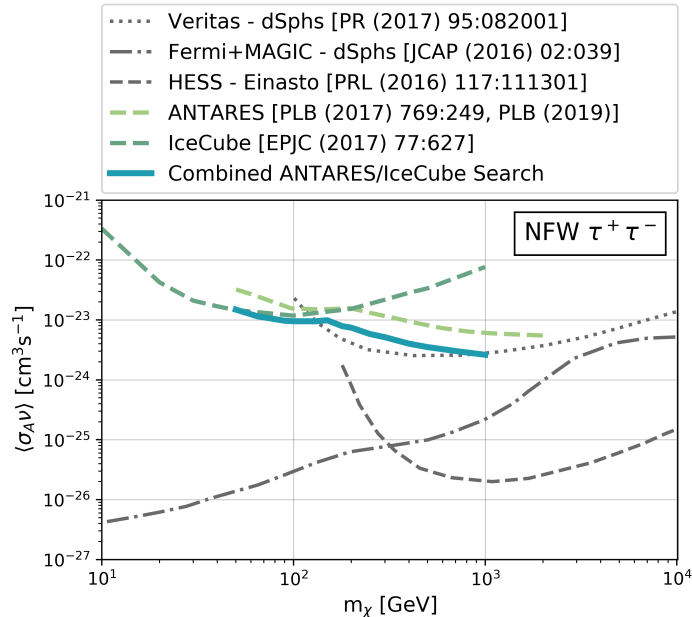


Figure 4.12—Combined 90% C.L. upper limits on $\langle\sigma_A v\rangle$ as a function of the dark matter mass assuming the NFW halo profile and annihilation through $\tau^+\tau^-$. Limits from ANTARES [118], IceCube [119], Fermi+MAGIC [112], H.E.S.S. [110] and Veritas [111] are also shown.

otherwise expect the contribution from IceCube to the combined limit to be small, and for the resulting limit to be similar to that set for the ANTARES-only analysis. Moreover, the combined limits are computed using the Feldman-Cousins method, while the ANTARES limits are obtained using the classical Neyman construction [175]. The λ Fit PDFs used for the combined analysis are also slightly different from the one used for the ANTARES analysis, with a distinct binning and a different cut on the λ quality parameter.

4.8.2 Comparison to other experiments

In Figure 4.12, the combined limit obtained for the $\tau^+\tau^-$ annihilation channel and the NFW halo profile is presented alongside the limits from the previous ANTARES and IceCube analyses from which the data sets used for the combined search are taken. The discussed limits are shown together with the latest limits set by γ -ray experiments in the search for photons from dark matter annihilation through $\tau^+\tau^-$. Unlike the other presented limits, the results from VERITAS and Fermi+MAGIC are not obtained by looking for dark matter annihilation in the Galactic Centre but rather from the study of dwarf spheroidal galaxies (dSphs). Another noticeable difference is that the H.E.S.S. limit is computed assuming the Einasto halo profile. This profile, even though also assuming a high dark matter density towards the Galactic Centre, presents non-negligible deviation from the NFW profile when focusing on a region close to the centre of the dark matter halo. As stated in Subsection 4.7, the biggest source of uncertainty comes from the choice of halo parameters. Although the halo parameters are ensured to

NFW profile – $\langle\sigma_{Av}\rangle [10^{-24} \text{ cm}^3\text{s}^{-1}]$								
m_{DM} [GeV]	90% C.L. sensitivity				90% C.L. upper limit			
	$b\bar{b}$	$\tau^+\tau^-$	$\mu^+\mu^-$	W^+W^-	$b\bar{b}$	$\tau^+\tau^-$	$\mu^+\mu^-$	W^+W^-
50	456	15.6	12.8	—	424	14.9	12.3	—
65	337	12.5	10.6	—	315	11.4	9.8	—
90	251	11.2	9.6	26.7	236	9.7	8.3	23.4
100	232	11.0	9.5	25.6	217	9.5	8.2	21.7
130	195	11.1	9.8	25.4	178	9.5	8.2	21.5
150	181	1.17	10.4	27.2	163	9.9	8.6	22.9
180	169	9.2	8.2	18.0	152	7.8	6.9	15.0
200	163	8.8	7.6	16.7	144	7.4	6.3	13.6
250	156	7.3	6.5	13.6	136	5.8	5.2	10.5
300	154	6.6	5.8	12.4	132	5.1	4.5	9.5
350	152	5.9	5.4	11.1	130	4.5	4.2	8.0
400	153	5.5	4.9	10.6	131	4.0	3.6	7.8
500	127	4.9	4.5	9.6	107	3.5	3.2	6.9
750	92.9	4.2	3.9	8.5	72.9	2.9	2.7	5.8
800	89.2	4.1	3.7	8.5	69.7	2.8	2.6	5.9
900	85.8	3.9	3.6	8.4	66.0	2.8	2.4	5.6
1000	85.3	3.8	3.6	8.1	66.1	2.6	2.4	5.5
Burkert profile – $\langle\sigma_{Av}\rangle [10^{-23} \text{ cm}^3\text{s}^{-1}]$								
m_{DM} [GeV]	90% C.L. sensitivity				90% C.L. upper limit			
	$b\bar{b}$	$\tau^+\tau^-$	$\mu^+\mu^-$	W^+W^-	$b\bar{b}$	$\tau^+\tau^-$	$\mu^+\mu^-$	W^+W^-
50	174	7.2	5.7	—	118	5.9	4.5	—
65	134	6.4	5.2	—	96.8	5.3	4.2	—
90	107	6.1	5.1	14.4	81.2	5.1	4.3	11.9
100	101	6.1	5.2	14.1	77.1	5.3	4.4	11.9
130	89.1	6.4	5.5	14.6	69.6	5.6	4.8	12.6
150	86.4	6.8	6.0	15.5	68.6	5.9	5.3	13.6
180	82.7	7.2	6.6	16.7	65.7	6.2	5.7	14.3
200	80.3	7.6	6.7	17.3	64.5	6.5	5.9	14.4
250	79.0	8.7	8.1	20.3	64.2	7.2	6.7	15.9
300	78.9	9.8	9.3	22.6	64.4	7.9	7.4	17.1
350	80.3	10.7	10.5	23.8	65.9	8.4	8.3	17.9
400	81.3	8.8	8.0	17.9	66.8	8.9	8.1	17.8
500	85.7	8.4	7.9	17.1	69.1	8.4	7.7	16.4
750	95.2	8.0	7.3	16.2	75.9	7.7	6.9	15.3
800	99.5	7.8	7.2	15.8	78.7	7.3	6.7	14.8
900	102.1	7.6	7.1	16.2	79.8	7.1	6.5	15.0
1000	96.6	6.9	7.0	15.9	98.7	7.0	6.5	14.8

Table 4.7: Final 90% C.L. combined sensitivities (left column) and 90% C.L. combined upper limits (right column) in terms of $\langle\sigma_{Av}\rangle$ for the NFW (upper table) and the Burkert (lower table) halo profiles.

be identical for ANTARES and IceCube in order to carry out the combined analysis, the choice of these parameters varies for the other limits. The halo parameters considered for the combined search and the previous ANTARES and IceCube analyses are quite conservative when compared to more optimistic values used by other experiments. The combination of these factors is partially responsible for the difference between limits sets by the combined analysis and more stringent limits presented in Figure [4.12](#).

Chapter 5

Low energy dark matter search with eight years of IceCube data

The previously published low energy search for dark matter annihilation in the Galactic Centre used three years of IceCube data. Since then, more years of IceCube data were released. As a result, this second analysis consists in a search for neutrinos from dark matter annihilation in the Galactic Centre with 8.03 years of IceCube data. In addition to the inclusion of more years of data, this analysis aims to improve the detection potential of such dark matter search by considering an improved event selection targeting low energy. More precisely, this analysis uses an event selection developed as a global effort within the IceCube collaboration and described extensively in Section 5.2. This event selection, known as the oscNext event selection, was initially designed and optimised to perform atmospheric neutrino oscillation measurements. The related Monte Carlo simulations, which are used at several levels of this analysis, are detailed in Section 5.1. In Section 5.3, the properties of this event selection are compared to the IceCube event selection used for the combined search. The weight given to neutrino simulations in order to mimic the signal expectations from dark matter annihilation in the Galactic Centre are specified in Section 5.4, while Section 5.5 summarise the analysis method used for this particular dark matter search. Lastly, the sensitivities obtained for this analysis are reported and discussed in Section 5.6, along with future prospects. Upon non-detection, the goal will be to place stronger limits on the thermally-averaged dark matter self-annihilation cross-section for the Galactic Centre.

5.1 Monte Carlo Simulation

Similarly to the MC sets used for the combined DM search in Chapter 4, the MC simulations considered for this analysis are used for several purposes. Among other things, these simulations are needed in order to estimate both the background and signal expectations of this analysis. Simulations also provide a better understanding of the detector response. The general steps followed to develop these simulation sets are once again following a standard pipeline. First the primary particles, i.e. muons and neutrinos, are generated and propagated. The second step consists in the propagation of the Cherenkov photons created by these particles or their secondaries when travelling

through the ice. Lastly, the response of the DOM is simulated in order to represent the incident photons in terms of hits. During this step, noise is also included. The basic filtering applied at the detector level (L1 and L2) as described in Section 2.8 are also applied in order to match the processing level of the recorded data for further event selection.

5.1.1 Atmospheric muons

Background from atmospheric muons is simulated using the MuonGun MC generator [176]. This software supersedes CORSIKA [138] as it generates atmospheric muons without generating the extensive air showers, making it faster. MuonGun takes several inputs in order to generate the atmospheric muon simulations. The first of these parameters is the spectrum used for the generation of muons. For this sample, a power law with a constant index of -3 and an offset of 150 is considered, for energies ranging from 150 GeV to 5 TeV. A second spectrum is then used in order to reweight the MC events to match the expected atmospheric muons flux. This weighing spectrum is assuming the hadronic interactions to follow the SIBYLL model, while the primary cosmic rays are simulated based on the GaisserH4a model [177]. In addition to these two spectra, an outer volume and an inner volume must be provided to MuonGun. The outer volume consists of a cylinder taken to be slightly larger than the fiducial volume of IceCube, and delimiting the surface on which the muons are generated. These muons are then propagated inwards, such that only muons intercepting the surface of the inner volume, chosen to be a smaller cylinder surrounding DeepCore, are simulated. Another argument taken by MuonGun is the number of events per file, which correspond to the initial number of generated events. A kernel density estimator (KDE) is used to optimise the simulation process [178], such that only the simulated unweighted muons following the target distribution built using the KDE are selected.

5.1.2 Neutrinos

Neutrinos and their interaction products are simulated with the GENIE neutrino MC generator [145] integrated to the IceTray framework. First, the neutrino interaction cross-section for all neutrino flavour and all types of interactions are computed for energies ranging from 0 to 10 TeV. The MC neutrinos are generated assuming a production spectrum following a power law with a constant spectral index of E^{-2} over the entire energy range. The neutrino to anti-neutrino generation ratio, previously referred to as c_{type} , is of 70% to 30%. The events are weighted, according to Equation 4.3, with an atmospheric neutrino flux chosen to be the HKKM2014 flux, also known as Honda 2014 [179]. The generation livetime is also included in this equation for the weighted MC distribution to be available in terms of rate. The MC production is done by energy ranges with specific associated generation volume. These energy ranges, which slightly vary depending on the generated neutrino flavour, are designed to optimise the number of events passing DeepCore L3 filtering while minimising the computational resource requirements.

5.1.3 Particle propagation and light production

The propagation of the MC muons generated by both MuonGun and GENIE is handled with PROPOSAL. The ice properties are treated by a sub-script called mediadef. Electromagnetic and hadronic showers are simulated using GEANT4 for energies below 100 MeV and 30 GeV respectively. For cascade events above these energies, Cherenkov photons are estimated using an internal parametrisation instead of simulating the individual propagation of particles in the cascade. The resulting photon propagation in the ice are then simulated using CLSim according to the geometry encoded in a dedicated GCD file. The response of the detector is emulated with a script specifically developed for the oscNext project. This simulation process is separated in multiple steps relying on, among others, CLSim and Vuvuzela, consecutively. The following steps are the simulation of the PMT response, conducted with PMTResponseSimulator, which is used to evaluate the amount of photo-electrons extracted from the photocathode. The digitisation process performed by the DOM is simulated with the DOMLauncher project, while bad DOMs are excluded with the I3DOMLaunchCleaning.

5.1.4 Noise emulation and detector response

Just like for the combined DM search, the simulation of pure noise events is done with the Vuvuzela package, with which both thermal and non-thermal noise are reproduced. As a reminder, the distribution of the uncorrelated hits from thermal noise are drawn from a Poisson distribution with a uniform time distribution. The correlated hits from non-thermal noise are also sampled from a Poisson distribution, while the relative times between the different hits are sampled from a log-Gaussian distribution. The Vuvuzela software provide information about the simulated noise in terms of MC photo-electrons (MCPEs). Therefore, the output of Vuvuzela still needs to be expressed in terms of charge. The associated charges are sampled from the SPE charge template [180]. From this step, the simulated noise events go through the same simulation procedure as the photons from neutrinos and muons, starting from the optical sensor response.

5.2 Event Selection

In order to perform this low energy dark matter search, the oscNext samples are used. This sample consists of IceCube data recorded from 2012 to 2020. More precisely, this particular event selection focuses on events starting within the volume of the DeepCore sub-detector and contains events with both track and cascade topologies, coming from all directions of the sky. The event selection considered for this analysis can be divided in several stages starting from the level common to the entire collaboration, i.e. Level 2. In this section, the various cuts and reconstructions applied at each level of the oscNext event selection are described. Up to level 6, the cuts used for this particular analysis are unchanged with respect to the global oscNext event selection. However, some changes have been made to the cut applied at the last level of the event selection, i.e. level 7.

Cut	Selection criteria
I	DeepCore filter conditions are met
II	Cut on SLOP trigger events
III	Cut on events with flaring DOMs

Table 5.1: Summary of the cuts and selection conditions applied at level 3.

5.2.1 Level 3

The main purpose of the selection performed at this level is to reduce the background contribution by applying a variety of simple cuts, which are listed in Table 5.1. To this end, the DeepCore L3 filter is used, allowing to remove a considerable part of the muon and noise events. With this filter, the fiducial volume is reduced to the bottom 22 DOMs of the 7 IceCube strings surrounding the DeepCore strings (26, 27, 35, 36, 37, 45, 46) and the bottom 50 DOMs on the DeepCore strings (79, 80, 81, 82, 83, 84, 85, 86). The rest of the DOMs present in the detector constitutes the veto region. The basic principle of this filter is that events are classified as possible atmospheric muons if light is first detected in the veto region, while pure noise events are identified based on the number of occurrences and their arrival time. In addition to the cuts related to the DeepCore L3 filter, a cut on slow particle (SLOP) trigger events is applied. This cut is introduced since some events fulfilling the conditions of the DeepCore L3 filter are contained within the long time window of SLOP trigger events. As the aim of this trigger is to select slow-moving particles, such as monopoles, their typical time window length is of the order of 500 μ s and up to a few ms. Since these events are not properly accounted for in the simulation sets, they need to be rejected as they might lead to a poor agreement between MC and data events. Events containing flaring DOMs are also removed from the event selection. A DOM is considered to be flaring when only that particular DOM records a significant charge over a short period of time. The flaring DOM effect is expected to result from phenomena happening within the DOM itself, such as thermal noise from electronics, rather than be caused by neutrino or muon events. The cuts applied at L3 remove around 93% of the atmospheric muon background, while keeping about 62% of the neutrino events. The selection criteria also result in a reduction of more than 99% of the background from pure noise events. The selection efficiency of neutrinos varies depending on their energy and flavour. For neutrino energies between 10 and 100 GeV, the efficiency is of about 70%, while events with higher energies can be wrongly rejected due to cuts based on light detection in the veto region, especially for muon neutrinos. For lower energies, the efficiency is reduced by cuts intending to remove pure noise hits. The highest efficiency is obtained for tau neutrinos with about 67%, while the electron neutrinos have the lowest efficiency with \sim 58%.

5.2.2 Level 4

The cuts applied at L4, shown in Table 5.2, rely on machine learning methods to distinguish between background and signal events. Two separate classifiers are used,

Cut	Selection criteria
I	L4 noise classifier > 0.7
II	L4 muon classifier > 0.65

Table 5.2: Summary of the cuts and selection conditions applied at level 4.

one of which aims to pick muon events out, while the second focuses on the identification of pure noise events. The LightGBM machine learning algorithm used is used for both classifiers [181]. This algorithm is based on Gradient Boosting Decision Trees (GBDTs), which consists of tree-like constructions boosted by fitting the negative gradients. The supervised training of the BDT is handled with two separate data sets used to consecutively train and test the BDT models. For the muon classifier, parts of the detector data is considered as background to train the BDT since atmospheric muons makes up around 99% of the data at this selection level. On the other hand, the GENIE MC set is used as the signal training set. The noise classifier is trained on Vuvuzela simulations for background and GENIE simulations for signal. The fraction of the MC samples used for training is $\sim 33\%$, while the remaining part is used as the verification set. About 40 variables were initially considered for the BDT, among which ten are used for the muon classifier and five for the noise classifier. The two classifiers provide scores between 0 and 1, giving the probability of the event to be a neutrino. The cut applied on the output of the muon classifier is only selecting events with a score above 0.65. This cut suppresses $\sim 94\%$ of the background contribution from atmospheric muon, while preserving $\sim 87\%$ of the neutrinos. From the noise classifier, only events with a score above 0.7 are kept in the sample. The resulting background from pure noise events is reduced by about two orders of magnitudes. The selection efficiency of neutrinos once again depends on the flavour, with up to over 92% for the CC interactions of tau neutrinos. The lowest efficiency is observed for CC interactions of muon neutrinos with $\sim 82\%$.

5.2.3 Level 5

The L5 selection aims at discarding more atmospheric muons from the selection in order for the neutrino contribution to prevail. The SPEFit reconstruction algorithm is also run at this level. This infinite track reconstruction is, among other things, used as a seed for further reconstruction applied in the following levels of the event selection. The cuts applied at this level follow two guidelines, namely the selection of events starting in the fiducial volume and the removal of muons sneaking in the detector, as seen in Figure 5.3. The first type of cuts are referred to as starting containment cuts and have for purpose to exclude events which started near or outside the boundaries of the DeepCore volume. Following this idea, a radial containment condition is introduced, which is fulfilled if events fall within a certain radius of string 36 located at the centre of DeepCore. This maximum radial distance is set to be $\rho_{36}=150$ m. For this, three distinct ways to estimate the vertex are considered, being the position of the first HLC, the L3 vertex estimate and the position of the brightest string. The vertical containment is also evaluated by rejecting events for which the interaction vertex falls

Cut	Selection criteria
I	$\rho_{36} < 150$ m
II	$z_{\text{reco}} = [-490, -220]$
III	Corridor cut hits ≤ 2
IV	L4 noise classifier > 0.85
IV	L4 muon classifier > 0.9

Table 5.3: Summary of the cuts and selection conditions applied at level 5.

outside $z = [-490, -220]$ m. Only the first HLC and the L3 vertex estimate are considered here as the position of the brightest string does not provide information about the vertex position in z . Sneaky muons are discarded through corridor cuts, named after the corridors through which muons can travel through the veto region without triggering any DOM. After computing the centre of gravity of each event and pinpointing the closest DeepCore string, the orientation of the poorly instrumented corridors leading to this particular string are identified. The algorithm then proceeds to search for hits along the associated corridors occurring within a specific time window, set to $[-1000, 1000]$ ns, and contained in a cylinder of radius $R = 250$ m. The event is rejected if more than two hits are recorded in these corridors, except if the angular distance between the track direction reconstructed with SPEFit and the corridor is below 0.7 rad. For the latter scenario, the corridor hits might be caused by noise events in coincidence with a neutrino event rather than by a sneaky muon. In addition to these cuts, a hardening of the classifier cuts applied at L4 is also implemented. This translates into a selection of score above 0.85 for the noise classifier and above 0.9 for the muon classifier. The combination of these cuts, summarised in Table 5.3, enable to obtain a dominant contribution of neutrino over atmospheric muons in the sample, with a ratio of about two to one. From this level onwards, two separated event selection are conducted. Out of these two event selections, this analysis uses the data sets known as the high statistic sample, for which two additional selection levels are processed.

5.2.4 Level 6

The final event reconstruction algorithm is run at this level. This more advanced event reconstruction, called RetroReco, is a table-based algorithm optimised for the reconstruction of DeepCore events. The RetroReco algorithm works similarly to the other table-based algorithms described in Chapter 4, except that the related photon tables are built as if PMTs were emitting light. That way, the emitter and receiver roles are inverted, under the assumption that scattering and absorption phenomena are symmetric in time. The Retro photon tables are generated from CLSim according to the Spice-Lea ice model. As running RetroReco is resource intensive, with an average of 40 s per event, each event is only reconstructed once with this algorithm. RetroReco is used to reconstruct a total of eight variables, namely the electromagnetic cascade energy, the track length and orientation, as well as the interaction vertex position and time. In RetroReco, each event is assumed to have both a track and cascade component, which

Cut	Selection criteria
I	SPE charge > 0.25 PE
II	Pre-cleaning pulses > 8
III	RetroReco fit status == True
IV	RetroReco iterations > 10

Table 5.4: Summary of the cuts and selection conditions applied at level 6 for the high statistic samples.

are simulated separately. Tracks are emulated as a succession of collinear Cherenkov emitters exhibiting a constant luminosity, while cascades are simulated with only one Cherenkov emitters located at the interaction vertex and the same direction as the muon track. The only cuts applied at L6 are linked to the reconstruction quality of the events. Prior to running RetroReco, a cut on the charge of the pulse series is applied, removing all charges below 0.25 PE (see Table 5.4). As the event hypothesis of RetroReco has eight degrees of freedom, events for which less than eight recorded pulses are removed. This results from the fact that the number of pulses are used as a rough estimate of the amount of information available per event. In addition to RetroReco, the SANTA track reconstruction algorithm is also applied to the sample for comparison purposes. SANTA is based on the QFit algorithm initially developed by the ANTARES collaboration [157]. Thanks to causality cuts, SANTA only uses direct pulses, i.e. pulses caused by unscattered photons. As direct pulses are the least affected by the ice properties, they constitute the most reliable hits for event reconstruction. At least five direct pulses are required by SANTA to perform the track reconstruction.

5.2.5 Level 7

Further cuts dedicated to atmospheric muon rejection are applied at L7 using the variables reconstructed at L6, which are summarised in Table 5.5. The cuts applied at this level slightly diverge from the ones performed for the official oscNext samples. Namely, two cuts are removed with respect to the global oscNext event selection. The first cut to be discarded for this analysis is only selecting events with energies between 5 GeV and 300 GeV. This cut is eliminated in order to extend the range of dark matter masses that can be probed for this analysis. As discussed in Section 5.4, signal expectations from the annihilation of dark matter particles with masses ranging from 5 GeV to 8 TeV are scanned, depending on the considered annihilation channel. The second discarded cut is on the zenith angle and keeps events for which the reconstructed zenith angle satisfies $\cos \theta_{\text{reco}} \leq 0.3$. As this analysis focuses on events coming from the Galactic Centre, which is located above the horizon of IceCube, this cut could simply not be kept since it removes down-going events. Therefore, events coming from all directions of the sky are included in the final event selection used for this low energy dark matter search, with energies between 5 GeV and 8 TeV. The remaining cuts described in this section are identical to the one applied for the official oscNext event selection.

In order to further reduce background from atmospheric muons, a classifier based

Cut	Selection criteria	Cut	Selection criteria
I	L7 muon classifier > 0.4	V	Direct pulse multiplicity > 3
II	L4 Noise classifier > 0.95	VI	$N_{\text{top15}} < 3$
III	$-500 \text{ m} < z_{\text{reco}} < -200 \text{ m}$	VII	$N_{\text{outer}} < 8$
IV	$\rho_{36} < 300 \text{ m}$	VIII	Reconstructed time $< 14\,500 \text{ ns}$

Table 5.5: Summary of the cuts and selection conditions applied at level 7.

on LightGBM is trained at L7 from the quantities reconstructed with RetroReco or additional variables built from those. This way, the reconstructed vertical position of the vertex, z , is used along the radial distance of the vertex from string 36, ρ_{36} . These variables provide an important separation power as sneaky muons are expected to have an interaction vertex close to the borders of the fiducial volume while the vertexes of events originating from a neutrino interaction would be spread over the entire DeepCore volume. The classifier also takes into consideration the separation angle between the direction reconstructed with SANTA and RetroReco. The second of variable built from RetroReco outputs indicates which of the corridor hits have the lowest position in z . Finally, the output of the L4 muon classifier is also used as an input of the new muon classifier. As with the classifier used at L4, a score indicating the probability that the event to be caused by a neutrino, ranging from 0 to 1, is provided by the muon classifier of L7. Only events with a score above 0.4 are kept in the final event selection. This cut remove about 81% of the remaining atmospheric muons, while keeping more than 88% of the neutrino events. In order to reduce the contribution from noise to a negligible level, a stronger cut on the score given by the L4 noise classifier is set, such that only events with a score above 0.95 are kept.

The quantities reconstructed with RetroReco are also useful for the computation of the particle ID (PID), which provide an indication of the topology of the events. The distinction between cascade and track provide some information about the flavour of the event. As mentioned in Section 2.5, the CC interactions of muon neutrinos and, in about 17% of the cases, tau neutrinos will result in track-like events, while the remaining neutrino interactions will lead to cascade-like events. Various variables, such as the reconstructed track length and cascade energy, are used as input for the PID computation. The length of the track is the best indication of how similar an event is to a track. The longer the track, the more probable it is for the event to be a track. The cascade energy provides the proportion of light deposited in the cascade part of the reconstructed RetroReco event. In addition to the reconstructed variables listed in Sub-section 5.2.4, RetroReco also provide a variable carrying information on the probability of the shape of the event to be described by a track, which is also used as input for the PID calculation. This information is obtained by performing the same fit but with the track length set to zero, leaving only the remaining seven parameters free. If the log-likelihood (LLH) output of the seven-parameter fit is worse than the one of the standard eight-parameters fit, it indicates that the track component is necessary to explain the shape of the event. The last two input parameters are the reconstructed zenith and its related uncertainty. This is because the performance of

the event identification is expected to have a zenith dependence caused by the instrumentation geometry. Meanwhile, since a better angular reconstruction is expected for track, a small uncertainty on the reconstructed zenith is another indicator of a track-like event. The BDT used to compute the PID is trained on events with a L7 muon classifier score equal to or above 0.3. The training samples for tracks and cascades are respectively given by the CC interactions of muon (anti-)neutrinos and electron (anti-)neutrinos, for energies between 5 and 500 GeV. The weights associated to these events are obtained from the Honda2014 flux without including neutrino oscillations. The BDT provide a PID score taking values ranging between 0 and 1. PID values close to 0 indicate a cascade-like event, while values near 1 suggest that the event is track-like. Besides the cuts listed above, some containment cuts are also applied at this level. Radial containment is once again ensured through a cut on the distance between the central DeepCore and the reconstructed vertex, $\rho_{36} < 300$ m, while the vertical containment conditions requires $-500 \text{ m} < z_{\text{reco}} < -200$ m. A cut based on direct pulses is also applied at this level, requiring at least 3 DOMs to observe direct pulses. Such requirements further reduce background from muon and noise events. As events with little recorded direct pulses are subject to large reconstruction uncertainties, this cut reduces the contribution from poorly reconstructed events. Two cuts are implemented with the purpose to get rid of coincident events. The events resulting from the coincident arrival of a muon and a neutrino in the detector volume are not simulated in the MC samples. To reject coincident events, the cuts focus on removing events for which a significant charge is recorded by DOMs located in the outermost ($N_{\text{outer}} < 8$) and uppermost ($N_{\text{top15}} < 3$) regions of IceCube. Finally, late events are also removed by requiring the reconstructed time to be below 14 500 ns.

5.3 Effective area

In this section, the effective area corresponding to the OscNext event selection is presented. The surface area covered by this hypothetical perfect detector is computed from MC simulations. For this, the MC events weighted with the weight containing information about the detector response, known as OneWeight, is filled into a histogram logarithmically binned in neutrino energy, E_ν . The values of each bin are then corrected for their width in energy and solid angle. Figure 5.1 compares the neutrino effective area of the OscNext event selection (solid purple line) to the one obtained with the event selection used for the combined analysis presented in Chapter 4 (dashed blue line), which was developed for the latest published dark matter search in the Galactic Centre with three years of IceCube data [119]. As both analyses focus on the central region of the Milky Way, only events with declinations between $\delta_{\text{GC}} - 30^\circ$ and $\delta_{\text{GC}} + 30^\circ$ are considered in order to provide a fair comparison. The effective area of the event selection considered for this analysis shows clear improvement over the effective area of the data set used for both the combined DM search and the prior IceCube-only DM search in the GC. The enhancement is particularly important for the lowest energies where one order of magnitude improvement can be seen.

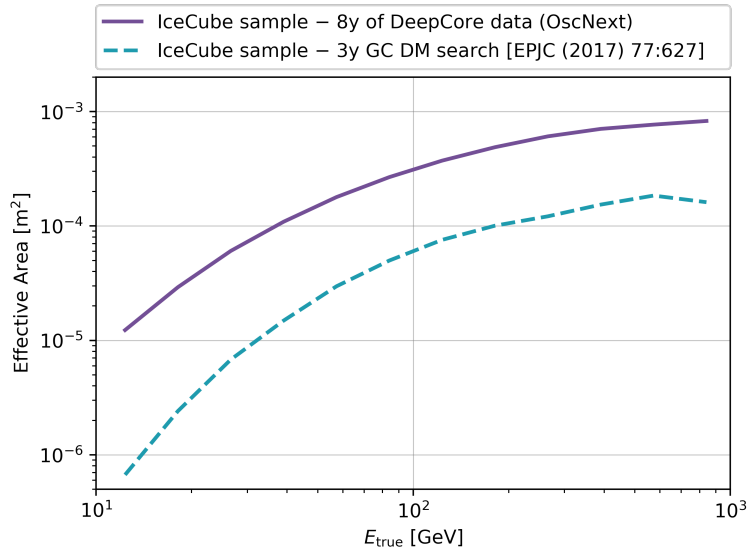


Figure 5.1—Comparison of the neutrino effective area obtained with the OscNext event selection (described in Section 5.2) and the IceCube sample used for the combined DM search presented in Section 4.3 for declinations ranging from $\delta_{\text{GC}} - 30^\circ$ to $\delta_{\text{GC}} + 30^\circ$.

5.4 Signal Expectation

In this section, the ingredients used to weight the MC neutrino samples in order to mimic the signal expectation from dark matter annihilation are described. This particular analysis focuses on low energies with an extended DM mass range going from 5 GeV to 8 TeV. In addition to the four annihilation channels considered for the combined DM search, dark matter annihilation through the three neutrino flavours are also taken into account. As a result, dark matter annihilation through seven channels, namely W^+W^- , $\mu^+\mu^-$, $\tau^+\tau^-$, $b\bar{b}$, $\nu_e\bar{\nu}_e$, $\nu_\mu\bar{\nu}_\mu$ and $\nu_\tau\bar{\nu}_\tau$, are tested separately with an assumed B.R. of 100%. The corresponding neutrino spectra from DM annihilation are taken from the PPC4 tables [168]. Neutrino oscillation is accounted for with the values of the mixing angles and squared mass differences presented in Table 1.1. The resulting muon neutrino spectra at Earth are visible in Figure 5.2 for dark matter annihilation through the seven channels considered and dark matter masses of 100 GeV (left panel) and 1 TeV (right panel). As mentioned in Section 4.4, the spectra encoded in the PPC4 tables are computed with PYTHIA 8.1 with an implementation of the EW corrections according to the guidelines provided in [170]. The inclusion of the EW corrections have for effect to boost the messenger fluxes at low energies when considering dark matter masses well above the mass of the W and Z bosons. This effect is clearly visible when comparing the two plots shown in Figure 5.2, especially for the neutrino channels. In the PPC4 tables, EW corrections are only included when considering dark matter masses above 100 GeV as this effect is only expected to be significant for dark matter masses well above the mass of the W and Z bosons. Therefore, the left panel of Figure 5.2 show spectra computed without EW corrections as dark matter particles with masses of 100 GeV are considered to simulate these spectra, while this

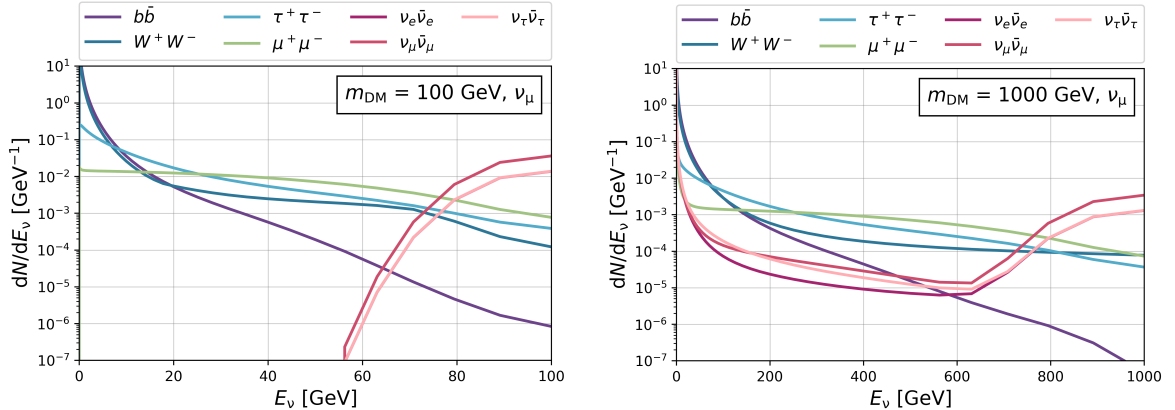


Figure 5.2—Expected neutrino spectra at Earth for dark matter annihilation through the four channels considered and dark matter masses of 100 GeV (left) and 1 TeV (right).

effect is accounted for in the right panel, which displays the spectra obtained for a dark matter mass of 1 TeV. In the following, let us focus on the PPC4 spectra for the neutrino annihilation channels, i.e. $\nu_e\bar{\nu}_e$, $\nu_\mu\bar{\nu}_\mu$ and $\nu_\tau\bar{\nu}_\tau$ for which the effect of the EW corrections is particularly noticeable. Without EW corrections (up to 100 GeV), the neutrino signal from dark matter annihilation into one of the neutrino channels is expected to take the form of a monochromatic line showing at energy equivalent to the simulated DM mass. In the PPC4 tables, these lines, often referred to as monochromatic neutrino lines, are artificially broadened by a Gaussian in order to account for the resolution of neutrino telescopes. This broadening, which is performed so that the total neutrino flux is preserved, is also necessary for the computation of EW correction at higher energies. It is therefore visible both in the left and right plots of Figure 5.2. For dark matter masses above 100 GeV, EW corrections come into play. These corrections are responsible for the low energy tail seen in the neutrino spectra from dark matter annihilation into the three neutrino channels, as noticeable in the right panel of Figure 5.2. Although less distinguishable, similar effects are present at low energies for the other dark matter annihilation channels displayed in these plots.

The halo profiles considered for this analysis are the same as for the combined DM search, namely the NFW and Burkert profile formulations discussed in Section 3.4. Once again, the J-factors computed with CLUMPY using the halo parameters values shown in Table 3.1 are considered. As a reminder, the considered J-factors are shown in Figure 3.9 for both the NFW and the Burkert profiles.

All combinations of DM mass, annihilation channel and halo profile were initially considered. As MC simulations are used to estimate the background in this analysis, the expected signal combinations for which the majority of signal lies outside the energy response of the detector are excluded. In practice, this is implemented by computing the weighted median of the distribution in reconstructed energy, E_{reco} , for each expected signal association. Whenever the resulting median is above the upper bound of the region containing 95% of the energy response of the detector, the corresponding signal combination is discarded. The procedure is illustrated in Figure 5.3, where the

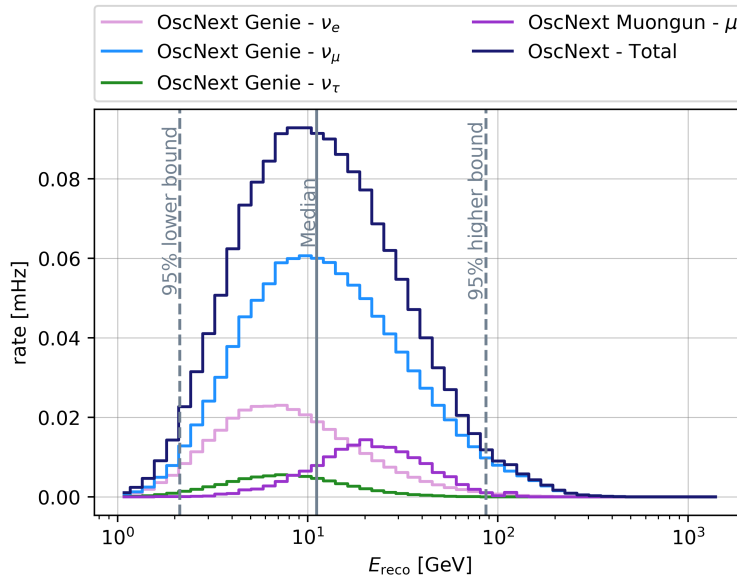


Figure 5.3—Distribution of the background events as a function of the reconstructed energy, E_{reco} . The weighted contributions from the different MC samples are shown along the total background distribution. The weighted median is shown along the lower and upper bound containing 95% of the background.

lower and upper bound of this region are shown as dashed grey lines. The individual contributions of the three flavours of atmospheric neutrinos and atmospheric muons are shown along the total energy distribution. The combinations of dark matter masses and annihilation channels scanned for this analysis are summarised in Table 5.6. As visible in this table, the selected mass range for hard channels, such as the three neutrino channels, is limited to masses below 200 GeV. On the contrary, for softer channels like $b\bar{b}$, higher DM masses can be scanned.

5.5 Analysis Method

Similarly to the combined dark matter search, the aim of this analysis is to look for an excess of signal neutrino coming from the direction of the Galactic Centre. For this, a binned likelihood method is considered, which compares the data to what is expected from the signal and background distributions. When building our probability density functions, the energy and the neutrino flavour are considered along the angular information.

5.5.1 Probability density functions

The PDFs considered for this analysis take the form of three-dimensional binned distribution of the events. In previous GC dark matter searches, the two-dimensional histograms used as PDFs only contained information about the direction of the neutrino, namely the right ascension and the declination of the events. In this work, the

Mass [GeV]	W^+W^-	$b\bar{b}$	$\mu^+\mu^-$	$\tau^+\tau^-$	$\nu_e\bar{\nu}_e$	$\nu_\mu\bar{\nu}_\mu$	$\nu_\tau\bar{\nu}_\tau$
5	✓	✓	✓	✓	✓	✓	✓
10	✓	✓	✓	✓	✓	✓	✓
30	✓	✓	✓	✓	✓	✓	✓
50	✓	✓	✓	✓	✓	✓	✓
70	✓	✓	✓	✓	✓	✓	✓
90	✓	✓	✓	✓	✓	✓	✓
100	✓	✓	✓	✓	✓	✓	✓
200	✓	✓	✓	✓	✓	✓	✓
400	✓	✓	✓	✓	✗	✗	✗
600	✓	✓	✓	✓	✗	✗	✗
800	✓	✓	✓	✓	✗	✗	✗
1000	✓	✓	✓	✓	✗	✗	✗
1500	✓	✓	✗	✓	✗	✗	✗
2000	✓	✓	✗	✓	✗	✗	✗
3000	✓	✓	✗	✓	✗	✗	✗
4000	✓	✓	✗	✓	✗	✗	✗
5000	✓	✓	✗	✗	✗	✗	✗
6000	✓	✓	✗	✗	✗	✗	✗
8000	✓	✓	✗	✗	✗	✗	✗

Table 5.6: Summary of the dark matter mass and annihilation channel combinations scanned for the dark matter search in the GC with 8.03 years of DeepCore data.

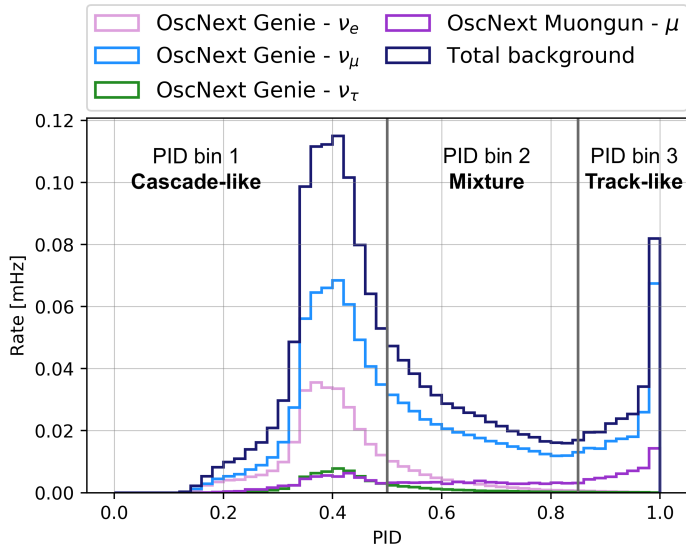


Figure 5.4—Event distribution with respect to the particle ID. The weighted contributions from the different MC samples are shown along the total background distribution. The separations of the PID bins are indicated by the vertical grey lines.

reconstructed energy and neutrino flavour are considered along the reconstructed direction of the events. Information about the neutrino flavour is included in the PDFs through the particle ID (PID). Although it is not possible to clearly identify the flavour of the neutrinos interacting within the IceCube volume or in its surroundings, some information can be retrieved from the topology of the observed event. As specified in Section 2.5, track events result mainly from the CC interaction of muon neutrinos, while cascade events can originate both from the NC interaction of all neutrino flavours, and the CC interaction of electron and tau neutrinos. The event topology of each event is identified through a score known as the PID, which is allocated by a BDT as described in subsection 5.2.5. In this analysis, the PID is used to make the distinction between cascade-like and track-like events. As a result, the three dimensions of the considered event distributions are: the opening angle to the GC (Ψ), the reconstructed energy (E_{reco}) and the PID.

Since the PDFs do not only contain angular information, the background distribution can not simply be obtained by scrambling data in RA as it is done for the combined dark matter search (see Sub-section 4.6.1). Therefore, the background PDF is constructed from simulation weighted with atmospheric flux expectations, according to Equation 4.3. The atmospheric flux is chosen to be the Honda2014 flux, while neutrino oscillations are applied with the NuFit v2 package [182, 183]. Since three dimensions are considered when building the event distribution, the number of bins in the three-dimensional PDFs will quickly raise with the number of bins considered for each dimension separately. This important number of bins could lead to a small or null number of events falling in some bins. Yet, it is important to avoid the presence of empty bins in the background distribution in order to compute the sensitivities.

Kernel density estimation

In order to get smooth distributions of the background and signal events, as well as to avoid empty bins in the background PDF, a kernel density estimation is applied to build the probability density functions. On the contrary of histograms, using a KDE provide a smooth evaluation of the PDF. The basic principle of the KDE is to approximate each point in the sample by a specific distribution centred around that particular point. The kernel estimate of the unknown probability density function $f(x)$ can be obtained as follows [184]:

$$\hat{f}(x) = \frac{1}{n} \sum_{i=1}^n K(x_i, x), \quad (5.1)$$

where K is the kernel function estimated at each point x_i of the sample from which the PDF is evaluated and n is the size of the sample. The kernel function must be positive and normalised to one. Both symmetrical and asymmetrical functions can be considered as kernel. When assuming the kernel function to be symmetric, one can rewrite Equation 5.1 as the middle term of the following expression:

$$\hat{f}(x) = \frac{1}{nh} \sum_{i=1}^n K\left(\frac{x_i - x}{h}\right) = \frac{1}{nh} \sum_{i=1}^n \frac{1}{\sqrt{2\pi}} e^{-\frac{1}{2}\left(\frac{x_i - x}{h}\right)^2}, \quad (5.2)$$

which correspond to the definition of the KDE, where the right-hand expression corresponds to the use of a Gaussian kernel. The level of smoothing applied on the sample is determined by the parameter h , which is known as the bandwidth or the smoothing parameter. As a Gaussian kernel is chosen for this analysis, each point of the sample is approximated by a normal distribution. When considering symmetrical kernels, the choice of the kernel shape has little influence on the final estimate. However, the choice of the bandwidth is crucial as a small value of h might lead to irrelevant characteristic of the sample to be represented in the PDF and thus an under-smoothing of the initial distribution. On the contrary, over-smoothing might occur when a large value of h is selected, resulting in valuable features of the initial event distribution to be lost.

For this analysis, the KDE method is applied on the two-dimensional distributions of the events in terms of the opening angle, Ψ_{reco} , and the energy, E_{reco} . This is done separately for each bin in PID. The edges of the PID bins are chosen to optimise the separation between track and cascade events (see the PID distribution above). The resulting binning is shown in Figure 5.4 and consists of three bins with the edges defined as $[0, 0.5, 0.85, 1]$. As previously mentioned, events with PID values close to zero are expected to be cascade-like while PID values close to 1 indicate track-like events. This implies that the first bin ranging from 0 to 0.5 contain the cascade-like events, while the bin with edges taking the values 0.85 to 1 holds track-like events. The middle bin is a mixture of both cascade and track-like events, consisting of events for which the distinction is not clear.

Since Ψ_{reco} is defined over the range $[0^\circ, 180^\circ]$ and an important signal contribution is expected towards the centre of the GC, i.e. $\Psi_{\text{reco}} \sim 0^\circ$, special attention needs to be paid to this region when building the KDE. Approximating the points of the sample by normal distributions might cause part of the estimated function to escape

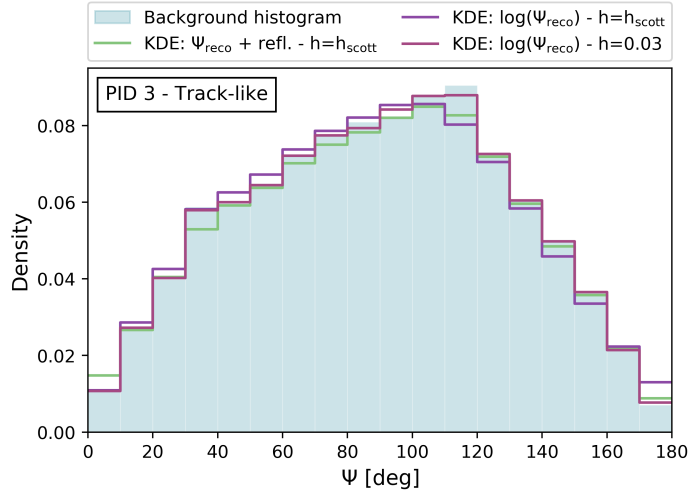


Figure 5.5—Projections of the background PDF for third PID bin in Ψ_{reco} when no KDE is applied (shaded blue) compared to the PDF obtained with KDE built in $\log(\Psi_{reco}) - \log_{10}(E_{reco})$ with bandwidth computed with the Scott’s rule of thumb (purple) and the cross-validation method (pink), along with the KDE built in $\Psi_{reco} - \log_{10}(E_{reco})$ with boundary reflection (green).

outside the evaluation range. This is especially true when many events fall next to the edges of the evaluation range, which is the case for the event distribution in Ψ_{reco} close to zero. Furthermore, the range over which Ψ_{reco} is evaluated is also the definition range of this variable, implying that the function would then exist outside its definition range, by for instance taking negative values. Evaluating the KDE in $\log(\Psi_{reco})$ rather than in terms of Ψ_{reco} , avoids this issue altogether, while still providing an accurate evaluation of the distribution for $\Psi_{reco} \sim 0^\circ$. This is illustrated in Figure 5.5, where the projection in Ψ_{reco} of the normalised histogram of the background events (shaded blue) is compared to several PDF estimations obtained with various assumptions for the KDE method. In particular, this figure shows the projection of the background PDF evaluated with a KDE built in Ψ_{reco} and for which the event distribution escaping outside the boundaries is simply reflected (represented in green). This reflection is performed in order to include the eventual non-null values obtained when evaluating the kernel estimate outside the considered range, i.e. for values of Ψ below 0° and above 180° , following the issue discussed above. For this, the binning of the PDF is performed over a broader range of $\Psi \in [-40^\circ, 220^\circ]$. The content of the bins falling outside the definition range of Ψ are then added to the mirroring bins inside $[0^\circ, 180^\circ]$, such that the boundaries seem to act as mirrors. In particular, the content of bin $-i$ is added to bin i , assuming the boundary at 0° to draw the line between negative and positive bins. Although the effect is less problematic for higher values of Ψ , the same operation is applied for the boundary at 180° . The PDF obtained with this method provides a worse description of the background shape for events close to the Galactic Centre, i.e. for Ψ_{reco} close to zero, than the PDFs evaluated with the two KDEs built in $\log(\Psi_{reco})$ (in purple and pink). This is visible in the first bin of the PDF projection, which is over-evaluated with the KDE using boundary reflection. On the contrary,

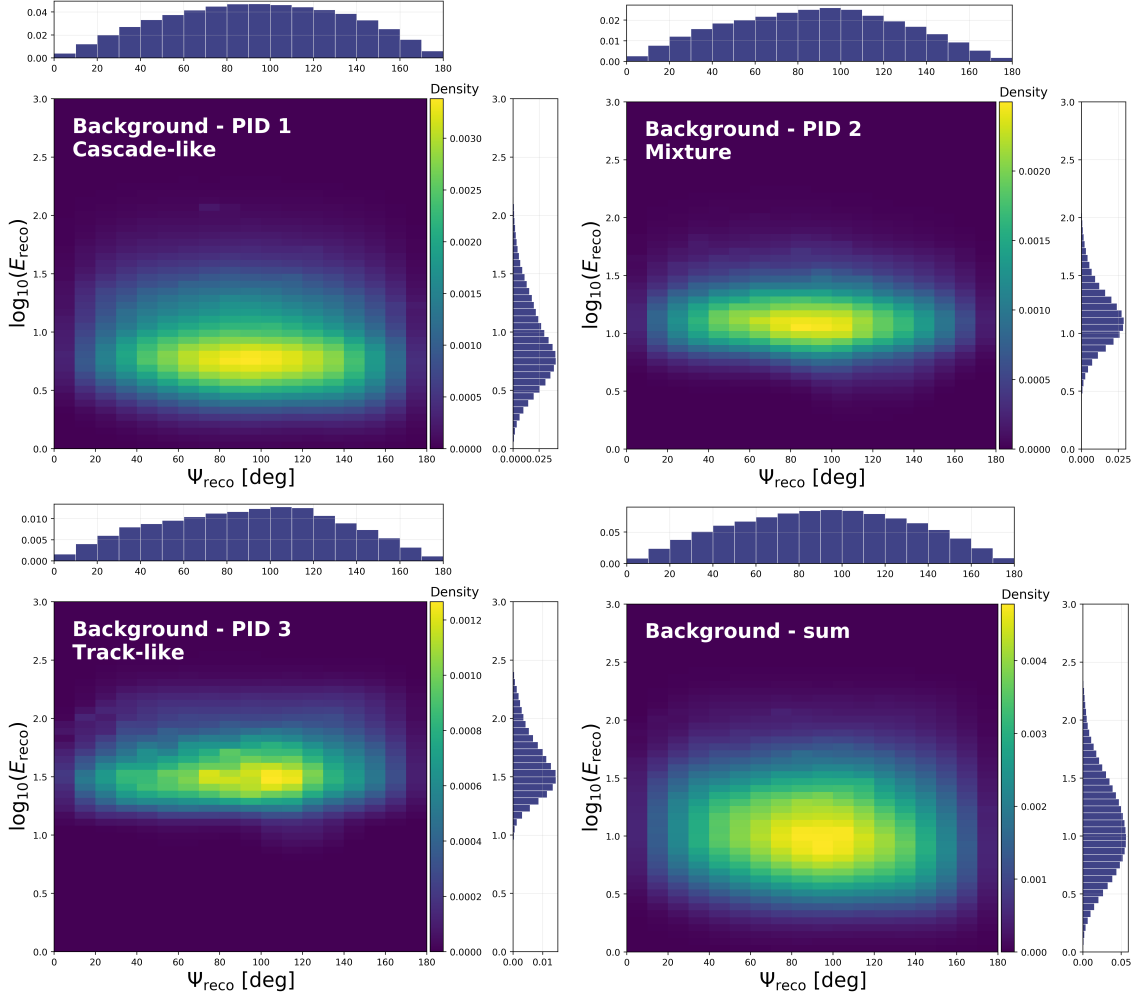


Figure 5.6—Three-dimensional background PDF split into the individual contributions of each of the three PID bins. The bottom right histogram shows the 2D projection of the events in Ψ_{reco} and $\log_{10}(E_{\text{reco}})$. The colour scale expresses the probability density.

the KDEs built in $\log(\Psi_{\text{reco}})$ provide an accurate estimation of this first bin in Ψ_{reco} . Similarly, the distribution of the events in energy is evaluated in $\log_{10}(E_{\text{reco}})$, which fall considerably at the borders of the evaluation range.

Background PDF

To estimate our background probability density function, the KernelDensity method implemented in the Scikit-learn package is used [185]. This method includes the consideration of weights in the kernel estimation and a wide choice of kernels. In order to find the optimal bandwidth to compute the PDFs, a cross-validation method is used [186]. Although not directly implemented in the kernel function, such cross-validation method is available in the Scikit-learn package. The built-in function consists in a cross-validated search over a grid of possible bandwidth values. The best estimate

of the bandwidth, i.e. the bandwidth providing the best description of the sample while avoiding under or over-smoothing, is obtained through likelihood maximisation. More specifically, a K-fold cross-validation method is used. With this method the sample is divided into K "folds", K-1 of which are used to train the algorithm while the remaining fold is used for testing. This process is repeated K times, with each time a new training set, and the final result of the cross-validation is given by the average of the results obtained at each iteration. For this analysis, the default cross-validation method of Scikit-Learn was used, for which K is set to 5. The bandwidth obtained with this cross-validation method is $h = 0.03$. In Figure 5.5, the KDE obtained with this bandwidth is compared to KDEs for which the smoothing bandwidth is computed with Scott's rule of thumb. This rule provides an estimate of the bandwidth given by $h_{\text{scott}} = n^{-1/(d+4)}$, where n is the number of points in the sample and d is the number of spatial dimensions, i.e. $d = 2$ in this particular case. Although providing a fast evaluation of the bandwidth, this rule assumes the underlying distribution to be unimodal and often leads to over-smoothing. This over-smoothing of the event distribution with h_{scott} is particularly visible for the bins between 80° and 140° of the background PDF projection.

Using this package, the kernel estimate is evaluated for each PID bin from the two-dimensional distribution of the events in $\log(\Psi_{\text{reco}})$ and $\log_{10}(E_{\text{reco}})$. The function is then evaluated for specific values of $\log(\Psi_{\text{reco}})$ and $\log_{10}(E_{\text{reco}})$ distributed linearly in their respective ranges, i.e. $\Psi_{\text{reco}} \in [0^\circ, 180^\circ]$ and $\log_{10}(E_{\text{reco}}) \in [0, 3]$. Thereupon, the resulting distribution is binned by creating a two-dimensional histogram in Ψ_{reco} and $\log_{10}(E_{\text{reco}})$, which is then used in our binned likelihood method. The chosen binning consists of 18 bins ranging from 0° to 180° in Ψ_{reco} and 50 bins in $\log_{10}(E_{\text{reco}})$ from 0 to 3 for the energy. This particular binning ensure a good balance between the number of bins in each dimension, and thus the resolution of each bin, and the total number of bins, which have a considerable impact on the computation time.

The background PDF computed with the KDE is represented in Figure 5.6. This figure shows the three two-dimensional histograms in Ψ_{reco} and $\log_{10}(E_{\text{reco}})$ obtained for each of the PID bin according to the KDE method described above. As visible in Figure 5.4, the first PID bin refers to PID scores ranging from 0 to 0.5, the second bin corresponds to values between 0.5 and 0.85, while the third bin contains events with PID scores above 0.85 and up to 1. The bottom-right plot is the projection of the 3D histogram in Ψ_{reco} and $\log_{10}(E_{\text{reco}})$. The upper and right-hand sub-plots of each histogram display the projection of the events contained in this particular histogram in Ψ_{reco} and $\log_{10}(E_{\text{reco}})$, respectively.

Signal PDF

The signal PDFs are constructed following the same steps as for the background. However, in this particular case, only the MC neutrino simulations obtained with GENIE are used. Following the signal expectation given by Equation 3.16, the MC neutrino events are weighted according to the source morphology and neutrino spectrum. Consequently, a different weight is computed for each possible association of DM halo profile, annihilation channel and mass discussed in Section 5.4. The resulting weighted distributions are used as inputs for the KDE method. Figure 5.7, shows the signal

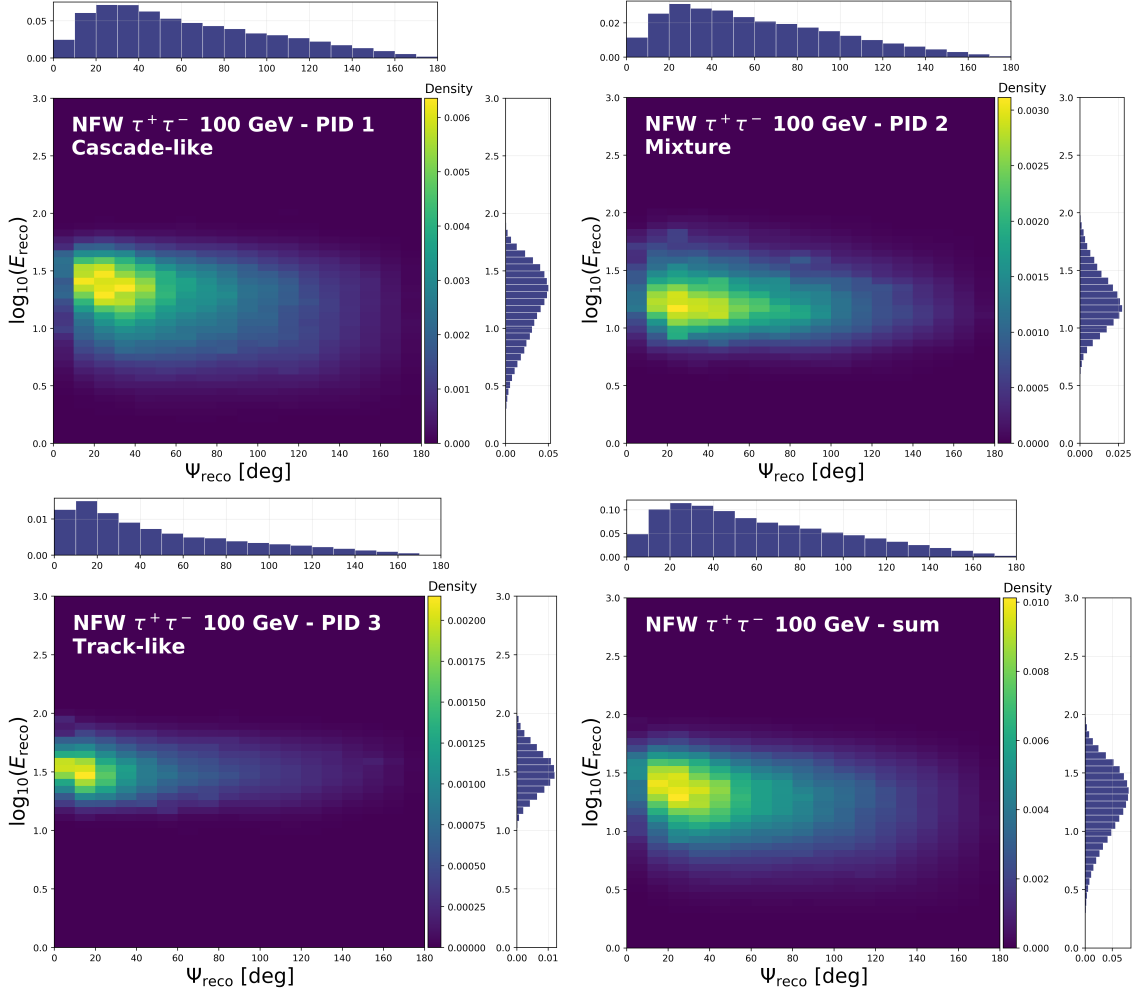


Figure 5.7—Three-dimensional signal PDF split into the individual contributions of each of the three PID bins for DM particles with masses of 100 GeV annihilating through the $\tau^+\tau^-$ channel, assuming the NFW halo profile. The bottom right histogram shows the 2D projection of the events in Ψ_{reco} and $\log_{10}(E_{\text{reco}})$.

PDF when considering DM particles with masses of 100 GeV annihilating through the $\tau^+\tau^-$ channel and distributed in our Galaxy according to the NFW halo profile.

These PDFs are considerably smoother than the initial signal distributions built by putting into histograms the MC neutrino events weighted according to expectations from Equation 3.16. This is visible in Figure 5.8 for dark matter annihilation through $\nu_\mu\bar{\nu}_\mu$ when considering DM particles with masses of 100 GeV distributed in our galaxy according to the NFW profile. The left-hand plot show the signal PDF obtained with the KDE method described above, while the plot in the right panel consists of the normalised histogram containing the weighted MC neutrino events. This comparison shows that the calculation of the signal PDFs with the KDE method smoothes the fluctuations caused by the statistical fluctuations of the sample of MC neutrinos, allowing to focus on the important features of the signal distribution.

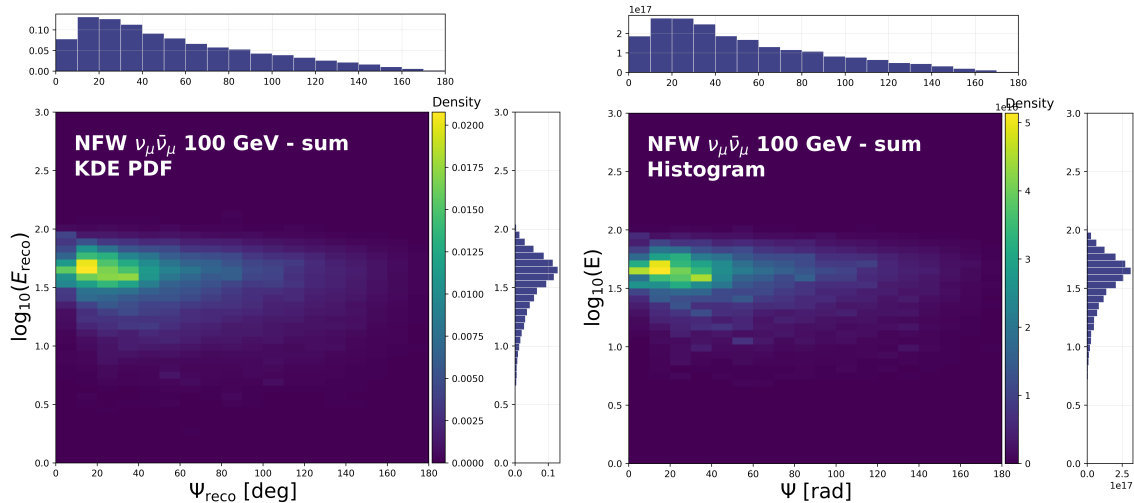


Figure 5.8—Comparison of the two-dimensional projections of the signal PDF in Ψ_{reco} (left) and $\log_{10}(E_{\text{reco}})$ and the raw histogram containing the signal events (right). This comparison is shown for DM particles with masses of 100 GeV annihilating through the $\nu_{\mu}\bar{\nu}_{\mu}$ channel, assuming the NFW halo profile. The colour scale expresses the probability density.

5.5.2 Limit computation

Similarly to the first analysis presented in this thesis, the considered likelihood function is built as the product of the Poisson probabilities to observe n_{obs}^i events in a specific bin i , as expressed in Equation 4.13. The expected fraction of events in this bin, $f^i(\mu)$, is also given by Equation 5.8 and consists of the weighted sum of the i -th bin content of the signal (f_s^i) and the background (f_{bg}^i) PDFs. The relative weights rely on the signal fraction, $\mu \in [0, 1]$, which constitute the only parameter to be fitted by the binned likelihood method.

The confidence intervals are constructed according to the Likelihood Interval construction method as defined in 1187. In this paper, two distinct test statistics are introduced for upper-limit calculation and discovery. For the computation of the upper limit on the signal fraction, μ , the test statistic is defined as

$$q_{\mu} \equiv \begin{cases} 2 \log \frac{\mathcal{L}(\hat{\mu})}{\mathcal{L}(\mu)} & \text{if } \hat{\mu} \leq \mu, \\ 0 & \text{otherwise,} \end{cases} \quad (5.3)$$

where $\hat{\mu}$ is the value of the signal fraction maximising the likelihood function. As data for which the best-fit signal fraction is such that $\hat{\mu} > \mu$ does not indicate a smaller degree of agreement with the hypothesised value of μ than the data, the TS is set to zero for these values, i.e. they are not included in the exclusion region of the test. Rather than being expressed as a specific case of the q_{μ} , the test statistic used for

discovery has its own specific definition given by

$$q_0 \equiv \begin{cases} 2 \log \frac{\mathcal{L}(\hat{\mu})}{\mathcal{L}(0)} & \text{if } \hat{\mu} \geq 0, \\ 0 & \text{otherwise,} \end{cases} \quad (5.4)$$

which takes values of 0 for $\hat{\mu} < 0$ as these values, however showing a disagreement with the background-only hypothesis, don't indicate the presence of signal events in the sample, but rather its incompatibility with the background model. In both cases, the level of disagreement between data and the hypothesised signal fraction ($\mu = 0$ for discovery) is quantified by computing the following p-value

$$p_\mu = \int_{q_{\mu, \text{obs}}}^{\infty} f(q_\mu | \mu) dq_\mu, \quad (5.5)$$

where $f(q_\mu | \mu)$ represents the PDF of q_μ under the assumption that the signal fraction equals the hypothesised μ . The sensitivity in terms of exclusion limits is given by the median value of the TS distribution equalling ϵ , such that

$$\text{median}[f(q_\mu | 0)] = \epsilon, \quad (5.6)$$

under the assumption that data is generated from the background-only hypothesis, i.e. $\mu = 0$. For this, 100,000 pseudo-experiments generated from the background-only event distribution are used. The value of ϵ depends on the chosen confidence level, such that the 90% (95%) C.L. sensitivity is obtained by setting ϵ to 1.64 (2.71). This choice of ϵ is motivated by the fact that when injecting signal at the level μ , the TS distribution, q_μ , should satisfy the following equation:

$$\int_{1.64(2.71)}^{\infty} f(q_\mu | \mu) dq_\mu = 0.1. \quad (5.7)$$

This confidence interval construction relies on Wilks' theorem [188], which requires the TS distribution to asymptotically follow a χ^2 distribution. The distributions $f(q_\mu | \mu)$ and $f(q_\mu | 0)$ are shown in Figure 5.9, along the median value of $f(q_\mu | 0)$ and the percentage of $f(q_\mu | \mu)$ falling on both part of this median value. These TS distributions are shown for dark matter particles with masses of 100 GeV (left) and 1000 GeV (right) annihilating through the $\tau^+ \tau^-$ annihilation channel, assuming DM to be distributed according to the NFW halo profile. As can be seen in these plots, the conditions required to use the likelihood interval construction are satisfied. This is true for all the scanned signal combinations. These plots are obtained by injecting μ at the level of the sensitivity when computing the TS distribution, implying that $\mu = \hat{\mu}_{90\%}$ in this particular case. The signal injection consists of creating the pseudo-samples from the background and signal distributions with the desired signal fraction $\hat{\mu}_{90\%}$, such that the resulting distributions are given by

$$f_{\text{p.e.}}(\mu) = (1 - \hat{\mu}_{90\%}) f_{\text{bg}} + \hat{\mu}_{90\%} f_{\text{sig}}, \quad (5.8)$$

where f_{bg} and f_{sig} are the background and signal PDFs, respectively.

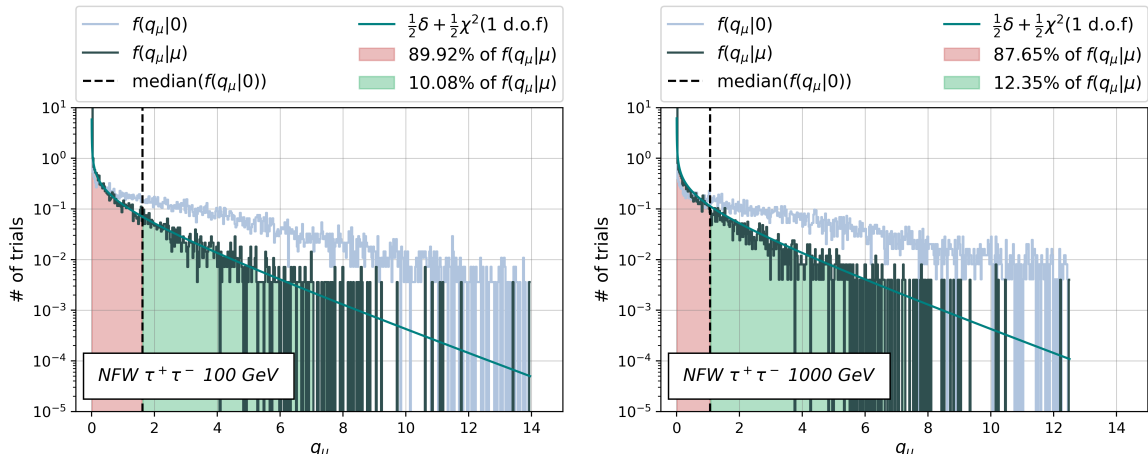


Figure 5.9—Test statistic distribution $f(q_\mu|\mu)$ and $f(q_\mu|0)$ computed for dark matter particles with masses of 100 GeV (left) and 1000 GeV (right) annihilating through the $\tau^+\tau^-$ annihilation channel, assuming DM to be distributed according to the NFW halo profile. The median value of $f(q_\mu|0)$ and the percentage of $f(q_\mu|\mu)$ falling on each part of this median value are also shown. The distribution $f(q_\mu|\mu)$ is compared to a χ^2 fit (green line) in order to visualise the validity of the assumptions made in order to apply Wilks’ theorem.

5.6 Sensitivities

The sensitivities of this search to the various dark matter annihilation scenarios investigated are presented in this section. These sensitivities are computed according to the method introduced in Section 5.5, for each combination of dark matter halo profile, annihilation channel and mass introduced in Section 5.4. The 90% C.L. sensitivities provided by the likelihood method are initially expressed in terms of the fitted parameter, i.e. the fraction of signal events in the sample. Following Equation 3.16, one can derive the sensitivity in terms of the DM self-annihilation cross-section from this $\hat{\mu}_{90}$, according to

$$\langle\sigma_{AV}\rangle = \hat{\mu}_{90} \frac{N_{\text{event}}}{T_{\text{live}}} \frac{8\pi m_{\text{DM}}^2}{AJ}, \quad (5.9)$$

where N_{event} is the number of recorded data events and T_{live} is the total livetime of the detector. The other terms included in this re-weighting are the dark matter mass (m_{DM}) and the J-factor (J), as well as the acceptance (A) computed according to Equation 4.10. For this analysis, a total of 366,260 events are considered, which were recorded over a livetime of 2,937.1 days. The obtained sensitivities in terms of $\langle\sigma_{AV}\rangle$ are shown in Figure 5.10 for dark matter annihilation through all seven considered channels and DM masses ranging from 5 GeV to 8 TeV, assuming both the NFW (left) and Burkert (right) halo profiles. The best sensitivities are obtained for dark matter annihilation into the three neutrino channels, i.e. $\nu_e\bar{\nu}_e$, $\nu_\mu\bar{\nu}_\mu$ and $\nu_\tau\bar{\nu}_\tau$, with a difference of almost two orders of magnitude compared to the sensitivities computed for the $b\bar{b}$

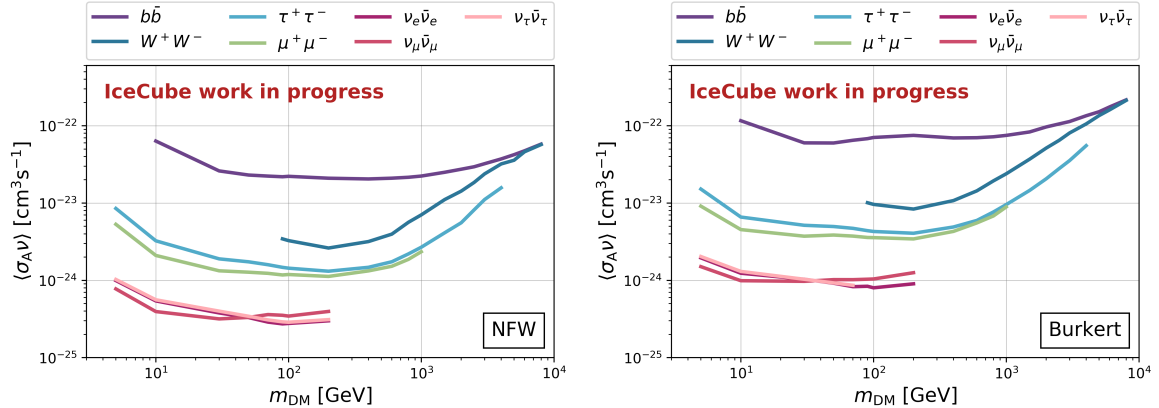


Figure 5.10—90% C.L. median upper limits on $\langle\sigma_A v\rangle$, which are quoted as sensitivities, shown for the NFW (left) and Burkert (right) dark matter halo profiles.

The sensitivities are obtained with the oscNext samples, consisting of 8.03 years of DeepCore data.

annihilation channel. This gap is due to the very shape of the neutrino spectra relative to the different annihilation channels. As seen in Figure 5.2, dark matter annihilation into the $b\bar{b}$ and W^+W^- channels results in the softest spectra, which will result in weaker signal expectations. Meanwhile, the neutrino annihilation channels provide the strongest spectra, presenting a sharp spectral feature around energies equivalent to dark matter mass. Due to this particular spectral feature, signal expectations for dark matter annihilation into the neutrino channels are more distinguishable from the smooth background, resulting in the strongest limits set for this analysis.

5.6.1 Comparison to previous results

The present sensitivities show considerable improvements over previous results published by the IceCube collaboration. This enhancement is visible in Figure 5.11 for the benchmark dark matter combination, namely for DM annihilation through the $\tau^+\tau^-$ channel and the NFW profile. In addition to the latest published IceCube limit, this figure also includes the limits obtained by the search for DM annihilation in the GC with 11 years of data, as well as the combined DM search conducted with both ANTARES and IceCube. Below 1 TeV, this analysis provides the leading sensitivities from neutrino experiments. More than one order of magnitude improvement is visible over the entire mass range when compared to the previous IceCube-only search, with as much as a factor 102.9 at 10 GeV.

This significant gain is due to the conjunction of several factors. Firstly, this analysis is performed with more years of data than the previous IceCube search, with a total livetime of 2,937.1 days versus 1,007 days. Moreover, as previously seen in Section 5.3, the event selection considered for this search exhibits a better effective area than the event selection of the 3 years GC DM search. Since the oscNext event selection is optimised for low energies, this is especially true for energies below 100 GeV. The oscNext event selection also allows to extend the range of scanned DM masses down

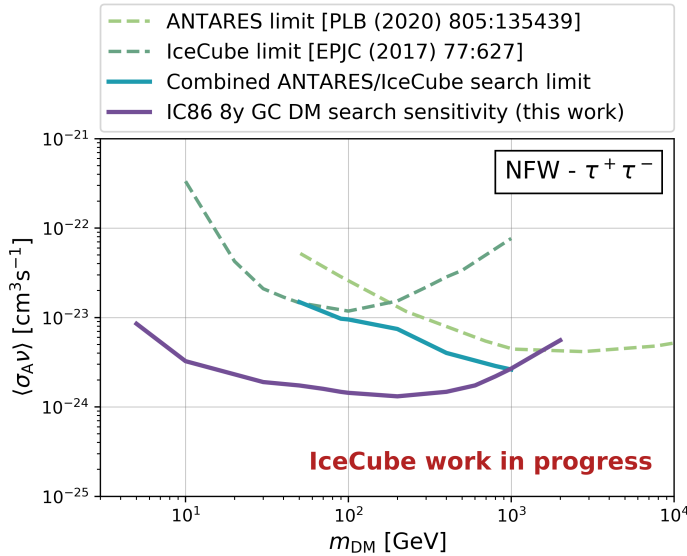


Figure 5.11—90% C.L. sensitivity in terms of the thermally-averaged DM self-annihilation cross-section $\langle\sigma_{AV}\rangle$ for DM annihilation through $\tau^+\tau^-$, assuming the NFW halo profile. This sensitivity is presented alongside the latest published limits from IceCube and ANTARES, as well as the results from the combined DM search presented in Chapter 4.

to 5 GeV. Lastly, additional information are included in the PDFs. While the PDFs used for the other DM searches presented in Figure 5.11 solely include information about the angular direction of the events, the PDFs considered for the present search are also carrying information about the energy and the topology of the events. The inclusion of the energy has a greater impact for higher dark matter masses as the spectral characteristics of the corresponding expected dark matter fluxes are more distinct from the background expectation at these energies.

5.7 Treatment of systematic uncertainties

The systematic uncertainties affecting this DM search can be regrouped under three categories: atmospheric flux predictions, detector response, and astrophysical uncertainties. In this section, the impact of the various systematics on this analysis are studied and quantified. The implementation of their respective effects is also discussed. It has to be noted that these systematic effects are quantified in terms of efficiency and not with respect to the nominal sample. Namely, the pseudo-experiments computed to obtain the systematic sensitivities presented below are obtained from a background PDF computed with the corresponding systematic set rather than from the nominal background PDF.

Atmospheric flux uncertainties

As the background expectation is drawn from MC simulations weighted according to the expected atmospheric flux, uncertainties in the modelling of the atmospheric neutrino and muon fluxes must be considered. Uncertainties on the neutrino flux are studied by re-weighting the MC neutrino simulations according to alternative atmospheric neutrino fluxes, which are generated with the Matrix Cascade Equations (MCEq) toolkit [189]. This program allows provides the atmospheric flux of leptons for various assumptions on the primary cosmic ray flux, the interaction model of the hadronic cascade and the atmosphere of the Earth. Therefore, MCEq is used to evaluate the impact of modifying the hadronic interaction model and the primary CR spectrum on this analysis. The Earth's atmosphere is simulated according to a similar parameterisation as the one used in CORSIKA, based on the US standard (USStd) atmosphere model [190]. When computing the alternative neutrino fluxes, two different types of hadronic interaction models are evaluated: the SIBYLL 2.3c [191] and the QGSJET-II [192] models. Similarly, two primary cosmic rays models are considered, both of which include the five standard mass groups composition, i.e. p, He, CNO, Mg-Si and Fe. The first of these models was proposed by Honda and Gaisser and is thus referenced as the "HondaGaisser" (HG) model [193]. This model assumes the primary CR flux to follow a power-law, according to

$$\phi(E_k) = K \times (E_k + b \exp[-c\sqrt{E_k}])^{-\alpha}, \quad (5.10)$$

where the parameters α , K , b and c are fitted to observations from AMS [194] and BESS [195]. Since this model is adjusted to data measurements with energies below the PeV-scale, it is optimised for lower energies. The second model, referred to as the "HillasGaisser2012" (H3a) model, introduces three distinct populations of primary CR [177]. These populations are separated as follows: the low-energy component is assumed to originate from supernova remnants, the second population is expected to be generated by unknown high energetic processes in our galaxy, while the population at the highest energies is predicted to arise from extra-galactic phenomena. The resulting spectrum of primary CR can be expressed as

$$\phi_i(E) = \sum_{j=1}^3 a_{i,j} E^{-\gamma_{ij}} \times \exp\left[-\frac{E}{Z_i R_{c,j}}\right] \quad (5.11)$$

where the index i covers the five mass groups considered, while j refers to the three CR populations. The parameter $R_{c,j}$ is known as the characteristic rigidity, which denotes the point at which the population j is cut off. Once computed for all combinations of the hadronic interaction model and the primary CR spectrum, the outputs of MCEq are oscillated separately with the same oscillation parameters as the nominal neutrino flux. The resulting oscillated flux are used to re-weight the MC neutrino sets according to Equation 4.3. As MuonGun simulations does not allow for a simple re-weighting of the MC muons with the alternative muon flux produced by MCEq, uncertainties on the atmospheric muon flux are handled by scaling the nominal flux according to a normalisation factor, α_μ . This factor takes values computed according to the variations

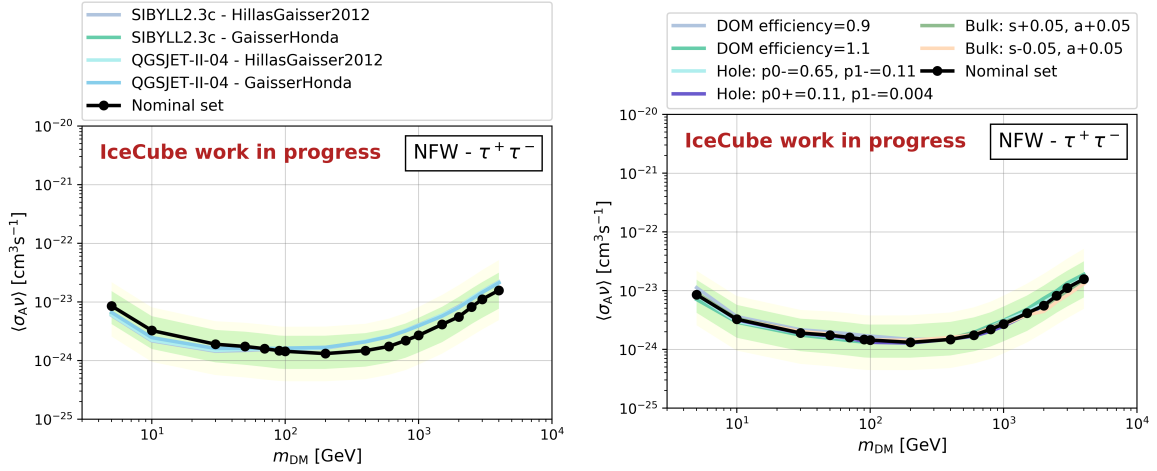


Figure 5.12—Impact of the atmospheric flux (left) and detector (right) systematics on the 90% C.L. sensitivities for DM annihilation through the $\tau^+\tau^-$ channel, assuming DM distribution according to the NFW halo profile.

of the corresponding alternative neutrino flux with respect to the nominal neutrino flux, according to:

$$\alpha = \frac{\sum(\phi_\nu)_{\text{nominal}}}{\sum(\phi_\nu)_{\text{syst}}}. \quad (5.12)$$

From the re-weighted MC simulations, new background PDFs are computed following the same method applied for the nominal background PDF. The sensitivities computed using these systematic background PDFs are visible in the right-hand panel of Figure 5.12 for the $\tau^+\tau^-$, along with the nominal sensitivity, and the corresponding 1σ and 2σ bands. The modifications of the atmospheric weight lead to improvements or worsening of the sensitivities by 24% to 50%.

Detector uncertainties

The treatment of systematics linked to the detector response is implemented using dedicated MC simulation sets, which are computed for variations of the optical efficiency of the DOMs, as well as for changes in the model describing the ice properties. After generating the PDFs for all of these systematic sets, the relative sensitivities are evaluated for every DM signal combinations. A few of these sensitivities are visible in the left panel of Figure 5.12 for the NFW halo profile and DM annihilation through the $\tau^+\tau^-$ annihilation channel. The effects of the various systematics on the analysis are then quantified by evaluating the deviation of each of these sensitivities with respect to the corresponding nominal sensitivity. The impact of each type of systematics is then quoted as a variation range. For instance, modifying the detection efficiency of the IceCube DOMs by $\pm 10\%$ results in improvements or worsening of the sensitivities by 1% to 32%. For the properties of the bulk ice, the scattering and absorption lengths are modified by $\pm 5\%$ compared to the nominal values. Therefore, four different systematic sets with all possible combinations of these variations are evaluated, as visible

Bulk ice		
	Absorption length	Scattering length
Systematics	$a_{\text{nom}}+0.05$	$s_{\text{nom}}+0.05$
	$a_{\text{nom}}+0.05$	$s_{\text{nom}}-0.05$
	$a_{\text{nom}}-0.05$	$s_{\text{nom}}+0.05$
	$a_{\text{nom}}-0.05$	$s_{\text{nom}}-0.05$
Hole ice		
	Angular acceptance p0	Angular acceptance p1
Nominal	+0.101569	-0.049344
Systematics	-0.0648	-0.1088
	-0.4839	-0.0171
	+0.2803	-0.0754
	+0.1122	+0.0035

Table 5.7: Summary of the model parameters used for the four bulk ice systematic sets (upper half) and the four hole ice systematic sets (lower half).

in the upper part of Table 5.7. Considering these alternative values in the bulk ice model causes variation of the sensitivities by 8% to 25%. For the oscNext samples, the properties of the hole ice are simulated using a new model internal to the IceCube collaboration, called the Unified Angular Acceptance model. This model relies on two parameters known as the angular acceptances p0 and p1. Therefore, the MC simulation sets used to evaluate the effects of the considered hole ice on the analysis are computed with variations of these two parameters. As a strong correlation is expected between p0 and p1, these parameters are varied simultaneously in each of the four systematic sets. The values considered for these samples are listed in the lower half of Table 5.7. Computing the sensitivities with the systematic sets results in deviations ranging between 2% to 11%.

Astrophysical uncertainties

Just as for the first dark matter search presented in this thesis, the dominant source of systematics of this analysis arise from astrophysical uncertainties. Uncertainties on the choice of DM halo model are treated by considering both a cusped and cored halo profile, namely the NFW and the Burkert profile formulations. Sensitivities obtained with these two profiles are shown side by side in Figure 5.10, giving an indication of the influence of the halo model uncertainties. In addition to this, the impact of the errors on the free halo parameters used to compute the J-factors (see Table 3.1) is roughly evaluated for the NFW halo profile. Two alternative J-factors are computed with Clumpy, using the lower and upper error bounds of these free parameters, respectively. These J-factors are shown in Figure 5.13 alongside the nominal NFW J-factor. The effect of the uncertainties of the halo parameters are quantified by considering their

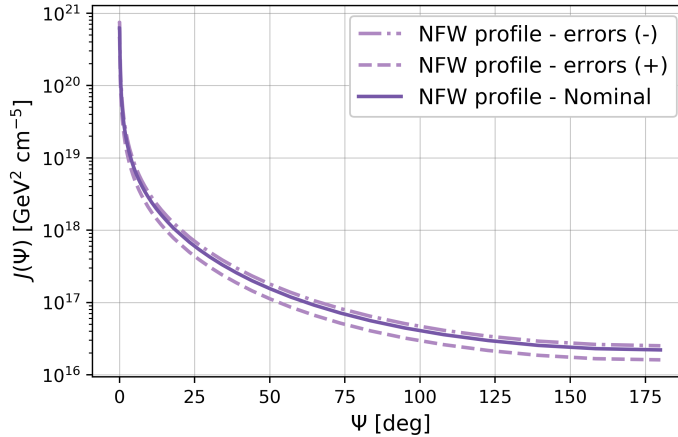


Figure 5.13—Impact of uncertainties on the free halo parameters used to compute the J-factor (shown in Table 3.1) for the NFW halo profile.

effects on the integrated J-factor, i.e. J-factor integrated over the entire Ψ range. Considering values of the halo parameters given by the upper error bounds results in an increase of the integrated J-factor by a factor 2.08 with respect to the nominal value, while the integrated J-factor computed with the parameter values relative to the lower error bound is reduced by a factor 1.85.

5.8 Unblinding procedure

As the analysis was in its final stage, it was submitted for review by the IceCube collaboration. Following this process, the permission to unblind the analysis was granted, such that the analysis method could be applied to the recorded data. In this section, the steps following this unblinding approval are described.

5.8.1 Pre-unblinding check

Before applying the binned likelihood method to the actual data set, a pre-unblinding check was performed. This test consisted of first using data scrambled in RA in order to perform the likelihood method, so that the directional information would still be blinded. The results of this pre-unblinding test raised concerns about a possible strong discrepancy between background expectation computed from weighted MC simulations and data.

After a thorough investigation, it became clear that such MC/data disagreement is present in the event selection, leading to considerable signal fractions to be fitted by the likelihood method even in a RA scrambled dataset. Comparisons of the data distribution (dots) with the background distributions obtained from MC simulations (histograms) are visible in Figure 5.14 and Figure 5.15 in terms of reconstructed energy (E_{reco}) and opening angle to the GC (Ψ_{reco}), respectively. Due to the change in the processing of the files containing the geometry of the IceCube detector, known as the GCD files, the data are split into two separate time periods. The right-hand plots

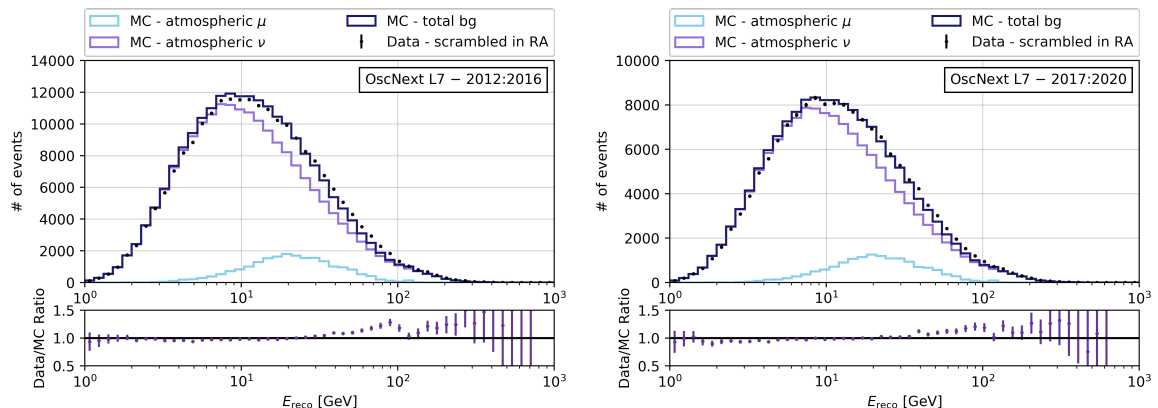


Figure 5.14—Comparisons of the MC background (histograms) and the data (dots) distributions in terms of the reconstructed energy. Each plot show the separate contribution from atmospheric neutrinos (purple) and muons (light blue) to the total background distribution (dark blue). The data/MC ratio is also shown in the lower panel of each figure.

show data collected from 2012 to 2016, while the left-hand plot display data recorded between 2017 and 2020. The lower panel of each plot gives an indication of the ratio between the content of each bin of the data and MC histograms. From these plots, one can see that the angular distributions display fairly good agreement, with deviation between data and MC contained within 10% over the entire range. When considering the energy distribution, more important deviations can be seen towards 100 GeV. For energies above 100 GeV, large statistical fluctuations are visible as fewer events with those energies are present in the sample.

To overcome this problem, one of the evaluated solution consists of fitting separately the various contribution to the background distribution. In addition to background expectations from atmospheric neutrinos and muons, the contribution from expected astrophysical neutrino flux is also included. So far, the contribution from astrophysical neutrinos was neglected as, at the considered energies, it is negligible when compared to other background and signal expectations. Instead of having a single background PDF built from the weighted contributions of the MC muon and neutrino simulations, three separated PDFs are built and the fraction of these events contributing to the total background PDF, α_i , is fitted such:

$$f_{bg} = \alpha_1 f_{\mu_{atm}} + \alpha_2 f_{\nu_{atm}} + \alpha_3 f_{\nu_{astro}}, \quad (5.13)$$

where $f_{\mu_{atm}}$, $f_{\nu_{atm}}$ and $f_{\nu_{astro}}$ are the atmospheric muon, the atmospheric neutrino and the astrophysical neutrino PDFs, respectively. The separate fitting of these three expected background sources does not contribute to the resolution of the apparent mismatch between data and MC simulations. Instead, a large fraction of astrophysical neutrinos, incompatible with observations, is fitted by the likelihood method in the attempt to fill the gap between MC and data. As fitting separately the different background contributions proved to be unsuccessful, other approaches are proposed in the following. These alternatives could however not be implemented in this work as they

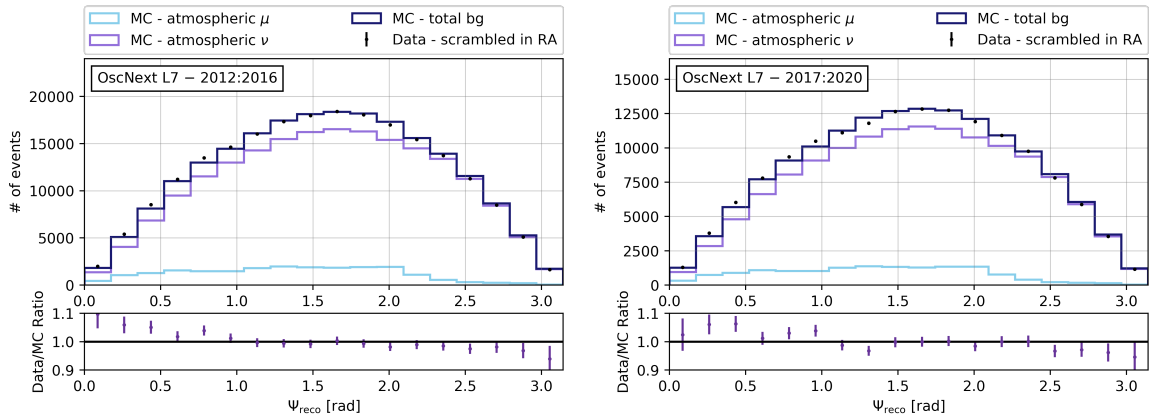


Figure 5.15—Comparisons of the MC background (histograms) and the data (dots) distributions in terms of the opening angle to the Galactic Centre. Each plot show the separate contribution from atmospheric neutrinos (purple) and muons (light blue) to the total background distribution (dark blue). The data/MC ratio is also shown in the lower panel of each figure.

would have requested the unblinding process to be restarted and would have led to an indeterminate delay incompatible with the time constraints of this thesis.

5.8.2 Outlooks

A possible explanation to the lack of agreement between data and MC simulations observed during the pre-unblinding check could arise from the fact that the cross-section models used by GENIE are not valid above 100 GeV. In order to account for this, the oscillation analyses using the oscNext event selection implemented a smooth transition between the neutrino samples simulated with GENIE and the ones obtained from the Neutrino Generator (NuGen). NuGen is a software internal to IceCube based on the ANIS package [196]. This event generator is optimised for higher energies, starting at tenth of GeV and therefore only takes into account DIS. This option would require to be further investigated in order to ensure the MC simulations to be in better agreement with data.

Another suggested solution involves to compute the background PDFs from data. Just as for the combined DM search, this could be done by assigning random values of right ascension to each data event. However, this will only result in a randomisation of the angular information of the events, while the possible signal features present in the two other dimensions of the histograms will remain unaffected. Therefore, the likelihood method will need to be modified to account for signal subtraction in the model PDF construction. This is needed under the assumption that the scrambled data PDF consists of both background and scrambled signal events, such that:

$$f_{\text{scr.data}} = (1 - \mu)f_{\text{BG}} + \mu f_{\text{scr.sig}}, \quad (5.14)$$

where $f_{\text{scr.data}}$ is the scrambled data distribution and $f_{\text{scr.sig}}$ is built by scrambling the signal PDF in right ascension. Therefore, this will require to adapt the fraction of

expected events computed for each specific bin i (given by Equation 5.8) as:

$$f^i(\mu) = \mu f_{\text{sig}}^i + f_{\text{scr.data}}^i - \mu f_{\text{scr.sig}}^i. \quad (5.15)$$

The analysis could then be repeated using the data driven background PDF and the modified likelihood method. Once approved by the IceCube collaboration, the data set could be properly unblinded and results could be computed. If no neutrino excesses are found upon unblinding, upper limits on the dark matter self-annihilation cross-section could still be computed. It is worth noting that using data present a disadvantage in terms of statistics in the sample, possibly leading to a considerable amount of empty background bins. However, this issue could again be solved by building the background PDF with a KDE built from the scrambled data.

Conclusion and outlooks

In this section, general conclusions about the two analyses presented in this thesis are drawn, and possible related outlooks are discussed. The common idea behind these two analyses is the indirect detection of dark matter with the IceCube neutrino telescope, both targeting the Galactic Centre. The first of these two analyses consists of a combined search using data recorded by both the ANTARES and the IceCube detectors, while the second analysis focuses on the detection of dark matter at low energies with eight years of IceCube data. Both analyses are sensitive to any dark matter candidate interacting weakly with matter, self-annihilating into particles of the SM.

Combined dark matter search with ANTARES and IceCube

This analysis is the first combined dark matter search focusing on the Galactic Centre which uses data recorded by neutrino experiments. Three years of IceCube data taken from 2012 to 2015 with the full IC86 detector configuration are considered for this joint analysis, along eight years of ANTARES data recorded from 2007 to 2015. Dark matter annihilation through four distinct DM self-annihilation channels (W^+W^- , $\mu^+\mu^-$, $\tau^+\tau^-$ and $b\bar{b}$) is considered for both the NFW and Burkert halo profile. In total, 16 DM masses ranging from 50 GeV to 1 TeV are scanned. As no excess of signal neutrino is observed over the background expectations, limits on the thermally-averaged DM self-annihilation cross-section, $\langle\sigma_a v\rangle$, are set for all combinations of DM signal expectations. These limits show up to a factor two improvement in the considered mass range, providing the most stringent limits on the thermally-averaged DM self-annihilation cross-section set by neutrino experiments for DM masses ranging from 50 GeV to 1 TeV. For instance, a limit on $\langle\sigma_a v\rangle$ of $7.44 \times 10^{-24} \text{ cm}^3 \text{ s}^{-1}$ is obtained for the annihilation of DM particles with masses of 200 GeV through the $\tau^+\tau^-$ channel, assuming the DM halo to be shaped according to NFW profile. In addition to these improvements, the thorough investigation conducted in order to guarantee consistent model parameters to be used for the signal expectations of both experiments brought to light an interpolation error of the DM spectrum in the previous nine years ANTARES-only search. The rectification of this miscalculation led to the erratum of the related paper.

While this analysis demonstrates the possible gain from a combined dark matter search, there is still room for improvement. For instance, future combined DM searches could be ameliorated by considering more years of data, as well as more advanced event selections. Since the MoU between the ANTARES and IceCube collaborations agreed

upon the use of data sets from previously published dark matter searches conducted by each experiment, the number of years used for this joint analysis was limited compared to the number of years actually available. This analysis could also benefit from the inclusion of additional features such as the energy of the events rather than only considering the spatial event distribution in the PDFs. While the two data sets considered in this work are optimised for the selection of track-like events, i.e. mainly events resulting from the interaction of muon neutrinos, another improvement could arise from the inclusion of cascade-like events, that is to say CC interactions of electron and tau neutrino, as well as NC interactions of all neutrino flavours, in future combined DM searches. Lastly, the combination could be extended to other astrophysical messengers, such as gamma-rays. For DM masses below 10 TeV, gamma-ray experiments provide the leading limits in terms of $\langle\sigma_A v\rangle$ obtained from observations of dwarf spheroidal galaxies.

Low energy dark matter search with eight years of IceCube data

This analysis consists of a search for neutrinos from DM annihilation in the GC with a total of 2,937.1 days of IceCube data recorded from 2012 to 2020. More specifically, the considered event selection focuses on low energy events starting in the DeepCore sub-detector volume. Using this event selection, known as OscNext, the range of dark matter masses could be extended as low as 5 GeV and up to 8 TeV. In addition to the four dark matter annihilation channels considered for the combined DM search, direct annihilation into all neutrino flavours ($\nu_e\bar{\nu}_e$, $\nu_\mu\bar{\nu}_\mu$ and $\nu_\tau\bar{\nu}_\tau$) is also probed, bringing the total number of tested channel to seven. Just as for the combined dark matter search, both the NFW and the Burkert halo profiles are evaluated. The sensitivities obtained for the various combinations of signal expectations show considerable improvement when compared to the results previously published by the IceCube collaboration. Such amelioration arise from the implementation of some of the improvements suggested in the previous section. Namely, this analysis uses more years of data than the latest published IceCube DM search focusing on the Galactic Centre, with around eight years of data compared to three years. The OscNext event selection also shows considerable improvement over the entire evaluated DM mass range with respect to the previously used data sample, with up to an order of magnitude amelioration at 10 GeV. Lastly, this analysis is the first dark matter search targeting the GC conducted with IceCube to include information about the energy and topology of the events along the angular information.

Unfortunately, the final results of this analysis could not be processed during the time span of this PhD. As the pre-unblinding checks revealed an intrinsic disagreement between background expectation from MC simulations and data, the analysis method could not be applied to the unblinded data. The proposed solution to this problem is to construct the background distribution from data by allocating a random right ascension to each event. As this will only scramble information in right ascension, it will also be necessary to consider signal subtraction while building the model PDF in order to account for possible signal signatures in energy and PID.

Bibliography

- [1] C. L. Cowan et al. Detection of the free neutrino: A Confirmation. *Science*, 124:103–104, 1956.
- [2] J. A. Formaggio and G. P. Zeller. From eV to EeV: Neutrino Cross Sections Across Energy Scales. *Rev. Mod. Phys.*, 84:1307–1341, 2012.
- [3] S. L. Glashow. Resonant Scattering of Antineutrinos. *Phys. Rev.*, 118:316–317, 1960.
- [4] M. G. Aartsen et al. Detection of a particle shower at the Glashow resonance with IceCube. *Nature*, 591(7849):220–224, 2021. [Erratum: *Nature* 592, E11 (2021)].
- [5] G. Huang and Q. Liu. Hunting the Glashow Resonance with PeV Neutrino Telescopes. *JCAP*, 03:005, 2020.
- [6] Z. Maki, M. Nakagawa, and S. Sakata. Remarks on the unified model of elementary particles. *Prog. Theor. Phys.*, 28:870–880, 1962.
- [7] B. Pontecorvo. Neutrino Experiments and the Problem of Conservation of Leptonic Charge. *Zh. Eksp. Teor. Fiz.*, 53:1717–1725, 1967.
- [8] Y. Fukuda et al. Measurement of a small atmospheric muon-neutrino / electron-neutrino ratio. *Phys. Lett. B*, 433:9–18, 1998.
- [9] F. Capozzi, E. Lisi, A. Marrone, and A. Palazzo. Current unknowns in the three neutrino framework. *Prog. Part. Nucl. Phys.*, 102:48–72, 2018.
- [10] P. A. Zyla et al. Review of Particle Physics. *PTEP*, 2020(8):083C01, 2020.
- [11] L. Wolfenstein. Neutrino Oscillations in Matter. *Phys. Rev. D*, 17:2369–2374, 1978.
- [12] S. P. Mikheev and A. Yu. Smirnov. Resonant amplification of neutrino oscillations in matter and solar neutrino spectroscopy. *Nuovo Cim. C*, 9:17–26, 1986.
- [13] E. Vitagliano, I. Tamborra, and G. Raffelt. Grand Unified Neutrino Spectrum at Earth: Sources and Spectral Components. *Rev. Mod. Phys.*, 92:45006, 2020.
- [14] A. D. Dolgov. Neutrinos in cosmology. *Phys. Rept.*, 370:333–535, 2002.

- [15] G. Steigman. Neutrinos And Big Bang Nucleosynthesis. *Adv. High Energy Phys.*, 2012:268321, 2012.
- [16] E. Vitagliano, J. Redondo, and G. Raffelt. Solar neutrino flux at keV energies. *JCAP*, 12:010, 2017.
- [17] O. Smirnov. Experimental Aspects of Geoneutrino Detection: Status and Perspectives. *Prog. Part. Nucl. Phys.*, 109:103712, 2019.
- [18] J. K. Ahn et al. Observation of Reactor Electron Antineutrino Disappearance in the RENO Experiment. *Phys. Rev. Lett.*, 108:191802, 2012.
- [19] F. P. An et al. Observation of electron-antineutrino disappearance at Daya Bay. *Phys. Rev. Lett.*, 108:171803, 2012.
- [20] H. de Kerret et al. The Double Chooz antineutrino detectors. 1 2022.
- [21] K. Eguchi et al. First results from KamLAND: Evidence for reactor anti-neutrino disappearance. *Phys. Rev. Lett.*, 90:021802, 2003.
- [22] JUNO collaboration. JUNO physics and detector. *Prog. Part. Nucl. Phys.*, 123:103927, 2022.
- [23] H. T. Janka, T. Melson, and A. Summa. Physics of Core-Collapse Supernovae in Three Dimensions: a Sneak Preview. *Ann. Rev. Nucl. Part. Sci.*, 66:341–375, 2016.
- [24] A. Mirizzi et al. Supernova Neutrinos: Production, Oscillations and Detection. *Riv. Nuovo Cim.*, 39(1-2):1–112, 2016.
- [25] L. Marti-Magro. SuperK-Gd: The Gd future of Super-Kamiokande. *PoS, ICRC2019:957*, 2020.
- [26] D. Guetta et al. Neutrinos from individual gamma-ray bursts in the BATSE catalog. *Astropart. Phys.*, 20:429–455, 2004.
- [27] M. G. Aartsen et al. Multimessenger observations of a flaring blazar coincident with high-energy neutrino IceCube-170922A. *Science*, 361(6398):eaat1378, 2018.
- [28] M. G. Aartsen et al. Neutrino emission from the direction of the blazar TXS 0506+056 prior to the IceCube-170922A alert. *Science*, 361(6398):147–151, 2018.
- [29] P. A. Cherenkov. Visible luminescence of pure liquids under the influence of γ -radiation. *Dokl. Akad. Nauk SSSR*, 2(8):451–454, 1934.
- [30] I. M. Frank and I. E. Tamm. Coherent visible radiation of fast electrons passing through matter. *Compt. Rend. Acad. Sci. URSS*, 14(3):109–114, 1937.
- [31] M. Ageron et al. ANTARES: the first undersea neutrino telescope. *Nucl. Instrum. Meth. A*, 656:11–38, 2011.

- [32] J. A. Aguilar et al. AMADEUS - The Acoustic Neutrino Detection Test System of the ANTARES Deep-Sea Neutrino Telescope. *Nucl. Instrum. Meth. A*, 626-627:128–143, 2011.
- [33] J. A. Aguilar et al. First results of the Instrumentation Line for the deep-sea ANTARES neutrino telescope. *Astropart. Phys.*, 26:314–324, 2006.
- [34] M. G. Aartsen et al. The IceCube Neutrino Observatory: Instrumentation and Online Systems. *JINST*, 12(03):P03012, 2017.
- [35] R. Abbasi et al. The Design and Performance of IceCube DeepCore. *Astropart. Phys.*, 35:615–624, 2012.
- [36] P. Amram et al. The ANTARES optical module. *Nucl. Instrum. Meth. A*, 484:369–383, 2002.
- [37] R. Abbasi et al. Calibration and Characterization of the IceCube Photomultiplier Tube. *Nucl. Instrum. Meth. A*, 618:139–152, 2010.
- [38] F. Feinstein. The analogue ring sampler: A front-end chip for ANTARES. *Nucl. Instrum. Meth. A*, 504:258–261, 2003.
- [39] R. Abbasi et al. The IceCube Data Acquisition System: Signal Capture, Digitization, and Timestamping. *Nucl. Instrum. Meth. A*, 601:294–316, 2009.
- [40] D. E. Groom. Atomic and nuclear properties of materials. Technical report, 2008.
- [41] L. Gerhardt and S. R. Klein. Electron and Photon Interactions in the Regime of Strong LPM Suppression. *Phys. Rev. D*, 82:074017, 2010.
- [42] D. Chirkin and W.g Rhode. Muon Monte Carlo: A High-precision tool for muon propagation through matter. Technical report, 7 2004.
- [43] V. F. Hess. Über Beobachtungen der durchdringenden Strahlung bei sieben Freiballonfahrten. *Phys. Z.*, 13:1084–1091, 1912.
- [44] P. Blasi. The Origin of Galactic Cosmic Rays. *Astron. Astrophys. Rev.*, 21:70, 2013.
- [45] E. Aslanides et al. A deep sea telescope for high-energy neutrinos. Technical report, 5 1999.
- [46] M. G. Aartsen et al. Anisotropy in Cosmic-ray Arrival Directions in the Southern Hemisphere Based on six Years of Data From the Icecube Detector. *Astrophys. J.*, 826(2):220, 2016.
- [47] M. G. Aartsen et al. Measurement of Atmospheric Neutrino Oscillations at 6–56 GeV with IceCube DeepCore. *Phys. Rev. Lett.*, 120(7):071801, 2018.
- [48] A. Albert et al. Measuring the atmospheric neutrino oscillation parameters and constraining the 3+1 neutrino model with ten years of ANTARES data. *JHEP*, 06:113, 2019.

- [49] R. Abbasi et al. Improved Characterization of the Astrophysical Muon-Neutrino Flux with 9.5 Years of IceCube Data. 11 2021.
- [50] J. A. Aguilar et al. Transmission of light in deep sea water at the site of the ANTARES Neutrino Telescope. *Astropart. Phys.*, 23:131–155, 2005.
- [51] H. Yepes Ramírez. *Characterization of the optical properties at the ANTARES site using the Optical Beacon system. Influence on the detector performance*. PhD thesis, Valencia U., IFIC, 2014.
- [52] S. Adrian-Martinez et al. Measurement of the Group Velocity of Light in Sea Water at the ANTARES Site. *Astropart. Phys.*, 35:552–557, 2012.
- [53] P. B. Price, K. Woschnagg, and D. Chirkin. Age vs depth of glacial ice at south pole. *Geophysical Research Letters*, 27(14):2129–2132, 2000.
- [54] S. L. Miller. Clathrate hydrates of air in antarctic ice. *Science*, 165(3892):489–490, 1969.
- [55] M. Ackermann et al. Optical properties of deep glacial ice at the South Pole. *J. Geophys. Res.*, 111(D13):D13203, 2006.
- [56] M. G. Aartsen et al. Measurement of South Pole ice transparency with the IceCube LED calibration system. *Nucl. Instrum. Meth. A*, 711:73–89, 2013.
- [57] D. Chirkin. Evidence of optical anisotropy of the South Pole ice. In *33rd International Cosmic Ray Conference*, page 0580, 2013.
- [58] F. Zwicky. Die Rotverschiebung von extragalaktischen Nebeln. *Helv. Phys. Acta*, 6:110–127, 1933.
- [59] F. Zwicky. On the Masses of Nebulae and of Clusters of Nebulae. *Astrophys. J.*, 86:217–246, 1937.
- [60] E. Hubble and M. L. Humason. The Velocity-Distance Relation among Extra-Galactic Nebulae. *Astrophys. J.*, 74:43–80, 1931.
- [61] N. Aghanim et al. Planck 2018 results. VI. Cosmological parameters. *Astron. Astrophys.*, 641:A6, 2020.
- [62] S. Smith. The Mass of the Virgo Cluster. *Astrophys. J.*, 83:23–30, 1936.
- [63] H. I. Ewen and E. M. Purcell. Observation of a Line in the Galactic Radio Spectrum: Radiation from Galactic Hydrogen at 1,420 Mc./sec. *Nature*, 168(4270):356–356, 1951.
- [64] C. A. MULLER and J. H. OORT. Observation of a Line in the Galactic Radio Spectrum: The Interstellar Hydrogen Line at 1,420 Mc./sec., and an Estimate of Galactic Rotation. *Nature*, 168(4270):357–358, 1951.

- [65] J. L. PAWSEY. Observation of a Line in the Galactic Radio Spectrum: The Interstellar Hydrogen Line at 1,420 Mc./sec., and an Estimate of Galactic Rotation. *Nature*, 168(4270):358–358, 1951.
- [66] V. C. Rubin and W. K. Jr. Ford. Rotation of the Andromeda Nebula from a Spectroscopic Survey of Emission Regions. *Astrophys. J.*, 159:379–403, 1970.
- [67] K. C. Freeman. On the disks of spiral and SO Galaxies. *Astrophys. J.*, 160:811, 1970.
- [68] H. Hoekstra, H. Yee, and M. Gladders. Current status of weak gravitational lensing. *New Astron. Rev.*, 46:767–781, 2002.
- [69] W. Tucker et al. 1e0657-56: a contender for the hottest known cluster of galaxies. *Astrophys. J. Lett.*, 496:L5, 1998.
- [70] D. Clowe et al. A direct empirical proof of the existence of dark matter. *Astrophys. J. Lett.*, 648:L109–L113, 2006.
- [71] A. A. Penzias and R. W. Wilson. A Measurement of excess antenna temperature at 4080-Mc/s. *Astrophys. J.*, 142:419–421, 1965.
- [72] C. Alcock et al. The MACHO project: limits on planetary mass dark matter in the galactic halo from gravitational microlensing. *Astrophys. J.*, 471:774, 1996.
- [73] P. Tisserand et al. Limits on the Macho Content of the Galactic Halo from the EROS-2 Survey of the Magellanic Clouds. *Astron. Astrophys.*, 469:387–404, 2007.
- [74] M. Kawasaki et al. Primordial black holes as dark matter in supergravity inflation models. *Phys. Rev. D*, 94(8):083523, 2016.
- [75] Y. B. Zel’dovich and I. D. Novikov. The Hypothesis of Cores Retarded during Expansion and the Hot Cosmological Model. *Soviet Astron. AJ (Engl. Transl.)*, 10:602, 1967.
- [76] S. Hawking. Gravitationally collapsed objects of very low mass. *Mon. Not. Roy. Astron. Soc.*, 152:75, 1971.
- [77] B. Carr, K. Kohri, Y. Sendouda, and J. Yokoyama. Constraints on primordial black holes. *Rept. Prog. Phys.*, 84(11):116902, 2021.
- [78] N. Bartolo et al. Primordial Black Hole Dark Matter: LISA Serendipity. *Phys. Rev. Lett.*, 122(21):211301, 2019.
- [79] V. A. Acciari et al. Constraining Dark Matter lifetime with a deep gamma-ray survey of the Perseus Galaxy Cluster with MAGIC. *Phys. Dark Univ.*, 22:38–47, 2018.
- [80] M. Aker et al. Improved Upper Limit on the Neutrino Mass from a Direct Kinematic Method by KATRIN. *Phys. Rev. Lett.*, 123(22):221802, 2019.

- [81] K. Abazajian, G. M. Fuller, and M. Patel. Sterile neutrino hot, warm, and cold dark matter. *Phys. Rev. D*, 64:023501, 2001.
- [82] R. D. Peccei and H. R. Quinn. Constraints Imposed by CP Conservation in the Presence of Instantons. *Phys. Rev. D*, 16:1791–1797, 1977.
- [83] L. J. Rosenberg and K. A. van Bibber. Searches for invisible axions. *Phys. Rept.*, 325:1–39, 2000.
- [84] Th. Kaluza. Zum Unitätsproblem der Physik. *Sitzungsber. Preuss. Akad. Wiss. Berlin (Math. Phys.)*, 1921:966–972, 1921.
- [85] G. Servant and T. M. P. Tait. Is the lightest Kaluza-Klein particle a viable dark matter candidate? *Nucl. Phys. B*, 650:391–419, 2003.
- [86] D. Hooper and S. Profumo. Dark Matter and Collider Phenomenology of Universal Extra Dimensions. *Phys. Rept.*, 453:29–115, 2007.
- [87] G. Jungman, M. Kamionkowski, and K. Griest. Supersymmetric dark matter. *Phys. Rept.*, 267:195–373, 1996.
- [88] M. Milgrom. A Modification of the Newtonian dynamics as a possible alternative to the hidden mass hypothesis. *Astrophys. J.*, 270:365–370, 1983.
- [89] S. S. McGaugh. A tale of two paradigms: the mutual incommensurability of Λ CDM and MOND. *Can. J. Phys.*, 93(2):250–259, 2015.
- [90] E. Aprile et al. Dark Matter Search Results from a One Ton-Year Exposure of XENON1T. *Phys. Rev. Lett.*, 121(11):111302, 2018.
- [91] X. Cui et al. Dark Matter Results From 54-Ton-Day Exposure of PandaX-II Experiment. *Phys. Rev. Lett.*, 119(18):181302, 2017.
- [92] D. S. Akerib et al. Results from a search for dark matter in the complete LUX exposure. *Phys. Rev. Lett.*, 118(2):021303, 2017.
- [93] R. Ajaj et al. Search for dark matter with a 231-day exposure of liquid argon using DEAP-3600 at SNOLAB. *Phys. Rev. D*, 100(2):022004, 2019.
- [94] P. Agnes et al. DarkSide-50 532-day Dark Matter Search with Low-Radioactivity Argon. *Phys. Rev. D*, 98(10):102006, 2018.
- [95] R. Agnese et al. Results from the Super Cryogenic Dark Matter Search Experiment at Soudan. *Phys. Rev. Lett.*, 120(6):061802, 2018.
- [96] Q. Arnaud et al. Optimizing EDELWEISS detectors for low-mass WIMP searches. *Phys. Rev. D*, 97(2):022003, 2018.
- [97] A. H. Abdelhameed et al. First results from the CRESST-III low-mass dark matter program. *Phys. Rev. D*, 100(10):102002, 2019.

- [98] M. G. Aartsen et al. Velocity Independent Constraints on Spin-Dependent DM-Nucleon Interactions from IceCube and PICO. *Eur. Phys. J. C*, 80(9):819, 2020.
- [99] C. Amole et al. Dark Matter Search Results from the Complete Exposure of the PICO-60 C₃F₈ Bubble Chamber. *Phys. Rev. D*, 100(2):022001, 2019.
- [100] R. Bernabei et al. First results from DAMA/LIBRA and the combined results with DAMA/NaI. *Eur. Phys. J. C*, 56:333–355, 2008.
- [101] R. Bernabei et al. First model independent results from DAMA/LIBRA-phase2. *Nucl. Phys. Atom. Energy*, 19(4):307–325, 2018.
- [102] G. Adhikari et al. Initial Performance of the COSINE-100 Experiment. *Eur. Phys. J. C*, 78(2):107, 2018.
- [103] J. Amaré et al. ANAIS-112 status: two years results on annual modulation. *J. Phys. Conf. Ser.*, 1468(1):012014, 2020.
- [104] J. Cherwinka et al. First data from DM-Ice17. *Phys. Rev. D*, 90(9):092005, 2014.
- [105] P. Adhikari et al. Understanding internal backgrounds in NaI(Tl) crystals toward a 200 kg array for the KIMS-NaI experiment. *Eur. Phys. J. C*, 76(4):185, 2016.
- [106] A. Förster. Gamma-ray astronomy with H.E.S.S. *Nucl. Instrum. Meth. A*, 766:69–72, 2014.
- [107] T. C. Weekes et al. VERITAS: The Very energetic radiation imaging telescope array system. *Astropart. Phys.*, 17:221–243, 2002.
- [108] J. Cortina, F. Goebel, and T. Schweizer. Technical Performance of the MAGIC Telescopes. 7 2009.
- [109] W. B. Atwood et al. The Large Area Telescope on the Fermi Gamma-ray Space Telescope Mission. *Astrophys. J.*, 697:1071–1102, 2009.
- [110] H. Abdallah et al. Search for dark matter annihilations towards the inner Galactic halo from 10 years of observations with H.E.S.S. *Phys. Rev. Lett.*, 117(11):111301, 2016.
- [111] S. Archambault et al. Dark Matter Constraints from a Joint Analysis of Dwarf Spheroidal Galaxy Observations with VERITAS. *Phys. Rev. D*, 95(8):082001, 2017.
- [112] M. L. Ahnen et al. Limits to Dark Matter Annihilation Cross-Section from a Combined Analysis of MAGIC and Fermi-LAT Observations of Dwarf Satellite Galaxies. *JCAP*, 02:039, 2016.
- [113] P. Picozza et al. PAMELA: A Payload for Antimatter Matter Exploration and Light-nuclei Astrophysics. *Astropart. Phys.*, 27:296–315, 2007.

- [114] M. Incagli. Astroparticle physics with AMS02. *AIP Conf. Proc.*, 1223(1):43–49, 2010.
- [115] O. Adriani et al. An anomalous positron abundance in cosmic rays with energies 1.5–100 GeV. *Nature*, 458:607–609, 2009.
- [116] M. Ackermann et al. Measurement of separate cosmic-ray electron and positron spectra with the Fermi Large Area Telescope. *Phys. Rev. Lett.*, 108:011103, 2012.
- [117] M. Aguilar et al. First Result from the Alpha Magnetic Spectrometer on the International Space Station: Precision Measurement of the Positron Fraction in Primary Cosmic Rays of 0.5–350 GeV. *Phys. Rev. Lett.*, 110:141102, 2013.
- [118] A. Albert et al. Results from the search for dark matter in the Milky Way with 9 years of data of the ANTARES neutrino telescope. *Phys. Lett. B*, 769:249–254, 2017. [Erratum: *Phys.Lett.B* 796, 253–255 (2019)].
- [119] M. G. Aartsen et al. Search for Neutrinos from Dark Matter Self-Annihilations in the center of the Milky Way with 3 years of IceCube/DeepCore. *Eur. Phys. J. C*, 77(9):627, 2017.
- [120] M. G. Aartsen et al. First search for dark matter annihilations in the Earth with the IceCube Detector. *Eur. Phys. J. C*, 77(2):82, 2017.
- [121] A. Albert et al. Search for Dark Matter Annihilation in the Earth using the ANTARES Neutrino Telescope. *Phys. Dark Univ.*, 16:41–48, 2017.
- [122] M. G. Aartsen et al. Search for annihilating dark matter in the Sun with 3 years of IceCube data. *Eur. Phys. J. C*, 77(3):146, 2017. [Erratum: *Eur.Phys.J.C* 79, 214 (2019)].
- [123] S. Adrian-Martinez et al. Limits on Dark Matter Annihilation in the Sun using the ANTARES Neutrino Telescope. *Phys. Lett. B*, 759:69–74, 2016.
- [124] C. El Aisati, C. Garcia-Cely, T. Hambye, and L. Vanderheyden. Prospects for discovering a neutrino line induced by dark matter annihilation. *JCAP*, 10:021, 2017.
- [125] A. Albert et al. Search for dark matter towards the Galactic Centre with 11 years of ANTARES data. *Phys. Lett. B*, 805:135439, 2020.
- [126] LHC Machine. *JINST*, 3:S08001, 2008.
- [127] A. Tumasyan et al. Search for new particles in events with energetic jets and large missing transverse momentum in proton-proton collisions at $\sqrt{s} = 13$ TeV. *JHEP*, 11:153, 2021.
- [128] J. An and H. Zhao. Fitting functions for dark matter density profiles. *Mon. Not. Roy. Astron. Soc.*, 428:2805–2811, 2013.

- [129] F. Nesti and P. Salucci. The Dark Matter halo of the Milky Way, AD 2013. *JCAP*, 07:016, 2013.
- [130] J. F. Navarro, C. S. Frenk, and S. D. M. White. The Structure of cold dark matter halos. *Astrophys. J.*, 462:563–575, 1996.
- [131] A. Burkert. The Structure of dark matter halos in dwarf galaxies. *Astrophys. J. Lett.*, 447:L25, 1995.
- [132] W. J. G. de Blok. The Core-Cusp Problem. *Adv. Astron.*, 2010:789293, 2010.
- [133] A. Charbonnier, C. Combet, and D. Maurin. CLUMPY: a code for gamma-ray signals from dark matter structures. *Comput. Phys. Commun.*, 183:656–668, 2012.
- [134] G. Carminati, A. Margiotta, and M. Spurio. Atmospheric MUons from Parametric formulas: A Fast GENERator for neutrino telescopes (MUPAGE). *Comput. Phys. Commun.*, 179:915–923, 2008.
- [135] M. Bazzotti et al. An update of the generator of atmospheric muons from parametric formulas (MUPAGE). *Comput. Phys. Commun.*, 181:835–836, 2010.
- [136] J. Brunner. Antares simulation tools. In *VLVnT Workshop on Technical Aspects of a Very Large Volume Neutrino Telescope in the Mediterranean Sea*, pages 109–113, 10 2003.
- [137] Y. Becherini et al. A Parameterisation of single and multiple muons in the deep water or ice. *Astropart. Phys.*, 25:1–13, 2006.
- [138] D. Heck et al. CORSIKA: A Monte Carlo code to simulate extensive air showers. Technical report, 2 1998.
- [139] A. Albert et al. Monte Carlo simulations for the ANTARES underwater neutrino telescope. *JCAP*, 01:064, 2021.
- [140] P. Antonioli et al. A Three-dimensional code for muon propagation through the rock: Music. *Astropart. Phys.*, 7:357–368, 1997.
- [141] A. Margiotta. Common simulation tools for large volume neutrino detectors. *Nucl. Instrum. Meth. A*, 725:98–101, 2013.
- [142] S. Agostinelli et al. GEANT4—a simulation toolkit. *Nucl. Instrum. Meth. A*, 506:250–303, 2003.
- [143] C. Kopper. A software framework for KM3NeT. *Nucl. Instrum. Meth. A*, 602:107–110, 2009.
- [144] L.A. Fusco and A. Margiotta. The Run-by-Run Monte Carlo simulation for the ANTARES experiment. *EPJ Web Conf.*, 116:02002, 2016.

- [145] C. Andreopoulos et al. The GENIE Neutrino Monte Carlo Generator: Physics and User Manual. Technical report, 10 2015.
- [146] R.S. Fletcher et al. SIBYLL: An Event generator for simulation of high-energy cosmic ray cascades. *Phys. Rev. D*, 50:5710–5731, 1994.
- [147] T.K. Gaisser and F. Halzen. Soft Hard Scattering in the TeV Range. *Phys. Rev. Lett.*, 54:1754, 1985.
- [148] L. Durand and P. Hong. QCD and Rising Total Cross-Sections. *Phys. Rev. Lett.*, 58:303–306, 1987.
- [149] T. K. Gaisser. Spectrum of cosmic-ray nucleons, kaon production, and the atmospheric muon charge ratio. *Astropart. Phys.*, 35:801–806, 2012.
- [150] C. H. Llewellyn Smith. Neutrino Reactions at Accelerator Energies. *Phys. Rept.*, 3:261–379, 1972.
- [151] L. A. Ahrens et al. Measurement of Neutrino - Proton and anti-neutrino - Proton Elastic Scattering. *Phys. Rev. D*, 35:785, 1987.
- [152] D. Rein and L. M. Sehgal. Neutrino Excitation of Baryon Resonances and Single Pion Production. *Annals Phys.*, 133:79–153, 1981.
- [153] A. Bodek and U. K. Yang. Higher twist, xi(omega) scaling, and effective LO PDFs for lepton scattering in the few GeV region. *J. Phys. G*, 29:1899–1906, 2003.
- [154] J.H. Koehne et al. PROPOSAL: A tool for propagation of charged leptons. *Comput. Phys. Commun.*, 184:2070–2090, 2013.
- [155] M.J. Larson. *Simulation and identification of non-Poissonian noise triggers in the IceCube neutrino detector*. PhD thesis, Alabama U., 2013.
- [156] C. Weaver. *Evidence for Astrophysical Muon Neutrinos from the Northern Sky*. PhD thesis, Wisconsin U., Madison, 2015.
- [157] J.A. Aguilar et al. A fast algorithm for muon track reconstruction and its application to the ANTARES neutrino telescope. *Astropart. Phys.*, 34:652–662, 2011.
- [158] S. Adrian-Martinez et al. Search for Cosmic Neutrino Point Sources with Four Year Data of the ANTARES Telescope. *Astrophys. J.*, 760:53, 2012.
- [159] M.G. Aartsen et al. Improvement in Fast Particle Track Reconstruction with Robust Statistics. *Nucl. Instrum. Meth. A*, 736:143–149, 2014.
- [160] J. Ahrens et al. Muon track reconstruction and data selection techniques in AMANDA. *Nucl. Instrum. Meth. A*, 524:169–194, 2004.

- [161] J. Hulss. *Search for neutrinos from the direction of the Galactic Center with the IceCube neutrino telescope*. PhD thesis, RWTH Aachen, Tech. Hochsch., 2010.
- [162] S. Flis. Extending IceCube Low Energy Neutrino Searches for Dark Matter with DeepCore. In *33rd International Cosmic Ray Conference*, 2013.
- [163] Y. Freund and R. E. Schapire. A Decision-Theoretic Generalization of On-Line Learning and an Application to Boosting. *J. Comput. Syst. Sci.*, 55(1):119–139, 1997.
- [164] C. H. Ha. *Observation of Atmospheric Neutrino-induced Cascades in IceCube with DeepCore*. PhD thesis, Penn State U., 2011.
- [165] S. Euler. *Observation of oscillations of atmospheric neutrinos with the IceCube Neutrino Observatory*. PhD thesis, RWTH Aachen, 2014.
- [166] F. Feroz, M. P. Hobson, and M. Bridges. MultiNest: an efficient and robust Bayesian inference tool for cosmology and particle physics. *Mon. Not. Roy. Astron. Soc.*, 398:1601–1614, 2009.
- [167] A. Hocker et al. TMVA - Toolkit for Multivariate Data Analysis. Technical report, 3 2007.
- [168] M. Cirelli et al. PPC 4 DM ID: A Poor Particle Physicist Cookbook for Dark Matter Indirect Detection. *JCAP*, 03:051, 2011. [Erratum: *JCAP* 10, E01 (2012)].
- [169] T. Sjostrand, S. Mrenna, and P. Z. Skands. A Brief Introduction to PYTHIA 8.1. *Comput. Phys. Commun.*, 178:852–867, 2008.
- [170] P. Ciafaloni et al. Weak Corrections are Relevant for Dark Matter Indirect Detection. *JCAP*, 03:019, 2011.
- [171] C. Amsler et al. Review of Particle Physics. *Phys. Lett. B*, 667:1–1340, 2008.
- [172] G. J. Feldman and R. D. Cousins. A Unified approach to the classical statistical analysis of small signals. *Phys. Rev. D*, 57:3873–3889, 1998.
- [173] P. J. McMillan. The mass distribution and gravitational potential of the Milky Way. *Mon. Not. Roy. Astron. Soc.*, 465(1):76–94, February 2017.
- [174] S. Adrian-Martinez et al. Search for Cosmic Neutrino Point Sources with Four Year Data of the ANTARES Telescope. *Astrophys. J.*, 760:53, 2012.
- [175] J. Neyman. Outline of a Theory of Statistical Estimation Based on the Classical Theory of Probability. *Phil. Trans. Roy. Soc. Lond. A*, 236(767):333–380, 1937.
- [176] J. van Santen. *Neutrino Interactions in IceCube above 1 TeV: Constraints on Atmospheric Charmed-Meson Production and Investigation of the Astrophysical Neutrino Flux with 2 Years of IceCube Data taken 2010–2012*. PhD thesis, Wisconsin U., Madison, 11 2014.

- [177] T. K. Gaisser. Spectrum of cosmic-ray nucleons, kaon production, and the atmospheric muon charge ratio. *Astropart. Phys.*, 35:801–806, 2012.
- [178] S. Weglarczyk. Kernel density estimation and its application. *ITM Web Conf.*, 23:00037, 2018.
- [179] M. Honda et al. Atmospheric neutrino flux calculation using the NRLMSISE-00 atmospheric model. *Phys. Rev. D*, 92(2):023004, 2015.
- [180] M. G. Aartsen et al. In-situ calibration of the single-photoelectron charge response of the IceCube photomultiplier tubes. *JINST*, 15(06):P06032, 2020.
- [181] Ke, G. and others. LightGBM: A Highly Efficient Gradient Boosting Decision Tree. In *Advances in Neural Information Processing Systems*, volume 30, 2017.
- [182] M. C. Gonzalez-Garcia, M. Maltoni, and T. Schwetz. Updated fit to three neutrino mixing: status of leptonic CP violation. *JHEP*, 11:052, 2014.
- [183] Nufit 2.0 (2014). <http://www.nu-fit.org/>. Accessed: 2021-12-14.
- [184] B.W. Silverman. *Density Estimation for Statistics and Data Analysis*. Chapman and Hall/CRC, 1998.
- [185] F. Pedregosa et al. Scikit-learn: Machine Learning in Python. *Journal of Machine Learning Research*, 12:2825–2830, 2011.
- [186] D. Scott and G. Terrell. Biased and Unbiased Cross-Validation in Density Estimation. *Journal of the American Statistical Association*, 82:1131–1146, 12 1987.
- [187] G. Cowan, K. Cranmer, E. Gross, and O. Vitells. Asymptotic formulae for likelihood-based tests of new physics. *Eur. Phys. J. C*, 71:1554, 2011. [Erratum: *Eur.Phys.J.C* 73, 2501 (2013)].
- [188] S. S. Wilks. The Large-Sample Distribution of the Likelihood Ratio for Testing Composite Hypotheses. *Annals Math. Statist.*, 9(1):60–62, 1938.
- [189] A. Fedynitch et al. Calculation of conventional and prompt lepton fluxes at very high energy. *EPJ Web Conf.*, 99:08001, 2015.
- [190] U.S. Standard Atmosphere. Technical report, National Oceanic and Atmospheric Administration, National Aeronautics and Space Administration, United States Air Force., 1976.
- [191] F. Riehn et al. The hadronic interaction model SIBYLL 2.3c and Feynman scaling. *PoS, ICRC2017:301*, 2018.
- [192] S. Ostapchenko. Monte Carlo treatment of hadronic interactions in enhanced Pomeron scheme: I. QGSJET-II model. *Phys. Rev. D*, 83:014018, 2011.
- [193] T. K. Gaisser and M. Honda. Flux of atmospheric neutrinos. *Ann. Rev. Nucl. Part. Sci.*, 52:153–199, 2002.

- [194] J. Alcaraz et al. Cosmic protons. *Phys. Lett. B*, 490:27–35, 2000.
- [195] T. Sanuki et al. Precise measurement of cosmic ray proton and helium spectra with the BESS spectrometer. *Astrophys. J.*, 545:1135, 2000.
- [196] A. Gazizov and M. P. Kowalski. ANIS: High energy neutrino generator for neutrino telescopes. *Comput. Phys. Commun.*, 172:203–213, 2005.